A NUMERICAL METHOD FOR TWO-DIMENSIONAL STUDIES OF LARGE AMPLITUDE MOTIONS OF FLOATING BODIES IN STEEP WAVES

DEBABRATA SEN

A NUMERICAL METHOD FOR TWO-DIMENSIONAL STUDIES OF LARGE AMPLITUDE MOTIONS OF FLOATING BODIES IN STEEP WAVES

by

© Debabrata Sen, *B. Tech. (Hons.), M. Eng.*

A thesis submitted to the School of Graduate Studies in partial fulfillment of the requirements for the degree of Doctor of Philosophy

Faculty of Engineering & Applied Science
Memorial University of Newfoundland
St. John's, Newfoundland
Canada

June, 1988

To

My Parents

Abstract

A numerical time-domain method is developed to simulate large-amplitude motions of two-dimensional floating bodies in steep waves. The method employs an integral relation derived from Green's second identity and a discretization scheme of centrally located collocation points on linear boundary segments for solution of the full non-linear potential flow problem. Propagating unsteady waves are simulated by imposing an Airy wave potential as a source of excitation on a hypothetical vertical boundary of a rectangular fluid domain. Solutions of linearized wave-propagation problems are in very good agreement with analytical solutions. For the non-linear problem, an Eulerian description of the free surface is used in which vertical movements of the collocation points on the free surface are followed. Smoothing schemes in space and time at the upstream boundary, intermittent smoothing of the free surface and adaptation of a numerical radiation condition permit modelling of very steep progressing waves over 20 wave periods. Numerical experiments reveal insignificant degeneration of the solution resulting from the embodied techniques. The effectiveness of the method is further illustrated by its application to a study of steep waves interacting with vertical walls. Comparison with experimental and analytical results demonstrates the capability of the method in accomplishing non-linear steady state solutions with very good quality of agreement with experimental data.

In the study of behaviour of floating bodies in steep waves, numerical instability leads to failure of the simulation scheme unless special care is taken with regard to the discretization and treatment of the coupled force-motion relation. The motion of the body with respect to the free surface may result in large variations of the spatial grid sizes in the vicinity of the body and the free surface

intersection, which results in destabilizing force effects through the computation of the linear dynamic pressure term $(d\phi/dt)$. These difficulties are resolved by means of an appropriate spatial regridding scheme, and by employing a central difference rule for computation of the $d\phi/dt$ term at the corrector level of the adopted Adams-Bashforth-Moulton rule in the time-integration scheme and by utilizing explicit rules for integration of the equations of motion. A number of computations simulating motions of a rectangular floating body in different situations provides evidence of the efficacy of the algorithm. The presented results contain large roll and heave motions as well as drifting behaviour of a completely unrestrained body.

A complementary experimental study is also described, in which a rectangular body of rounded-off corners restricted from swaying was subjected to wave excitations inside a channel. Comparison of experimental and computational results shows in general very good agreement over the entire range of the tested conditions, inclusive of resonant behaviour in heave and moderately large roll motions. For this latter behaviour, accounting for viscous effects by means of a semi-empirical procedure improves the correlation significantly.

Acknowledgements

First and foremost, sincere gratitude is expressed to my supervisors, Dr. James H. Lever, Dr. Michael J. Hinchey and Dr. Jacek S. Pawlowski, for their guidance, constructive suggestions and encouragement, as well as for their support in form of finances and/or other resources. Additionally, I take this opportunity to express my deep appreciation to the latter (J.S.P.) for his persistent interest in this work and teaching me many aspects of numerical hydrodynamics; I recall the number of hours he spent in providing me with valuable ideas, encouragement and advice, specially during the computational work when repeated occurrence of numerical instability in its insidious form often led to disappointments. I also wish to thank Dr. C. C. Hsiung, my former supervisor during the master's program and presently Professor at the Technical University of Nova Scotia, for introducing me to the interesting subject of marine hydrodynamics and teaching with care the basics of the subject.

I am indebted to Dr. F. A. Aldrich and Dr. C. A. Sharpe, former and present Dean of Graduate Studies respectively, for providing me with financial supports, which enabled my stay and study here. Thanks are also due to ICOD (International Center for Ocean Development), Halifax, for awarding me a Bursary and a Fellowship during the years 1985-86 and 1986-87 respectively.

Appreciation is extended to Dr. J. R. Peters and Dr. T. R. Chari, Dean and Associate Dean of this faculty (Engineering and Applied Science) for their support during the overall course of my study here. Further, the latter and Mrs. Moya Crocker, secretary of the Associate Dean's office, are acknowledged for ensuring a smooth and efficient operation of the associated administrative tasks of my graduate program. I also wish to thank Dr. D. B. Muggeridge, who chairs the Ocean Engineering Research Group, for his interest and encouragement in general, and support during the experimental part of this work in particular. This opportunity is taken to extend appreciation to the members of the technical services and the wave tank group, particulary Mr. J. Andrews, Mr. P. Robinson and Mr. D. Tilley of the former, and Mr. M. Sullivan, Mr. Wayne Brown and Mr. L. Little of the latter, as well as Mr. I. Fradsham, who at that time was attached to the wave tank group as a work-term student; their help and support contributed to completion of the experimental program to its present form. The quality of some of the illustrations, specially those pertaining to the experimental set-up, resulted from Mr. T. Dyer and Mr. B. Bower's careful draftsmanship, both of whom I thank.

The assistance provided by the staff of the Computing Center of this University in frequently supplying computer plots is remembered with a sense of gratitude. Deep appreciation is also extended to the staff of the CCAE of this faculty, who assisted in every aspect during preparation of the text. Additionally, I wish to thank my colleagues and fellow graduate students for their support, encouragement and company, specially during stressful periods. In anticipation of any oversight that remains, at this time I wish to express my appreciation to all who contributed directly or indirectly to this work.

This acknowledgement would be incomplete if I did not express my deep gratitude to my parents; towards my studies here, their silent support from across the miles has always been the most important source of inspiration.

Table of Contents

List of Tables

List of Figures

Nomenclature

α	:	a factor used in studying the radiation condition
γ'	:	angular coordinate of a point on the body surface in the body coordinate system
δI_θ	:	added moment of inertia
$\delta_{i,j}$	:	Kronecker's delta
$\delta\tau_{(\,,\,)}$	:	difference between various $\tau_{(\,)}$ values
δS	:	a segment on the boundary
$\Delta\beta_F, \Delta\beta_z, \Delta\beta_\theta$	:	difference of the peak-to-peak values of force and motions between experiment and theory
$\Delta F_x, \Delta z_G, \Delta\theta$	:	phase differences of force and motions between experiment and theory
$\Delta\ell, \Delta S$	:	length of a segment
Δt	:	temporal grid size
$\Delta x, \Delta x_{(\,)}$	:	spatial grid sizes
η	:	free surface elevation
θ	:	angular displacement/roll angle
$\lvert\theta\rvert$	:	peak-to-peak roll displacement
θ_A	:	amplitude of roll oscillation (Appendix B)
λ	:	wave length
ξ	:	wave-maker displacement
$\tau_{(\,)}$	:	time of occurence of peaks in various records
ρ	:	fluid density
σ	:	time span over which the excitation potential is modulated
ϕ	:	velocity potential
ϕ^*	:	modulated velocity potential
ω	:	radian frequency
ω_n^h	:	natural frequency in heave
ω_n^r	:	natural frequency in roll
ϖ	:	angular velocity
$\vec{\varpi}$	:	vectorial form of ϖ
Ω	:	a quantity in the integral relation (2.6)
$\partial(\;)$	:	parts of the fluid boundary
φ	:	a function of (....)
a	:	wave amplitude
a_1, a_2	:	coefficients in eqns. (2.14) and (4.10)
a_x, a_z, b	:	coefficients in eqn. (2.14)

a_3	:	coefficient in eqn. (4.10)
a_{22}	:	added mass in heave
$A_{i,j}$	:	influence coefficients
b	:	half breadth of the body
$b_{()}^{()}$	:	damping moments
B	:	full breadth of the body
$\mathcal{B}$	:	the body
$B_{()}^{()}$	:	damping coefficients
$\bar{B}_{()}^{()}$	:	non-dimensionalized damping coefficients
$B_{i,j}$	:	influence coefficients
BM	:	distance between center of buoyancy and metacenter
c	:	wave celerity
c'	:	αc
c_g	:	wave group speed
c_{22}	:	heave restoring force
C_θ	:	roll restoring moment
d	:	water depth
$\bar{d}$	:	mean water depth
$\mathcal{D}$	:	fluid domain
$\mathcal{D}^*$	:	reduced fluid domain (excluding matching region)
f	:	ordinates of a curve (also indicates frequency in Tables 7.5 and 8.1)
$\bar{f}$	:	ordinates of a curve after smoothing
$f_1(x), f_2(x), f_2^*(x), f_g$	:	functions representing various curves (as explained in §4.2.1)
$\mathbf{F}$	:	force vector
F_x, F_z	:	x and z components of force
$\hat{F}_x$	:	total horizontal force on the model
$\lvert F_x\rvert, \lvert F_z\rvert$	:	peak-to-peak values of F_x and F_z
$\lvert\bar{F}_x\rvert$	:	non-dimensional $\lvert F_x\rvert$
g	:	gravitational acceleration
$g(x)$	:	a function used for the matching procedure
G	:	origin of the $Gx'z'$ coordinate system (i.e. the body's center of gravity)
$\mathbf{G}$	:	submatrices of influence coefficients
GM	:	metacentric height
$Gx'z'$	:	body coordinate system
H, H^*, H_s	:	wave heights

$\mathbf{H}$	:	sub-matrices of influence coefficients
I_θ	:	roll moment of inertia
k	:	wave number
K	:	c/c_g
KG	:	vertical distance of center of gravity measured from keel
l	:	length of the matching region
L	:	length of the fluid domain
L_1, L_2, L_1^*, L_2^*	:	various distance in the fluid domain (as defined in Figure 6.4)
L_B	:	length of the model
L_C	:	length of the channel
M	:	a variable indicating a number
$M(t)$	:	the modulation function
M_θ	:	roll moment
$\tilde{M}_\theta$	:	roll moment in a single degree of freedom roll equation of motion
$\|M_\theta\|$	:	peak-to-peak value of M_θ
M_B	:	mass of the body
M_d	:	overturning moment, taken about the foot of a wall
M_k	:	number of segments in the kth part of the boundary contour
$\mathbf{n}$	:	unit normal vector outward of $\mathcal{D}$
n_x, n_z	:	x and z components of $\mathbf{n}$
N	:	total number of segments on the boundary
N_Γ	:	time steps in numerical difference formulae
N_τ	:	number of periods in the selected window
N_B	:	number of segments on the submerged surface of the body
N_{CFL}	:	a number defining Courant-Friedrichs-Lewy condition
N_P	:	number of periods
N_S	:	number of boundary parts in the full boundary
N_t	:	number indicating time-step level
N_w	:	number of segments on a wall
O	:	origin of the inertial coordinate system
Oxz	:	inertial coordinate system
p, p_1, p_2, p_3	:	pressure and its components
p_a	:	atmospheric pressure
P, Q, q	:	representative of a point
Q'	:	image of Q on sea-bottom
r	:	relative run-up on the lee side of the body

$\mathbf{R}$	:	matrix of coordinate transformation
s	:	half-stroke of the wave-maker
S_A	:	submerged area of the undisturbed body
t	:	time
T_1, T_2, T_1^*, T_2^*	:	times at which the fully developed wave-front is likely to reach given locations
T^h	:	natural period in heave
U	:	impulsive velocity of a translating vertical wall
u_G, v_G	:	x and z components of velocity of G
$\mathbf{v}, \mathbf{v}_G, \mathbf{v}_q$	:	velocity vectors
V_n	:	normal component of velocity vector
x, z	:	coordinates
$\mathbf{x}$	:	radius vector in the inertial coordinate system
$\mathbf{x}'$	:	radius vector in the body coordinate system
$\mathbf{x}_{(\,)}$	:	radius vector of ( ) in the inertial system
$\mathbf{x}'_{(\,)}$	:	radius vector of ( ) in the body system
$x_{(\,)}, z_{(\,)}$	:	x and z coordinates of ( )
x_G	:	horizontal displacement of the body
z_G	:	vertical displacement of the body
$\hat{z}_G$	:	vertical displacement of the body measured from G
$\|x_G\|, \|z_G\|$	:	peak-to-peak values of x and z displacements
$\|\bar{z}_G\|$	:	non-dimensional $\|z_G\|$

1 Introduction

1.1 General

Interaction of floating bodies with water waves has been a prominent and active area of research since last century when notable contributions on the subject were made by J.H.Michell and Sir William Thompson (Lord Kelvin). Subsequently, considerable advancements of primarily analytical nature were made during the first half of this century. In this early period, works were mainly concerned with understanding of the behaviour of displacement-type ships. Consequent to the mathematical undertone of hydrodynamics as well as the areas of applications, most workers of that period belonged to the group of applied mathematicians and ship-hydrodynamicists. From about middle of the century, a progressive change in this general picture can be observed. The field of application widened considerably due to emergence of the parallel discipline of Ocean Engineering. A variety of offshore structures of different sizes and geometries arose to append to the list of floating bodies. The simultaneous development of the power of computing machines opened avenues for newer methods of analyses. Consequential increase in the number of workers was complementary. Recently, international workshops devoted entirely to the behaviour of floating bodies in water waves have been initiated on an annual basis (Evans and Newman 1987)[1], which serves to indicate the growth of research activities in this field. Despite a substantial body of accumulated knowledge, a number of important and interesting problems await satisfactory resolutions. One such problem is that of large motions of floating bodies in steep waves.

[1]Name and/or year included in the parentheses refer to the publications listed under 'References' at the end of the text

The present dissertation is directed towards the development of a method that predicts extreme motions of floating bodies in steep waves. The practical implications of such predictions need no elaboration. Suffice it to say that knowledge of extreme behaviours constitutes an essential foundation for efficient and safe design tasks.

The following section provides a review of the present state of understanding of the subject (i.e. motions of floating bodies in waves). The discussion is directed towards development of computational tools for general studies of bodies in waves, in contrast to application of established techniques (e.g. well known linear solutions) in studies of the motion responses of continually emerging newer geometries. The scope, objective, and the nature of the present task are outlined in the section that follows, with the view that a better perspective of the work to be presented can be attained. This section also includes brief descriptions of the rest of the text.

1.2 Previous Work

1.2.1 Background

For most engineering purposes, the Navier-Stokes equations can be regarded as the fundamental relations governing fluid motions that adequately describe flow surrounding marine structures (Batchelor 1967). Neglect of viscous effects usually leads to potential flow (ideal fluid) formulations. For a number of hydrodynamic problems, including studies of wave forces and motions of ships and offshore structures, the importance of potential flow theories is universally recognized. A large body of analytical, numerical and experimental investigations would support that treatment of water as an ideal fluid indeed yields fruitful results for many situations of practical interest. Although a growing literature currently exists addressing solution of Navier-Stokes equations at a variety of levels (see Aref 1986), applications of such methods, or methods based on Lagrangian vortex schemes, to studies concerning wave-body interactions appear to be a subject of further research (see e.g. Nichols and Hirt 1973, 1975, 1977; Miyata, Kajitani, Zhu and Kawano 1986; Stansby and Dixon 1983). For circumstances where viscous effects become significant, a practical means for incorporating such effects, at present, is through semi-empirical formulations. A classical example of this is provided by the Morison's formula (Morison et al. 1950) which in its original and modified forms continues to be a popular and practical means for considering viscous effects in computation of wave forces on certain 'slender' structural members (Faltinsen 1985, Pawlowski 1987). Among other situations where fluid viscosity require attention, a relevant example is provided by large roll motions of ships, and these effects are usually considered via semi-empirical relations appropriately guided by experimental data (Himeno 1981). For studies of body motions in waves, a general solution approach with the use of Navier-Stokes equations appears to be too difficult at present. In view of these remarks, the discussion that follows is confined to studies based on potential theory formulations[2].

Two classes of hydrodynamic problems are generally recognized in studies of marine structures interacting with water: diffraction and radiation problems. The former is concerned with an object held fixed in an incident wave train while in the latter the object is forced to oscillate in an otherwise quiescent

[2]In the regime of direct numerical methods (§1.2.2.2 below), however, some of the cited works based on finite-difference algorithms consider solution of Navier-Stokes equations

fluid. Analyses for motions of floating bodies excited by oncoming waves encompass both these problems. Upon approximation of smallness in wave steepness and in body motions, the familiar linearized problems emerge. In the realm of linearized potential theory, established relations (e.g. Haskind's relation) exist interconnecting the radiation and diffraction problems. Therefore solution methods for radiation problems generally suffice in studies of body motions in waves (for the linearized problems). More elaborate descriptions of theoretical developments including expressions for quantities of practical interest (e.g. forces and motions) are well documented in texts of Wehausen and Laitone (1960) and Newman (1980).

Analyses of the above linearized problems are usually performed in frequency domain. Over the past three decades or so, a multitude of computational methods have evolved for such studies. A comprehensive review outlining fundamentals of various methods can be found in Mei (1978). Amongst these, methods founded upon integral relation formulations have a relatively enriched background in hydrodynamic applications, in contrast to, for example, the methods of finite elements known for their phenomenal success in structural dynamics problems (Zienkiewicz 1979). Integral relations can themselves be formed in a variety of ways: distribution of monopoles, dipoles, mixed distributions, multipoles, etc. (see e.g. Burton and Miller 1971; Takagi et al. 1983). For the linear hydrodynamic problems in context, popularity of techniques that employ singularity distributions is evident from their widespread applications. These numerical models, often referred to as 'panel' methods, necessarily proceed by representing the immersed body boundary by an ensemble of appropriately arranged surface 'panels' over which singularities are distributed in some prescribed manner. The development of these techniques is believed to have followed from their successful implementation in analogous aerodynamic studies (Hess and Smith 1964, 1967), although an inquisitive search reveals inception of similar ideas in von Karman's works in 1927 (Baddour and Pawlowski 1985). The relative delay in progress for parallel applications in free surface hydrodynamics is usually attributed to the complicated form of the associated Green's functions. Numerical schemes based on these functions started being realized since the beginning of the past decade (Faltinsen and Michelsen 1974; Garrison and Seetharama Rao 1971; Garrison 1974, 1975). At present, a substantial amount of literature exists addressing various aspects of the available methods. For a comprehensive review, the texts by Sarpakaya and Isaacson (1979) and Mei (1983) can be consulted. Computational models evaluating forces and motion responses of bodies of arbitrary three-dimensional geometries in linearized harmonic potential flow field are regarded to be sufficiently well established at present. Indeed, several computer codes are currently available for such predictions, and studies have been initiated for assessing relative merits of these codes (Takagi et al. 1985; Eatock-Taylor and Jefferys 1986). Recent developments are primarily towards improvements in computational efficiencies. For example, in panel based methods, efforts are towards faster numerical evaluation of the associated Green's functions (Noblesse 1982; Newman 1984, 1985b, 1985c; Telste and Noblesse 1986; Endo 1987), or refinements in the discretization procedure leading to higher order panel methods (Breit, Newman and Sclavounos 1985), or at a more fundamental level, development of alternative integral relation representations possessing superior features (Kleinman 1982; Angell, Hsiao and Kleinman 1986).

Application of time domain analyses in this connection is relatively scarce since for the linearized problems frequency domain analyses usually satisfy practical needs. These modes of analyses appear more suitable for studies of transient responses. Two related problems can be identified in this context: (i) an initial displacement or velocity is imposed on a body, and the ensuing motion of the body is to be determined; (ii) fluid motion is initiated by an impulse provided by the body which is then held fixed, and the subsequent motion of the fluid is to be followed. Theoretical backgrounds on solution methods for these can be found in e.g. Finkelstein (1957), Wehausen (1967, 1971) and Ursell (1964). Computational studies include Adachi and Ohmatsu (1980), Yeung (1981), Newman (1985a), Lee (1985), Beck and Liapis (1987), etc. Recently there is an indication that time domain analyses may prove competitive in radiation-diffraction studies in that the associated computational burdens may be smaller in comparison with analogous frequency domain studies, specially for bodies that demand a large number of panels (Newman 1985a, Korsemeyer 1987).

A logical extension of the above linearized solutions is to relax, to some degree, the underlying assumptions of the smallness of motions and wave steepness. Research towards non-linear analyses immediately follows. In addition to the theoretician's interest in developing general solutions for these classes of non-linear problems as exactly as possible, practical importance of such extensions cannot be ignored. Indeed, several phenomena, e.g. mean drift forces and slow drift oscillations are now recognized to have considerable practical implications, which are not describable through a linearized analyses even to a first approximation (Ogilvie 1983). Other examples of importance include extreme motions of floating bodies in steep waves and impact slamming, both of which may have catastrophic consequences. Recent analytical and experimental work of Longuet-Higgins (1986) have shown that capsizing of a floating object can occur on passage of a single steep wave. Application of linear methods in such situations yields results of questionable accuracy. Clearly, the fundamental assumptions of the smallness of motions and wave steepnesses are violated to a large degree. Motivation towards non-linear analyses is therefore well founded.

1.2.2 Non-linear Body-Wave Problems

The subject of water waves, with more than 150 years of history behind, is not simple. An exact analytical description of the propagation of surface gravity waves still remains a formidably difficult task. Several texts, e.g. Stoker (1966) serve to illustrate the mathematical difficulties involved in solutions of non-linear free surface motions even when additional justifiable approximations are made. The complexity substantially compounds with the introduction of a body into the wave field. It is instructive to remark here that surface waves and free surface motions are intimately related. The definition provided by Wehausen and Laitone (1960) which states that any motion of a fluid with a free surface in a gravitational force field can be called a wave motion is presumed to be understood for the following discussion.

Major difficulties in non-linear free surface problems arise due to the highly non-linear free surface conditions (eqns. (2.2) and (2.3) in §2). The domain of interest is bounded by a continually changing unknown geometry (the free surface) upon which the condition of constant pressure is applicable. Additional non-linearities are posed by the body kinematic condition (eqn. (2.5) in §2) which is to be met on the instantaneous body surface. Once again, the location of the body at any instant presupposes a knowledge of its motion – an unknown sought for in the solution. For problems in unbounded fluid domains, imposition of radiation conditions (or its equivalent) is a source of further difficulties. For non-linear problems, such conditions are either not known or are available in forms that are difficult to apply (see Yeung 1982).

Without loss of generality, two broad divisions can be made with regard to general solution methods for the body-wave problems under discussion: methods based on perturbation solutions and direct numerical methods. It is recognized that methods whose ultimate objective is to enable a quantitative evaluation of the flow field and body responses, resort to numerical techniques at some level is almost inevitable. The confusion in classification however disappears when the division is meant to focus on the manner in which the governing equations are tackled.

1.2.2.1 Methods of Perturbation Solutions

Solution methods constructed on systematic expansions, or matched asymptotic expansions, have an extensive background. The principles behind perturbation-type solution techniques are relatively well known. For a treatment of such methods in fluid dynamics problems, readers may refer to van Dyke (1964). These techniques provide a recognized approach to consider non-linearities of a system in a successive manner and are commonly employed in frequency domain analyses. In connection to wave theories, classical examples are provided by Stokes higher order wave theories and shallow water non-linear theories, both of which have undergone extensive sophistication and refinements in the recent past. Analytical expansions for Stokian, cnoidal and solitary waves beyond the limit at which theories become inapplicable are currently available, e.g. Schwartz 1974, Fenton 1972, 1979 (see also the recent reviews by Miles 1980 and Schwartz and Fenton 1982). In contrast, parallel developments for body-wave interactions have been less rapid. As already noted, introduction of a body into the fluid raises the level of difficulty considerably. A number of second order terms emerge upon appropriate expansions, some of which arise essentially from linear wave effects. For example, Pinkster has identified upto five second order terms in connection to studies of bodies responding in an irregular seaway, the sea being essentially composed of small amplitude waves (Pinkster 1976, 1979). A theoretically rigorous solution method requires inclusion of all second order effects for consistency in approximations. Confronted with the difficulty in incorporating all higher order terms in the solution while recognizing the importance of some of the second order terms, researchers often develop models that consider specific non-linear effects in an effort to partially account for non-linearities in the system.

Non-linear diffraction solutions for the fundamental case of a bottom mounted circular cylinder have received much attention from Ocean Engineers. Extensions of the linear diffraction solution of MacCamy and Fuchs (1954) upto second order in a Stokian wave field are considered by Chakrabarti (1972, 1975), Raman et al. (1976, 1977), Molin (1979), Hunt and Baddour (1981), Garrison (1984a), among others. Garrison's solution aims at the complete three-dimensional radiation-diffraction problem. Analogous studies in cnoidal and solitary waves are reported in Isaacson (1977, 1983a). Literature indicates controversies over theoretical validities and merits of the various solutions. Although the underlying basic principles are similar, solutions differ in details and lead to quantitatively inconsistent results. For more on this, interested readers may refer to the reviews by Standing (1984) and Garrison (1984b), or consult the text by Chakrabarti (1987).

A lucid exposition on fluids interacting with fixed offshore structures is provided by Lighthill (1979), succeeded by a later publication (Lighthill 1986). Starting from fundamental principles of fluid behaviour, the author derives expressions for various components of fluid forces. In the context of non-linear forces, some of his cautionary notes are worth mentioning here. Incorporation of second order effects requires careful evaluation of the terms involved, and consistency in expansions has important implications in this regard. In particular, the school of thought in which higher order wave theories are employed in considering the incident wave field while a consistent order of expansion is not accounted for in the diffraction effects is remarked to be not logically satisfactory. Without properly (quantitatively) assessing the relative importance of the second order effects, inclusion and/or omission of specific higher order terms in the solution may lead to estimates of rather unclear accuracies. Experimental evaluation of the specific second order effects is generally not a simple task due to problems in separating them. Additionally, relative smallness of their magnitudes makes accurate measurements difficult.

Subsequent to the publication of Lighthill's (1979) work, a number of studies appeared in literature reporting on computational methods to calculate some or all of the non-linear effects (Debnath and Rahman 1981; Rahman and Chakravartty 1981; Rahman 1984; Sabuncu and Goren 1985). In the process, more generalizations of some of the terms are also reported (Demirbilek and in considering complicated geometric configurations. Additionally, a direct numerical approach is often indispensible for many problems of practical interest due to lack of appropriate analytical (closed-form) solutions. Depending on the manner in which the basic equations are treated, three broad classifications can be made: methods of finite differences, finite elements and integral equations. Nevertheless, more outstanding methods are continuously emerging which exploit specific merits of each. An informative account of methods that have been developed or applied to problems which have the free surface as a boundary can be found in Yeung (1982), with an extensive list of references therein. Details with regard to convergence, stability, accuracy etc. are important attributes to the ultimate success of the specific models or their particular implementations. Many of these methods are developed for general fluid dynamics problems to which study of body-free surface interactions is one of the possible applications. At present, the literature on computational fluid dynamics is enormous. To keep the following discussion in perspective, it will be limited to those studies which have direct relevance to the non-linear body-wave problems.

A forerunner of the methods which consider a body in a wave field is clearly the numerical studies on steep waves themselves. In particular, these studies aid in establishing numerical treatment of the highly non-linear free surface conditions. Substantial progress has been made in studies of waves that are steady in a time frame, complementary to the parallel progress in perturbation based models. Beginning with Dean's numerical treatment of the free surface conditions (Dean 1965), developments reported in Rienecker and Fenton (1981) and Fenton and Rienecker (1982) are now believed to be more than adequate in precision and versatility for engineering applications (Isaacson 1985).

Studies for unsteady waves pose further problems in that the time dependence can not be removed from the basic method of solution. Initial-value formulations offer attractive means of solutions for problems of this class. The generalized finite-difference methods for fluid flows, viz. MAC (Marker and Cell) type algorithms (see e.g. Welch et al. 1966) in their successively refined and sophisticated versions have been applied for simulation of a variety of unsteady waves (e.g. Chan and Street 1970, Chan 1975; Yen, Lee and Akai 1977). Other similar studies include von Kerczek and Salvesen (1974) and Salvesen and von Kerczek (1976). Finite element methods have also been applied for such studies (see e.g. Betts and Asaat 1981; Wellford and Ganaba 1981; Toro and Caroll 1984; Toro 1986, Katopodes and Wu 1987).

The most successful studies of unsteady steep waves are perhaps those that employ an integral relation formulation. These methods of simulation have been pioneered by Longuet-Higgins and Cokelet (1976). Elegant in its simplicity, their method modelled the propagation of unsteady steep waves, and subsequently wave breaking was simulated. Complementary studies following the same line of approach appeared subsequently. Three different techniques in the formulation of the basic integral relation have so far been applied: application of Cauchy's integral theorem (Vinje and co-workers 1981, 1982); distribution of dipoles or vortices (Baker, Meiron and Orszag 1981, 1982); and application of Green's second identity (New, McIver and Peregrine 1985). These formulations have implications with regard to the efficiency of the algorithms and other subtle computational differences. For example, the vortex method yields a Fredholm's integral equation of the second type for the unknowns, which has superior features with respect to numerical solutions of the resulting system of linear equations. On the other hand, the formulation based on Green's second identity can in principle be extended to three dimensions, and such extensions are not available through the formulation based on Cauchy's integral theorem. The simulation of highly non-linear, steep breaking waves appears possible at present. Nevertheless, investigations continue to be reported, either demonstrating use of other techniques, or improving efficiency, or making them more amenable to specific applications (Alleney 1981; Kobayashi, Otta and Roy 1987; Lu, Wang and Le Mehaute 1987).

Numerical studies when a body is introduced beneath or piercing the free surface, following the use of finite-difference algorithms, e.g. modified versions of MAC type algorithms, can be found in several studies (Nichols and Hirt 1973, 1975, 1977; Chan and Hirt 1974). Such finite-difference algorithms have been applied for simulating flow around forward-moving ships in two- and three-dimensions (Ohring and Telste 1977; Chan 1977; Chan and Chan 1980). Though a relatively larger number of studies can be found in connection with ship-maneuvering and wave-resistance problems via analogous (but sufficiently modified) finite-difference techniques (e.g. Bourianoff and Penumalli 1977; Bourianoff 1981; Miyata and Nishimura 1985; Miyata, Nishimura and Kajitani 1985; Miyata, Nishimura and Masuko 1985; Chamberlain and Yen 1985), comparatively smaller number of studies have been attempted for the simulation of motions of freely floating bodies, specially the non-linear ones. Some recent works in this category include Telste (1985), and Wu and Yeung (1987), both of which deal with non-linear forced oscillation problems in two dimensions. Methods of finite elements have apparently not been applied for similar non-linear studies.

Most recent works concerning motions of freely floating bodies have followed from the integral equation approach, combined with time stepping of the non-linear free surface conditions, originally employed by Longuet-Higgins and Cokelet (1976) in studies of steep waves as already discussed. Faltinsen (1977) considered forced heave motions of a two-dimensional circular cylinder as well as a related problem of sloshing (Faltinsen 1978). Vinje and co-workers extended their earlier works on breaking wave simulation (Vinje and Brevig 1981a) to include submerged and surface-piercing bodies in the fluid (Vinje and Brevig 1981b; Brevig et al. 1982), and next attempted the problem of motions of floating bodies (Vinje and Brevig 1981c; Vinje, Xie and Brevig 1982). Subsequently the simulation of a capsizing of Salter's duck, an ocean energy extracting device, was reported (Greenhow et al. 1982). For this latter study, experimental results supplemented the numerical simulation. Following in large parts the techniques of Vinje and co-workers with an important modification in consideration of the body-free surface intersection point (discussed later, §1.2.2.2 (b)), Lin (1984) simulated two-dimensional waves generated by a wave maker in a finite rectangular tank. This study was succeeded by an extension to consider forced oscillation of axi-symmetric three-dimensional cylinders (Lin, Newman and Yue 1984). Subsequently, Dommermuth and Yue (1986b, 1987) reconsidered the three-dimensional axi-symmetric problem and were able to simulate large amplitude forced heave oscillation of cylinders and inverted cones in an otherwise undisturbed free surface. Greenhow and co-workers also employed the approach of Vinje and colleagues and applied the method for studying the two-dimensional impact problem (Greenhow and Lin 1985; Greenhow 1987, 1988). In the process, specific improvements and developments of the algorithm were made to make it suitable for the particular application. Isaacson (1982, 1983b) reported on a similar method for studying the generalized two- and three-dimensional fixed and floating body problems, although lack of computed results leaves his method rather unconvincing.

Another line of 'intermediate' approach, in which the exact body kinematic conditions are satisfied at the instantaneous location of the body surface, but the free surface conditions are linearized, has been proposed by Chapman (1979), and followed by Kim and Hwang (1986). These approaches, although computationally efficient, are restricted to their applications to problems where the generated free surface elevations are small, and thus preclude consideration of steep incident waves.

Prior to the development of any reliable algorithm for the complete problem of motions of floating bodies, some specific problems remain to be resolved. In particular, an appropriate numerical closure method, numerical treatment of the contact point between the body and the free surface, and numerical stability of the solution on the free surface, have received considerable attention in the literature just cited, most of which appeared in this decade, some within past three years. In view of the emphasis on details in recent research activities as well as their connection to the work presented in this dissertation, discussion at this point is directed to these specifics.

(a) Non-reflective Exterior Boundaries

For exterior free surface problems, a satisfactory treatment of the exterior boundaries is essential. Earlier analogous studies in which exterior boundaries are replaced by walls (e.g. Chan and Street 1970) result in a prohibitively large interior domain and are clearly undesirable for long time simulations. If the physical problem under consideration is assumed to possess spatial periodicity, this difficulty is easily resolved by exploiting the relatively well known periodicity boundary conditions. The interior domain can be folded onto itself and the exterior boundaries simply disappear from the numerical treatment. This assumption was justified and used in the breaking wave simulations by Longuet-Higgins and Cokelet (1976), and still remains popular for analogous wave problems (e.g. Schultz et al. 1986; Calisal and Chan 1987). Presence of an isolated body in the fluid however raises serious concerns regarding validity of such periodicity conditions. Nevertheless, in earlier works that introduced a body in the fluid, similar assumptions were retained (Vinje and Brevig 1981b, 1981c; Greenhow et al. 1982).

In Faltinsen's (1977) method, the exterior radiated waves are matched with the non-linear inner solution by means of a simple Rankine dipole at the body's centre. This procedure restricts the application of the method from simulations extending over any reasonable length of time (i.e. several periods of oscillations), and was noted to be not satisfactory by the author. Isaacson's (1982, 1983b) assumption of no radiated and diffracted wave effects at the truncation boundaries is even more restrictive in that motions for only a fraction of a period is achievable. To remove the periodicity assumption, in their later work, Vinje et al. (1982) attempted to match the non-linear inner solution with a linear outer solution in their two-dimensional formulation, but encountered considerable difficulties. Following similar ideas, however, Dommermuth and Yue (1987) were able to implement a matching across the fictitious outer (exterior) boundaries and were able to continue simulations for sufficiently long periods in their three-dimensional axi-symmetric computations (for example, about 10 period of steady state solutions of the interior fluid motion generated by forced heave oscillations of cylinders could be achieved). Such a matching is permissible in three dimensions, since the radiated waves attenuate inversely with the radial distance and are therefore expected to be of small amplitude at sufficiently large distances from the body where the exterior boundaries can be placed. In two dimensions, a similar closure is not tenable because the non-linearities of the outgoing waves persist in the entire exterior domain. In linearized formulations of the interior domain, an analogous matching with the outer solution is perfectly admissible and has been implemented earlier in a variety of two- and three-dimensional free surface problems, both in frequency and time domain analyses (see e.g. Ijima and Yoshida 1976; Finnigan and Yamamoto 1979; Lee 1985; Liu and Ligget 1979).

The importance of implementing a proper radiation boundary condition for propagation of non-linear waves in unbounded domains is well documented in literature. Requirements for equivalent conditions occur in variety of other areas such as acoustics and meteorology. A number of procedures have been suggested: approximate 'absorbing' type conditions (Israeli and Orszag 1981); use of 'sponge' or 'viscous' layers (Chan 1975); methods derived from the well known Sommerfeld's radiation condition (Sommerfeld 1949), also known in the form of Orlanski's radiation condition (Orlanski 1976), etc. It is generally recognized that in absence of analytically 'perfect' conditions, many of the efforts are to construct 'workable' conditions, specially in the context to their numerical implementations. Similar attempts continue (see e.g. Jensen 1987).

(b) Body-Free Surface Intersection Point

A confluence of boundary conditions exists at the intersection of the body and the free surface which in turn leads to numerical difficulties. Analytically this is characterized by the presence of a weak type of singularity. For a vertical translating wall, a logarithmic type of singularity in the velocity potential for that point was known from linear analysis (Kravtchenko 1954). Existence of an analogous singularity in three dimensions was subsequently identified (Miloh 1980). A perturbation solution predicts a logarithmic singularity for the free surface elevation (η) at the intersection of an impulsively started horizontally moving impermeable surface in water of depth d (as derived by D.H.Peregrine in an unpublished note and reported in several references, e.g. Lin, Newman and Yue 1984; Greenhow and Lin 1985):

$$\eta = -\frac{2Ut}{\pi} \ln\left[\tanh\left(\frac{\pi x}{4d}\right)\right] + O(t^2) \qquad .....(1.1)$$

where U denotes the start up (impulsive) velocity of the surface, x measures the horizontal distance from the intersection and t denotes time. This behaviour has been experimentally validated by Greenhow and Lin (1983) and is believed to be confirmed (see e.g. Evans and Newman 1987). Computationally the singularity poses difficulties in the numerical method and may ruin the time domain simulation scheme unless special care is taken. In earlier works of Vinje and colleagues, the intersection was treated by specifying the body kinematic condition without prescribing the free surface potential, which was determined via extrapolation (Vinje and Brevig 1981c). As the authors note in their subsequent works, this procedure was not entirely satisfactory, and experimental data had to be used to fix the location of this point before acceptable results could be produced (Greenhow et al. 1982). An extensive treatment of this region was considered later by Lin (1984), and he was able to remove the associated difficulties, in a numerical sense, by prescribing both the free surface and body kinematic conditions. Here it is worth noting that a similar idea was followed by Ligget (1977) in an earlier work, where two points were considered very close to the intersection point, one on each part of the boundary, with respective boundary conditions prescribed on them. Lin's approach, although strictly finite due to numerical discretizations, predicted the analytic singularity very closely. Such a numerical treatment was noted to be very encouraging, and further experimental confirmations were reported (Dommermuth and Yue 1986a). A similar idea was generalized and extended for the three-dimensional axi-symmetric problem in Dommermuth and Yue(1987), where the authors provided numerical evidence of satisfactory treatment of the intersection point (for example, the locus of the intersection point for the forced heave oscillation of an inverted cone). Refinements following essentially similar treatments for the specific application to impacting bodies were subsequently considered by Greenhow (1987, 1988).

It must be noticed that the above treatment is purely numerical, and is more concentrated on removing the associated numerical difficulties than on resolving the flow in the immediate vicinity of the intersection in detail. Attempts for analytical solutions have not been completely successful and inclusion of surface tension or viscosity has not improved the situation (Lin 1984), but similar attempts continue (Cointe, Jami and Molin 1987). Recently, Roberts (1987) investigated the analytic nature of the transient unsteady flow near the contact point between a vertical plate and the free surface. His solution, however, does not appear to be easy to incorporate in the framework of numerical schemes.

More information about this contact point has come from the numerical works of Wu and Yeung (1987) in connection to their studies on two-dimensional forced heave oscillations by finite-difference algorithms. It appears that the singular behaviour of the potential is closely related to the local body geometry and its mode of motion. For wall shaped bodies in heave, no singularity was observed by them, while in sway mode (analogous to the translating wall case), the logarithmic singularity was reconfirmed. For the general case of a body free to heave, sway and roll, the singular behaviour is therefore inevitable, regardless of the body geometry.

An observation of important consequences is appropriate here. Numerical experiments of Lin (1984) and Lin, Newman and Yue (1984) indicate that the local behaviour of flow in the immediate neighbourhood of the intersection has an insignificant effect on the rest of the fluid. The physical characteristics (e.g. velocities, pressures) of the fluid slightly away from the intersection point apparently remain uninfluenced even for a relatively cruder resolution of the flow at that point. Further corroborative numerical evidence was reported by Greenhow and Lin (1985) and Greenhow (1987, 1988) where the pressures and forces on impacting cylinders were found to be practically unaffected by such cruder resolutions. Therefore, although a scientific curiosity exists to examine in detail the analytical behaviour of the flow associated with such singularities, from the point of view of studying global responses of the body (i.e. forces and motions), a satisfactory numerical treatment appears sufficient.

(c) Numerical Stability

Numerical stability considerations are critical enough to determine success of any computational scheme, specially those for time domain simulations. In the original works of Longuet-Higgins and Cokelet (1976), a 'sawtooth' instability of the free surface was encountered, which was subsequently suppressed by means of an artificial smoothing procedure. Later studies on steep wave simulations have also reportedly suffered from similar instabilities. Characteristically this instability appears in the form of oscillations of the free surface elevations and potentials between adjacent nodal points, analogous to physical presence of high frequency short length waves. In the earlier works, the inception and growth of these undesired oscillations were thought to be physical in origin, but later numerical studies strongly suggested their origin to be of purely numerical nature, specially since they always appeared between adjacent nodes with frequencies determined by the temporal grid size (see e.g. Dommermuth and Yue 1987). Their initiation is however not yet clearly understood, but they are believed to be strongly dependent on the subtle numerical details of particular methods. For example, no such instability was noticed in the method of Vinje and co-workers (1981, 1982) based on Cauchy's integral theorem. However, using essentially similar integral relations, Baker et al. (1981, 1982) and Lin et al. (1984) encountered instabilities and had to apply artificial smoothing in order to advance their solution in time without breakdown. The instability was found less pronounced when using a dipole distribution in contrast to vortex methods (Baker et al. 1982). The problem appears to be closely linked to the local steepness of free surface elevations. The solutions exhibit stronger instabilities for larger gradients in elevations. Works have since then appeared addressing similar instability problems. Roberts (1983) investigated the problem using a Fourier spectral analyses and reported a modified scheme that was found free from the instability. Dold and Peregrine (1986) employed special integration techniques for the free surface conditions, improving on accuracy in time integrations as well as reducing the instability considerably. Although without complete elimination, they were able to keep the instability controlled by a careful selection (reduction) of the time step size without having to resort to any artificial smoothing. More recently, Dommermuth and Yue (1987) reported on complete elimination of this problem by employing modified time integration schemes (somewhat analogous to that of Dold and Peregrine 1986) and regridding the free surface at every time step. The authors suggested that the violation of local Courant condition is attributable to the initiation of this instability. Since in all of the studies mentioned here, physical fluid particles on the free surface are followed in time (fully Lagrangian description of the free surface), the nodal points tend to concentrate in regions of large changes in local elevations (e.g. near the crest, see Longuet Higgins and Cokelet 1976) which inevitably results in a violation of the local Courant condition. Such clustering of particles however has the beneficial feature in that they provide better resolutions at regions of maximum interest.

Active current research towards improvements in stability characteristics can be identified in the works of Schultz et al. (1986) and Han and Stansby (1987). In particular, the former authors reported on improvements obtained by employing least square solution techniques for the free surface. It appears that, although different solutions suffer from it at varying degrees, some not exhibiting any detectable growth, the problem of instability has not been completely eradicated.

It should be noticed that regridding schemes also introduce artificial smoothing effects in an indirect way (see e.g. Moore 1981) as Dommermuth and Yue (1987) also note in their work.

1.2.3 Summarizing Remarks

The following general remarks summarize and conclude the above discussion:

(i) Approaches based on perturbation methods are noted for their suitability in frequency domain analyses. A general perturbation solution method for motions of floating bodies in non-linear waves, which encompasses a number of subproblems including the usual non-linear diffraction and radiation problems, appears to be very complicated from a theoretical standpoint. At present, research is still being reported addressing some of the pertinent individual subproblems. These techniques are particularly useful for predicting some 'mild' non-linear phenomena in body responses (Pawlowski 1987). However, for prediction of strongly non-linear responses such as that of extreme motions, these modes of analyses are impeded by their restricted applicability (see e.g. Papanikolaou and Nowacki 1980).

(ii) In contrast, direct numerical methods appear to be more promising in studies of steep waves and extreme body motions. Most recent research indicates this direction, and activities in this regard have come mainly from methods based on integral relations. Suitability of finite-difference or finite element methods can not be firmly assessed due to a comparatively smaller number of reported studies. Although substantial progress has been made in general finite difference based algorithms, specially in developments of 'boundary fitted' coordinate systems removing the earlier restrictions attached with irregular (curved) body geometries and surfaces (see e.g. Haussling and Coleman 1977, 1979), relatively limited applications in studies of extreme motions in steep waves indicate possibilities of algorithmic complications in these methods.

(iii) Satisfactory treatment of a number of component problems becomes decisive for the ultimate success of a model. In particular, problems with regard to the body and free surface intersection points, numerical stability considerations and a satisfactory treatment of exterior boundaries are identified to require special attention. Although very recent research has thrown light on these aspects of numerical modelling and computations have been performed simulating nonlinear free surface motions in the presence of fixed or moving objects, numerical simulations of motions of freely floating bodies in steep waves, the so called 'numerical wave tank' studies for floating bodies, have not yet been reported. It would appear that this 'complete' simulation awaits resolutions of some further numerical difficulties.

1.3 Scope and Objective

1.3.1 Objective

The work presented in this dissertation is aimed towards development of a numerical method for studies of the behaviour of floating bodies in steep incident wave fields. The discussion in the preceding section is hoped to have provided an overview of the present level of developments to this particular problem. The rationale behind the choice of a direct numerical method rather than a perturbation approach for the present *modus operandi* is apparent as well.

Within the framework of direct numerical methods, two interrelated but slightly different directions in which this task could proceed can be identified :

1. a detailed and rigorous study of some of the specific features that constitute the complete simulation model, in order that a stronger foundations of contributory components can be established (e.g. a more thorough study, perhaps of analytical nature, on the behaviour of the body-free surface contact point; attempts towards general solution algorithms for some simpler free surface flow problems possessing superior stability characteristics, etc.)
2. development of a full simulation model by using appropriate techniques to deal with the specific difficulties as and when encountered in the process, with due consideration to the specific attributes of stability, convergence and accuracy.

The present task belongs to the latter category.

1.3.2 Scope

The problem considered is two-dimensional in a potential flow field. An integral relation formulation is employed in which the integral relation is derived by utilizing Green's second identity such as not to preclude future generalizations to three dimensions. The solution is advanced in time by integrating appropriate evolution equations and establishing boundary data at every time instant.

The method is first applied to study unsteady propagation of small amplitude waves, followed by its application to simulate propagation of steep (non-linear) waves. Subsequently interaction of steep waves with fixed surface-piercing objects is studied, and finally simulation of extreme motions of freely floating bodies is accomplished.

An experimental program was undertaken to validate the simulation method thus developed. To achieve two-dimensionality of the flow, vertical boundaries were constructed within a wave flume. The experimental object was of rectangular cross section and was restricted to respond in selected modes of motions.

The numerical model developed differs in several aspects from the studies available in literature. In particular, the method of following the free surface is different (as discussed in §4). The manner in which an incident steep wave is generated as well as the treatment of the exterior boundary are additional features not readily identifiable in the reported studies.

This development follows the general direction for establishing a two dimensional 'numerical wave tank' simulation model, analogous to aerodynamicist's 'digital wind tunnel' (Aref 1986). Computer codes are written in FORTRAN language and the computing system of MUN consisting of DEC -VAX 8800 and -VAX 8530 cluster is used. This work has utilized an estimated total CPU time in excess of 2000 hrs. in the system mentioned. Due to the inherent developmental nature of the method, no special emphasis is placed on efficient structuring of the software. However, care has been taken to ensure minimization of computational efforts wherever possible.

1.3.3 Outline of the Text

The text is arranged following the manner in which successive developments were made. After providing the basic theoretical background and the numerical discretization scheme in §2, the immediately following section (§3) ascertains the effectiveness of the basic algorithm by choosing three examples of small amplitude wave propagation as test cases. In the succeeding section (§4), the non-linear problem is treated. Here the simulation of an unsteady steep propagating wave is accomplished. This section also includes some computational features that are developed to overcome the numerical difficulties encountered in the process. In particular, techniques are developed to preserve stability characteristics, and an outgoing wave condition is implemented. Supporting computational results follow. In §5, a surface-piercing object, in the form of a vertical wall, is introduced in the fluid. The choice of a wall is prompted because of availability of experimental and perturbation solutions for equivalent interactions. Comparative results are presented. §6 considers the next step. Development of the final numerical model for the motions of floating bodies in waves, together with the necessary details, is reported here. Computational results demonstrating simulation of large motions in steep waves are presented. In §7, the experimental verification program is discussed. The experimental setup, its purpose and other necessary details are described here. Also included are some sample experimental results. The objective of the penultimate section (§8) is to compare the numerical and experimental results. Finally, the concluding section (§9) contains summary and conclusions. Appendix A provides details of the finite-difference and numerical integration formulae utilized, while details with regard to the estimation of roll viscous damping coefficients are discussed in

Appendix B. A majority of the comparative experimental and numerical results, not provided in the main text for brevity, are included in Appendix C.

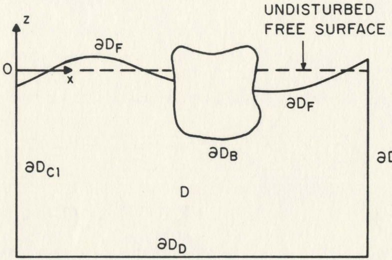

Figure 2.1 Definition diagram.

condition

$$\frac{\partial \eta}{\partial t} = \frac{\partial \phi}{\partial z} - \frac{\partial \phi}{\partial x}\frac{\partial \eta}{\partial x} \qquad \text{.....(2.2)}$$

and the dynamic condition

$$\frac{\partial \phi}{\partial t} = -\frac{p_a}{\rho} - g\eta - \frac{1}{2}(\nabla\phi)^2 \qquad \text{.....(2.3)}$$

where η denotes free surface elevations, g denotes gravitational acceleration and ∇ represents the gradient operator: $\nabla = \partial/\partial\mathbf{x}$; p_a is the applied (external, including atmospheric) pressure on the free surface and ρ signifies fluid density. Following usual practice, p_a is set equal to 0 in the sequel.

The condition applied on ∂D_D is that of impermeability:

$$\frac{\partial}{\partial n}\phi = 0 \qquad \text{.....(2.4)}$$

where $\partial/\partial n = \mathbf{n} \cdot \partial/\partial\mathbf{x}$, in which $\mathbf{n}$ designates the unit normal vector on ∂D directed outwards of $\mathcal{D}$.

The condition applicable on the wetted body surface ∂D_B is the kinematic condition:

$$\frac{\partial}{\partial n}\phi = V_n \qquad \text{.....(2.5)}$$

where V_n is the velocity component of ∂D_B along its inward normal (outwards to $\mathcal{D}$). For bodies fixed in space, (2.5) becomes identical with (2.4).

Conditions on the control boundaries ∂D_{C1} and ∂D_{C2} are not explicitly stated at the moment, but are assumed to exist in such a form that either ϕ or $\partial\phi/\partial n$ are determinable at all time instants $t \geq 0$. The imposed conditions are clarified later, in connection with the specific applications.

---

henceforth for simplicity either none or only the applicable dependence will be indicated.

2.2 Integral Relation and Its Discretization

2.2.1 The Integral Relation

Application of Green's second identity to ϕ and the fundamental singularity $\ln r(P,Q)$ in $\mathcal{D}$ results in the following well known integral relation (Kellog 1929):

$$\Omega(P)\phi(P) = \int_{\partial D} [\phi(Q) \frac{\partial}{\partial n_{(Q)}} \ln r(P,Q) - \frac{\partial}{\partial n_{(Q)}} \phi(Q) \ln r(P,Q)] dS \qquad .....(2.6)$$

with Q located on ∂D . Here $r(P,Q) = |\mathbf{x}(P) - \mathbf{x}(Q)|$, which is the distance between the points P and Q ; the subscript in $\partial/\partial n$ indicates the point at which the differentiation is taken; $\Omega(P) = 0$ or 2π respectively for P inside or outside $\mathcal{D}$, but not on ∂D. For P on ∂D, $\Omega(P)$ is the angle subtended by the tangents to ∂D, measured from inside $\mathcal{D}$, and equals π when the normal to ∂D is continuous at P.

Formula (2.6) expresses the potential at any point P by means of a mixed distribution of simple sources of strengths $-\partial\phi(Q)/\partial n$ and normal dipoles of moments $\phi(Q)$ on ∂D. When P is taken on ∂D, (2.6) is a Fredholm's integral equation of the second kind for unknown $\phi(P)$ and of the first kind for unknown $\partial\phi(P)/\partial n$. For problems for which alternatively Dirichlet and Neumann conditions (i.e. ϕ and $\partial\phi/\partial n$ respectively) are imposed on parts of the boundary, a set of coupled integral equations results. For problems which can be formulated in terms of an integral relation of the second kind for the unknown, advantages in computations can be derived since for such equations a global Neumann series exists which admits a simple iterative solution at reduced computer time and storage requirements (Baker et al. 1982). This advantage is lost for the coupled set of equations. It is noticed that relation (2.6) is valid at any time instant. For solutions advancing in time, this relation is utilized at every consecutive time step.

2.2.2 Discretization

For convenience as well as to retain generality in the discretization scheme, it is assumed that ∂D consists of N_S piece-wise smooth parts:

$$\partial D = \sum_{k=1}^{N_S} \partial D_k \qquad .....(2.7)$$

Relation (2.6) can then be written as

$$\Omega(P)\phi(P) - \sum_{k=1}^{N_S} \int_{\partial D_k} [\phi(Q) \frac{\partial}{\partial n_{(Q)}} \ln r(P,Q) - \frac{\partial}{\partial n_{(Q)}} \phi(Q) \ln r(P,Q)] dS = 0 \qquad .....(2.8)$$

Surfaces ∂D_k are further subdivided into a finite number of segments, approximated as straight lines:

$$\partial D_k = \sum_{i=1}^{M_k} \delta S_i^k \qquad .....(2.9)$$

and a collocation point Q_i^k is chosen on each of the segments δS_i^k. Here the superscript indicates a particular part of the boundary in consideration and M_k denotes the number of segments in which the kth boundary contour is subdivided. An illustration of the above discretization is shown in Figure 2.2.

The variations of ϕ and $\partial \phi / \partial n$ over ∂D are now approximated by a constant value of these over each segment δS_i^k, the values being determined at the corresponding collocation points Q_i^k. Following usual practice, the collocation points are placed at the centre of each segment. However, for future reference we remark here that in principle Q_i^k need not be located centrally in δS_i^k.

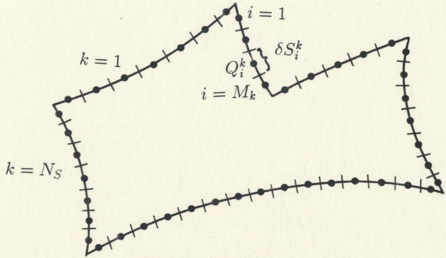

Figure 2.2 Discretization of ∂D.

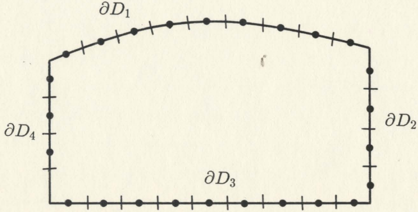

Figure 2.3 Illustration of a domain with $N_S = 4$.

the free surface are different (Neumann condition on the body boundary and Dirichlet condition on the free surface). In this respect, the central collocation discretization scheme adopted here is the most straightforward for numerical implementation. In particular, the following benefit are derivable from its application :

(a) The necessity of explicitly prescribing any boundary data at the intersection point is avoided, which is computationaly advantageous for treatment of the body-free surface contact point (recall the discussion in §1.2.2.2 (b)). It may be noticed that the method is essentially collocative, implying relation (2.6), within the approximations of the boundary geometry and the variations of boundary data, is satisfied only at a finite number of collocation points. Therefore, not considering any particular point as a collocation point in principle does not invalidate the application of the method.

(b) Lower order b.e.m. are expected to possess better stability characteristics of the solution. Successively higher order applications of the b.e.m., although recognized to represent improvements in the discretization scheme leading to better resolution with lesser number of segments (see Hess 1975; Breit, Newman and Sclavounos 1985), are known to be more susceptible to numerical instability (see Schultz 1987) which is a major concern in the present application.

In addition to the above, another, perhaps not so objective reason, which prompted the present choice is the belief that a 'workable' model can be built up on this simplest discretization scheme for the final task in question (namely, simulation of large motions of floating bodies in steep waves), since it is conjectured that many of the anticipated problems to be encountered may not necessarily be remedied by applying more refined and sophisticated discretization schemes. Such refinements can, in principle, be incorporated latter.

In forming eqns. (2.10), it is convenient to number the collocation points sequentially : 1 to M_1 for ∂D_1 , (M_1+1) to (M_1+M_2) for ∂D_2 , etc. Eqns. (2.10) contain $2N$ discrete values of the boundary data, N values of ϕ and an additional N values of $\partial\phi/\partial n$. Therefore, if any M values of ϕ and the $(N–M)$ values of $\partial\phi/\partial n$ are known $(M \leq N)$, one boundary data at each collocation point, then the remaining unknowns, $(N–M)$ values of ϕ and M values of $\partial\phi/\partial n$ can be determined from a suitable rearrangement of (2.10.) and then solving the resulting system of N linear algebraic equations by any standard method of solution (e.g. direct matrix inversion, Gaussian elimination technique, etc.). For illustration, consider the domain with $N_S = 4$ depicted in Figure 2.3 and assume that on ∂D_1 and ∂D_2 , ϕ is known while on ∂D_3 and ∂D_4, $\partial\phi/\partial n$ is known. The system of equations becomes

$$\begin{bmatrix} \mathbf{G}_{\partial D_1,\partial D_1} & \mathbf{G}_{\partial D_1,\partial D_2} & \mathbf{H}_{\partial D_1,\partial D_3} & \mathbf{H}_{\partial D_1,\partial D_4} \\ \mathbf{G}_{\partial D_2,\partial D_1} & \mathbf{G}_{\partial D_2,\partial D_2} & \mathbf{H}_{\partial D_2,\partial D_3} & \mathbf{H}_{\partial D_2,\partial D_4} \\ \mathbf{G}_{\partial D_3,\partial D_1} & \mathbf{G}_{\partial D_3,\partial D_2} & \mathbf{H}_{\partial D_3,\partial D_3} & \mathbf{H}_{\partial D_3,\partial D_4} \\ \mathbf{G}_{\partial D_4,\partial D_1} & \mathbf{G}_{\partial D_4,\partial D_2} & \mathbf{H}_{\partial D_4,\partial D_3} & \mathbf{H}_{\partial D_4,\partial D_4} \end{bmatrix} \begin{Bmatrix} (\partial\phi/\partial n)_{\partial D_1} \\ (\partial\phi/\partial n)_{\partial D_2} \\ (\phi)_{\partial D_3} \\ (\phi)_{\partial D_4} \end{Bmatrix}$$

$$= \begin{bmatrix} \mathbf{H}_{\partial D_1,\partial D_1} & \mathbf{H}_{\partial D_1,\partial D_2} & \mathbf{G}_{\partial D_1,\partial D_3} & \mathbf{G}_{\partial D_1,\partial D_4} \\ \mathbf{H}_{\partial D_2,\partial D_1} & \mathbf{H}_{\partial D_2,\partial D_2} & \mathbf{G}_{\partial D_2,\partial D_3} & \mathbf{G}_{\partial D_2,\partial D_4} \\ \mathbf{H}_{\partial D_3,\partial D_1} & \mathbf{H}_{\partial D_3,\partial D_2} & \mathbf{G}_{\partial D_3,\partial D_3} & \mathbf{G}_{\partial D_3,\partial D_4} \\ \mathbf{H}_{\partial D_4,\partial D_1} & \mathbf{H}_{\partial D_4,\partial D_2} & \mathbf{G}_{\partial D_4,\partial D_3} & \mathbf{G}_{\partial D_4,\partial D_4} \end{bmatrix} \begin{Bmatrix} (\phi)_{\partial D_1} \\ (\phi)_{\partial D_2} \\ (\partial\phi/\partial n)_{\partial D_3} \\ (\partial\phi/\partial n)_{\partial D_4} \end{Bmatrix}$$

.....(2.12)

to be solved for the unknowns. The elements of the above matrices represent submatrices of influence coefficients:

$$\mathbf{G}_{\partial D_n,\partial D_m} \text{ or } \mathbf{H}_{\partial D_n,\partial D_m} = A_{i,j} \text{ or } B_{i,j} \qquad .....(2.13(a))$$

where i and j run for

$$i = \sum_{k=1}^{n-1} M_k + 1, \cdots, \sum_{k=1}^{n} M_k \qquad .....(2.13(b))$$

$$j = \sum_{k=1}^{m-1} M_k + 1, \cdots, \sum_{k=1}^{m} M_k \qquad .....(2.13(c))$$

except for $n = 1$ and $m = 1$, for which the first terms on the r.h.s. of (2.13(b)) and (2.13(c)) are to be taken as 1.

The influence coefficients depend only on the geometry of the boundary contour and can be determined explicitly (see e.g. Faltinsen 1978) for the present type of straight line segments. These are given below in a form convenient for computer implementation:

$$\begin{aligned} A_{i,j} &= \frac{1}{\pi}\{a_2 \ln(b^2 + a_2^2) - 2a_2 + 2b \arctan\frac{a_2}{b} \\ &\quad - a_1 \ln(b^2 + a_1^2) + 2a_1 - 2b \arctan\frac{a_1}{b}\} \qquad .....(2.14(a)) \\ B_{i,j} &= 1 \text{ for } i = j \\ &= -\frac{n_{x_j}}{\pi}\{a_x \ln\frac{b^2 + a_2^2}{b^2 + a_1^2} - 2a_z(\arctan\frac{a_2}{b} - \arctan\frac{a_1}{b})\} \\ &\quad + \frac{n_{z_j}}{\pi}\{a_z \ln\frac{b^2 + a_2^2}{b_2 + a_1^2} + 2a_x(\arctan\frac{a_2}{b} - \arctan\frac{a_1}{b})\} \\ &\quad \text{for } i \neq j \qquad .....(2.14(b)) \end{aligned}$$

where,

$$\begin{aligned} b &= \{(x_i - x_{1j})(z_{2j} - z_{1j}) - (z_i - z_{1j})(x_{2j} - x_{1j})\}/\Delta\ell_j \\ a_1 &= -\{(x_i - x_{1j})(x_{2j} - x_{1j}) + (z_i - z_{1j})(z_{2j} - z_{1j})\}/\Delta\ell_j \\ a_2 &= -\{(x_i - x_{2j})(x_{2j} - x_{1j}) + (z_i - z_{2j})(z_{2j} - z_{1j})\}/\Delta\ell_j \end{aligned}$$

$$.....(2.14(c))$$

boundary data for the next time level. In particular, appropriate evolution equations for the free surface, deduced from (2.2) and (2.3), are integrated in time to determine the updated free surface contour (i.e. the configuration of ∂D_F for the advanced time level) and the values of ϕ on this updated boundary. On the body, $\partial\phi/\partial n$ on ∂D_B is related to the body velocity by virtue of (2.5), which in turn is related to ϕ through the equations of motion (to be discussed in detail in §6). For the moment, we assume that $\partial\phi/\partial n$ on ∂D_B is determinable at all time instants. The boundary contour ∂D as well as the boundary data for the advanced time level are now established and the solution process can be repeated. ϕ at any desired location in $\mathcal{D}$ can be calculated from a discretized form of relation (2.6). Other information, e.g. fluid velocity and pressure are easily calculable from ϕ by utilizing Bernoulli's equation and employing numerical difference techniques in space and time. Evolution of the free surface and the motion of the body, which constitute necessary information for advancing the solution in time, are extracted as the simulation proceeds.

The system of linear equations to be solved for the unknowns (cf. eqn. (2.10)) in general corresponds to a full coefficient matrix and thus benefits admissible in solutions of matrices with special features (e.g. banded matrix, triangular matrix) are not available. In the present algorithm, a standard IMSL (abbreviation for International Mathematical and Statistical Library) routine is utilized which employs a Gaussian elimination technique for matrix inversion (see e.g. Forsythe and Moler 1967).

The evolution equations for the free surface can be cast in the following general form :

$$\frac{dy}{dt} = f(y,t) \qquad .....(2.15)$$

In the present algorithm, a fourth order implicit Adams-Bashforth-Moulton scheme is adopted and is found to be convergent for all required integrations. To achieve an accuracy of $O(10^{-4})$, usually not more than one corrector step is found necessary in most cases. This scheme requires information at the preceding four steps. In the initiation of the solution, the first three steps are therefore treated by means of successively lower order schemes with higher number of iterations (see Appendix A.1).

A variety of other schemes exists for integration of the equations of the form (2.15), e.g. Runge-Kutta schemes, Hamming's method, etc. 4th order Runge-Kutta starters are popular for analogous initial-value problems (e.g. Faltinsen 1977; Longuet-Higgins and Cokelet 1976, Dommermuth and Yue 1987). However, the starter scheme employed here is found adequate for the applications considered. Limited numerical experiments with other schemes have also been performed and the algorithm is found insensitive to the choice of any particular scheme. Further remarks on this are deferred till the relevant applications are discussed but it is to be noted that the number of iteration levels to achieve a desired degree of accuracy dictates the bulk of the computation time, since the system of linear equations must be solved at every iteration level.

The bottom condition (2.4) permits exclusion of ∂D_D from the contour of integration in the integrand in (2.6) if ∂D_D is horizontal (see e.g. Wehausen and Laitone 1960). This can be achieved by augmenting the fundamental singularity with its symmetric image with respect to ∂D_D. Thus when the sea bottom is a flat surface at a depth d, $\ln r(P,Q)$ in (2.6) is replaced by $[\ln r(P,Q) + \ln r(P,Q')]$ and ∂D_D is discarded from ∂D. Here Q' is the symmetric image of Q on ∂D_D. This results in a reduction in the system of linear equations in (2.10) by the number of segments used in discretizing ∂D_D. For example, referring to Figure 2.3 and taking ∂D_3 as the horizontal bottom, the third rows and columns of the matrices in (2.12) along with the corresponding rows of the associated vectors are simply deleted. The influence coefficients in this case contain additional integrations over the image segments:

$$A_{i,j} = \frac{1}{\pi}\int_{\delta S_j} \ln|\mathbf{x}_i - \mathbf{x}_j| dS + \frac{1}{\pi}\int_{\delta S'_j} \ln|\mathbf{x}_i - \mathbf{x}'_j| dS \qquad .....(2.16(a))$$

$$B_{i,j} = \delta_{i,j} - \frac{1}{\pi}\int_{\delta S_j} \frac{\partial}{\partial n_j} \ln|\mathbf{x}_i - \mathbf{x}_j| dS + \frac{1}{\pi}\int_{\delta S'_j} \frac{\partial}{\partial n_j} \ln|\mathbf{x}_i - \mathbf{x}'_j| dS \qquad .....(2.16(b))$$

where the primes denote the respective variables for the image panel. The image panel has the end coordinates : $(x'_{1j}, z'_{1j}) = (x_{1j}, z_{1j} - 2d)$ and $(x'_{2j}, z'_{2j}) = (x_{2j}, z_{2j} - 2d)$. For evaluation of the integrands over $\delta S'_j$ in (2.16), relations (2.14) apply with $(x_{1j}, z_{1j}), (x_{2j}, z_{2j})$ replaced by $(x'_{1j}, z'_{1j}), (x'_{2j}, z'_{2j})$.

3 Linear Free Surface Flow Problems

3.1 General Considerations

A simple means of testing the effectiveness and reliability of the algorithm is to apply it to problems involving small amplitude free surface elevations. The use of relation (2.6) for free surface flow problems is not new. It is believed to have been first proposed by Yeung (1973) for hydrodynamic problems and was subsequently applied to studies involving linear free surface motions (e.g. Bai and Yeung 1974; Sahin and Magnuson 1984) in the frequency domain. However, its application for time domain simulations, where it is used at every time step to obtain information for the next level of computation, requires a more careful assessment. In particular, possible degeneration of the solution due to accumulation of numerical errors must be investigated prior to developing any reliable algorithm for studies of complex, realistic problems. Convergence of the numerical solution is not equivalent to accuracy. Converged solutions can indeed produce results far from the desired solution (see the recent article by Aref 1986). To this end, the simulation of propagation of small amplitude waves provides an excellent means of examining the basic solution algorithm because of two different reasons: the permissible linearization of the free surface conditions aids in focussing on the algorithm in its simplest form, thereby reducing the possible sources of contamination of the solution; secondly, solutions of linearized flows are usually available in closed form, thereby permitting an exact basis for comparison.

Upon applying the usual approximation associated with small amplitude waves, the free surface conditions (2.2) and (2.3) take the following linearized forms:

$$\frac{\partial\eta}{\partial t} = \frac{\partial\phi}{\partial z} \qquad .....(3.1)$$

$$\frac{\partial\phi}{\partial t} = -g\eta \qquad .....(3.2)$$

to be applied on the undisturbed free surface $z = 0$.

For the applications considered in this section, the fluid domain is represented by the rectangular area depicted in Figure 3.1. The bottom surface is taken to be at a constant depth d , and the advantage of eliminating this part of the boundary is utilized. The free surface part of the boundary on which the integrand in (2.6) is to be evaluated remains undisturbed at all time instants, and $\partial/\partial n = \partial/\partial z$ on ∂D_F. The entire boundary ∂D is therefore independent of time. Consequently, the elements of the matrices in (2.12) (or a similar system of equations) remain unchanged with time. A significant saving in computer time can be realized by evaluating, inverting and saving the coefficient matrix once for all. The remaining operations are then simple matrix multiplications.

3.2 Specific Applications

At the outset, the following symbols are introduced: Δx denotes the length of the segments (or the spatial grid size), suffixed appropriately to indicate the parts of ∂D on which they are chosen, viz. $\Delta x_F, \Delta x_{C1}, \Delta x_{C2}$ are the segment sizes on $\partial D_F, \partial D_{C1}$ and ∂D_{C2} respectively. The time step size is denoted by Δt. The spatial grid sizes are kept constant on each part of the boundary, and Δt is constant over the entire time of simulation. N_t represents the time step level of computation: $N_t = t/\Delta t$. The distance between the control boundaries ∂D_{C1} and ∂D_{C2} , i.e. the horizontal extent of the free surface, is denoted by L.

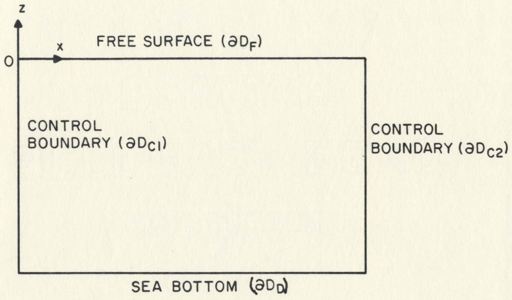

Figure 3.1 The rectangular fluid domain

Most of the following computed results are presented in terms of the free surface elevation $\eta(x,t)$ and the distribution of ϕ on ∂D_F.

3.2.1 Simulation of Airy Waves

As a test case, the method is first applied to simulate the propagation of steady Airy waves in the control domain. The initial values of the potential on the undisturbed free surface $z = 0$ are specified according to the Airy potential:

$$\phi(\mathbf{x},t) = \frac{H\lambda}{2T}\frac{\cosh[2\pi(z+d)/\lambda]}{\sinh 2\pi d/\lambda}\sin\frac{2\pi}{\lambda}(x-ct) \qquad .....(3.3)$$

with $t=0$. This corresponds to an Airy wave of height H, length λ and period T, progressing in the positive x direction with celerity c. The value of $\partial\phi/\partial n$ at any point Q on ∂D can be determined from :

$$\begin{aligned}\frac{\partial\phi}{\partial n} &= n_{x(Q)}\frac{\pi H}{T}\frac{\cosh[2\pi(z+d)/\lambda]}{\sinh(2\pi d/\lambda)}\cos\frac{2\pi}{\lambda}(x-ct) \\ &\quad + n_{z(Q)}\frac{\pi H}{T}\frac{\sinh[2\pi(z+d)/\lambda]}{\sinh(2\pi d/\lambda)}\sin\frac{2\pi}{\lambda}(x-ct)\end{aligned} \qquad .....(3.4)$$

where $(n_{x(Q)}, n_{z(Q)})$ denote components of the outward unit normal at Q in the suffixed directions. For ∂D_{C1} and ∂D_{C2}, these are $(-1,0)$ and $(1,0)$ respectively. For the following simulations, either ϕ or $\partial\phi/\partial n$ computed from (3.3) or (3.4) respectively are provided on the control boundaries.

Figures 3.2 (a) and (b) show the computed free surface elevations and potential distribution on ∂D_F, normalized with respect to H and $(H\lambda/2T)$ respectively, at three time instants: t/T = 1.0, 2.5 and 4.0. For this simulation, $L/\lambda = 1$ and water depth is, $d = \lambda$. The discretization parameters are $\Delta x_F = \lambda/20$ and $\Delta t = T/40$. The grid sizes on the other boundaries are kept the same as on the free surface: $\Delta x_{C1}, \Delta x_{C2} = \Delta x_F$. Dirichlet conditions are

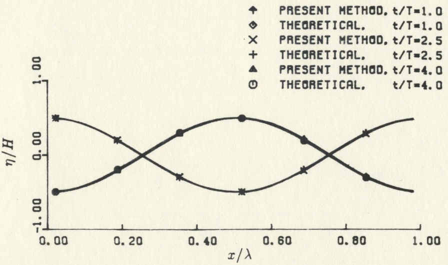

(a) Free surface elevations

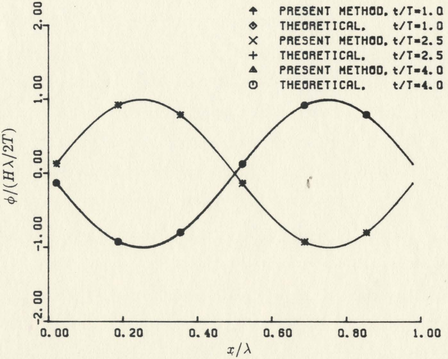

(b) Distribution of ϕ on the free surface

Figure 3.2 Free surface elevations and potentials of a linear steady progressive wave; $L/\lambda = 1$, $d/\lambda = 1.0$, $\Delta x_F/\lambda = 1/20$ and $\Delta t/T = 1/40$.

imposed on the control boundaries, i.e. the values of ϕ are specified on ∂D_{C1} and ∂D_{C2} at all time instants, which are determined from the Airy potential (eqn. (3.3)). The theoretical free surface profile for an Airy wave, given by

$$\eta(x,t) = H \cos \frac{2\pi}{\lambda}(x - ct) \qquad .....(3.5)$$

and the potential calculated from (3.3) are also plotted for comparison. The agreement is evidently very good.

For the results shown in Figures 3.3 (a) and (b), all parameters (size of Δx, Δt and conditions on ∂D_{C1} and ∂D_{C2}) are retained the same except that the control domain is stretched to $L = 4\lambda$ and water depth is reduced to $d = 0.5\lambda$. As can be seen, curves at $t/T = 4.0$ are practically indistinguishable from the corresponding theoretical curves.

Results shown in Figures 3.4 (a) and (b) are achieved by specifying different conditions on the control boundaries, Dirichlet condition on ∂D_{C1} and Neumann condition on ∂D_{C2}. The control domain extends over $L = \lambda$ and water depth is only $d = 0.25\lambda$. The temporal and spatial grid sizes are the same as in the above examples. Results are presented at the same time instant of $t/T = 4.0$ and compared with theoretical results. Good agreement is once more evident.

In Figures 3.5 (a) and (b), the free surface elevations are shown for a simulation where Neumann conditions are imposed on both the control boundaries. Here the control domain is relatively long, $L = 7\lambda$, and water has a depth of $d = 0.4\lambda$. Other parameters are: $\Delta x_F, \Delta x_{C1}, \Delta x_{C2} = \lambda/25$ and $\Delta t = T/40$. The plot showing evolution of the free surface in time at the center of $\mathcal{D}$ is also included. The comparison with theoretical free surface contours clearly demonstrate that the present method is capable of following the wave motion with

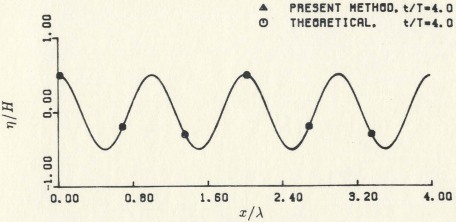

(a) Free surface elevations

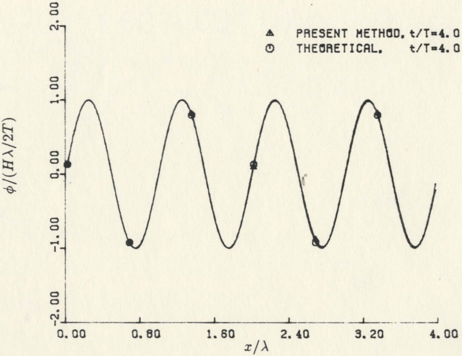

(b) Distribution of ϕ on the free surface

Figure 3.3 Free surface elevations and potentials of a linear steady progressive wave; $L/\lambda = 4$, $d/\lambda = 0.5$, $\Delta x_F/\lambda = 1/20$ and $\Delta t/T = 1/40$

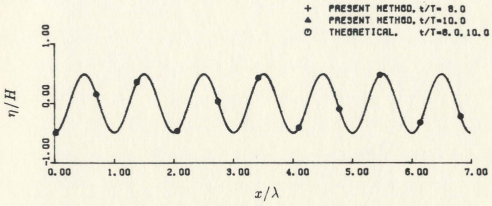

(a) Free surface elevations

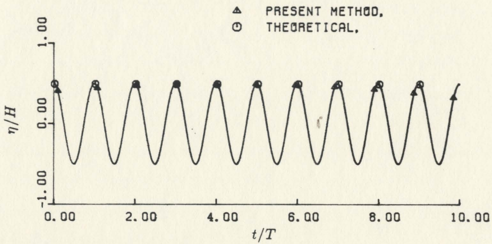

(b) Evolution of the free surface in time at the center of the domain $x = 3.5\lambda$

Figure 3.5 Free surface elevations of a linear steady progressive wave; $L/\lambda = 7$, $d/\lambda = 0.4$, $\Delta x_F/\lambda = 1/25$ and $\Delta t/T = 1/40$.

acceptable degree of precision over long periods of simulation time.

Computations were also performed for a wide variety of combination of the spatial and temporal grid sizes, for different values of L/λ and d/λ, and for different initial distributions of the free surface potential (i.e. initial values of ϕ on ∂D_F given by (3.3) with values of t different than 0). In all computations, the quality of agreement between the numerical and theoretical results is similar to the presented examples. The numerical solution does not appear to exhibit any discernible evidence of degeneration even after reasonably long periods of simulation (for example, after 400 time steps or up to 10 wave periods).

3.2.2 Unsteady Wave Propagation

The method is now applied to simulate propagation of unsteady waves. This is achieved by specifying a potential on one of the control boundaries. The fluid in $\mathcal{D}$ is initially at rest with $z = 0$ as the initial contour of ∂D_F. The potential given by (3.3) corresponding to an Airy wave propagating in the positive x direction is applied on ∂D_{C1} at all time instants. This simulation is therefore that of an unsteady wave propagation in the sense that a disturbance is provided at one end of the control domain to excite fluid motion in an initially unperturbed fluid in $\mathcal{D}$. The initial values of the potential on ∂D_F and ∂D_{C1} are: $\phi(\mathbf{x}, t) = 0$. For this simulation, the boundaries ∂D_{C1} and ∂D_{C2} can be referred to as upstream and downstream boundaries respectively.

The simulation attempted as described above was not successful due to a numerical instability initiating at the origin (at $\partial D_{C1} \cap \partial D_F$) and slowly spreading over the entire domain. Although this instability is of a weak type in the sense that the solution can still be progressed, the free surface contour shows undesired 'zigzag' patterns and eventually diverges from the desired Airy wave profile. A typical computational wave profile is shown in Figure 3.6 where this unwanted behaviour is evident. By the time of $t = 4T$, the entire solution is contaminated. Investigation to the cause of this instability reveals that the problem is associated with an incompatibility of the imposed initial conditions, which is now discussed.

3.2.2.1 Initial Boundary Data

The initially unperturbed state of fluid in $\mathcal{D}$ indicates that $\phi(\mathbf{x},t)|_{t=0} = 0$ in the entire of $\mathcal{D}$, including ∂D (the value of ϕ could strictly be any constant, but it is convenient to make this constant 0 by redefining ϕ, see e.g. Lamb 1945). What is not so apparent is the requirement of $\partial\phi(\mathbf{x},t)/\partial t|_{t=0} = 0$ to be maintained simultaneously. Examining eqns. (2.3), it can be noted that $\eta(x,t)|_{t=0} = 0$ and $\phi = 0$ imply $\partial\phi/\partial t|_{t=0} = 0$ on ∂D_F. It follows that $\partial\phi/\partial t$ on ∂D_{C1} must have a zero value at $t = 0$ for compatibility of the initial boundary data, in particular at the intersection of ∂D_{C1} and ∂D_F. The potential given by (3.3) maintains $\phi(\mathbf{x},t)|_{t=0} = 0$ on ∂D_{C1}, but $\partial\phi(\mathbf{x},t)/\partial t|_{t=0}$ has a finite value.

In the present formulation, the excitation potential is modified by introducing a modulation function $M(t)$:

$$\phi^*(t) = M(t)\phi(t) \qquad .....(3.6)$$

with

$$M(t) = \begin{cases} 0.5(1-\cos(\pi t/\sigma)) & t < \sigma \\ 1 & t \geq \sigma \end{cases} \qquad .....(3.7)$$

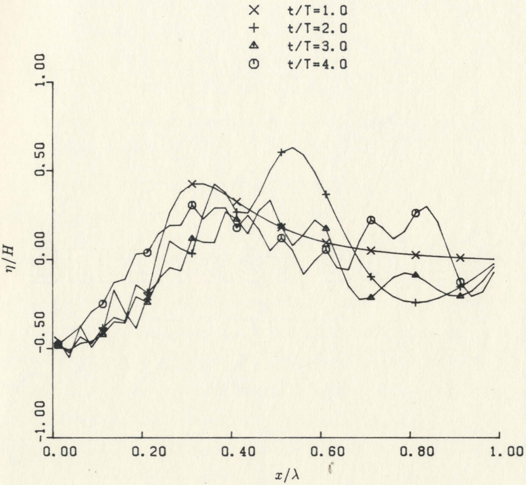

Figure 3.6 Initiation of instability on the free surface at $\partial D_{C1} \cap \partial D_F$ from application of (3.3) on ∂D_{C1}; for this computation the fluid domain is, $L = \lambda$, $d/\lambda = 0.5$, and $\Delta x_F, \Delta x_{C1}, \Delta x_{C2} = \lambda/40$, $\Delta t = T/80$; the imposed condition on ∂D_{C2} is, $\phi(t) = 0$.

This function has the property that $M(t)|_{t=0} = 0$ and $\partial M(t)/\partial t|_{t=0} = 0$. Therefore, regardless of the form of ϕ on ∂D_{C1}, the initial values of ϕ and $\partial\phi/\partial t$ are guaranteed to be zero by virtue of (3.6) and (3.8) below:

$$\frac{\partial \phi^*(t)}{\partial t} = M(t)\frac{\partial \phi(t)}{\partial t} + \frac{\partial M(t)}{\partial t}\phi(t) \qquad .....(3.8)$$

The time span over which the excitation potential is modulated can be controlled by selecting an appropriate σ.

It is of some interest to comment on the physical interpretation of the above compatibility requirement. From Bernoulli's equation:

$$p(\mathbf{x}, t) = -\rho g z - \rho\frac{\partial}{\partial t}\phi(\mathbf{x}, t) - \frac{1}{2}\rho(\frac{\partial \phi}{\partial \mathbf{x}})^2 \qquad .....(3.9)$$

a non-zero value of $\partial\phi/\partial t$ indicates existence of a finite dynamic pressure in the fluid. Clearly, a finite value of $\partial\phi/\partial t$ on ∂D_{C1} at $t = 0$ implies an abrupt or impulsive application of pressure on this boundary. Large fluid motions on the free surface near the intersection are then an expected consequences. Other forms of $M(t)$ have been attempted (e.g. $M(t) = 1 - \exp(-\sigma t)$ or $M(t) = \cos(\pi t/\sigma)$ in which the growth of ϕ values are comparatively more gradual during the initial period, but $\partial\phi/\partial t$ has a nonzero initial value, and $M(t) = \sin(\pi t/\sigma)$ in conjunction with a cos function for ϕ in the l.h.s. of (3.3), which enforces $\partial\phi/\partial t$ to be zero at the expense of nonzero ϕ at $t = 0$), but were found to produce similar numerical instabilities of varying severity (usually less severe). It is therefore important that both ϕ and $\partial\phi/\partial t$ have zero initial values.

Recent studies on the wave-maker problem (Cointe, Jami and Molin 1987) indicate that the impulsive wave-maker problem does not admit a unique solution unless proper account is taken for the transient period in which the wave-maker motion grows from zero to a finite value. The present simulation is analogous to the wave-maker problem in that in the latter the Neumann condition is posed on the wave-maker according to its prescribed motion (studied in the sequel, §3.2.3). The present experience of a numerically ill behaved solution when zero values of ϕ and $\partial\phi/\partial t$ at $t = 0$ are not imposed, which is equivalent to the application of an impulsive pressure on this boundary, appears to confirm the results of the analytical study. When (3.6) is applied with a finite value of σ in $M(t)$ given by (3.7), the associated difficulty disappears. As a demonstration, in Figures 3.7 (a) - (d), the free surface elevations are shown for values of σ/T = 0, 0.5, 1.0 and 2.0. Here a discretization of $\Delta x_F = \lambda/40$ and $\Delta t = T/80$ is utilized. Note that $\sigma/T = 0$ corresponds to the absence of modulation of the applied potential, i.e. to the application of the impulsive pressure (this plot was already shown in Figure 3.6, but is reproduced once more for convenience of comparison). The progressive reduction in the 'zigzag' patterns with increasing values of σ is evident. For $\sigma/T = 1.0$, a careful inspection reveals still some existence of the undesired behaviour (see the profile at $t/T = 2.0$). With further increase of σ/T to 2, the wave begins to evolve smoothly.

3.2.2.2 Computed Results

Computed results in terms of the free surface elevations are shown in Figures 3.8 and 3.9. For these computations, the downstream boundary is placed at a distance of 2λ from the upstream boundary. The discretization parameters are: $\Delta x_F = \lambda/24$ and $\Delta t/T = 1/36$, where λ and T refer to the length and period of the excitation wave. The downstream boundary is considered to be a rigid wall, thus the condition posed on ∂D_{C2} is $\partial\phi(t)/\partial n = 0$ at all time instants.

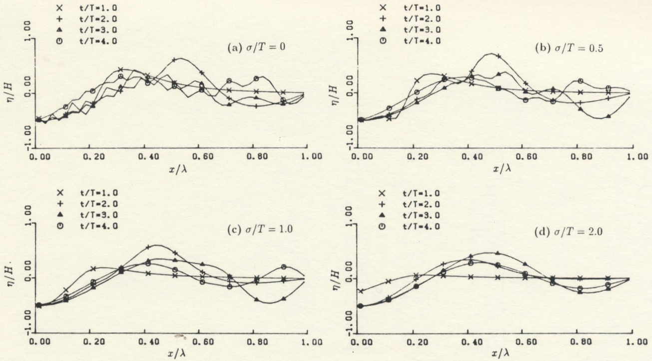

Figure 3.7 Instability at the intersection of ∂D_{C1} and ∂D_F from application of (3.3) and its effective suppression/elimination; for this result , $L = \lambda$, $d/\lambda = 0.5$, and $\Delta x_F, \Delta x_{C1}, \Delta x_{C2} = \lambda/40$ and $\Delta t = T/80$; the imposed condition on ∂D_{C2} is, $\phi(t) = 0$; (a) above is same as Figure 3.6.

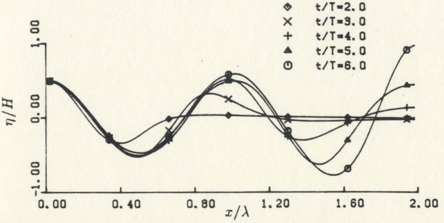

Figure 3.8 Free surface elevations of an unsteady small amplitude wave progressing into an initially undisturded fluid region; $L/\lambda = 2$, $d/\lambda = 0.5$, $\Delta x_F/\lambda = 1/24$ and $\Delta t/T = 1/36$; the downstream boundary is a wall.

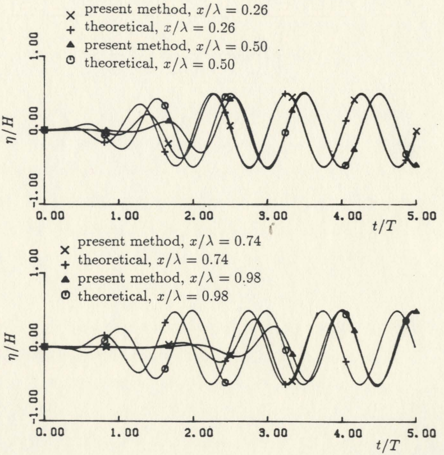

Figure 3.9 Evolution of the free surface in time for the wave shown in Figure 3.8 above.

The water has a depth of $d = 0.5\lambda$, and the excitation potential is modulated over $2T$, i.e. $\sigma/T = 2$. The wave is observed to form gradually, subsequently it grows and propagates along the positive x axis. At about $t/T = 3$, the wave begins to reflect from ∂D_{C2}, and at $t/T = 6$, almost full reflection takes place at that boundary, indicated by the growth of the free surface elevation. Linear theory predicts a magnification of the wave amplitude by a factor of two for full reflection on ∂D_{C2} (i.e. $\eta/H = 1$), and the present results show a closely comparable factor, at the last collocation point the corresponding numerical value of η/H is 0.985. Figure 3.9 shows plots of the free surface elevations at four stations situated at $x = 0.26\lambda, 0.50\lambda, 0.74\lambda$ and 0.98λ, together with the theoretical Airy wave profiles computed from (3.5) at the corresponding periods. For comparative purposes, the Airy wave profiles are also modulated by the same modulation function. It is clear that for $t/T \leq 5$, the reflected waves do not reach the location $x/\lambda = 0.98$. At locations $x/\lambda = 0.24$ and 0.50, more than two wave periods of steady state results are achieved. The comparisons with theoretical profiles before reflected waves contaminate the profile are very encouraging. These results demonstrate that reasonably long periods of steady state results can be achieved in a region closer to the upstream boundary by shifting the downstream boundary further downstream.

In order to further investigate on the effect conditions imposed on the downstream boundary have upon the interior solution, computations are performed with the condition $\phi(t) = 0$ prescribed on ∂D_{C2}. This condition physically implies that the tangential velocity at the downstream boundary is zero at all times, in contrast to a zero normal velocity when ∂D_{C2} is a wall, and is appropriate in the limit of high frequency waves (such conditions are usually applicable in studies of flow due to earthquake (Garrison and Berklite 1972), impacting bodies on the free surface (Geers 1982; Troesch and Kang 1986). Figure 3.10 compares the free surface contours obtained for the two imposed conditions of $\phi = 0$ and $\partial\phi/\partial n = 0$ on ∂D_{C2}. In the region $0 \leq x \leq \lambda$, the profiles differ negligibly until about $t/T \leq 5$. Clearly, waves reflected from ∂D_{C2} have not yet reached this region. This indicates that reasonably accurate results upto few periods of steady state can be achieved in parts of the fluid closer to the downstream boundary, if the control domain is suitably large, irrespective of whether a wall condition or a zero potential condition is applied at the downstream boundary.

3.2.3 The Wave-Maker Problem

This application relates to the wave-maker problem. A piston type wave-maker is undergoing a horizontal sinusoidal motion:

$$\xi = s \cos \frac{2\pi t}{T} \qquad .....(3.10)$$

at one end of the control domain, with period T and half-stroke s. The mean position of the wave-maker coincides with ∂D_{C1}. The boundary condition for the wave-maker is applicable at its mean position, consistent with linear theory approximations. For the simulation, the condition prescribed on ∂D_{C1} is therefore

$$\frac{\partial\phi}{\partial n} = \frac{2\pi}{T} s \sin \frac{2\pi t}{T} \qquad .....(3.11)$$

Observe that the wave-maker has a zero initial velocity. Nevertheless, earlier remarks concerning the compatibility of initial boundary data apply, and it is found necessary to modulate the velocity by the same modulation function (3.7):

$$\frac{\partial\phi^*(t)}{\partial n} = M(t)\,\frac{\partial\phi(t)}{\partial n} \qquad .....(3.12)$$

Results are shown in terms of the free surface elevations. The control domain chosen is relatively large. The downstream boundary is located at a distance 4λ from the wave-maker and is taken as an impermeable wall with the condition $\partial\phi(t)/\partial n = 0$ prescribed on it. The water has a depth of $d = 0.5\lambda$. Here λ represents the length of an equivalent Airy wave of period T in water depth d. Relatively coarse discretizations (compared to the preceding examples) of $\Delta x_F, \Delta x_{C1}, \Delta x_{C2} = \lambda/15$ and $\Delta t = T/24$ are used, and $\sigma/T = 2$. Figure 3.11 shows the space plots of the free surface elevations at times $t/T = 3.0$, 4.0, 5.0 and 6.0, while the time-evolutions at locations $x/\lambda = 0.5$, 1.0 and 1.5 are shown in Figure 3.12. Generation of a wave is evident. The generated wave eventually exhibits a steady state periodic behaviour with period T. The gain function for this type of wave-maker, according to linear theory, is given by (Biesel 1951)

$$\frac{a}{s} = \frac{2\sinh^2(kd)}{kd + \sinh(kd)\cosh(kd)} \qquad .....(3.13)$$

with a denoting the amplitude of the generated wave and k = wave number $= 2\pi/\lambda$. This expression yields a value of $a/s = 1.9468$, while the present simulation has the corresponding value of $a/s = 1.95$ (the numerical value is evaluated by averaging the elevations at crests and troughs after the wave reaches a steady state). The difference is less than 0.2%.

For a single flap type wave-maker hinged at depth d, the wave-maker motion is given by

$$\xi(z) = s(1 + \frac{z}{d})\cos\frac{2\pi t}{T} \qquad .....(3.14)$$

from which the normal component of the wave-maker velocity, applicable at its mean position, is deduced as

$$\frac{\partial\phi}{\partial n} = -\frac{2\pi}{T}(1 + \frac{z}{d})s\sin(\frac{2\pi t}{T})\cos\{\frac{s\cos(2\pi t/T)}{d}\} \qquad .....(3.15)$$

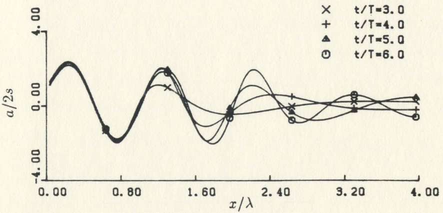

Figure 3.11 Free surface elevations generated by a piston type wave-maker at ∂D_{C1}; $L/\lambda = 4$, $d/\lambda = 0.5$, $\Delta x_F/\lambda = 1/15$ and $\Delta t/T = 1/24$; boundary ∂D_{C2} is a wall.

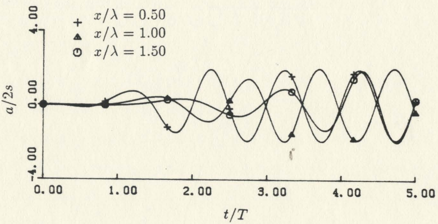

Figure 3.12 Evolution of the free surface in time corresponding to the plots in Figure 3.11 above.

This condition is imposed on ∂D_{C1}, together with $\sigma/T = 2$, to achieve the results presented in Figures 3.13 and 3.14. Other parameters are retained the same as in the application of the piston type above. Free surface elevations at times t/T = 3.0, 4.0, 5.0 and 6.0 are plotted in Figure 3.13, while Figure 3.14 shows time evolutions at three locations x/λ = 0.5, 1.0 and 1.5. Once again, formation of a wave exhibiting a steady state behaviour with period T is apparent. The appropriate gain function for this case, given by (Biesel 1951)

$$\frac{a}{s} = \frac{2\sinh(kd)}{kd}\frac{[1-\cosh(kd)+kd\sinh(kd)]}{[kd+\sinh(kd)\cosh(kd)]} \quad .....(3.16)$$

produces a value of $a/s = 1.3785$. In comparison, the simulated wave has a gain function of $a/s = 1.39$, a value not more than 1% in error.

3.3 Discussion and Summarizing Remarks

The presented results demonstrate the robustness of the numerical time domain simulation scheme for fluid flow problems that include a free surface. Computations are performed for a number of combinations of other parameters, and have shown a similar quality of agreement with theoretical solutions. Regarding discretizations, no rigorous rule could be established for the minimum size of Δx. As a rough guide, a size of $\Delta x = \lambda/12$ is found to describe adequately the evolution of the free surface for most of the simulations. Further relaxation results in lack of resolution, although the fluid motion can still be followed (which means the solution does not break down). For temporal grid size, the usual Courant-Friedrichs-Lewy condition (Roache 1972) of

$$N_{CFL} \equiv |c\frac{\Delta t}{\Delta x}| \leq 1 \quad .....(3.17)$$

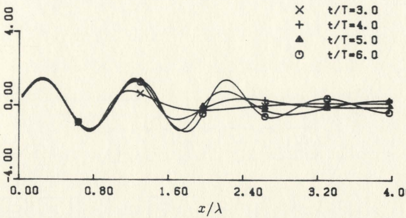

Figure 3.13 Free surface elevations generated by a flap type wave-maker at ∂D_{C1}; $L/\lambda = 4$, $d/\lambda = 0.5$, $\Delta x_F/\lambda = 1/15$ and $\Delta t/T = 1/24$; boundary ∂D_{C2} is a wall.

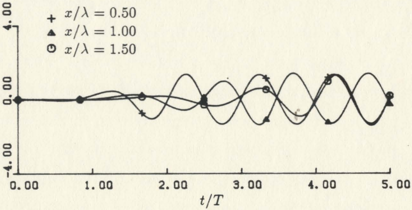

Figure 3.14 Evolution of the free surface in time corresponding to the plots in Figure 3.13 above.

with c representing the wave celerity, is followed. In the present computations, for most of the cases, a value of N_{CFL} between 0.5 and 0.7 is used. Further examination of the possible size of $\Delta t/T$ by successive relaxation was not pursued in view of the expected upper limit posed on it by (3.17).

The solution is found to exhibit a tendency towards numerical instability upon successive refinements of the spatial mesh sizes. When a collocation point is located very close to a corner where the boundary undergoes sharp changes in curvature, such as the intersection of ∂D_F with ∂D_{C1} and ∂D_{C2}, relatively larger errors of the computed velocities are found in these locations, in comparison with points far from such corners. This is confirmed by a number of numerical experiments for the application case 1 (§3.2.1), for which the theoretical values of both the boundary data (ϕ and $\partial\phi/\partial n$) are calculable from (3.3) and (3.4). Comparisons of computed and theoretical values of $\partial\phi/\partial n$ on ∂D_F show an increasing difference as the collocation points approach the intersections on both sides. These non-uniform differences are believed to introduce numerical instability when the grid size is very fine, typically when $\Delta x/\lambda \leq 1/100$. A similar behaviour of solutions near corners in applications of boundary element methods appears to be fairly well documented in literature (see Schultz 1987). For the present time simulation scheme, numerical stability considerations are crucial, since the computed free surface elevations and potentials at any time instant form the input for the next level of computations. Considering the segment sizes for which accurate results (in comparison with the theoretical results) are obtained, this instability is thought not to be a serious limitation in the applications of the algorithm, but serves to indicate a lower bound of the grid sizes. As a guide, values in the range of $1/80 \leq \Delta x/\lambda \leq 1/20$ are suggested.

It is also found important to choose an appropriate value of σ while modulating the exciting potential (or the velocity). A very small value of σ does not entirely remove the instability as can be seen from Figure 3.7. For the application cases presented in §3.2.2.2 and §3.2.3, a value of $\sigma/T < 0.5$ resulted in some instability. For the spatial grid size of $\Delta x/\lambda = 1/24$, a value of $\sigma/T = 0.5$ was found to cause the instability to initiate after about 80 time steps, regardless of the temporal grid size. For a more refined mesh size, this was found to start even earlier (for example, when the mesh size was $\Delta x/\lambda = 1/40$, the free surface profile began to show distortions after about 50 steps). However, as the results demonstrate (cf. Figures 3.8 to 3.14), it is possible to achieve stable results by a suitable choice of σ. It should be observed that no artificial smoothing was applied on the free surface in any of the above computations. The suggested values of σ are: for $\Delta x/\lambda \leq 1/32$, $\sigma = T$ and for $\Delta x/\lambda \geq 1/32, \sigma = 2T$. These values can perhaps be lowered considerably depending on specific applications or if artificial smoothing schemes are applied.

When both ϕ and $\partial\phi/\partial n$ are defined on some parts of ∂D, the physical system is overdetermined. For such situations, it is possible to achieve a reduction in the number of linear algebraic equations to be solved for the unknowns. Such overdetermined systems (as was followed in Isaacson 1982) are soluble when the imposed boundary data are compatible. Results for the application case 1 (§3.2.1) were obtained by specifying both the boundary data (ϕ and $\partial\phi/\partial n$) on ∂D_{C1} and ∂D_{C2}. However, it was noticed that such overdetermined systems were inherently more susceptible to numerical instability (this was studied by specifying ϕ and $\partial\phi/\partial n$ given by eqns. (3.3) and (3.4) and then introducing a slight variation in the order of 0.001% in one of them). The computed velocities on the free surface were found more sensitive to the discretization near the intersection points when the boundary data were not perfectly compatible, as compared to the well posed problems. It is further observed that, in principle, a set of linear equations can be obtained when both the boundary data are imposed on a particular part of the boundary while none are specified on some other part, provided the number of segments in discretizing these boundaries are equal. Though this provides a tempting situation, specially for suggesting a means of avoiding imposition of any open boundary condition (i.e. imposition of both ϕ and $\partial\phi/\partial n$ on ∂D_{C1} and non-specification of any data on ∂D_{C2}), the resulting systems are nevertheless unsolvable. The coefficient matrix becomes singular. This is consistent with the well known property of elliptic boundary value problems; a well posed problem must have one boundary data, or an interrelation between the two must be specified, all across the boundary (see e.g. Polozhiy 1967).

Besides the 4th order A-B-M scheme, other schemes have also been considered. In particular, we find that explicit schemes do not always lead to a converged solution. This observation contradicts Isaacson's (1982) method where the author employed second order explicit schemes for time-integration of the free surface conditions. The first order implicit scheme is found inadequate in that the solution shows poor convergence characteristics as well as contains considerably large errors. In contrast, second order schemes lead to substantial improvements. Further improvements are achieved by using 3rd and 4th order schemes, although the relative improvements between these two latter orders are practically insignificant (the numerical values differ only in the 6th decimal place). In no cases was more than one corrector level required for a convergence of 1 in 10^{-4}. It is observed here that, from a computational point of view, higher order schemes do not require additional computational efforts. However, in view of the good convergence obtained with 4th order schemes, further experiments with still higher orders schemes were not pursued.

For the starter, the lower order A-B-M schemes are found to be adequate. For the application cases in §3.2.2.2 and §3.2.3, the fluid remains practically undisturbed (the associated non-dimensional velocities, $\partial\phi/\partial n/(\lambda/T)$, on the free surface do not exceed 10^{-7}). Since the final aim is to pursue such applications for the simulation of steep waves (considered in §4), further investigations employing higher order Runge-Kutta starters were not carried out.

Finally, the following concluding remarks can be made from the results presented in this section:

(1) The simulation scheme, although based on the lowest order of discretization of the boundary integral, produces sufficiently accurate and reliable results. The solution does not appear to degenerate to any significant degree as it progresses in time.

(2) The scheme is sensitive to the chosen initial conditions. In particular, impulsive application of pressure is found to produce numerical instability of a weak type. Therefore, it is important to maintain the compatibility of initial boundary data.

(3) It is feasible to apply the method to simulations of free surface motions that are of unsteady and transient nature.

4 Unsteady Propagation of Steep Waves

4.1 General Considerations

For simulation of fully non-linear free surface flow problems, it is imperative that the full non-linear free surface conditions given by eqns. (2.2) and (2.3) are considered without any simplifying approximations. Noticing that these equations are to be satisfied on the exact location of the free surface, the evolution of the free surface within the control domain must be followed such that the fluid domain can be redefined at every consecutive time instant. Furthermore, the values of the boundary data must be determined on the evolved free surface.

4.1.1 Evolution Equations for the Free Surface

The free surface conditions in eqns. (2.2) and (2.3) are in an Eulerian frame of reference. Identifying the collocation points on $\partial D_F(\mathbf{x}, t)$ as 'marker' points (the trace of which defines the free surface contour), time integration of eqn. (2.2) provides information on the location of these points vertically displaced. For determining the velocity potential on the instantaneous free surface contour, an appropriate evolution equation for ϕ on the evolved free surface is to be derived. The change in potential at points on the free surface undergoing vertical displacements is (see e.g. Faltinsen 1978)

$$d\phi = \frac{\partial \phi}{\partial t} dt + \frac{\partial \phi}{\partial z} d\eta \qquad .....(4.1)$$

since $\phi = \phi(z, t)$ for these points. Here $d\eta$ is the incremental vertical displacement of the 'marker' points:

$$d\eta = \frac{\partial \eta}{\partial t} dt \qquad .....(4.2)$$

From (2.2), (2.3), (4.1) and (4.2), the evolution equation for ϕ is readily deduced as

$$\frac{d\phi}{dt} = -g\eta - \frac{1}{2}[(\frac{\partial\phi}{\partial x})^2 - (\frac{\partial\phi}{\partial z})^2] - \frac{\partial\phi}{\partial x}\frac{\partial\phi}{\partial z}\frac{\partial\eta}{\partial x} \qquad ......(4.3)$$

which defines the rate of change of the potentials at these points. Here the symbol d/dt is used to signify that the differentiation is following the 'marker' points which are free to move along vertical lines. The evolution equations to be integrated in time for following the free surface contour and potential, in the present method, are therefore eqns. (2.2) and (4.3) respectively. In passing, it is remarked that Isaacson's (1982) strictly Eulerian method of following ϕ on the free surface by integrating eqn. (2.3) determines the potential at space fixed points. This introduces a further approximation on the computed free surface potentials in that the changes in them due to the updated location of the free surface are not accounted for. In contrast, eqns. (2.2) and (4.3) are exact.

The above method of following the free surface is different from the fully Lagrangian method utilized in most of the previous investigations of non-linear water waves based upon similar integral relation formulations (e.g. Longuet-Higgins and Cokelet 1976; Vinje and Brevig 1981; Baker, Meiron and Orszag 1982; Lin, Newman and Yue 1984; New, McIver and Peregrine 1985; Dommermuth and Yue 1987). It is worth comparing and contrasting the features of the two. In fully Lagrangian methods, the 'marker' points on the free surface coincide with physical fluid particles and the evolution equations take the form:

$$\frac{D}{Dt}\mathbf{x}_F = \frac{\partial\phi}{\partial\mathbf{x}} \qquad .....(4.4)$$

$$\frac{D}{Dt}\phi(\mathbf{x}_F) = -g\eta + \frac{1}{2}(\nabla\phi)^2 \qquad .....(4.5)$$

with D/Dt denoting the material derivative: $D/Dt = \partial/\partial t + \partial\phi/\partial\mathbf{x} \cdot \partial/\partial\mathbf{x}$ and

$\mathbf{x}_F$ representing the radius vector of the marked fluid particles. The vertical component of (4.4) provides information on the vertical displacements of the 'marker' points. It may be noticed that this component is identical to the kinematic free surface condition (2.2). Since the particles also undergo horizontal displacements, the horizontal component of (4.4) needs to be integrated as well.

The attractiveness of following fluid particles lies clearly in its ability to describe multivalued free surface contours. In contrast, the present method is restricted in its applicability to single-valued free surface profiles. The possibility for simulating overly extreme wave conditions, as in the case of wave breaking, is therefore excluded. Nevertheless, the present method provides several computational advantages:

(a) The 'marker' points are not allowed to cluster, which is expected to reduce adverse numerical effects associated with the Lagrangian methods in which the particles tend to concentrate in some regions. In other words, a better control is exercised on the points being followed. From previous experience of other workers, it is known that some form of control on these points is necessary to prevent them from clustering, e.g. introduction of a 'tangential' velocity component as discussed in Baker et al. (1982) as a controlling device, regridding of the free surface points at every step as employed by Dommermuth and Yue (1987). The present mode of following the free surface is free from such additional computational burdens.

(b) The 'marker' points can not leave the computational domain at any time, therefore the additional task of tracing such points is avoided.

(c) In the present discretization scheme, numerical difficulties are anticipated when a collocation point is situated very close to the vertical control boundaries, as found from the computational experience related to the linear case (recall the discussion in §3.3). By preventing horizontal displacements of the 'marker' points, such problems are also minimized.

Yet another point with regard to the applicability of the present method needs to be emphasized. The ultimate objective is to be able to simulate the body motions for a sufficiently long time, preferably over several periods of oscillation after a steady state is established, which is different from interaction of bodies with breaking waves. It must be noted that even in Lagrangian methods the simulation can not be extended much beyond the time when the wave breaks (the fluid domain ceases to be simply connected, and the methods become inapplicable). Therefore, inability to model multivalued free surface contours does not appear to be a serious limitation of applicability of the method. Similar restrictions in applications are typical of most finite-difference algorithms (see e.g. Telste 1985).

It must be noted that in both descriptions (Lagrangian and the present method), the fully non-linear free surface conditions are treated and the approximations are introduced by the numerical schemes employed in the integration of the appropriate evolution equations. The free surface contour in both cases is defined by the trace of the 'marker' points, representing either physical fluid particles or non-material points on the free surface.

4.1.2 Spatial Derivatives on the Free Surface

The evolution equations (2.2) and (4.3) require evaluation of spatial derivatives of η and ϕ at the collocation points j. To determine $(\partial\eta/\partial x)_j$, η as a function of x is approximated by a cubic spline. From this approximation, the components of the outward normal can be calculated:

$$n_{x_j} = \frac{-(\partial\eta/\partial x)_j}{[1+(\partial\eta/\partial x)_j]^{0.5}} \qquad .....(4.6(a))$$

$$n_{z_j} = \frac{1}{[1+(\partial\eta/\partial x)_j]^{0.5}} \qquad .....(4.6(b))$$

For the spatial derivatives of ϕ, we have

$$\begin{aligned}(\frac{\partial\phi}{\partial s})_j &= (\frac{d\phi}{dj})_j/(\frac{ds}{dj})_j \\ &= (\frac{d\phi}{dx})_j(\frac{dx}{dj})_j/(\frac{ds}{dx})_j(\frac{dx}{dj})_j \\ &= n_{z_j}(\frac{d\phi}{dx})_j \qquad .....(4.7)\end{aligned}$$

since $1/(ds/dx)_j = n_{z_j}$. Here $\partial/\partial s$ denotes the tangential derivative. To determine $(d\phi/dx)_j$, once again ϕ as a function of x is approximated by a cubic spline. From $\partial\phi/\partial s$ and $\partial\phi/\partial n$, other components of the spatial derivatives can be determined:

$$\frac{\partial\phi}{\partial x} = n_x\frac{\partial\phi}{\partial n} + n_z\frac{\partial\phi}{\partial s} \qquad .....(4.8(a))$$

$$\frac{\partial\phi}{\partial z} = n_z\frac{\partial\phi}{\partial n} - n_x\frac{\partial\phi}{\partial s} \qquad .....(4.8(b))$$

In the software, an IMSL routine for cubic splines with natural end conditions is used in which no conditions are prescribed at the end points but the penultimate points enforce continuity of second derivatives (see Ahlberg, Nilson and Walsh 1967).

4.1.3 Simulation Procedure

The simulation for unsteady propagation of steep waves is accomplished by a similar procedure as in the application described in §3.2.2. A wave potential, representing an oncoming wave travelling in the positive x direction, is imposed on ∂D_{C1} at all times. This applied potential is hereinafter called the excitation potential, since it provides the necessary excitation for initiating the fluid motion in $\mathcal{D}$. Unlike in the linear case, questions regarding selection of appropriate excitation potential arise in the present non-linear application. As a first approximation, the Airy potential given by eqn. (3.3) is chosen as the excitation potential. Subsequently other forms of excitations can be considered. However it will be shown later through numerical results that the form of the excitation potential has little influence on the generated numerical wave in the interior of $\mathcal{D}$.

An alternative way of simulating waves is to provide a physically moving wave-maker at one end of the control domain, analogous to the application case considered in §3.2.3. This procedure was followed in earlier works, e.g. Lin (1984), Lin,Newman and Yue (1985) and Greenhow and Lin (1985). In the present method of following the evolution of the free surface, such approach would necessitate either a redistribution of the free surface grid or a successive introduction and deletion of the collocation points, since the wave-maker is likely to either enter or withdraw from the free surface grid. The possibility of points coming too close to the wave-maker is also distinct, which is likely to cause numerical difficulties (cf. §3.3). Provided waves are produced within the control domain, the source of its generation is not important for the ultimate objective of wave-body interactions. Therefore, having gained some confidence from the equivalent linear application case, here the application of a known potential along a fixed ∂D_{C1} is adopted.

Several aspects of the numerical scheme, closely related to the specific details discussed in §1.2.2.2, were found to have important effects on the algorithm and required special attention. These are addressed below.

4.2 Specific Considerations

4.2.1 Instability at the Intersection of ∂D_{C1} and ∂D_F

On application of an appropriately time-modulated excitation Airy potential on ∂D_{C1} in the described algorithm, an instability is found to originate at the intersection of ∂D_{C1} and ∂D_F. The form of the instability is qualitatively similar to that in the analogous linear application case when not applying the modulation function. Between the adjacent collocation points on the free surface, the computed wave elevations and the values of the potential exhibit undesired oscillations, the amplitudes of which progressively diminish with the distance from the intersection. The severity of this, indicated by the amplitude of these oscillations, is considerably larger than those encountered earlier in the linear case (cf. Figures 3.6 and 3.7). These high frequency short length waves gradually travel inwards into the fluid domain. More importantly, the amplitudes magnify with such rapidity that within few time steps after they appear (typically within 10 time steps irrespective of the step size), the solution breaks down. In view of the fact that the exact free surface elevation defines the boundary of the domain (in contrast to the mean free surface in the linear case), the increase of the amplitudes of these oscillations is not surprising.

Application of the modulation function over increasingly larger periods of time (i.e. increasing the value of σ in $M(t)$ in eqn. (3.7)) helped to defer the initiation of the oscillations, but did not remove or suppress the instability. Several forms of artificial smoothing schemes failed to cure the problem. Partial success could be achieved in keeping the instability controlled by means of excessive smoothing at the expense of large numerical viscosity effects. A particular smoothing scheme devised on the basis of an averaging principle provided some success in suppressing the unwanted oscillations. In this scheme, the values of η and ϕ on ∂D_{C1} corresponding to the excitation potential were used to average the elevation and potential according to the following formulae:

$$\begin{aligned} \bar{f}_1 &= \frac{1}{4}[2f_g + f_1 + f_2] \\ \bar{f}_2 &= \frac{1}{16}[2f_g + f_1 + 9f_2 + 4f_3] \\ \bar{f}_3 &= \frac{1}{64}[2f_g + f_1 + 9f_2 + 36f_3 + 16f_4] \end{aligned} \qquad .....(4.9(a))$$

and for a general point i

$$\begin{aligned} \bar{f}_i &= \frac{1}{4^i}[2f_g + f_1 + 9(f_2 + 4f_3 \\ &\quad +4^2 f_3 + \cdots + 4^{i-2} f_i) + 4^{i-1} f_{i+1}] \end{aligned} \qquad .....(4.9(b))$$

where f_i and $\bar{f}_i$ are respectively the ith ordinates before and after smoothing, with i denoting the collocation points numbered in an increasing order in the positive x direction, and f_g represents the values of η or ϕ on ∂D_{C1}. Although free from instability, the resulting generated waves were found excessively damped and were clearly unacceptable.

In an effort to search for the root of these spurious high frequency waves, some numerical experiments were performed by selecting pre-assigned values of potentials on ∂D_F and ∂D_{C1}, and by prescribing the geometry of ∂D_F. A closer examination of the generated flow indicated that the computed normal velocities were extremely sensitive to the free surface contour and boundary data near the intersection. Large changes in the values of ϕ at the adjoining segments on the two boundaries produced large velocities on the free surface. In addition, incompatibilities between the contour of ∂D_F and the free surface elevation of the wave corresponding to the applied excitation potential on ∂D_{C1} resulted in similar erratic fluid motions at the intersection.

A possible explanation for the generation of these oscillations can now be given. Application of an excitation potential on ∂D_{C1} can be considered as the presence of a wave on the upstream side (left) of ∂D_{C1}, exterior to $\mathcal{D}$. For convenience of discussion, this wave will be called the 'upstream' wave in the sequel. The free surface elevation and potential of this wave conform to the free surface conditions within the approximations of the particular wave theory. For example, the Airy potential on ∂D_{C1} implies an upstream wave satisfying the linearized free surface conditions. To the immediate right of ∂D_{C1}, a solution is sought for such that the full non-linear free surface conditions are satisfied within the accuracy of the employed numerical scheme but without approximating the free surface conditions themselves. Consequently the free surface elevation and potential undergo discontinuity across ∂D_{C1}. In other words, the free surface conditions implicitly satisfied on the left of ∂D_{C1} (i.e. by the upstream wave) are inconsistent with the conditions on ∂D_F in the immediate right of ∂D_{C1}. This discontinuity is believed to cause large velocity gradients across the vertical boundary, which in turn initiate the instability. We remark that the application of other 'non-linear' excitation potentials, e.g. Stokes second order potential, was tried with the hope that the non-linear theoretical upstream wave and the numerical downstream wave across ∂D_{C1} would be more compatible and thus would result in a suppression of the instability. Unfortunately, the solution remained equally unstable. Difficulties originating from analogous discontinuities were known earlier, e.g. Han and Stansby (1987) discussed similar problems, and Lin, Newman and Yue (1985) identified the discontinuity with the difficulty in Vinje et al.'s (1982) matching of non-linear interior with linear exterior solutions.

In order to achieve a smooth variation of the free surface elevation and potential across ∂D_{C1}, a *matching procedure*, described below, is devised.

4.2.1.1 The Matching Procedure

This technique is illustrated by means of Figure 4.1. Consider another vertical boundary ∂D^*_{C1} in the interior of the control domain $\mathcal{D}$ at a short distance l from ∂D_{C1}. In the existing algorithm, the numerically evaluated free surface elevation and potential, represented by $f_2(x)$, typically exhibit large oscillatory behaviour as illustrated. A transfer function $g(x)$ is introduced to redefine $f_2(x)$ as $f^*_2(x)$ in the region between ∂D_{C1} and ∂D^*_{C1}, henceforth referred to as the 'matching zone':

$$f^*_2(x) = g(x) f_1(x) \qquad .....(4.10(a))$$

where $f^*_2(x)$ is the smoothed curve in $x_1 \leq x \leq (x_1 + l)$, $f_1(x)$ indicates the theoretical (upstream) wave elevation or the potential corresponding to the excitation potential on ∂D_{C1} and x_1 represents the x coordinate of ∂D_{C1}. A quadratic polynomial is chosen for $g(x)$:

$$g(x) = a_1x^2 + a_2x + a_3 \qquad .....(4.10(b))$$

whose coefficients a_1, a_2, a_3 are determined from the conditions:

$$f_2^*(x_1) = f_1(x_1)$$

$$f_2^*(x_1 + l) = f_2(x_1 + l) \qquad .....(4.10(c))$$

$$\frac{\partial}{\partial x} f_2^*(x_1 + l) = \frac{\partial}{\partial x} f_2(x_1 + l)$$

The derivations of a_1, a_2, a_3 are provided in Appendix A.2. The above procedure requires evaluation of $\partial[f_2(x_1 + l)]/\partial x$ which is determined from a second order central difference scheme (see Appendix A.4 for the formula).

In principle, a higher order polynomial representation of $g(x)$ is possible by exploiting additional conditions such as continuity of higher order derivatives at x_1 and $(x_1 + l)$. The quadratic function for $g(x)$ is however found to be very effective in keeping the instability locally arrested and enables the fluid motion to be followed without further problems originating at the intersection point. It is noted that a linear form of $g(x)$ was found not as satisfactory in completely suppressing the instability.

A note of caution is appropriate with respect to the implementation of the above technique. Due to the chosen coordinate system with origin at the undisturbed free surface level, $g(x)$ does not behave properly when $f_1(x_1 + l)$ and $f_2(x_1 + l)$ differ in sign (though not much in magnitudes). This results in a 'folding' of $f_2^*(x)$ as illustrated in Figure 4.2. Additionally, when $|f_1(x_1 + l)| \simeq 0$, a singularity appears in the derivation of the coefficients (see eqns. (A.2.3) in appendix A.2). A local shift of the coordinate system removes these difficulties.

Incorporation of the technique described above is found not to introduce adverse numerical effects into the interior solution. The computed wave in $\mathcal{D}$ does not degenerate to any significant extent. The additional boundary ∂D^*_{C1} can be interpreted as the upstream boundary of a reduced fluid domain $\mathcal{D}^*$ within which the fluid motion is sought (i.e. the full non-linear free surface conditions are satisfied in $\mathcal{D}^*$). In other words, the interior domain is stretched by a distance l to absorb the 'impulsive' nature of the flow which is believed to be an undesired outcome of the incompatibility of the free surface boundary conditions across the original boundary ∂D_{C1}. The penalty for stretching of $\mathcal{D}^*$ is that additional collocation points in l are required. The consequential additional expense in computer time is of the order of 10%. Results demonstrating the effectiveness of this procedure and typical values of l are presented in §4.3.

On the downstream side boundary, it is necessary to determine the intersection of ∂D_F with ∂D_{C2}. This is determined via a second order Lagrangian scheme using the data at the three preceding collocation points on ∂D_F (see eqn. (A.4.4) in Appendix A.4 for the formula).

4.2.2 Instability on the Free Surface

Apart from the instability originating at the upstream side intersection on the free surface, another instability develops on the entire free surface as the solution progresses. Similar 'saw-tooth' instability has been reported by earlier investigators (see the discussion in §1.2.2.2 (c)). Numerical experiments with various combinations of the spatial and temporal grid sizes were performed with the hope of establishing a criterion related to these discretization parameters.

No such criterion could be established. In the present formulation, in which the collocation points on the free surface points are restricted to move vertically, the arc lengths between adjacent collocation points never reduce below the horizontal grid spacing. Consequently, if the time step size is chosen properly in relation to the horizontal projection of the free surface segments, the local Courant condition is easily maintained. In all computations, the usual C-F-L condition (Courant-Friedrichs-Lewy condition, see eqn. (3.17)) is maintained in the entire fluid domain and throughout the simulation period. An alternative form for a stability criterion based upon a linear von Neumann stability analysis for the fourth order Runge-Kutta scheme is provided by Dommermuth and Yue (1987):

$$\left|\frac{\pi g \Delta t^2}{8 \Delta x_F}\right| \leq 1 \qquad .....(4.11)$$

which is also maintained in the present computations. The implicit fourth order A-B-M scheme used here has the same order of accuracy as the above R-K scheme, and in fact has a slightly higher accuracy than the modified R-K scheme of Dommermuth and Yue (both ∂D_F and ϕ on ∂D_F are upgraded at each iteration in the present algorithm while only the latter is upgraded in their scheme). Present computational experience indicates that this instability is closely associated with the free surface elevation. It becomes more pronounced as the wave steepens. It should be observed that in the analogous linear application (§3.2.2), no such problem was encountered. Computations with successively larger levels of iteration in the time-integration of the free surface conditions and closer examination of the computed free surface profiles and boundary data suggest insensitivity of the instability with respect to the time-integration schemes. The solution indeed converges, usually to an accuracy of 1 in 10^{-4} within the first cor-

1986). Remembering the goal of simulating body-wave interaction problems, the main concern is to avoid the problem of instability so that the solution can be progressed in time without breakdown and/or suffering from appreciable numerical viscosity effects. In view of these remarks, artificial smoothing appears justified.

4.2.3 Non-reflective Downstream Boundary

Consideration of the downstream boundary ∂D_{C2} as a wall, as it was done in the applications presented in §§3.2.2, 3.2.3, is not a satisfactory solution for long time simulations. Alternative means of treatment of the flow at this boundary is clearly necessary.

The specification of a condition on this boundary is analogous to an open boundary condition or a radiation condition. In the absence of theoretically rigorous 'non-linear' radiation conditions, the other recourse is to construct a 'numerical' radiation condition within acceptable limits of approximations. An appropriate open boundary condition must be sufficiently transmissive such that all the wave phenomena generated in the interior of $\mathcal{D}$ pass through the boundary without suffering from appreciable numerical reflection effects. Additionally, when the numerical errors attributable to such an imperfect radiation condition can not be reduced any further, it must be ensured that the stability and convergence characteristics of the entire computational scheme are not adversely affected and that the interior solution is not contaminated beyond an acceptable level.

In the present algorithm, a simple open boundary condition is adapted on

∂D_{C2} which assumes that the potential at this boundary can be written as a wave form of the same celerity as that of the applied excitation potential on ∂D_{C1}:

$$\phi(x,t) = \phi(x - ct) \qquad .....(4.12)$$

where c represents the celerity of the excitation wave (cf. eqn. (3.3)). This results in the following relation:

$$\frac{\partial \phi}{\partial t} = -c\frac{\partial \phi}{\partial n} \qquad .....(4.13)$$

in which the fact that $\partial/\partial n = \partial/\partial x$ on ∂D_{C2} has been utilized. Eqn. (4.13) has a form similar to Orlanski's radiation condition, but its application here is not strictly equivalent. In Orlanski (1976) or in many finite-difference algorithms (see e.g. Chan and Chan 1980), the value of c is taken as the celerity of the local exit waves approaching the downstream boundary, and c is determined from a numerical differentiation at the neighbouring grid points. In Wu and Wu (1982), a similar simple form is adopted with c determined from

$$c = \sqrt{g\bar{d}} \qquad .....(4.14)$$

where $\bar{d}$ denotes the local water depth at the downstream boundary. Eqn. (4.14) represents shallow water approximation for the phase velocity of an Airy wave, and is therefore different than the condition applied in the present method (both methods become equivalent in the limiting situations of $d/\lambda << 1$)

The evolution of ϕ is now easily determined from time-integration of eqn. (4.13) with the application of the same numerical schemes as the ones used in integration of eqns. (2.2) and (4.3). Simple as it appears, this procedure results in minimal reflection effects on ∂D_{C2}, as the results presented in §4.3 will demonstrate.

4.3 Computed Results and Numerical Studies

For the following presentations, the notations described at the beginning of §3.2 apply. It should be noticed that Δx_F in the present application denotes the spacing of the free surface collocation points instead of the actual lengths of the segments. Unless otherwise specified, the applied excitation potential on ∂D_{C1} is the Airy potential. The normalizing parameters for horizontal and vertical length scales and time scale are respectively the length λ, height H and period T of the Airy wave corresponding to the prescribed potential (cf. eqn. (3.3)). In all computations presented, $\Delta x_F, \Delta x_{C1}, \Delta x_{C2}$ and Δt are constants.

4.3.1 Matching at the Upstream Boundary

Results in terms of the computed free surface profile and distribution of ϕ on it for varying extent of the matching zone are presented in Figures 4.3 (a) - (d). For these computations, $L = 3\lambda, H/\lambda = 0.05$ and $d/\lambda = 0.50$. The discretization parameters are : $\Delta x_F, \Delta x_{C1}, \Delta x_{C2} = \lambda/24$ and $\Delta t = T/40$. The modulation function (3.7) with $\sigma/T = 1$ is applied and the free surface elevations and potential are smoothed using formulae (A.3.3) and (A.3.4) (see Appendix A.3) at the intervals of 4 time steps. n in these Figures represents the number of segments used in discretizing the distance l between ∂D_{C1} and ∂D^*_{C1} (see Figure 4.1), i.e. $l = n\Delta x_F$. The computations cover a range of n from 2 to 10 at an interval of 2. l therefore varies between the distance of 0.083λ and 0.42λ. The results are shown for $i = 12$ and $i = 24$ where i indicates the ith collocation point on the free surface counted from ∂D_{C1} in the positive direction of x. These stations are therefore taken relatively close to the upstream side

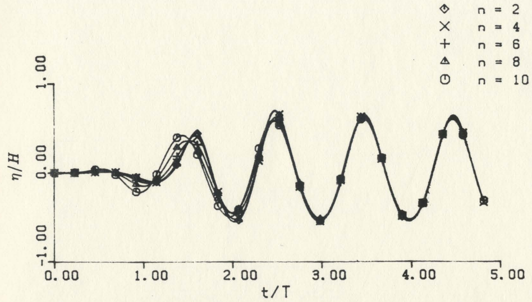

(a) Free surface elevations (η) at $i = 12$ ($x/\lambda = 0.48$)

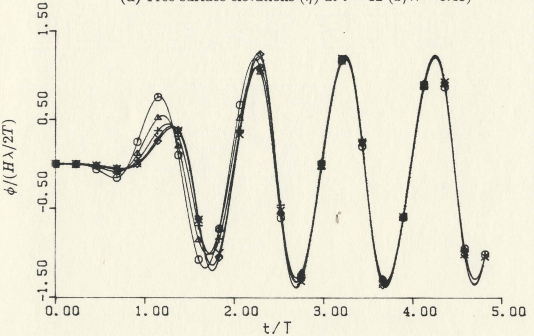

(b) Potentials on the free surface ($\phi(\eta)$) at $i = 12$ ($x/\lambda = 0.48$)

Figure 4.3 continued ⇓

boundary, approximately at distances $x = 0.5\lambda$ and $x = 1.0\lambda$ from ∂D_{C1}, and are expected to be most influenced by the matching procedure. The results clearly show the diminishing effect of the upstream matching with simulation time. The differences between the computed profiles and potentials are found to be contained within an initial period of approximately $t/T \leq 3$, after which the curves essentially converge. A number of computer runs with other combinations of Δx, Δt, λ, H, d and L show a similar trend with practically no influence of the adopted matching upon the interior solution after an initial transient (some additional supporting evidence will be shown in subsequent computations).

Numerical experiments indicate that the effectiveness of the matching procedure is related to the value of n as opposed to the length l. From a consideration of computer time, the value of n should be selected as low as possible. Even though the above results are presented for $n = 2$, for some steep waves ($H/\lambda \geq 0.10$) and small grid sizes ($\Delta x_F/\lambda \leq 1/40$), it is found that this value of n does not completely eliminate the instability. This is believed to be due to the use of a central difference scheme (eqn. (A.4.1) in Appendix A.4) in determining $\partial[f_2(x_1 + l)]/\partial x$ in (4.10 (c)), which applies the ill-behaved value of $f_2(x)$ at the first collocation point ($i = 1$) on ∂D_F. In contrast, the choice of $n = 4$ is found to be very effective in removing the oscillations, regardless of the grid sizes and wave heights. The subsequent results are all computed with this value of $n = 4$. Assuming the computation time to be proportional to N^3 where N is total number of segments on $\partial D_{C1} \cup \partial D_F \cup \partial D_{C2}$, for a typical value of $N = 100$ the increase in CPU time due to the introduction of the matching region is therefore less than 12.5%.

To demonstrate the initiation of the instability when the matching is not

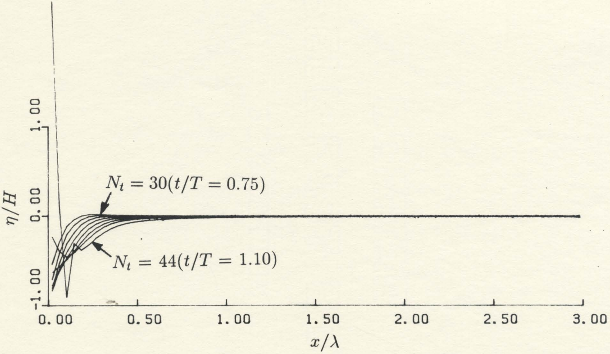

Figure 4.4 Free surface elevations when the matching scheme is not applied; $L = 3\lambda$, $d/\lambda = 0.5$, $H/\lambda = 0.05$, $\Delta x_F/\lambda = 1/24$ and $\Delta t/T = 1/40$.

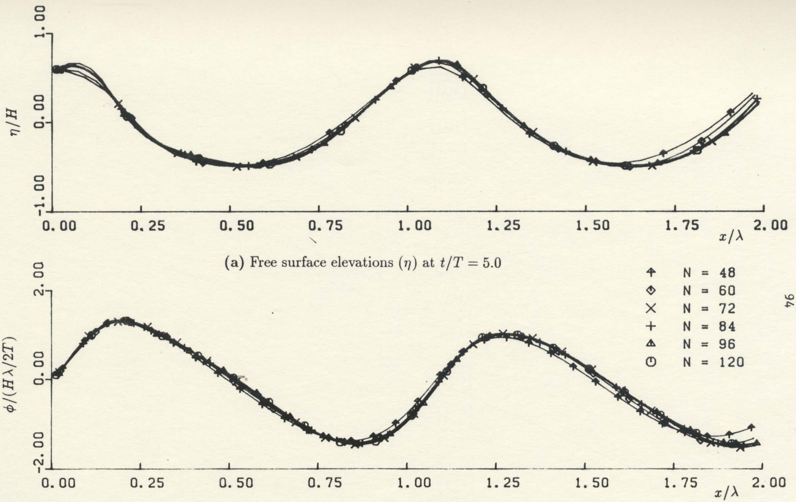

(a) Free surface elevations (η) at $t/T = 5.0$

(b) Potentials on the free surface ($\phi(\eta)$) at $t/T = 5.0$

Figure 4.5 continued ⇓

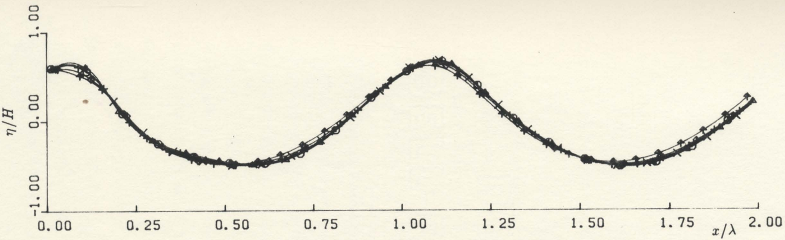

(c) Free surface elevations (η) at $t/T = 6.0$

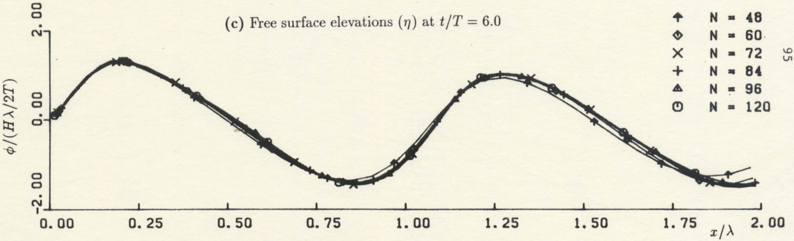

(d) Potentials on the free surface ($\phi(\eta)$) at $t/T = 6.0$

Figure 4.5 Free surface elevations and potentials; $L = 2\lambda$, $d/\lambda = 0.5$ and $H/\lambda = 0.10$.

appear slightly flat as a result of a comparatively poorer resolution. The slight raise in the ϕ curve near the downstream boundary (∂D_{C2}) for $N = 48$, which is perhaps due to the influence of numerical integration of eqn. (4.13), is not very significant and does not persist subsequently. Note that the computations correspond to values of the matching length l varying between $l = 0.10\lambda$ and 0.25λ, which further demonstrate the minimal influence of the employed matching on the interior solution.

These computations (and many others) indicate that a value of $\Delta x_F = \lambda/24$ and comparable values for $\Delta x_{C1}, \Delta x_{C2}$ are adequate for describing the fluid motion without appreciable effects of lack-of-resolution.

4.3.3 The Open Boundary Condition

The demonstration of the effectiveness of the open boundary condition (4.13) is the purpose of the following computations. This is examined by selecting a range of values for the celerity of the outgoing waves. Taking c in eqn. (4.13) as c' and writing $c' = \alpha c$ where c represents the celerity of the entering wave at ∂D_{C1} (as in eqn. (3.3)), computations cover a variation of α from 0 to 1, with specific values of α = 0, 0.25, 0.50, 0.75, 0.90 and 1.00. $\alpha = 0$ is recognized to be the condition for which $\phi(t)$ is unchanged on ∂D_{C2} at all times. The relevant parameters are : $L = 2\lambda$; $d/\lambda = 0.5$; $H/\lambda = 0.10$; $\Delta x_F, \Delta x_{C1}$ and $\Delta x_{C2} = \lambda/24$, and $\Delta t/T = 1/40$. The free surface elevations at progressing simulation times of t/T = 4.0, 5.0, 6.0, 7.0, 8.0 and 8.75 are shown in Figures (a) - (f). It is apparent that the reflection effects at the downstream boundary increase with the difference between α and 1. The interior solution progressively

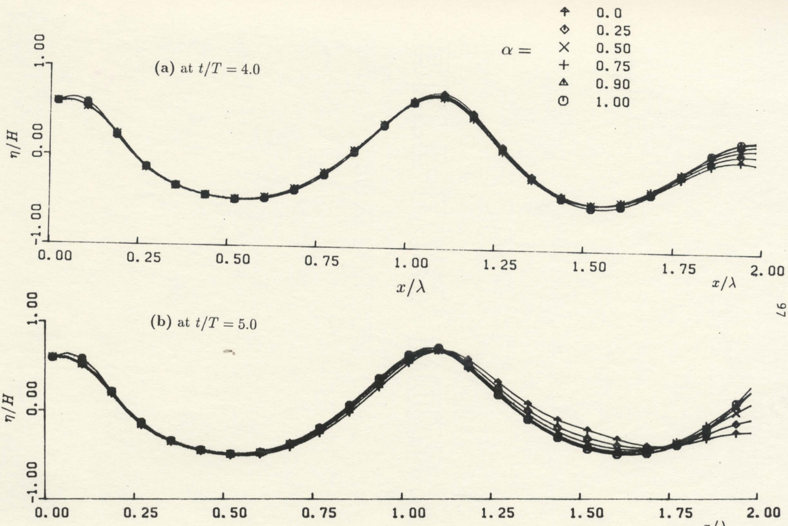

Figure 4.6 continued ⇓

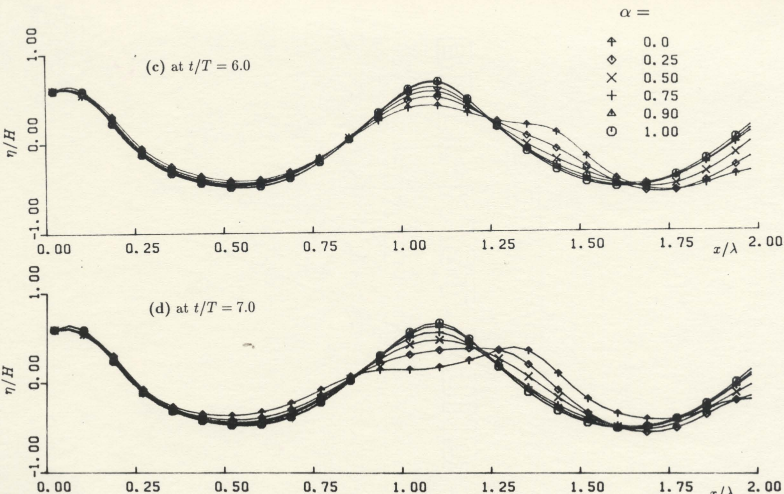

Figure 4.6 continued ⇓

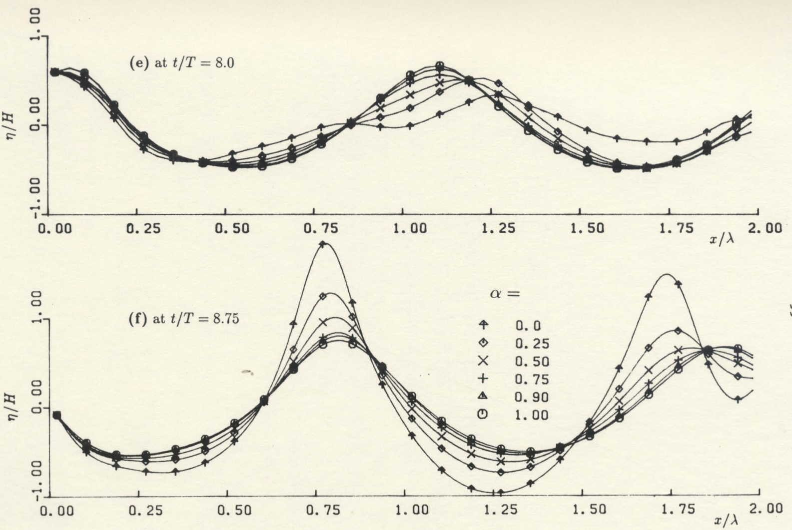

Figure 4.6 Free surface elevations for different values of α; $L = 2\lambda$, $d/\lambda = 0.5$, $H/\lambda = 0.10$, $\Delta x_F/\lambda = 1/24$ and $\Delta t/T = 1/40$.

gets contaminated by these reflected waves as the solution proceeds. At $t/T = 4$ (Figure 4.6 (a)), the wave just reaches ∂D_{C2} and not much reflection takes place. As time progresses, the reflected waves begin to travel inwards. At $t/T = 8.75$ (Figure 4.6 (f)), the free surface profile for $\alpha = 0$ with pronounced crest and trough indicates a full reflection from ∂D_{C2}. Here the wave profile shows a growth in height by a factor of more than 2. It appears that a standing wave system is formed by this time. In contrast, results for $\alpha = 1$ indicates that the wave passes through ∂D_{C2} with minimal reflections.

In Figures 4.7 (a) - (d), we show the time evolution of the free surface at collocation points $i = 36$, 40, 44 and 48, corresponding respectively to the distances of $x/\lambda = 1.48$, 1.65, 1.81 and 1.96 measured from ∂D_{C1}. The last station coincides with the last collocation point on the free surface, adjacent to ∂D_{C2}. The reflection effects for various values of α are clearly noticeable. At the station $i = 44$ (Figure 4.7 (c)), which is at a distance of 0.19λ measured from ∂D_{C2}, reflection effects for $\alpha \leq 0.50$ are visible immediately after the initial transient period of $t/T \approx 4.0$. Reflection effects for $\alpha \geq 0.75$ are comparatively much smaller. The effectiveness of choosing $\alpha = 1.0$ for making the downstream boundary transparent is evident, although values slightly less than 1 also appear to work well. Computations are also attempted for values of α greater than 1, but even for a value moderately greater than one, e.g. $\alpha = 1.05$, the solution breaks down after about $t = 5T$, which is approximately the time when the wave grows fully at the downstream boundary (this corresponds to the time estimated from the speed of linear wave group). This breakdown results from an instability originating at the downstream intersection of ∂D_F and ∂D_{C2}. In view of the success of $\alpha = 1.0$ in making the boundary sufficiently non-reflective,

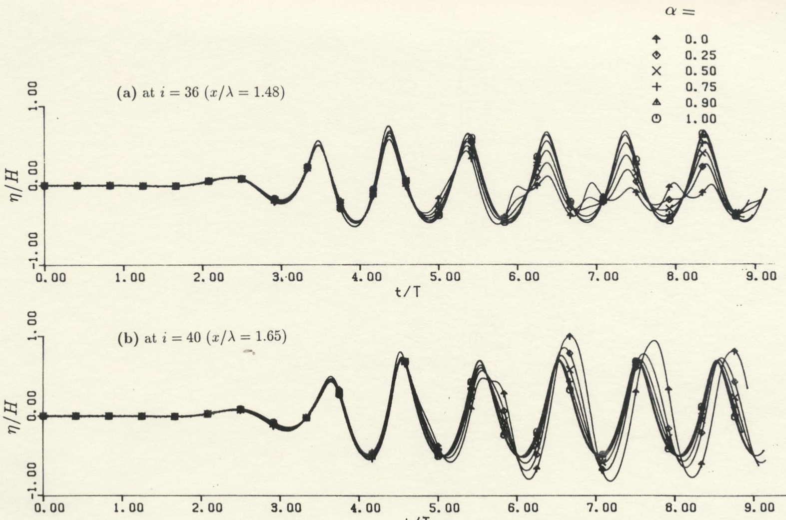

Figure 4.7 continued ⇓

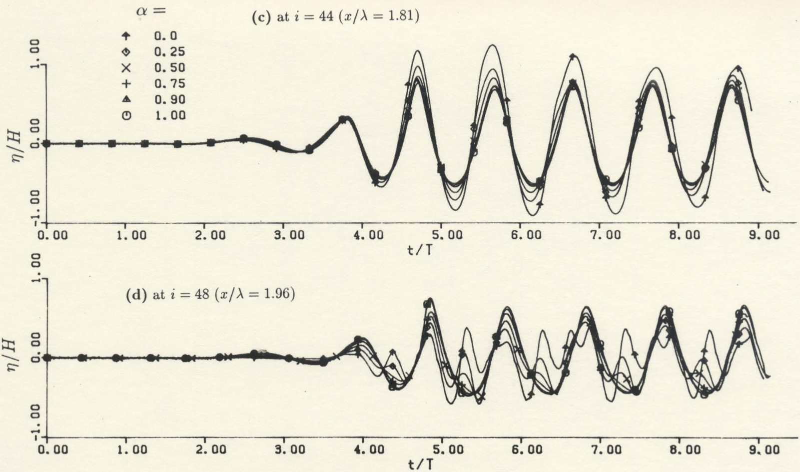

Figure 4.7 Evolution in time of the free surface for computations corresponding to Figure 4.6 above; (note that $i = 48$ is the last collocation point on ∂D_F, adjacent to ∂D_{C2}).

this aspect is not pursued any further.

It is found important to keep the length of the adjacent segments comparable at the intersection of two boundaries. In particular, care must be taken to ensure that the length of the uppermost segment on ∂D_{C2} is not reduced considerably in comparison to the adjacent segment length on ∂D_F (roughly less than 1/2). Due to wave run up effects, ∂D_{C2} continuously changes in length. Since l.h.s. of eqn. (4.13) is an Eulerian time derivative, the collocation points on this boundary are generally kept fixed in space, except for the uppermost segment. Depending on the length of ∂D_{C2}, a segment is deleted or an additional segment is introduced so that the length of the segment in comparison with the length of the adjacent segment on ∂D_F maintains a ratio between 0.5 and 2.0. The location of the collocation point within this segment is not changed such as to facilitate the integration of eqn. (4.13), which means that the collocation point for this segment is not always centrally located. Recalling the remarks in §2.2.2, this does not invalidate the numerical discretization. It is also possible to redistribute the collocation points at each time step with equal spacing and obtain the required information at the Eulerian points via spatial interpolation. However, retention of the original segments where possible is computationally beneficial in that some of the influence coefficients in (2.10) need not be recalculated at every step (although this is latter adopted for the wall (§5) and the body (§6) for reasons mentioned therein).

4.3.4 The Excitation Potential

To investigate the influence of the excitation potential on the interior solution, computations are performed for the excitation potential specified as Stokes second order potential:

$$\phi(\mathbf{x},t) = \frac{H\lambda}{2T}\frac{\cosh 2\pi(z+d)/\lambda}{\sinh 2\pi d/\lambda}\sin\frac{2\pi}{\lambda}(x-ct)$$

$$+\frac{3\pi H^2}{16T}\frac{\cosh 4\pi(z+d)/\lambda}{\sinh^4 2\pi d/\lambda}\sin\frac{4\pi}{\lambda}(x-ct) \qquad .....(4.15)$$

where the first term on the left represents the Airy wave potential (cf. eqn. (3.3)) while the second term is the second order correction to it. The applied excitations have a value of $H/\lambda = 0.10$, for which the second order correction in wave amplitude is almost 10% of the first order amplitude (note that both these excitations have the same energy density). The applied potentials are therefore considerably different. The fluid domain chosen and the discretization parameters are retained the same as in the preceeding application: $L = 2\lambda, d = 0.5\lambda, \Delta x_F = \lambda/24, \Delta t = T/40$. Figures 4.8 (a) and (b) show the free surface contour and potential distribution at $t/T = 4.0$ and 8.0. The plots are virtually indistinguishable. The small difference near the upstream boundary results from the application of the matching technique at this boundary and is contained within the matching zone of $l = 0.167\lambda$. The evolutions in time at $i = 12$ and 36 ($x/\lambda = 0.48$ and 1.48 respectively) are shown in Figures 4.9 (a) and (b). Except possibly to the sharpest eyes, the differences remain undetectable.

The above results suggest that the interior solution is insensitive to the applied excitations, provided the same first order amplitude and the period are retained. Additionally, the results further confirm that the applied matching

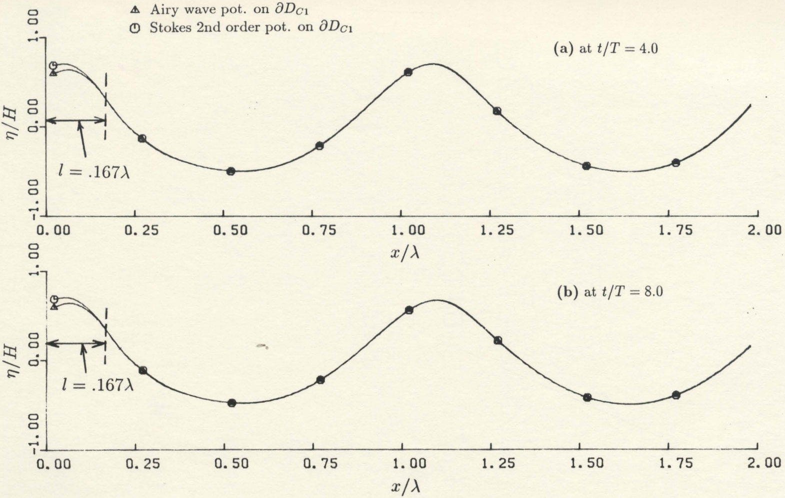

Figure 4.8 Free surface elevations for different excitation potentials; $L = 2\lambda$, $d/\lambda = 0.5$, $H/\lambda = 0.10$, $\Delta x_F/\lambda = 1/24$ and $\Delta t/T = 1/40$.

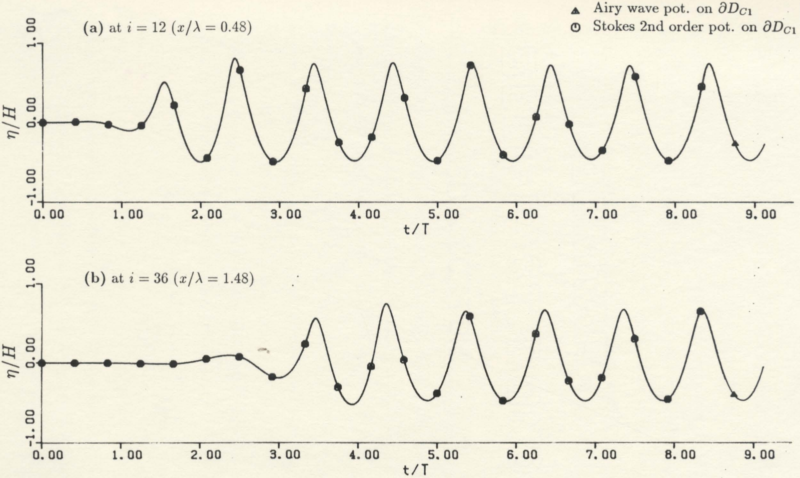

Figure 4.9 Evolution in time of the free surface for computations corresponding to Figure 4.8 above.

does not introduce adverse effects into the domain, since $f_1(x)$ in (4.10) is quite different for the two applied excitations. The application of Airy potential as an excitation then seems justified in general. Numerical experiments also indicate a close relation between H and H^*, where H^* denotes the height of the interior wave upon reaching a steady state. H^*/H is found to be within 5% of unity for most of the applications. This ratio is on the higher side for smaller values of H/λ, as to be expected (a supporting result is shown latter, see Figures 4.12 and 4.13 below).

4.3.5 The Effect of the Modulation Function

All computations presented thus far (for the non-linear wave) were obtained with the application of the modulation function given by (3.7). The objective of the following is to demonstrate whether the transients associated with different forms of modulation functions have any effect on the solution in long time simulations.

Figure 4.10 show five plots of the free surface elevations at $t/T = 8.5$. The relevant parameters for these computations are same as in the preceding section. The five curves correspond to the computations with the application of (3.7) with $\sigma/T = 0$, 1.0 and 2.0, and the following modulation function:

$$M(t) = \begin{cases} \sin(\pi t/2\sigma) & t < \sigma \\ 1 & t \geq \sigma \end{cases} \qquad .....(4.16)$$

with $\sigma/T = 1$ and 2. Notice that (3.7) with $\sigma = 0$ implies that the excitation potential is not modulated and that (4.16) violates the condition of $\partial\phi^*/\partial t|_{t=0} = 0$. The plots are practically indistinguishable. The evolutions in time of the free surface elevations at a location close to the centre of the domain (at $i = 24$ or

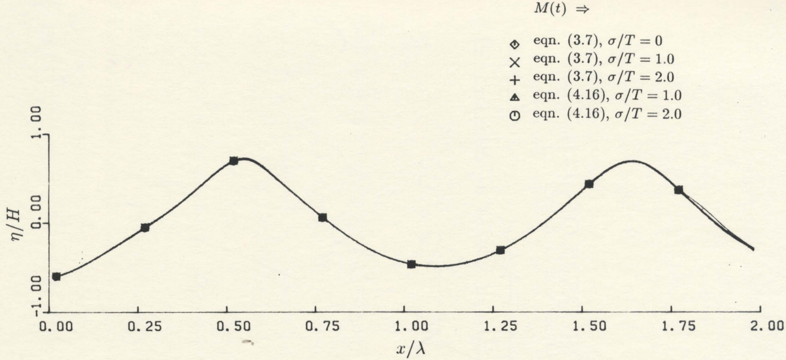

Figure 4.10 Free surface elevations at $t/T = 8.5$ for different modulations of the excitation potential; $L = 2\lambda$, $d/\lambda = 0.5$, $H/\lambda = 0.10$, $\Delta x_F/\lambda = 1/24$ and $\Delta t/T = 1/40$.

$x/\lambda = 0.98$) are shown in Figure 4.11. All differences are observed to be within the initial transient of $t/T \leq 3.0$, after which the plots are in remarkably good agreement.

This demonstrates that a modulation function, regardless of its form or the time span over which it is applied, does not introduce effects analogous to memory effect in simulations of large durations. Such effects, if any, disappear within a short time. Although the results indicate that the instability which is generated by the application of an impulsive pressure (as it was found in the equivalent linear case, §3.2.2) is smoothed out by the use of the matching procedure, following the arguments presented in §3.2.2.1, the application of the modulation function (3.7) with a finite value of σ is preferred (usually a value of $\sigma/T = 1$ is chosen).

4.3.6 Further Results : Comparison with Theories

Figure 4.12 shows the free surface contours for two nominal wave steepnesses of $H/\lambda = 0.05$ and $H/\lambda = 0.10$ at $t/T = 9.0$. The computational parameters are: $L = 2.25\lambda$, $d = 0.5\lambda$, $\Delta x_F, \Delta x_{C1}$ and $\Delta x_{C2} = \lambda/20$, and $\Delta t/T = T/40$. The evolutions in time at $x = 0.48\lambda$ and $x = 1.48\lambda$ (corresponding to $i = 12$ and $i = 36$ respectively) are presented in Figures 4.13 (a) and (b). A steady state behaviour with fundamental period T is apparent throughout the control domain. The waves display typical non-linear characteristics of comparatively more peaky crests and shallower troughs in comparison with Airy (sinusoidal) wave profiles. The profile for $H/\lambda = 0.10$ shows stronger non-linear characteristics compared to the profile for $H/\lambda = 0.05$, as to be expected.

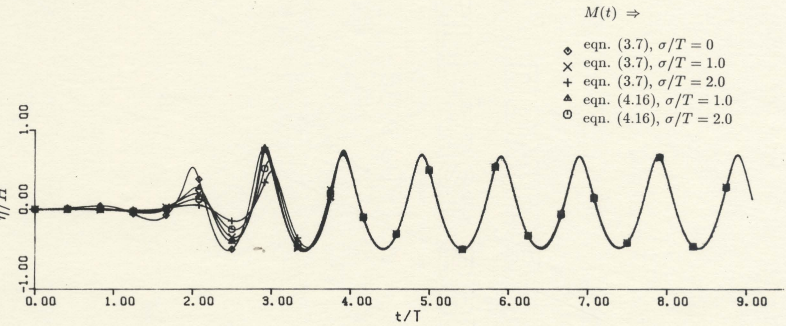

Figure 4.11 Evolution in time of the free surface at $x/\lambda = 0.98$ for computations corresponding to Figure 4.10 above.

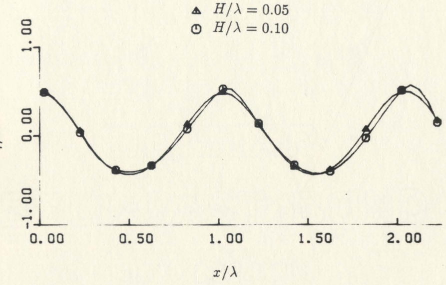

Figure 4.12 Free surface elevations at $t/T = 9.0$; $L = 2.25\lambda$, $d/\lambda = 0.5$, $\Delta x_F/\lambda = 1/20$ and $\Delta t/T = 40$.

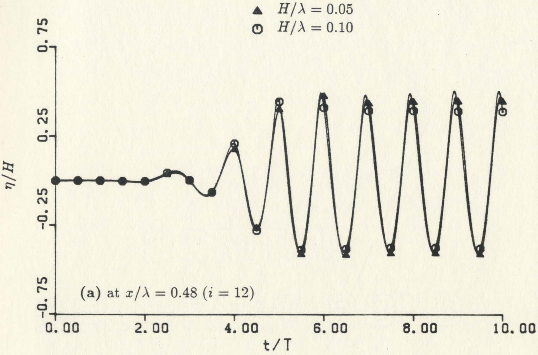

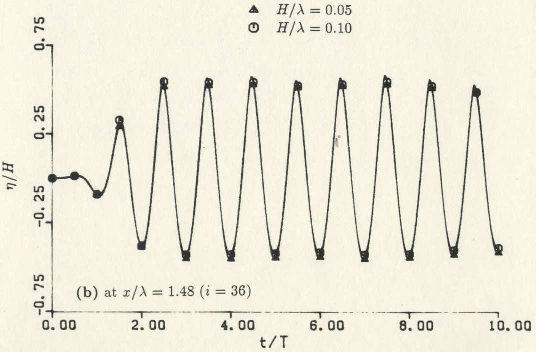

Figure 4.13 Evolution in time of the free surface corresponding to Figure 4.12.

A comparison of the profiles at $x/\lambda = 0.98$ with theoretical profiles for the Airy wave given by (3.5), Stokes second order wave and Miche's second order theoretical profile (Miche 1944) are shown in Figure 4.14. For completeness, the relevant equations for the second order profiles are reproduced below:

Stokes second order profile

$$\eta(x,t) = \frac{H}{2}\cos 2\pi(\frac{x}{\lambda}-\frac{t}{T}) + \frac{3\pi H^2}{8\lambda}\frac{\coth(2\pi d/\lambda)}{\sinh^2(2\pi d/\lambda)}\cos 4\pi(\frac{x}{\lambda}-\frac{t}{T}) + \frac{\pi H^2}{4\lambda}\coth\frac{2\pi d}{\lambda}\cos(\frac{x}{\lambda}-\frac{t}{T}) \quad .....(4.17)$$

Miche's profile

$$\eta(x,t) = \frac{H}{2}\cos 2\pi(\frac{x}{\lambda}-\frac{t}{T}) + \frac{3\pi H^2}{8\lambda}\frac{\coth(2\pi d/\lambda)}{\sinh^2(2\pi d/\lambda)}\cos 4\pi(\frac{x}{\lambda}-\frac{t}{T}) + \frac{\pi H^2}{4\lambda}\coth\frac{2\pi d}{\lambda} \quad .....(4.18)$$

The above two formulae differ only in the last term, which in the latter formula is independent of time. The numerically simulated wave compares well with the second order profiles, but displays stronger non-linear characteristics. For clarity, an expanded view for one period ($4.5 \leq t/T \leq 5.5$) is shown in Figure 4.15. The comparatively more peaky crest and shallower trough of the computed wave are clearly visible.

Finally, results are shown for a particularly long duration of simulation. The wave chosen is very steep in relatively shallow water: $H/\lambda = 0.12$ and $d/\lambda = 0.24$ (note that this gives $H/d = 0.5$). A relatively finer resolution of $\Delta x = \lambda/32$ and $\Delta t = T/64$ is used for space and time discretizations. Figure 4.16 contains 7 plots of the free surface profiles at times t/T = 10, 12, 14, 16, 18, 20 and 22. The comparatively smaller crest at ∂D_{C1} is due to the influence of the matching

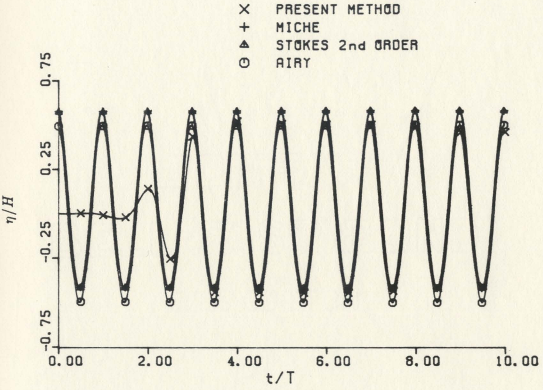

Figure 4.14 Comparison of the free surface elevations; the computed plot shows evolution at $x/\lambda = 0.98$ ($i = 24$) for the wave with $H/\lambda = 0.10$ in Figure 4.12.

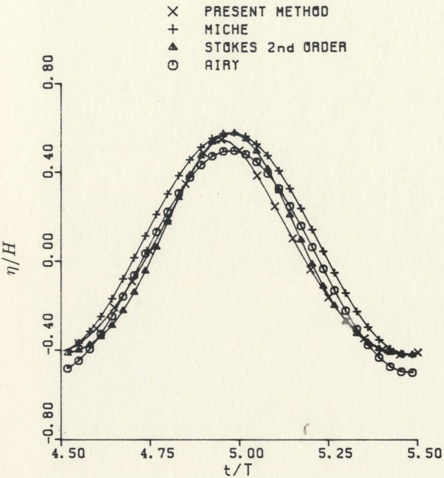

Figure 4.15 An expanded view of the region $4.5 \leq t/T \leq 5.5$ in Figure 4.14 above.

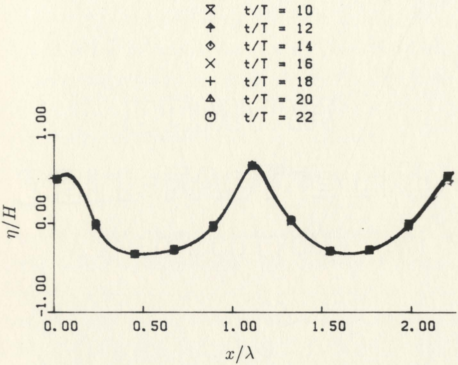

Figure 4.16 Free surface elevations; $L = 2.25\lambda$, $d/\lambda = 0.24$, $H/\lambda = 0.12$, $\Delta x_F/\lambda = 1/32$ and $\Delta t/T = 1/64$.

procedure and is mainly contained within the matching length of $l = 0.125\lambda$ ($n = 4$). The agreement of the profiles demonstrates that the wave retains a fundamental period of T. These plots also indicate that contamination due to numerical errors or numerical viscosity effects with time is insignificant, since the successive profiles do not show differences with progression of time. Such effects evidently do not persist with time. The evolutions in time at five locations ($x/\lambda = 0.375$, 0.750, 1.125, 1.50 and 1.875) are shown in Figures 4.17 (a) - (e). It appears that the simulation can be continued *ad infinitum*.

Figure 4.18 shows the comparison of the computed wave profile with the theoretical profiles. The computed profile clearly displays stronger non-linear characteristics. The same observation is apparent from the comparison shown in Figure 4.19. These plots suggest that the computed wave is travelling faster than the theoretical waves. It is possible that the associated transient effects could contribute to the differences; however, previous computational results indicate otherwise (cf. Figures 4.10 - 4.14). Indeed, careful inspection of Figure 4.12 and 4.16 reveals that the computed waves have a length larger than the incident λ for larger wave steepnesses. Comparison of Figure 4.18 with Figure 4.16 also indicates that present computations predict a comparatively higher celerity for steep shallow water waves. Although no quantitative evaluations of the quantities (e.g. celerity, wave length) have been made, these are qualitatively similar to well known features of steep shallow water waves (see e.g. Cokelet 1977).

4.4 Summarizing Remarks

This section is concluded with the following remarks:

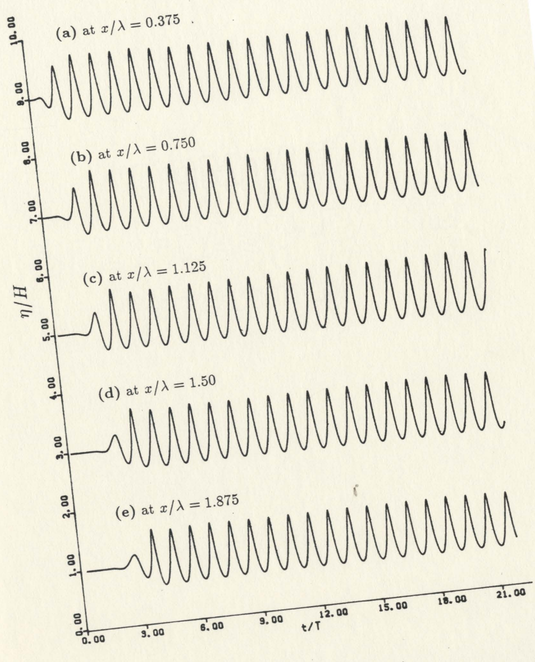

Figure 4.17 Evolution in time of the free surface corresponding to the wave in Figure 4.16 ; for convenience of plotting, these plots are vertically shifted.

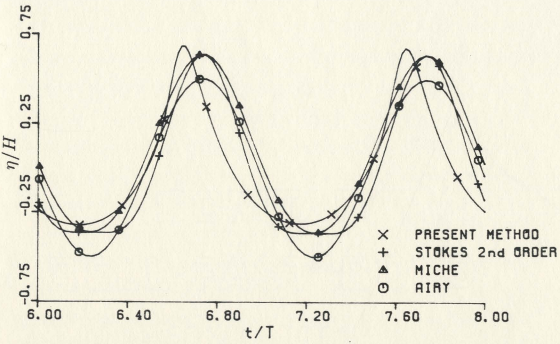

Figure 4.18 Comparison of the free surface elevations for the wave in Figures 4.16-4.17 above; the computed plot shown is at $x/\lambda = 0.750$.

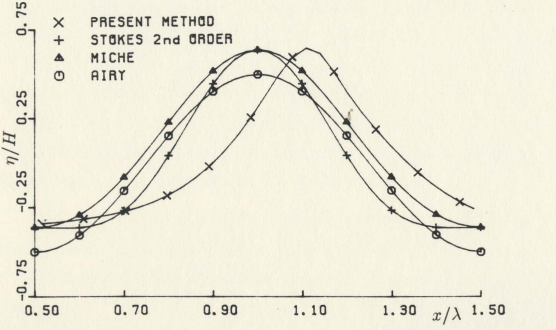

Figure 4.19 Comparison of the free surface elevations for the wave in Figures 4.16-4.17 above; the computed plot shown is at $t/T = 16$.

(1) The simulation of propagation of unsteady steep waves can be achieved by imposing an excitation potential on one of the vertical control boundaries encompassing a rectangular fluid domain. The interior solution is not sensitive to the exact form of the potential, as demonstrated by imposing Airy and Stokes second order potentials as excitations. The simulated wave profile displays typical non-linear characteristics of relatively more peaky crest and shallower trough in comparison with linear waves. As expected, the non-linearities are more pronounced for steeper waves. Very steep waves in reasonably shallow water were simulated for time durations of over 20 wave periods. A steady state behaviour occurs in the entire domain. It appears that a 'numerical wave tank' can be set up in the described manner, i.e. by imposing an Airy potential on ∂D_{C1} instead of providing a physically moving wave board.

(2) The instability originating at the intersection of ∂D_{C1} and ∂D_F is believed to be due to an incompatibility of the free surface boundary conditions at this boundary. The problem appears to be similar to the difficulties that are associated with the matching of an 'interior' non-linear solution with 'exterior' linear solutions in two dimensions (e.g. Vinje, Maogang and Brevig 1982 have encountered difficulties in a similar matching; Han and Stansby 1987 have discussed difficulties related to the impulsive wave-maker problem at the intersection due to an incompatibility of the boundary conditions).

In the present algorithm, this difficulty is circumvented by means of a matching technique, which employs a quadratic polynomial smoothing scheme in space. The effectiveness of this scheme is demonstrated by a number of computed results.

(3) Although in the present mode of following the free surface, clustering of the collocation points is avoided without having to resort to regridding, the free surface instability still persists. The present study suggests that violation of local Courant condition is not the primary mechanism of this instability, contrary to the postulation of Dommermuth and Yue (1987). It appears that the instability is intimately related to the accuracy of computation of $\partial\phi/\partial n$ on the free surface (i.e. the Laplace equation solver). The present experience indicates that the problem is associated with the well documented ill behaviour of boundary integral methods near sharp corners. In this respect, the present computations support the opinion expressed in Schultz (1987) (see also the discussion in §1.2.2.2 (c)). Furthermore, it does not appear that the schemes used for integrations in time are crucial with regard to instability. Improvements in time integration schemes are expected to increase computational efficiencies in that relatively crude discretizations can be made to achieve an increased accuracy (see e.g. Dold and Peregrine 1986), but it does not appear to provide a remedy for the instability, as the computations with progressively larger levels of iterations have indicated. In the present method, this instability is suppressed by means of a smoothing scheme applied intermittently.

(4) Albeit simple, the wave outgoing condition (4.13) produces good results extending over the entire period of computations as well as for all combinations of H, L and d for which computations are performed. The interior wave is not apparently contaminated by numerical reflection effects even after long time of simulations and at locations close to the downstream boundary (see e.g. Figure 4.17). This demonstrates effectiveness of (4.13) in modelling of non-linear wave propagation.

5 Steep Wave Interacting with Vertical Walls

5.1 General Considerations

In continuation of the preceding developments, this section considers the interaction of a steep wave with an impermeable object. As a first application, interaction with a vertical wall is investigated. This application represents the simplest case of introducing a surface-piercing body in the fluid. Additionally, available experimental and theoretical perturbation solutions for standing waves interacting with walls provide an excellent data for comparison.

Identifying the downstream boundary with an impermeable wall, the boundary condition imposed on ∂D_{C2} is that of zero normal velocity:

$$\frac{\partial \phi}{\partial n} = 0 \qquad .....(5.1)$$

The simulation proceeds in the similar way as in the preceding application with the exception that (5.1) now provides the necessary boundary data $(\partial\phi/\partial n)$ on ∂D_{C2} at all instants (similar applications have been previously considered in the linear application cases in §§3.2.2,3.2.3). The wall-free surface intersection point is determined from a three point (second order) Lagrangian extrapolation formula using η values at the three preceding points, as it was done earlier for determining $\partial D_F \cap \partial D_{C2}$.

The pressure on the wall is computed from unsteady Bernoulli's equation:

$$p = -\rho g z - \rho \frac{\partial \phi}{\partial t} - \frac{1}{2}\rho(\nabla\phi)^2 \qquad .....(5.2)$$

This involves time derivatives of ϕ at the Eulerian points on the wall, which is determined from a second order central difference scheme:

$$\frac{\partial \phi}{\partial t} = \frac{\phi(t + \Delta t) - \phi(t - \Delta t)}{2\Delta t} \quad .....(5.3)$$

$\nabla \phi$ on the wall is simply $\partial\phi/\partial z$, since from the imposed condition (5.1), $\partial\phi/\partial x = \partial\phi/\partial n = 0$. A second-order central difference schemes is used to compute $\partial\phi/\partial z$ from the nodal values of ϕ on the wall except for the end points, for which second order forward and backward schemes are employed (Appendix A.4 provides the necessary formulae).

In this application, it is found necessary to redistribute the collocation points on the wall at every time step such that the segments have an equal length. Otherwise, at the discrete time instants at which points are introduced or deleted, the abrupt changes in the uppermost segment size cause 'jumps' in computation of $\partial\phi/\partial t$ through (5.3) (in contrast, no difficulties were encountered in integrating (4.13) in the preceding application, cf. §4). These 'jumps', appearing as sharp peaks on the pressure curves, however, do not interfere with the time simulation procedure. The flow evolution is independent of the wall pressures which are an extracted interim data. From this consideration, it is possible to employ numerical filtering techniques to remove these high frequency disturbances. Redistribution of the collocation points on ∂D_{C2} necessitates determination of $\phi(t-\Delta t)$ and $\phi(t+\Delta t)$ at the Eulerian points at time t. These are determined by approximating ϕ_j as a function of z_j by a cubic spline. It is observed here that the spatial differentiations are found to introduce minimal numerical approximation effects, since the changes in the locations of the collocation points between consecutive time steps are of the order of $1/50$ th of the segments lengths. This was verified by employing linear and second order interpolation schemes which produced results within 0.01% difference.

The horizontal force (the vertical component of the force is zero) and the overturning moment about the foot of the wall are determined by a direct integration of pressure:

$$F_x = \int_{\partial D_{C2}} p.dS \qquad .....(5.4(a))$$

$$M_d = \int_{\partial D_{C2}} p(z+d)dS \qquad .....(5.4(b))$$

Force integration can be expressed as

$$F_x = \sum_{j=1}^{N_w} \rho[-gz_j - \frac{\partial \phi_j}{\partial t} - 0.5(\frac{\partial \phi_j}{\partial z})^2]\Delta S_j \qquad .....(5.5)$$

where $j = 1, N_w$ are the collocation points on the wall, ΔS_j indicate the suffixed segment lengths, and the pressure terms are calculated at the indicated collocation points. This is consistent with the approximation of constant value of ϕ_j over each segment. The static term is also correctly evaluated due to central location of the collocation points. For moment computation, the corresponding static term has a quadratic variation, and therefore integrated by means of Simpson's rule.

Most of the presented results are in terms of the pressures at the undisturbed free surface level $z = 0$ and at bottom of the wall $z = -d$. This maintains a uniformity in presentation as well as facilitates comparisons with experimental results of Nagai (1969) which are provided mostly for these locations. Since the collocation points on the wall continuously undergo changes of locations due to the redistribution, once more spatial interpolations/extrapolations are used to obtain the necessary information (note that the flow evolution is independent of these interpolations/extrapolations).

5.2 Computed Results and Numerical Studies

In view of the results discussed in §4, all computations hereinafter are performed by specifying the Airy potential (eqn. (3.3)) on the upstream boundary. The notations have the same meaning as described earlier, unless indicated otherwise.

5.2.1 Steady State Behaviour of Solution

The purpose of the following computations is to examine whether a steady state behaviour of the pressures on the wall can be achieved, as well as to establish the time span upto which the simulation can be carried out meaningfully. The simulation time within which reliable results can be extracted will clearly depend on the distance of the wall from the upstream boundary.

The test case selected corresponds to an oncoming steep wave at the upstream boundary (∂D_{C1}) with the parameters: $\lambda = 246$ cm., $H = 20.72$ cm., $d = 201$ cm. ($H/\lambda = 0.0817$, $d/\lambda = 0.82$), which means that the excitation potential has these values of H, λ and d. This particular case is chosen because of the corresponding experimental results available for comparisons. The free surface is discretized with segments of constant length with $\Delta x_F = \lambda/24$, and there are 20 segments on each of the vertical boundaries. The time step is, $\Delta t/T = 1/40$. The matching zone extends over 4 collocation points and the modulation function $M(t)$ given by eqn. (3.7) with $\sigma/T = 1$ is applied.

The time evolution of the run-up profiles, pressures on the wall at $z = 0$ and $z = -d$ are presented in Figures 5.1 (a) - (c) for the following six values: $L = 1.5\lambda$, 2.0λ, 2.5λ, 3.0λ, 3.5λ and 4.0λ (note that L signifies the distance of the wall from the excitation boundary). In all Figures, two times T_1 and T_2

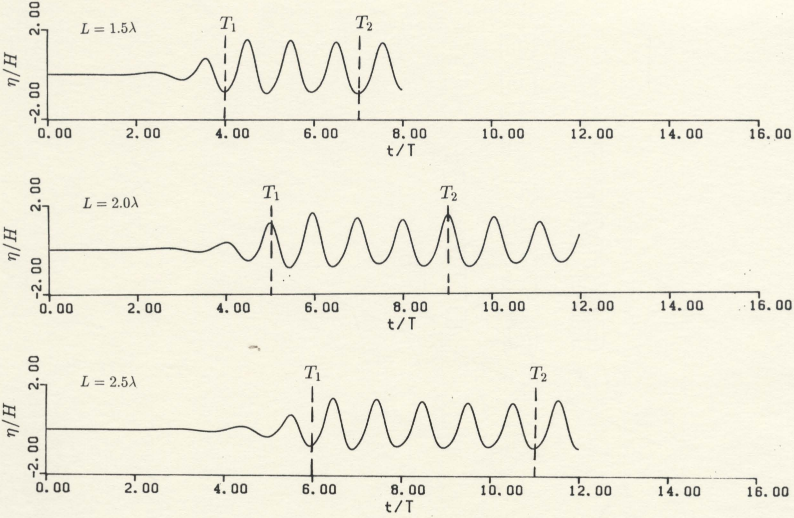

Figure 5.1 (a) continued ↓

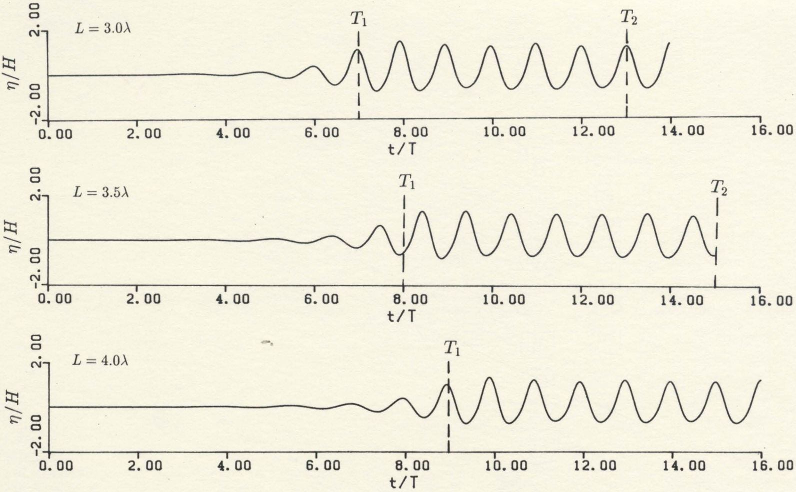

(a) Run-up

Figure 5.1 continued ⇓

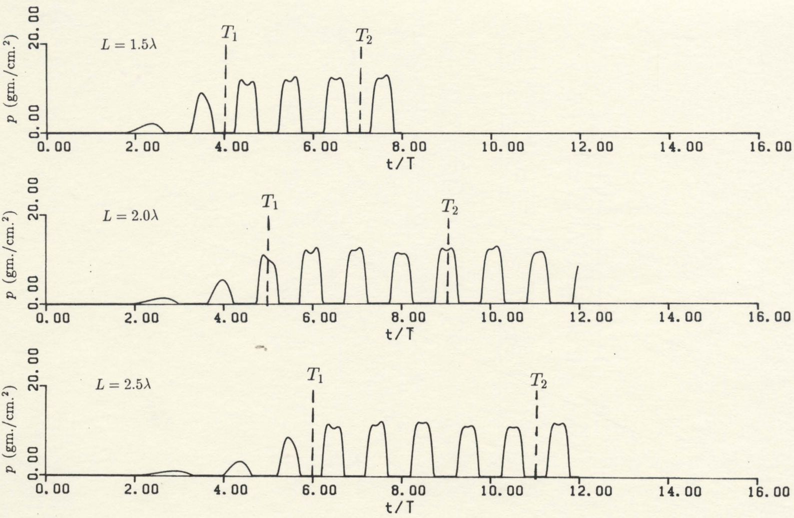

Figure 5.1 (b) continued ↓

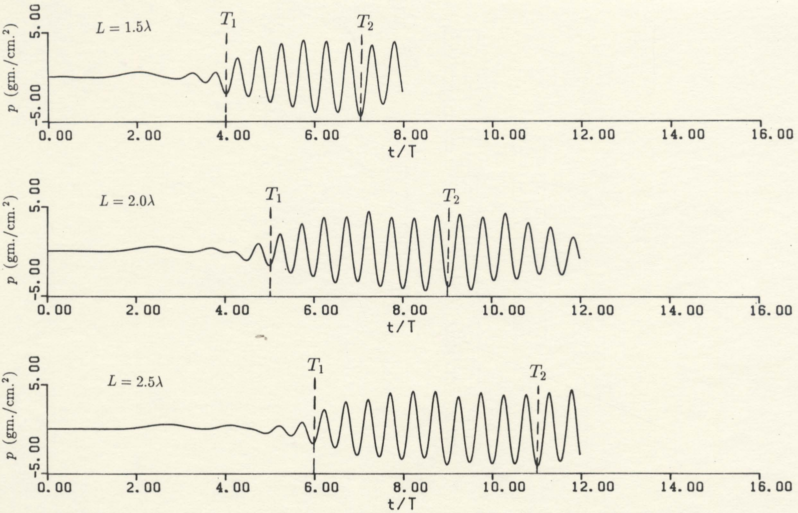

Figure 5.1 (c) continued ↓

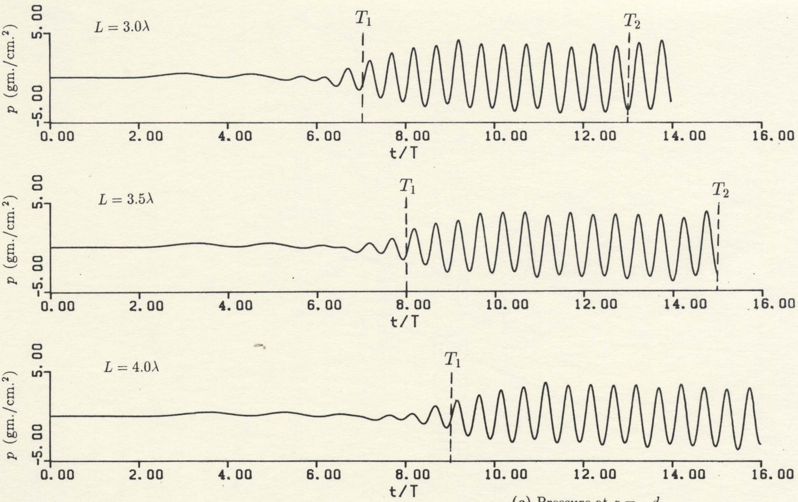

(c) Pressure at $z = -d$

Figure 5.1 Run-up and pressures on a vertical wall for different values of L; $\Delta x_F/\lambda = 1/24$, $\Delta t/T = 1/40$, $\sigma/T = 1$ and $n = 4$.

are marked. T_1 is the estimated time at which the fully developed front of the oncoming wave reaches the wall, which is approximated by:

$$T_1 = \sigma + L/c_g \qquad .....(5.6)$$

where c_g denotes the group speed of the linearized wave,

$$c_g = c(\frac{1}{2} + \frac{kd}{\sinh 2kd}) \qquad .....(5.7)$$

where $k = 2\pi/\lambda$ is the wave number. The above implies that we have assumed the wave front to travel at the linear group velocity *after* the excitation potential has acquired its full value (i.e. $\phi^* \equiv \phi$, cf. eqn. (3.6)). The reflected wave, also assumed to propagate with the same speed, travels back to the excitation boundary at T_2:

$$T_2 = T_1 + L/c_g \qquad .....(5.8)$$

These two time values indicate an approximate interval of time during which the results are expected to reach a steady state behaviour and can be used with some confidence. As can be observed, in all computations the run-up and top pressure (i.e pressure at $z = 0$) exhibit a steady state behaviour in the time interval T_1 to T_2, which extends over more than four periods for $L \geq 2.5\lambda$. The variations between successive peaks are usually not more than about 3%. The bottom pressure (pressure at $z = -d$) appears to acquire its steady state nature some time after T_1, approximately one wave period later. The cause for this delay is not known, nevertheless after this time the pressures do exhibit a similar behaviour, although the variations here seem to be slightly larger than in the other two time histories. This could be due to the extrapolation required to obtain these values, and/or the relative smallness of the magnitudes involved. For $L = 4\lambda$, the computation is carried out until $t = 16T$ because of larger

5.2.2 Quantitative Evaluation : Comparison with Experimental and Perturbation Results

A substantial amount of experimental data was reported by Nagai (1969) on results of experiments conducted over a broad range steepnesses (H/λ) and relative depths (d/λ). Here H and λ denote the height and length of the incident progressive wave respectively, and are taken as equivalent to H and λ of the prescribed potential on ∂D_{C1} (cf. eqn. (3.3)). These results are used extensively for the purpose of comparison. Besides, similar experimental results are scarce in open literature (some other results are available in Goda 1967, but are in forms not very suitable for comparison with the present results). Recognizing that a number of combinations of the relevant parameters admits the desired simulations as well as considering computer time, the computations are unified with the following parameters: $L = 2.5\lambda$, $\Delta x_F = \lambda/24$ and $\Delta t = T/40$; the segment sizes are decided depending on d such that Δx_{C1} and Δx_{C2} are closely comparable to Δx_F ; the matching zone extends over four collocation points; $\sigma/T = 1$ in modulating the applied potential; the free surface smoothing is applied in general at every fourth step (in some cases of large H/λ and small d/λ, the free surface instability had to be controlled by applying more smoothing, e.g. smoothing η at every 2nd step, ϕ at every 4th step, etc.) Additionally, only the results extending for two periods located centrally in the time interval T_1 to T_2 are used, although in all cases more than three periods of steady state behaviour in this interval were observed.

In Figures 5.2 - 5.5, results are presented in terms of the pressure at $z = 0$ and $z = -d$ for all four cases for which Nagai provides experimental data. The theoretical predictions from linear and third order standing wave theories are also plotted. The third order theory was originally developed by Tadjbaksh and Keller (1960) and was used by Nagai for comparison. For completeness, the relevant expressions are reproduced below:

(i) linear theory : $d/\lambda \geq 0.5$

$$\frac{p(z)}{\rho g} = -z - \frac{1}{2}kH^2e^{2kz}\sin^2\omega t + He^{kz}\cos\omega t - \frac{1}{2}kH^2\cos 2\omega t \quad .....(5.9)$$

(ii) linear theory : $d/\lambda \leq 0.5$

$$\frac{p(z)}{\rho g} = -z + \frac{kH^2\sin^2\omega t}{\sinh 2kd}[\cosh^2 k(d+\eta) - \cosh^2 k(d+z)]$$

$$+\eta\,[1 + \frac{\cosh k(d+z)}{\cosh kd} - \frac{\cosh k(d+\eta)}{\cosh kd}] \quad .....(5.10)$$

(iii) third order theory

$$\frac{p(z)}{\rho g} = -z + A\cos\omega t + \frac{1}{4}kH^2\frac{1}{\sinh 2kd}[1 - 2\sinh^2 k(d+z)]$$

$$+B\cos 2\omega t + C\cos\omega t - D\cos 3\omega t \quad .....(5.11(a))$$

where

$$A = H\frac{\cosh k(d+z)}{\cosh kd} \quad .....(5.11(b))$$

$$B = \frac{1}{4}kH^2\frac{1}{\sinh 2kd}[\frac{3\cosh 2k(d+z)}{\sinh^2 kd} - 1$$

$$+\,2\sinh^2 k(d+z) - 2\tanh kd\,\sinh 2kd] \quad .....(5.11(c))$$

$$C = \frac{k^2H^3}{256}[4(9\omega_0^{-8} - 12\omega_0^{-4} - 3 - 2\omega_0^4)\frac{\cosh k(d+z)}{\cosh kd}$$
$$+24\frac{\cosh k(d+z) - \cosh 3k(d+z)}{\cosh kd \sinh^4 kd}$$
$$+(1+3\omega_0^4)(3\omega_0^{-8} - 5 + 2\omega_0^4)\frac{\cosh 3k(d+z)}{\cosh 3kd}] \quad .....(5.11(d))$$

$$D = \frac{k^2H^3}{256}[3(9\omega_0^{-8} + 62\omega_0^{-4} - 31)\frac{\cosh k(d+z)}{\cosh kd}$$
$$+ 24\frac{\cosh k(z+d) - \cosh 3k(d+z)}{\cosh kd \sinh^4 kd}$$
$$+(1+3\omega_0^4)(-9\omega_0^{-12} + 22\omega_0^{-8} - 13\omega_0^{-4})\frac{3\cosh 3k(d+z)}{\cosh 3kd}]$$
$$.....(5.11(e))$$

$$\omega_0^2 = \tanh kd \quad .....(5.11(f))$$

In the above, $p(z)$ denotes pressure at a depth z , ω is the fundamental frequency: $\omega = 2\pi/T$, and the wave is at its crest at $t = 0$. Computer programs were written to calculate $p(z)$ from the above expressions. From the results obtained, the following observations can be made:

(i) Figure 5.2 corresponds to a very steep wave ($H/\lambda = 0.082$) in deep water ($d/\lambda \geq 0.5$), which is the same as the wave in Figure 5.1. The present result for the pressure at $z = 0$ is in closer agreement with experimental results than the theoretical predictions. The dip or double peak in the curve in the computed result is in agreement with the experimental curve. The agreement at bottom is also good. However, computed results indicate a phase difference, the numerical solution is leading by about $\pi/8$ radians.

(ii) Results in Figure 5.3, corresponding to a steep wave in shallow water, show once again that the computed pressure at $z = 0$ is comparatively in better

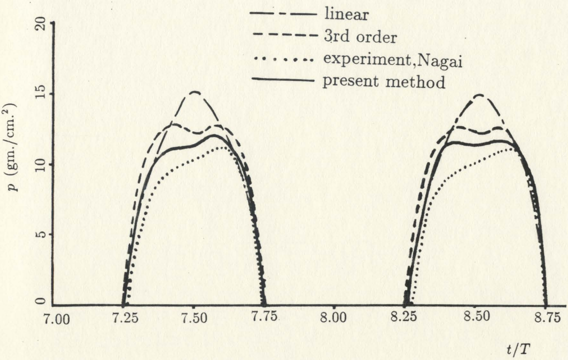

(a) Pressure at $z = 0$

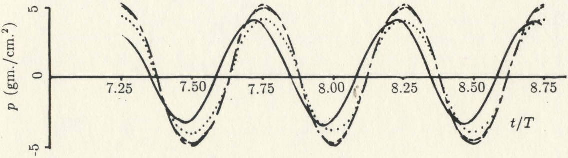

(b) Pressure at $z = -d$

Figure 5.2 Pressures on a vertical wall for $\lambda = 246$ cm., $H = 20.172$ cm., $d = 201$ cm. ($H/\lambda = 0.082$, $d/\lambda = 0.817$); $L = 2.5\lambda$, $\sigma/T = 1$, $\Delta x_F/\lambda = 1/24$, $\Delta t/T = 1/48$, $T_1 = 6\,T$ and $T_2 = 11\,T$.

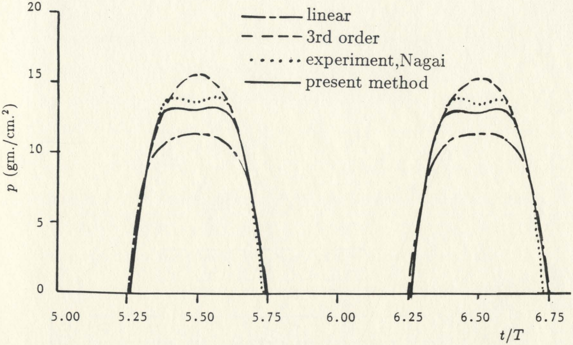

(a) Pressure at $z = 0$

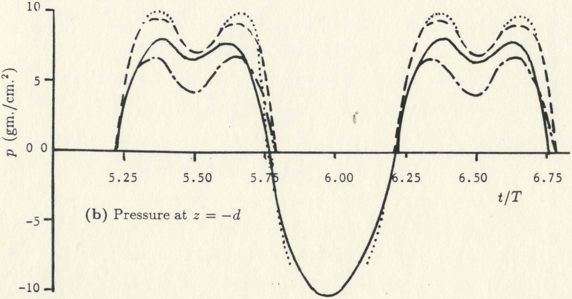

(b) Pressure at $z = -d$

Figure 5.3 Pressures on a vertical wall for $\lambda = 294$ cm., $H = 19.2$ cm., $d = 53.3$ cm. ($H/\lambda = 0.065$, $d/\lambda = 0.181$); $L = 2.5\lambda$, $\sigma/T = 1$, $\Delta x_F/\lambda = 1/24$, $\Delta t/T = 1/48$, $T_1 = 4.4\,T$ and $T_2 = 7.8\,T$.

correlation with experimental results than the theoretical solutions. The double peak observed in the experimental curve is again reproduced by the present computations, but the theoretical solutions are unable to predict this feature. The pressure at the bottom is not in as good an agreement.

(iii) Figure 5.4 shows the results for a small amplitude wave in shallow water ($d/\lambda = 0.133$). The experimental results are larger than either theoretical predictions or the present computations both at $z = 0$ and $z = -d$. This is somewhat surprising, since for waves of such small amplitude, theoretical predictions are expected to be in good agreement with experiment. The computed results, however, compare relatively well with the theories. For this case, it is believed that comparatively larger errors in experimental measurements are not unusual due to smallness of the measured quantities (similar doubts have been expressed in Fenton 1985).

(iv) In Figure 5.5, which corresponds to a shallow water wave of large steepness ($H/\lambda \geq 0.05$), the results for wave run-up on the wall are also presented, since the corresponding experimental data is available. The computed results for the run-up are in closer agreement with experimental data, displaying relatively more peaky crest and broader trough. An interesting feature is the occurrence of a double peak in the trough. Such behaviour is not unusual in the profile of a progressive steep water wave. Indeed, for $H/\lambda = 0.059$ and $d/\lambda = 0.13$, the second order Stokes theory predicts a null trough due to occurrence of a secondary crest in the trough (Wiegel 1964). Comparing the present values of $H/\lambda = 0.058$ and $d/\lambda = 0.133$, appearance of a secondary crest is then not surprising. The pressure results at the top are also in relatively good agreement, showing the double

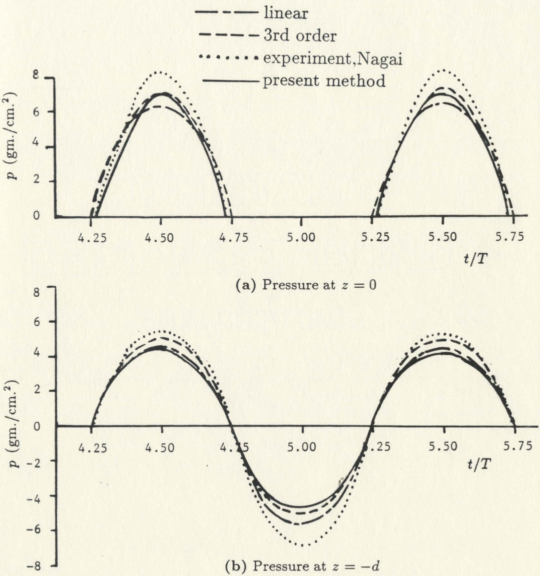

Figure 5.4 Pressures on a vertical wall for $\lambda = 400$ cm., $H = 7.0$ cm., $d = 53.3$ cm. ($H/\lambda = 0.0175$, $d/\lambda = 0.133$); $L = 2.5\lambda$, $\sigma/T = 1$, $\Delta x_F/\lambda = 1/24$, $\Delta t/T = 1/48$, $T_1 = 4\,T$ and $T_2 = 7\,T$.

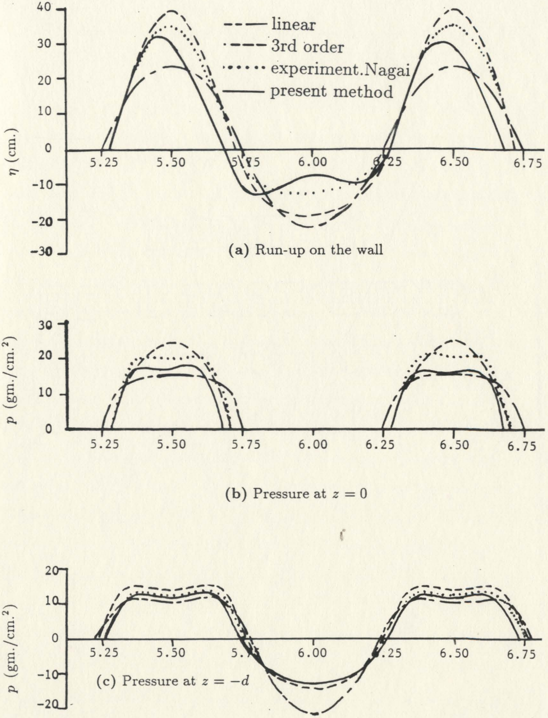

Figure 5.5 Run-up and pressures on a vertical wall for λ = 400 cm., H = 23.3 cm., d = 53.3 cm. (H/λ = 0.058, d/λ = 0.133); $L = 2.5\lambda$, $\sigma/T = 1$, $\Delta x_F/\lambda = 1/24$, $\Delta t/T = 1/48$, $T_1 = 4T$ and $T_2 = 7T$.

peak which once more the theoretical predictions can not reproduce. The agreement of the pressure at the bottom is very good.

Computations are also performed for a number of other conditions for which Nagai provides experimental results. Considering computer time, selected cases in the range of $d/\lambda \leq 0.5$ and $H/\lambda \geq 0.05$ are run. These conditions of shallow water steep waves are known to possess significant non-linear characteristics and are precisely the situations for which the usefulness of the present method is most appreciable. Majority of these exhibit presence of double peaks in the top pressure curves. For such cases, maximum simultaneous pressures, which correspond to the vertical distribution of pressures at the time instant when the total horizontal force exerted on the wall is maximum, do not occur under the wave crest (see e.g. Figures 5.2, 5.3 and 5.5). Since Nagai provides the pressure distributions only for maximum simultaneous pressures, a direct comparison is, in general, difficult. Instead, a qualitative description of the pressure curves is provided in Table 5.1, which describes and compares the peaks in the pressure curves both at $z = 0$ and $z = -d$. The experimental results are taken from Nagai's (1969) Figure 5, where graphs showing limiting values for H/λ and d/λ for which the pressure curves change from single to double peaks are provided. The comparison is remarkably good, including situations where the values fall very close to the limiting lines (indicating that a transition from single to double peaks is just beginning to occur). It appears that the present computations are able to reproduce all frequency components in very good qualitative agreement.

Figures 5.6 and 5.7 show the vertical pressure distributions for two cases for which the maximum simultaneous pressures occur under the wave crest. The computed results contain two curves, corresponding to the two peaks in the

Table 5.1 Comparisons of the qualitative nature of the pressures histories with the experimental results of Nagai (1969); 1 ≡ single peak; 2 ≡ double peak; 1 ~ 2 indicates that a transition from single to double peak (or vice-versa) is just beginning to occur.

Serial	λ	H	d	d/λ	H/λ	Experiment (Nagai 1969)		Present Method	
No.	(cm.)	(cm.)	(cm.)			$p(z=0)$	$p(z=-d)$	$p(z=0)$	$p(z=-d)$
1	246.0	20.17	201.0	0.814	0.082	2	2	2	2
2	294.0	19.20	53.3	0.181	0.062	2	2	2	2
3	400.0	7.0	53.3	0.133	0.018	1	1	1	1
4	405.0	23.20	53.3	0.132	0.058	2	2	2	2
5	237.6	8.55	48.0	0.202	0.036	1	$1\sim2$	1	$1\sim2$
6	181.5	13.61	45.0	0.248	0.075	2	2	2	2
7	171.8	9.62	45.0	0.262	0.066	2	2	2	2
8	400.0	9.20	200.0	0.500	0.023	1	2	1	2
9	844.0	40.51	200.0	0.237	0.048	1	2	1	2
10	619.2	37.15	200	0.323	0.060	$1\sim2$	2	$1\sim2$	2
11	550.3	35.22	197.0	0.358	0.064	2	2	2	2

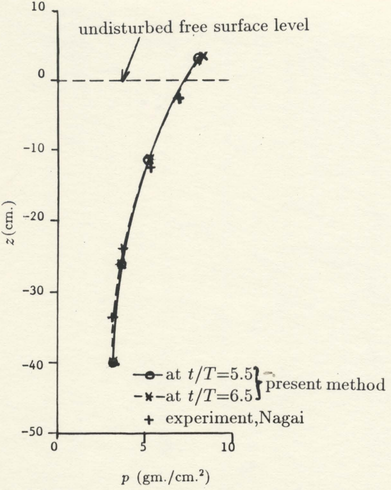

Figure 5.6 Vertical distribution of maximum simultaneous pressure on a wall; $\lambda = 237.6$ cm., $H = 8.55$ cm., $d = 48$ cm. ($H/\lambda = 0.036$, $d/\lambda = 0.202$); $L = 2.5\lambda$, $\sigma/T = 1$, $T_1 = 4.56\,T$ and $T_2 = 8.12\,T$.

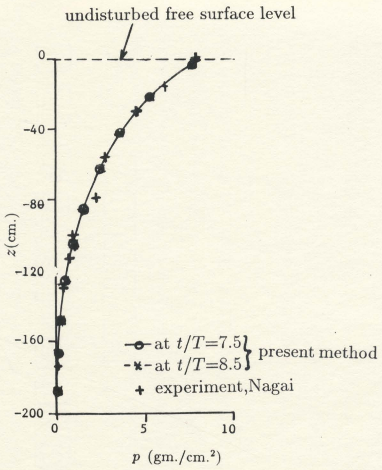

Figure 5.7 Vertical distribution of maximum simultaneous pressure on a wall; $\lambda = 400$ cm., $H = 9$ cm., $d = 200$ cm. ($H/\lambda = 0.023$, $d/\lambda = 0.50$); $L = 2.5\lambda$, $\sigma/T = 1$, $T_1 = 6\,T$ and $T_2 = 11\,T$.

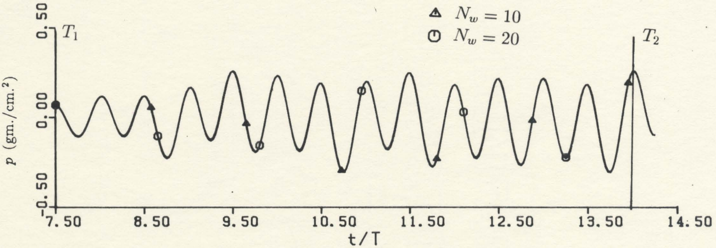

Figure 5.8 Pressure time-history at $z = -d$ for a deepwater wave of small amplitude; $d/\lambda = 0.817$, $H/\lambda = 0.020$, $L = 3.25\lambda$ and $\sigma/T = 1$; the plot is shown for the time interval T_1 - T_2.

5.2.3 Non-linear Effects

To demonstrate the non-linear effects in the total force, comparisons are made between results obtained for two different steepnesses: $H/\lambda = 0.082$ and $H/\lambda = 0.02$ for a water depth of $d = 0.817\lambda$ (the steeper wave corresponds to the results of Figure 5.1). The wall here is located at $L = 3.25\lambda$. The results in the interval of T_1 to T_2 are shown in Figure 5.10. The mean hydrostatic part ($\rho g d^2/2$) is excluded from the force which is non-dimensionalized with respect to ($\rho g H/k$). Non-linear effects with pronounced double peaks for the steeper wave are apparent. It is clear that the force amplitudes are considerably higher for the steeper wave. The increase is in order of 30% in negative amplitudes.

Figures 5.11 (a) - (c) show the run-up, non-dimensionalized horizontal force and overturning moment about the foot of the wall for a sequence of steepnesses: $H/\lambda = 0.0$, 0.25, 0.50, 0.75 and 0.10. The mean hydrostatic parts are excluded (which is $\rho g d^3/6$ for the moment part). The water has a depth of $d = 0.5\lambda$ and the wall is located at $L = 3\lambda$. The zero steepness case signifies a linearized solution in which the simulation is achieved by considering the linear free surface conditions (cf. §3). A monotonic increase in the non-linear effects with wave steepness is evident in the run-up profiles. For the steepness of $H/\lambda = 0.10$, the run-up profile is very close to the limiting value of a non-breaking standing wave ($H_s/\lambda = 0.218$ according to the theory by Penney and Price 1952 where H_s is the limiting height of the standing wave). An interesting observation is a phenomenon similar to beating, or presence of low frequency components, for the larger H/λ values. Closer examination reveals absence of such modulations of the amplitudes for the linear case and lower wave steepnesses, which suggests

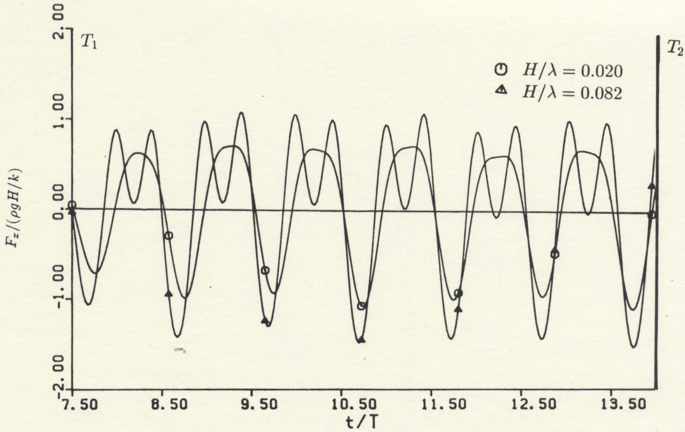

Figure 5.10 Horizontal force on a vertical wall : effect of wave steepness; $L = 3.25\lambda$, $\Delta x_F/\lambda = 1/24$ and $\Delta t/T = 1/40$; the plot is shown for the time interval T_1 - T_2.

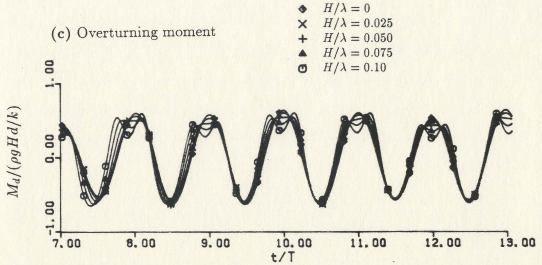

Figure 5.11 Run-up, horizontal force and overturning moment on a vertical wall for oncoming waves of different steepnesses; $L = 3\lambda$, $d/\lambda = 0.5$, $\Delta x_F/\lambda = 1/24$ and $\Delta t/T = 1/48$; the plots are shown within the interval T_1 $(= 7T)$ and T_2 $(= 13T)$; $H/\lambda = 0$ signifies a linearized application of the method where the boundary conditions on the free surface are linearized and ∂D_F is $z = 0$ (§3); the run-up plotted is the trace of $\partial D_F \cap \partial D_{C2}$, which is at $z = 0$ for the linearized solution, and hence not plotted.

this to be rather a non-linear phenomenon than outcome of numerical errors. Considering the force results, it is seen that the predicted positive amplitude is maximum under the wave crest for the linear solution and the effect of steepness is to reduce this amplitude. The negative amplitudes occur under the wave trough in all cases and an increase in the force amplitudes is apparent here. The amplitudes of the overturning moment do not exhibit as much variations with steepness. Here the effect of steepness appears to be formation of a double peak under the crest.

5.3 Summarizing Remarks

On the basis of the numerical study and the results presented above, the following conclusions can be reached:

(i) The described simulation can be applied to study the interaction of steep waves with a surface-piercing fixed object. The presented results demonstrate that a steady state behaviour in the pressure and forces on a wall in the presence of an oncoming steep wave can be achieved for time intervals extending over several wave periods, depending on the chosen computational domain. The run-up on the wall demonstrates that the wall and the free surface intersection point is determined within an acceptable limit of accuracy. This is further confirmed by the comparisons of pressures at $z = 0$ with experimental results, since pressure at this point depends directly on the run-up profile.

(ii) The present results in general correlate better with experimental results of Nagai in comparison with the agreements of the theoretical linear and third order perturbation solutions. The present method is able to predict the associated non-linear features, in particular the frequency components in the pressure curves, as demonstrated by the double peaks in the curves. This prediction is in very good agreement with experimental results and better than existing higher order perturbation solutions. The advantage of the numerical method over perturbation methods results from the validity in applicability of the present scheme over the entire range of relative depth and wave steepness. Additionally, irregular geometries of the wall and/or the bottom surface can be considered directly.

6 The Floating Body Problem

6.1 General Considerations

In this section, the problem of motions of floating bodies in steep waves is considered. As discussed in §2.1, a floating body $\mathcal{B}$ is introduced in the fluid such that its submerged part is completely contained in $\mathcal{D}$ (see Figure 2.1). The desired objective is to expose $\mathcal{B}$ to an incident steep wave train and to subsequently follow the motion of $\mathcal{B}$. A propagating steep wave is generated in the manner described earlier, developing at ∂D_{C1}, travelling towards positive x direction, and eventually interacting with $\mathcal{B}$. The aim is to simulate the subsequent responses of $\mathcal{B}$.

For this simulation, it is necessary to know the exact location of $\mathcal{B}$ at every time instant. In addition, a relation between ϕ and $\partial\phi/\partial n$ on the body surface (∂D_B) is to be established such that evolution of the boundary data on ∂D_B can be followed. The required information is obtained by invoking the equations of body motion and the body kinematic condition.

6.1.1 Equations of Body Motion

For the following developments, it is convenient to introduce an additional coordinate system fixed with the body. Accordingly, a body-fixed right handed rectangular Cartesian coordinate system $Gx'z'$ is defined such that its origin G lies at the body's centre of gravity (CG) and the axes coincide with the principal axes of inertia (Figure 6.1). Gz' is directed vertically upwards in the undisturbed position of the body. The body geometry is invariant in this coordinate system

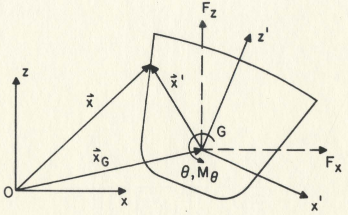

Figure 6.1 Inertial and body coordinate systems.

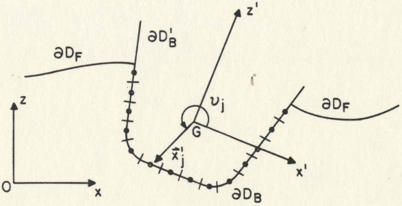

Figure 6.2 Interpolation for $\phi(\mathbf{x}')$ on ∂D_B.

and therefore the instantaneous contour of ∂D_B to an observer stationary in space is completely defined by the location and orientation of $Gx'z'$ system with respect to the Oxz system. The coordinates of the radius vector of a point fixed with the body in the $Gx'z'$ system, denoted as $\{\mathbf{x}\}'$, is related to the coordinates of radius vectors of the same point and the CG of the body in the space fixed system, denoted by $\{\mathbf{x}\}$ and $\{\mathbf{x_G}\}$ respectively, by the following:

$$\{\mathbf{x}\}' = [\mathbf{R}]\,\{\mathbf{x} - \mathbf{x}_G\} \qquad .....(6.1)$$

or alternatively

$$\{\mathbf{x} - \mathbf{x}_G\} = [\mathbf{R}]^T\{\mathbf{x}\}' \qquad .....(6.2)$$

$[\mathbf{R}]$ in the above represents the matrix of coordinate transformation and the superscript T indicates a transpose. $[\mathbf{R}]$ is given by:

$$[\mathbf{R}] = \begin{bmatrix} \cos\theta & \sin\theta \\ -\sin\theta & \cos\theta \end{bmatrix} \qquad .....(6.3)$$

where θ denotes the angular displacement of $Gx'z'$ system with respect to Oxz system, measured positive counterclockwise.

The general equations of motion for the body can be written in the familiar Newtonian forms:

$$F_x = M_B\,\frac{\partial^2 x_G}{\partial t^2} \qquad .....(6.4(a))$$

$$F_z = M_B\,\frac{\partial^2 z_G}{\partial t^2} \qquad .....(6.4(b))$$

$$M_\theta = I_\theta\,\frac{\partial^2 \theta}{\partial t^2} \qquad .....(6.4(c))$$

where F_x, F_z and x_G, z_G are the components of the force and radius vectors $\mathbf{F}$ and $\mathbf{x_G}$ in x and z directions respectively; M_θ represents the angular moment about an axis passing through G and orthogonal to Gx' and Gz'; M_B denotes the body mass and I_θ denotes the mass moment of inertia about the axis about which M_θ applies.

The external fluid forces and moment exerted on $\mathcal{B}$ can be obtained by direct integration of the fluid pressure on ∂D_B:

$$\mathbf{F} = \int_{\partial D_B} p(\mathbf{x})\ \mathbf{n} dS \qquad .....(6.5(a))$$

$$M_\theta = \int_{\partial D_B} p(\mathbf{x})\ (\mathbf{x}' \times \mathbf{n}') dS \qquad .....(6.5(b))$$

where $\mathbf{n}$ and $\mathbf{n}'$ are the unit normals on ∂D_B directed outwards of $\mathcal{D}$ (i.e. inwards to ∂D_B) in the inertial and body systems respectively and a '$\times$' indicates a vectorial cross-product. In the sequel, the primed and non-primed symbols are understood to be quantities with respect to the $Gx'z'$ and Oxz systems respectively, unless defined specifically. The expression for moment in (6.5 (b)) is written in terms of the variables in a mixed system of reference. This can be recast in the following form consistent with the force expressions:

$$M_\theta = \int_{\partial D_B} p(\mathbf{x})\ [\ (\mathbf{x}\ -\ \mathbf{x}_G) \times \mathbf{n}\ ] dS \qquad .....(6.6)$$

since $\mathbf{x}' \times \mathbf{n}' = (\mathbf{x} - \mathbf{x}_G) \times \mathbf{n}$. In their component form, these expressions are:

$$F_x = \int_{\partial D_B} p n_x dS \qquad .....(6.7(a))$$

$$F_z = \int_{\partial D_B} p n_z dS \qquad .....(6.7(b))$$

$$M_\theta = \int_{\partial D_B} p[-(z - z_G)n_x + (x - x_G)n_z] dS \qquad .....(6.7(c))$$

6.1.2 Body Kinematic Condition

On the body surface, the fluid side normal velocity $\partial\phi/\partial n$ is equal to the normal component of the body velocity V_n by virtue of (2.5). For any point q on ∂D_B,

$$(V_n)_q = \mathbf{v}_q \cdot \mathbf{n}_q \qquad .....(6.8)$$

where $\mathbf{v}_q$ denotes the velocity vector of ∂D_B at q. From rigid body kinematics, we have

$$\begin{aligned} \mathbf{v}_q &= \mathbf{v}_G + \vec{\varpi} \times \mathbf{x'}_q \\ &= \mathbf{v}_G + \vec{\varpi} \times (\mathbf{x}_q - \mathbf{x}_G) \end{aligned} \qquad .....(6.9)$$

where $\mathbf{v}_G$ denotes the translational velocity vector for G: $\mathbf{v}_G = \partial \mathbf{x}_G/\partial t$ and ϖ denotes the rotational velocity of $\mathcal{B}$ taken about G: $\varpi = \partial\theta/\partial t$. $\vec{\varpi}$ represents ϖ in a vectorial form, i.e. $\vec{\varpi} = \varpi\vec{k}$ where $\vec{k}$ is a unit vector orthogonal to Gx' and Gz' (positive when directed outwards of the paper in Figure 6.1). From (2.5),(6.8) and (6.9), the following relation results:

$$(\frac{\partial\phi}{\partial n})_j = n_{x_j}\frac{\partial x_G}{\partial t} + n_{z_j}\frac{\partial z_G}{\partial t} + \frac{\partial\theta}{\partial t}[-(z_j - z_G)n_{x_j} + (x_j - x_G)n_{z_j}] \quad ..(6.10)$$

where the suffix q has been replaced with j indicating a collocation point. The above expression provides the relationship between the fluid velocity $\partial\phi/\partial n$ at any point on ∂D_B in terms of the body displacement, velocity and geometry, all of which are defined consistently in the inertial frame of reference (the Oxz system).

6.1.3 Basic Algorithm for Following the Motion of the Body

The solution algorithm of §2.3 can now be adopted for simulation of motions of $\mathcal{B}$. The boundary data on ∂D_B are interconnected by means of relations (6.7), (6.10) and Bernoulli's equation (5.2). At any instant, presuming $\partial\phi/\partial n$ to be known on ∂D_B, the other boundary data ϕ is determined from the solution of the integral relation (2.6) (see §2.2). From this, the fluid pressure (p) exerted on the body can be determined by utilizing Bernoulli's equation (5.2), since p depends

(6.9) and (6.14), $\partial\phi/\partial t$ at the collocation points fixed to the body surface are:

$$\begin{aligned}(\frac{\partial\phi}{\partial t})_j &= (\frac{d\phi}{dt})_j - \{\frac{\partial x_G}{\partial t} - \frac{\partial\theta}{\partial t}(z_j - z_G)\}(\frac{\partial\phi}{\partial x})_j \\ &+ \{\frac{\partial z_G}{\partial t} + \frac{\partial\theta}{\partial t}(x_j - x_G)\}(\frac{\partial\phi}{\partial z})_j \qquad .....(6.15)\end{aligned}$$

Unlike in the determination of wave interaction with a fixed object (§5), a straight-forward central difference formula (5.3) can not be employed in determining $(\partial\phi/\partial t)_j$, since $\phi_j(t+\Delta t)$ in this case will not be known *a priori*. The evaluation of this term is discussed latter (§6.2.3). To determine the tangential derivative $\partial/\partial s$ of ϕ_j, we use

$$\begin{aligned}(\frac{\partial\phi}{\partial s})_j &= (\frac{\partial\phi}{\partial j})_j/(\frac{\partial s}{\partial j})_j \\ &= \frac{1}{\Delta S_j}(\frac{\partial\phi}{\partial j})_j \qquad .....(6.16)\end{aligned}$$

since for the straight line segments, $(\partial s/\partial j)_j = \Delta S_j$. To determine $(\partial\phi/\partial j)_j$, appropriate second-order difference formulae are employed (see Appendix A.4). This is found permissible despite sharp changes of ∂D_B, since ϕ on the surface is in general a smoothly varying continuous function. This has been confirmed by plotting ϕ_j against j for several conditions. The x and z derivatives of ϕ are readily obtainable from relations (4.8(a)) and (4.8(b)), from which

$$\begin{aligned}(\nabla\phi)_j^2 &= (\frac{\partial\phi}{\partial x})_j^2 + (\frac{\partial\phi}{\partial z})_j^2 \\ &= (\frac{\partial\phi}{\partial n})_j^2 + (\frac{\partial\phi}{\partial s})_j^2 \qquad .....(6.17)\end{aligned}$$

This completes the essential details in evaluation of the pressure terms. Recalling relations (6.13), the force expressions can be replaced by the following:

$$F_x = \sum_{j=1}^{N_B}[(p_1)_j + (p_2)_j + (p_3)_j]n_{x_j}\Delta S_j \qquad .....(6.18(a))$$

$$F_z = \sum_{j=1}^{N_B} [(p_1)_j + (p_2)_j + (p_3)_j] n_{z_j} \Delta S_j \qquad .....(6.18(b))$$

in which the approximation that ϕ_j's are constant over the segments is utilized. The static term p_1 and the geometry dependent term in p_2 (see eqn. (6.15)) are also correctly integrated due to their linear dependence on $\mathbf{x}$ and central location of j within the segments.

For evaluation of the moment part, the static term (M_{θ_1}) is

$$M_{\theta_1} = -\rho g \sum_{j=1}^{N_B} \int_{\Delta S_j} z[-(z - z_G)n_{x_j} + (x - x_G)n_{z_j}]dS \qquad .....(6.19)$$

which has a quadratic variation with $\mathbf{x}$ and is therefore integrated using Simpson's rule. The other two terms are linearly varying with $\mathbf{x}$ and thus expressions similar to (6.18) are applicable. In the present algorithm, however, Simpson's rule has been applied for evaluation of all the three terms.

It is straightforward to employ other more popular and refined rules, e.g. Gauss quadrature, for these integrations. In this context it is observed that such refinements do not lead to additional accuracies in the above integrations. Within the fundamental approximations of the present discretization scheme (§2), the integration rules adopted are exact.

6.2.2 Discretization

It is convenient to describe the body geometry with respect to $Gx'z'$ system in which it is invariant. Denoting $\partial D'_B$ as the complete contour of $\mathcal{B}$ (note that $\partial D'_B$ is not necessarily a closed contour), the surface can be subdivided into segments once for all. To determine the wetted contour ∂D_B ($\partial D_B \subseteq \partial D'_B$), the intersections $\partial D_F \cap \partial D_B$ need to be determined. These are determined via a second order extrapolation scheme in which a second degree polynomial is assumed through the three points on ∂D_F adjacent to $\partial D'_B$. In principle, this is similar to the Lagrangian extrapolation scheme applied earlier in determining $\partial D_F \cap \partial D_{C2}$ (§§4,5). The procedure here, however, is more elaborate in that it involves consideration of each segment on $\partial D'_B$ in succession, determination of the roots of a quadratic, followed by a searching procedure to locate the two roots which represent the intersection points.

The discretization of $\partial D'_B$ once for all, determination of $\partial D'_B \cap \partial D_F$ and subsequently consideration of only those segments in ∂D_B, is found to produce instability in the force computations and a consequential divergence of the solution. This is because this discretization scheme necessitates introduction or deletion of segments on the body near the intersection point, which in turn produces 'spikes' or pressure impulses in the computation of the dynamic part of the pressure p_2. Although similar problems were encountered earlier in the simulation of waves interacting with fixed objects (§5), here the computations can not be continued due to the coupling nature of the forces with the time advancement of the solution. Furthermore, since generally a backward difference scheme in time can be used for evaluating $\partial\phi/\partial t$, the solution is found to diverge almost immediately after starting. This problem is overcome by redistributing the collocation points on the body at every step such that the segment sizes vary smoothly in time. In the present algorithm, we first determine $\partial D_F \cap \partial D'_B$ and divide ∂D_B at every step, keeping N_B constant. We note that the variation of the segment sizes between adjacent segments is not as critical (i.e. the solution is relatively insensitive on the variation of $(\Delta x_B)_j$ with j while $\Delta x_B(t)$ must not have large and abrupt changes with t).

Redistribution of collocation points on ∂D_B implies change of the locations of the points (i.e. $\mathbf{x'}_j$'s change with time). In the computation of $d\phi/dt$ a spatial interpolation for ϕ_j becomes necessary. This can be more clearly seen from the following. On ∂D_B, we have

$$\phi_j = \phi(\mathbf{x'}_j(t), t) \qquad .....(6.20)$$

In general, for a backward difference scheme for $d\phi/dt$,

$$(\frac{d\phi}{dt})_j = \varphi[\phi(\mathbf{x'}_j(t), t), \phi(\mathbf{x'}_j(t), t - \Delta t), \cdots, \phi(\mathbf{x'}_j(t), t - N_\Gamma \Delta t);\ \Delta t] \qquad .....(6.21)$$

where φ means 'a function of'. The variable N_Γ in the above depends on the order of the difference scheme chosen (e.g. $N_\Gamma = 2$ for a second order scheme). Expression (6.21) indicates that we have to determine $\phi(\mathbf{x'}_j(t), t - m\Delta t)$ from the available $\phi(\mathbf{x'}_j(t - m\Delta t), t - m\Delta t)$ for $m = 1, \cdots, N_\Gamma$. This requirement is similar to the analogous wall case except that ϕ_j can not be considered a function of z_j, since z_j in this case is not necessarily a monotonically increasing or decreasing function for all $j = 1, \cdots, N_B$. It is also not possible to consider ϕ_j as a function of j as was done in determining the tangential derivatives of ϕ. We therefore introduce another variable γ_j, which is essentially the angular coordinate of $\mathbf{x'}_j$ as shown in Figure 6.2, and assume ϕ_j as a smoothly varying function of γ_j. Except for very uncommon geometries, γ_j will generally be a monotonically increasing function of j. To obtain the required information, we now approximate ϕ_j as a function of γ_j by piecewise polynomials and interpolate for $\phi(\mathbf{x'}_j(t), t - m\Delta t)$. In general this spatial interpolation is expected to introduce very little numerical approximation errors, since the changes in $\mathbf{x'}_j$ between two consecutive times are very small: typically $|\mathbf{x'}_j(t) - \mathbf{x'}_j(t - \Delta t)| \leq 0.02\Delta x_B$ where Δx_B denotes the length of a segment on ∂D_B. Computations using linear and second order interpolation rules were found to produce practically indistinguishable results. In the present algorithm, the second order rules are retained.

The above completes the discretization of ∂D_B. On the free surface, a similar redistribution of the collocation points becomes necessary. Except for a wall-sided body in heave motion, any other combination of the body geometry and modes of motion causes a change in the size of the segments adjacent to the body, eventually leading to a deletion or introduction of a collocation point. For the same reason as on the body, this destabilizes the force computations. Therefore the original location of the collocation points can not be retained, and must be redistributed at every time step. This necessitates an interpolation of η_j and ϕ_j in space for integration of the free surface evolution equations. Instead of storing and interpolating between η_j and ϕ_j, the values of the right hand side of (2.2) and (4.3) are stored (i.e. f in eqns. (A.1.3) in Appendix A.1) for the required number of past steps (four steps for the integration scheme employed) and used for interpolation. This results in a slight reduction of the computations in that the computations for the r.h.s. of (2.2) and (4.3) need not be repeated. The interpolations are accomplished by approximating f_j as a function of x_j by a cubic spline. With regard to the associated numerical inaccuracies, earlier remarks on discretization of ∂D_B apply.

6.2.3 Integration of the Equations of Motion

The system of equations of motion (6.4) can be decomposed into six ordinary differential equations of the first order:

$$\frac{\partial u_G}{\partial t} = \frac{F_x}{M_B} \quad .....(6.22(a))$$

$$\frac{\partial x_G}{\partial t} = u_G \quad .....(6.22(b))$$

$$\frac{\partial v_G}{\partial t} = \frac{F_z}{M_B} \quad .....(6.22(c))$$

$$\frac{\partial z_G}{\partial t} = v_G \quad .....(6.22(d))$$

$$\frac{\partial \varpi}{\partial t} = \frac{M_\theta}{I_\theta} \quad .....(6.22(e))$$

$$\frac{\partial \theta}{\partial t} = \varpi \quad .....(6.22(f))$$

A number of standard techniques are available for integrating above system of ordinary differential equations. In the present algorithm, for convenience as well as to be consistent with integrations of the free surface conditions, a fourth order A-B-M scheme was originally employed. However, application of this scheme was found to lead to an instability of the solution. The solution was found to be divergent and this could not be remedied by increasing the number of iterations per time step. This divergence starts at a very early stage of the solution, typically within 40 time steps of the simulation, and originates from the force computation. On examining the computed pressure components, it was found that the problem is associated with the calculation of the $d\phi/dt$ term. When an implicit scheme is used for the equations of motions, this term can only be computed from a backward difference scheme in time. As a demonstration, consider the following equation:

$$\mathbf{F}(\frac{d\phi}{dt}, \nabla\phi, t) = M_B\frac{d\mathbf{v}}{dt} \quad .....(6.23)$$

In the A-B-M scheme, a predictor step is:

$$\mathbf{v}^{(1)}(t+\Delta t) = \mathbf{v}(t) + \varphi[\mathbf{F}(t), \mathbf{F}(t-\Delta t), \cdots;\ \Delta t]/M_B \qquad .....(6.24)$$

and the corrector steps are:

$$\mathbf{v}^{(m)}(t+\Delta t) = \mathbf{v}(t) + \varphi[\mathbf{F}^{(m-1)}(t+\Delta t), \mathbf{F}(t), \mathbf{F}(t-\Delta t), \cdots;\ \Delta t]/M_B \qquad .....(6.25)$$

where the superscripts in the parenthesis denote the level of iterations, $m \geq 2$ for the corrector steps. Examining the corrector steps in the light of (6.23), it is seen that the contribution due to $d\phi/dt$ in $\mathbf{F}^{(m-1)}(t+\Delta t)$ can only be calculated using a backward difference scheme. Originally a backward second order difference scheme was applied for this computation, but successive increases in the order of the backward schemes did not rectify the situation (the situation was, in fact, found to worsen). This means that a stable difference formula must be used to determine this part of the pressure, at least for the second and subsequent iterations (for the first level , i.e. for the predictor step, a backward scheme is unavoidable). A stable difference formula in general requires values of relevant quantities at the advanced time level. This means the formula for $d\phi/dt$ involves estimated values of $\phi(t+\Delta t)$, which in turn suggests that explicit schemes are to be used for integrating the motion equations.

The algorithm used can be best described by means of the flow diagram shown in Figure 6.3. As illustrated, the predicted values are calculated using a backward difference for $d\phi/dt$ in the force evaluation and an explicit scheme is used for integrating the equations of motion. With this, the required information (ϕ) on the body for the advanced step is computed. For the second and higher iterations, the scheme returns to the previous step and upgrades the force, this

6.4):

L_1 : x distance of the body coordinate system from ∂D_{C1}

at $t = 0$; $\equiv x_G(0)$

L : horizontal distance between ∂D_{C1} and ∂D_{C2}

L_2 : $L - L_1$

L_1^* : x distance of the lee side of the body from ∂D_{C1}

at $t = 0$; $= L_1 - 0.5B$ .....(6.26)

L_2^* : x distance of the windward side of the body from

∂D_{C2} at $t = 0$; $= L_2 - 0.5B$

B : full breadth of the body

h : body draft at its static equilibrium (i.e. at $t = 0$)

d : water depth

Due to the redistribution of the collocation points, the size of the segments on ∂D_F and ∂D_B continuously changes. Therefore, the parameters indicated as Δx (with appropriate suffixes) in the following are meant to represent the size of the segments at $t = 0$. The times T_1 and T_2 have the same meaning as in the wall case (§5), i.e., the estimated times for the fully developed wave front to reach the lee side of the body and reflect back to ∂D_{C1}. Formulae (5.6) and (5.8) with L replaced by L_1^* apply for these estimations. The maximum peak-to-peak values for the x and z components of the forces and moment are denoted by $|F_x|$, $|F_z|$ and $|M_\theta|$ respectively while $|x_G|$, $|z_G|$ and $|\theta|$ represent the similar values for sway, heave and roll displacements. Simulations are achieved by imposing an Airy wave potential on ∂D_{C1} with H, λ, T and ω denoting the

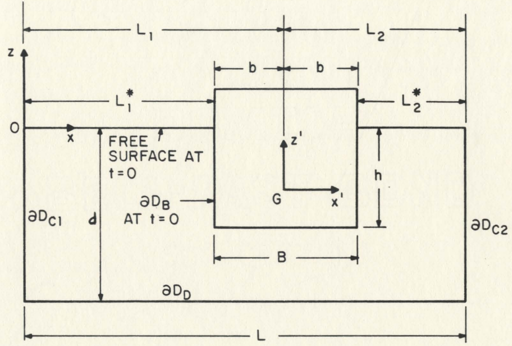

Figure 6.4 Geometric parameters of the body and the fluid domain.

height, length, period and frequency of an Airy wave in conformation with the applied excitation potential defined by eqn. (3.3).

A number of computational results are presented below to demonstrate and explore the effectiveness of the method in simulating large motions. Simulation for conditions in which the body is constrained in certain modes of motion are achieved easily by excluding the integration of the corresponding equations of motion, or alternatively equating the displacements and velocities to their initial values after each time level.

All computational results presented are for a rectangular body geometry.

6.3.1 Fixed Body Case

This corresponds to the situation of a 'fixed' floating body in which the body is fixed in all degrees of freedom.

Example : 1

The relevant parameters for this example are

$$\begin{aligned} h/B &= 0.5 \\ \lambda &= 2B \\ d/\lambda &= 0.5 \\ H/\lambda &= 0.075 \\ z_G(0)/B &= -B/8 \end{aligned} \qquad .....(6.27)$$

These parameters correspond to the non-dimensional frequency $\omega\sqrt{B/2g} =$ 1.253 which is within the interval of $1.5 \leq B\omega^2/2g \leq 2$ known for significant non-linear effects (Telste 1985). Results in terms of the run-up profile on the lee side of the body, non-dimensionalized forces and moment about the body's CG are shown in Figures 6.5 (a) - (d) for a control domain of $L_1^* = 2.5\lambda$ and $L_2^* = 2.0\lambda$. Other parameters are : $\sigma/T = 1.0$; $n = 4$; Δx_F, Δx_{C1}, Δx_{C2} and $\Delta x_B = \lambda/24$; and $\Delta t/T = 1/48$. The large run-up profile at the lee-side indicates an almost full reflection of the wave. Although the time histories show some variations in the amplitudes, the forces and moment appear to display a steady state behaviour in the indicated time interval T_1 to T_2 (cf. eqns (5.6) and (5.8)). It is not clear whether the observed modulations in the forces and moment histories are due to numerical effects or are non-linear effects.

In order to study the free surface motions, Figures 6.6 (a) - (d) show the evolutions in time of the free surface at distances $\lambda, 0.75\lambda, 0.5\lambda$ and 0.25λ in front of the body (distances here are measured from the lee side of the body). These plots suggest a gradual development of a standing wave profile of length λ in $0 \leq x \leq L_1^*$. Typical features displaying antinodes and nodes associated with standing waves are apparent. This standing wave has a steepness of approximately $H^*/\lambda = 0.15$ (H^* = height of the numerical wave in $\mathcal{D}$). The free surface evolution downstream of the body, shown in Figure 6.7 for a station at a distance of λ downstream of the windward side, suggests that practically no energy has been transmitted to the other side of the body.

Computations performed for this wave condition when the body is released in heave have shown that the resulting heave motions are extremely small, $|z_G|$ not exceeding $h/20$. This is perhaps not an unexpected behaviour, since from linear theory it is known that body motions at higher frequencies are usually negligible.

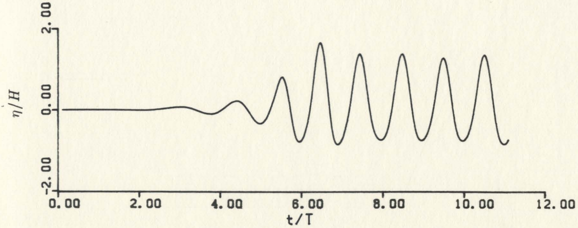

(a) Run-up on the lee side of the body

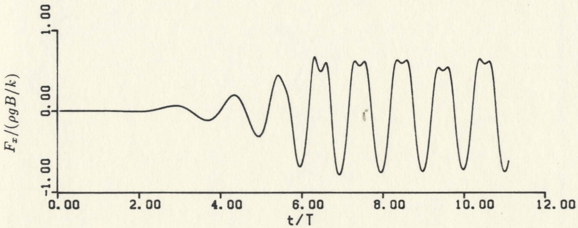

(b) Sway force

Figure 6.5 continued ⇓

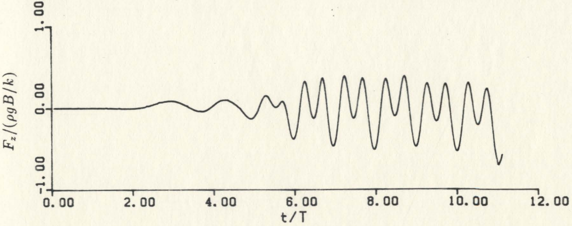

(c) Heave force

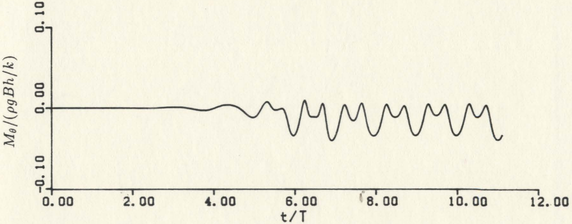

(d) Roll moment

Figure 6.5 Run-up, forces and moment on a rectangular 'fixed' floating body of $h/B = 0.5$; $L_1^* = 2.5\lambda$, $L_2^* = 2.0\lambda$, $\lambda/B = 2$, $d/\lambda = 0.5$, $H/\lambda = 0.075$, $T_1 = 6\,T$ and $T_2 = 11\,T$.

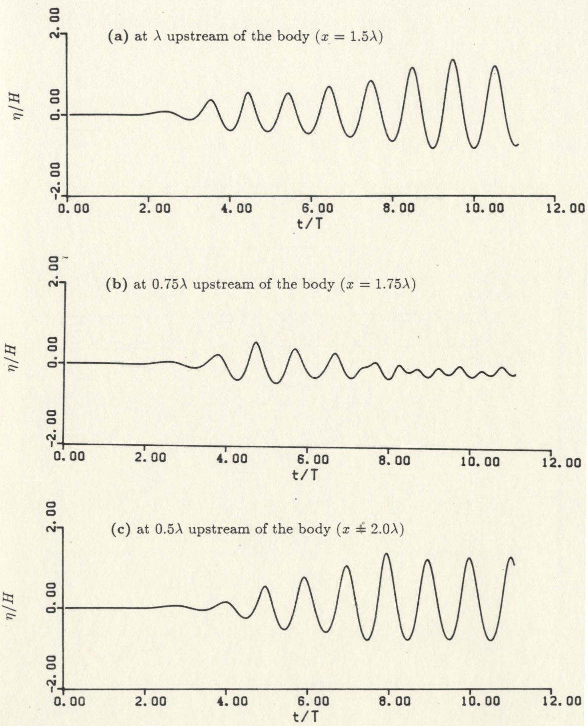

Figure 6.6 continued ⇓

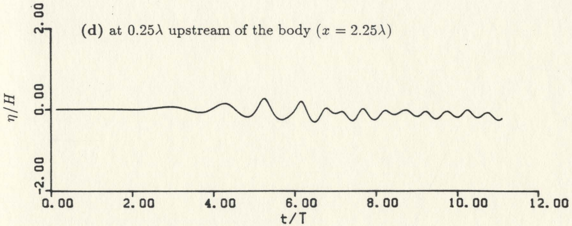

Figure 6.6 Evolution of the free surface in time at several locations in the region $0 \leq x \leq L_1^*$ corresponding to the 'fixed' floating body simulation of Figure 6.5; the distances quoted are measured from the lee side of the body.

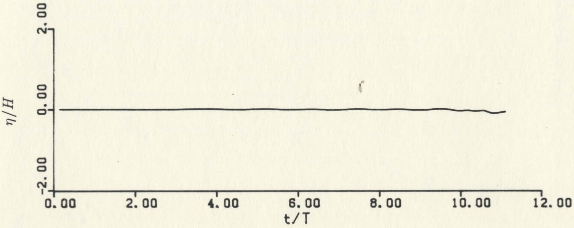

Figure 6.7 Evolution in time of the free surface at a distance λ downstream of the body, measured from the windward side ($x = 4\lambda$)

6.3.2 Heave Motions

Results shown here are for the situation where the body is free to heave but is fixed in the other two modes of motions.

Example : 1

The relevant parameters for this example are

$$\begin{aligned} h/B &= 0.5 \\ \lambda &= 6B \\ d/\lambda &= 0.5 \\ H/\lambda &= 0.05 \\ z_G(0)/B &= -B/8 \\ \omega\sqrt{B/2g} &= 0.723 \end{aligned} \qquad .....(6.28)$$

These parameters are chosen such as to correspond to the heave resonance of the body. The natural frequency in heave (ω_n^h) can be computed from (Newman 1980)

$$\omega_n^h = (\frac{c_{22}}{a_{22} + M_B})^{0.5} \qquad .....(6.29)$$

where c_{22} and a_{22} are restoring force and added mass in heave. From an estimate of $a_{22}/M_B = 1.0$ from the experimental results of Vugts (1969), the applied excitation frequency for this example corresponds to $\omega/\omega_n^h = 1.023$. The body is therefore expected to display resonant behaviour in heave.

Figures 6.8 (a) - (c) show the results in terms of non-dimensional sway force, roll moment and heave motions for $L_1^* = 2.0\lambda, 2.5\lambda$ and 3.0λ. In all computations $L_2^* = 2.0\lambda$. The plots clearly display a steady state behaviour in the interval T_1

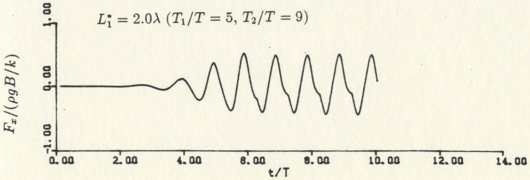

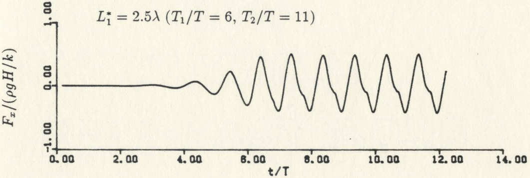

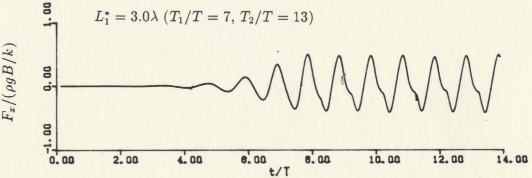

(a) Sway force

Figure 6.8 continued ⇓

$L_1^* = 2.0\lambda$ ($T_1/T = 5$, $T_2/T = 9$)

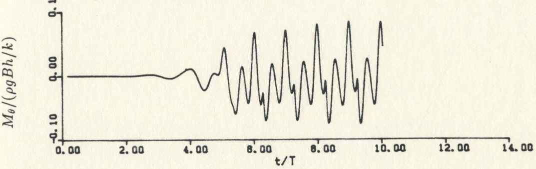

$L_1^* = 2.5\lambda$ ($T_1/T = 6$, $T_2/T = 11$)

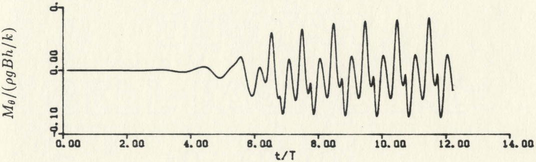

$L_1^* = 3.0\lambda$ ($T_1/T = 7$, $T_2/T = 13$)

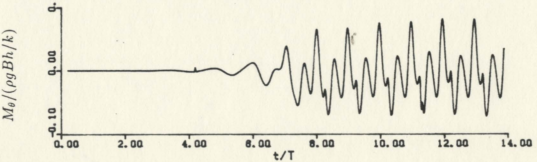

(b) Roll moment

Figure 6.8 continued ⇓

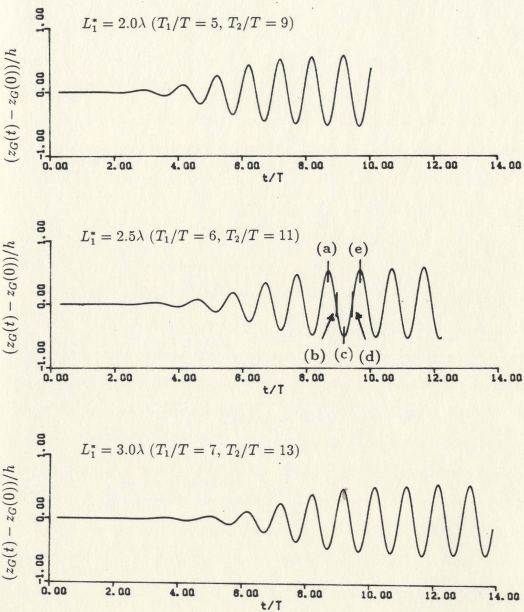

(c) Heave motion

Figure 6.8 Sway force, roll moment and heave motion of a rectangular body of $h/B = 0.5$; the body is free to heave only; $\lambda/B = 6$, $d/\lambda = 0.5$ and $H/\lambda = 0.05$; the body is in (or very close to) heave resonance.

to T_2. The effect of heave motion on sway force can be observed by comparing the curves in Figure 6.8 (a) with the sway forces for the earlier, fixed body, results in Figure 6.5 (b) (or the force results on vertical walls shown in §5 , cf. Figures 5.2 to 5.5). The time histories of the roll moment show the presence of higher frequency components, which are qualitatively different from the fixed body results of the preceding example. As expected, large heave motions are obtained. The maximum heave displacements are in excess of the initial draft: $|z_G|/h \approx 1.2$. The relative run-up profiles at the lee side of the body shown in Figure 6.9 illustrates that the heave motions are not in phase with the wave. Evidently the relative motion between the body and the free surface is not negligible. This relative run-ups vary from $r/h \approx 0.2$ to 1.5 indicating that the body tends to emerge more than it tends to immerse (r here is the height of the free surface measured from the keel, as illustrated in the accompanying diagram in Figure 6.9). A close-up view of the body and the free surface at several instants over a full cycle of heave motion shown in Figure 6.10 illustrates this feature more clearly. At its maximum positive heave displacements, the body is almost emerging out of the free surface (see Figures 6.10 (a) and (e)). Steady state behaviour of the solution is further evidenced by the repeatability of the free surface profiles when the body's displacements and velocities are identical. Compare, for example, the free surface profiles in Figures 6.10 (a) and (e) where the body displacements and velocities are the same. These plots when superposed are graphically indistinguishable. On the other hand, dependence of the fluid motion on the body's motion can be observed by examining Figures 6.10 (b) and (d), when the body is at the same displaced position but moving in opposite directions. The free surfaces here differ considerably.

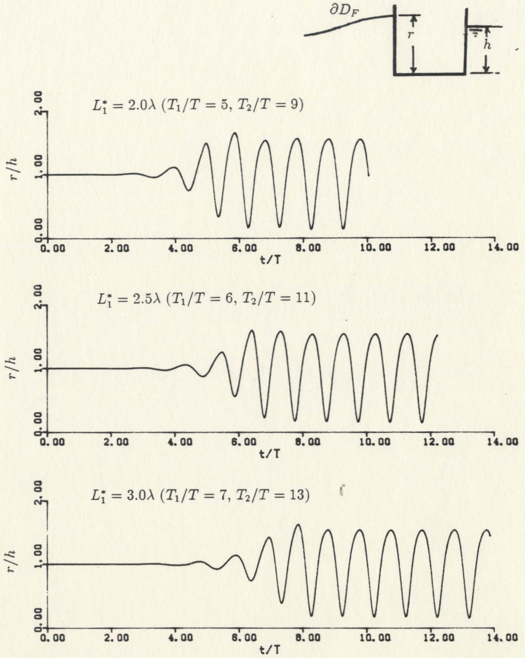

Figure 6.9 Relative run-up on the lee side of the body corresponding to Figure 6.8 above.

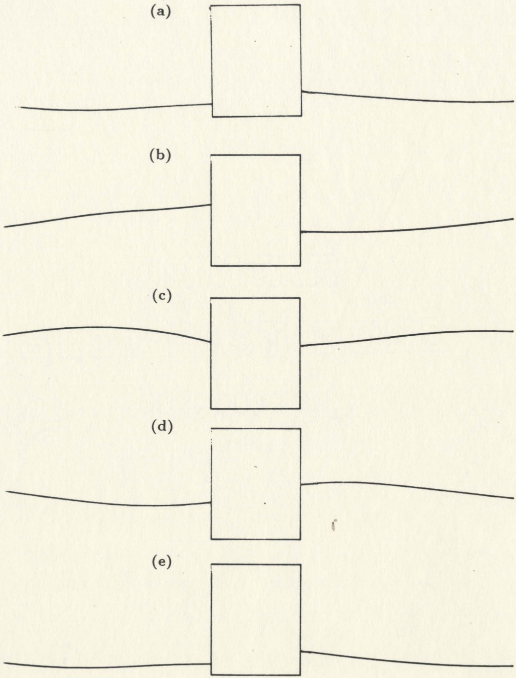

Figure 6.10 Plots of the instantaneous position of the body and a portion of the free surface; (a) - (e) refer to the corresponding time marks in Figure 6.8 (c) (for $L_1^* = 2.5\lambda$).

6.3.3 Roll Motions

In the following examples, the simulations are achieved by fixing the body in the heave and sway modes while it is free to roll.

Example : 1

The key parameters are

$$\begin{aligned} h/B &: 0.5 \\ \lambda &: 2B \\ d/\lambda &: 0.5 \\ H/\lambda &: 0.05 \\ z_G(0)/B &: -1/8 \\ \omega\sqrt{B/2g} &: 1.253 \\ I_\theta/\rho S_A B^2 &: 0.028 \\ GM &: B/24 \end{aligned} \qquad .....(6.30)$$

where S_A denotes the wetted area of the body at $t = 0$ and GM denotes metacentric height.

The roll natural period of the body (ω_n^r) can be estimated from :

$$\omega_n^r = (\frac{gM_B GM}{I_\theta + \delta I_\theta})^{0.5} \qquad .....(6.31)$$

where δI_θ represents added moment of inertia in roll about an axis through the body CG. A rough estimate of $\delta I_\theta/\rho S_A B^2 = 0.025$ from the experimental results of Vugts (1969) yields

$$\frac{\omega}{\omega_n^r} = 1.4 \qquad .....(6.32)$$

for this example.

The time histories for the sway and heave forces and roll motions are shown in Figures 6.11 (a) - (c) for $L_1^* = 2.0\lambda$ and 3.0λ. $L_2^* = 2\lambda$ in both computations. Although a steady state behaviour is established in the sway and heave force results in the interval T_1 to T_2, the roll motion history shows a somewhat different behaviour. The body apparently developed a list due to the influence of the oncoming waves from one side. Also the time histories for $L_1^* = 2\lambda$ and 3λ show some differences in the roll behaviour, although the qualitative behaviour is quite similar. Since this motion does not display a steady state behaviour, it is not clear whether the results shown are effects of transients or result from numerical inaccuracies. In both cases, however, the roll displacements are very small ($|\theta| < 2.5$ deg.). Considering (6.32), small roll motions are to be expected. The force histories indicate the associated non-linearities of the system. For example, the sway force history displays broader peaks and narrower troughs compared to linear theory predictions (which would be sinusoidal).

Example : 2

This example corresponds to the example for heave resonance of the rectangular body shown earlier (see (6.28) for the relevant parameters). The roll inertia of the body is $I_\theta/\rho S_A B^2 = 0.10$ and $GM = B/24$. These yield an estimated roll natural period of $\omega/\omega_n^r = 1.25$ (using a value of $\delta I_\theta/\rho S_A B^2 = 0.020$ from Vugts 1969). Results are presented in Figures 6.12 (a) - (c) for $L_1^* = 3.0\lambda, L_2^* = 2.0\lambda$. A steady state behaviour in the force histories in the interval of T_1 to T_2 is apparent. The roll displacements here are comparatively larger than those in

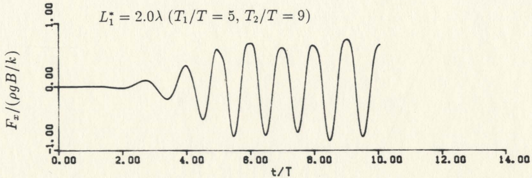

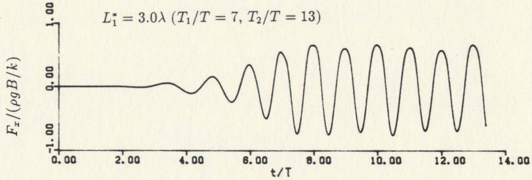

(a) Sway force

Figure 6.11 continued ⇓

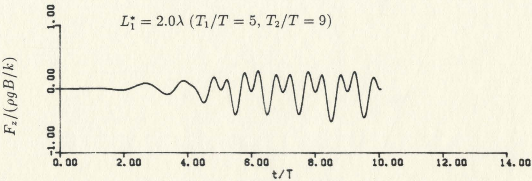

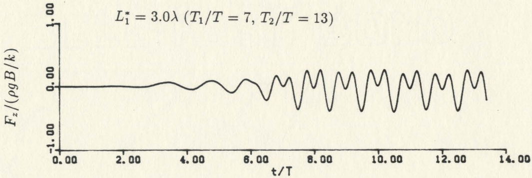

(b) Heave force

Figure 6.11 continued ⇓

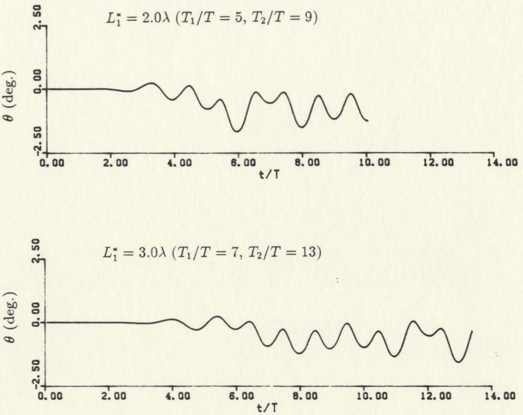

(c) Roll motion

Figure 6.11 Forces and roll motion of a rectangular body of $h/B = 0.5$; the body is free to roll only; $\lambda/B = 2$, $d/\lambda = 0.5$ and $H/\lambda = 0.05$.

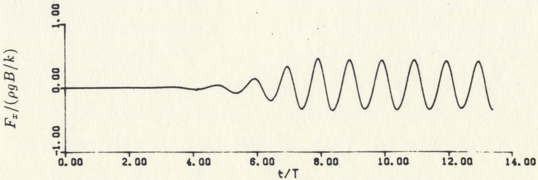

(a) Sway force

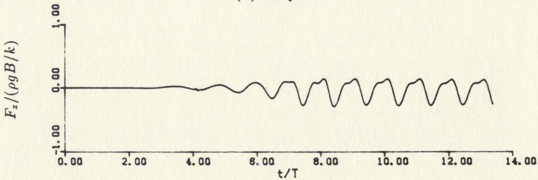

(b) Heave force

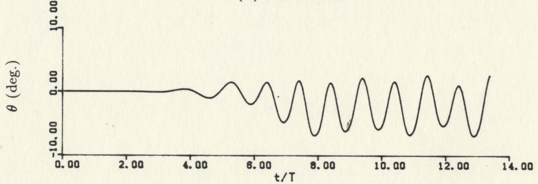

(c) Roll motion

Figure 6.12 Forces and roll motion of a rectangular body of $h/B = 0.5$; the body is free to roll only; $\lambda/B = 6$, $d/\lambda = 0.5$ and $H/\lambda = 0.05$, $L_1^* = 3.0\lambda$, $T_1 = 7T$ and $T_2 = 13T$.

the preceding example. This is to be expected from consideration of the ω/ω_n^r values (which is comparatively closer to unity in this example). Once again the body tends to develop a steady list. The time history of roll shows a close to steady state behaviour, although some modulations are still noticeable. It is not clear whether the simulated roll motions are due to numerical error or are the correct prediction of the body's behaviour. The time histories of forces in both these examples however tend to indicate that the non-steady state simulated histories of roll are perhaps not attributable to numerical errors, since the effect of numerical errors is expected show up in the force histories due to the coupled nature of the problem.

Comparing the force histories with those of Example 1 shown in Figures 6.11 (a) and (b), (note that in both cases the nominal oncoming wave steepness is $H/\lambda = 0.05$), it is evident that a reduction of the excitation frequency (or equivalently, an increase of the oncoming wave length) results in a reduction of the forces (in their non-dimensional forms). The ratio of maximum forces (i.e. $|F_x|, |F_z|$) in these examples is of the order of 2 for both sway and heave. A reduction in the associated non-linear features in the force histories is also apparent.

For both of the above examples, attempts to simulate roll by selecting a combination of I_θ and GM which yields $\omega/\omega_n^r \approx 1$ failed. The problem is associated with not allowing the body to heave simultaneously, which results in occurrence of flooding and consequent failure of the numerical scheme. Results for combined roll and heave will appear latter.

Example : 3

Here the rectangular body has a draft of $h/B = 1$, the excitation frequency corresponds to $\omega\sqrt{B/2g} = 0.723$ (same as in example 2 above) and the body has an inertia of $I_\theta/\rho S_A B^2 = 0.10$. The roll motions for six values of GM/B = 0.00825, 0.03325, 0.05825, 0.08325, 0.10825 and 0.13325 are shown in Figure 6.13 (a) - (f). The body is located at $L_1^* = 2.5\lambda$ and the downstream boundary is at $L_2^* = 2.0\lambda$.

In the first plot corresponding to a very small GM value ($GM = 0.00825B$), the body develops roll in one direction only which grows rapidly until the time the results are shown. After this time the solution breaks down due to flooding and consequent difficulty in locating the body-free surface intersection points. From the trend of the rolling behaviour, it would appear that the body eventually capsizes. Considering the associated small magnitude of the restoring force, this does not seem unlikely.

The increase of restoring forces on roll can be studied from these plots. For smaller restoring forces, the body tends to develop a list and rolls more towards the windward side. In the last two plots, with relatively larger GM, this trend is found to be reversed. The body begins to roll more evenly. An increase in the positive amplitudes compared to negative amplitudes can also be observed, showing that the body now rolls more towards the side of the oncoming wave. Increases of restoring forces are found to result in larger roll amplitudes. For the largest value of GM studied here, the roll amplitudes steadily grow and the solution breaks down after the time upto which the results are shown due to difficulties in locating the body-free surface intersection points by extrapolation. Since the value of ω/ω_n^r is associated with δI_θ which is not readily available for the chosen h/B value, it is not possible to relate the natural roll period with

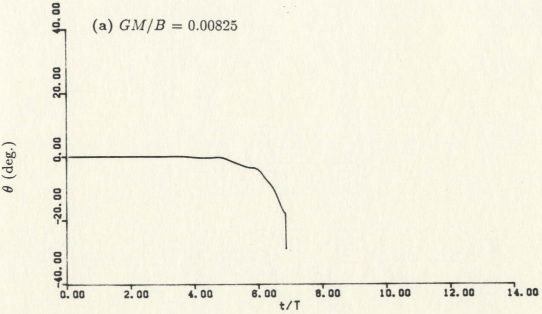

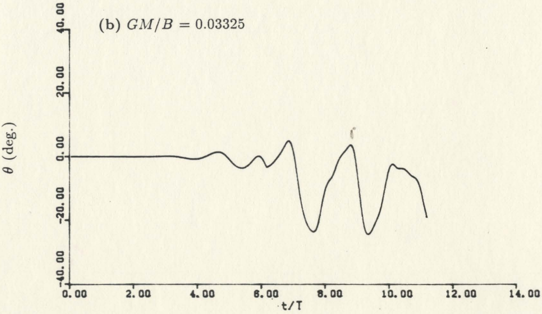

Figure 6.13 continued ⇓

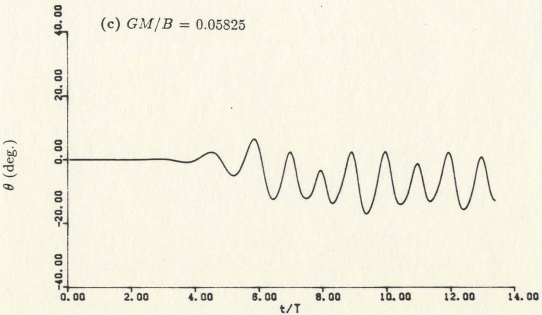

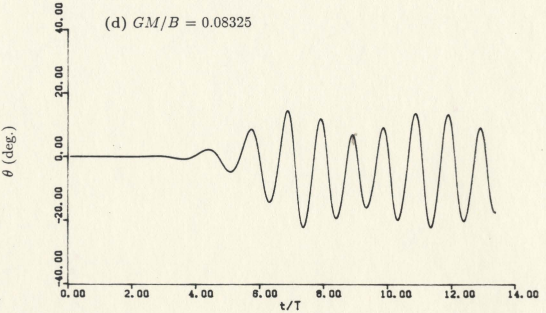

Figure 6.13 continued ⇓

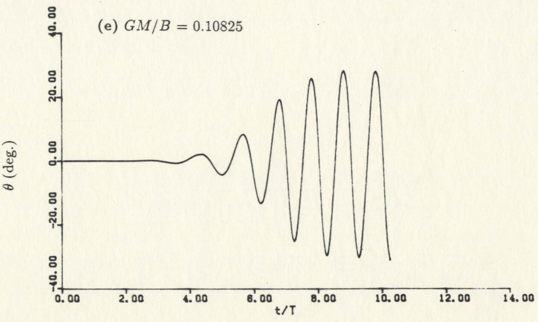

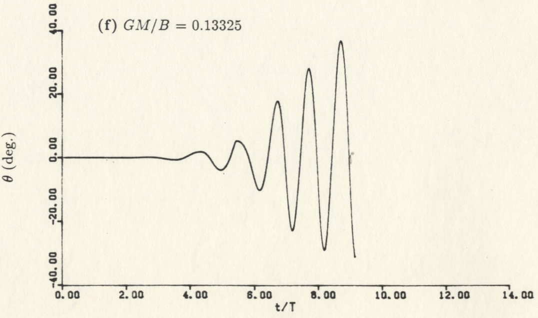

Figure 6.13 Roll motion of a rectangular body of $h/B = 1.0$ for various values of GM; $\lambda/B = 6$, $d/\lambda = 0.5$ and $H/\lambda = 0.05$; computations are for a domain of $L_1^* = 2.5\lambda$ and $L_2^* = 2.0\lambda$; $T_1 = 6\,T$, $T_2 = 11\,T$.

GM. It is however possible to determine the combinations of δI_θ and GM, shown below, which yields $\omega/\omega_n^r = 1$:

$\delta I_\theta/\rho S_A B^2$:	0.025	0.050	0.075	0.100	0.125	0.150
GM/B :	.0654	.0785	.0915	0.105	0.118	0.131

The plots shown suggest the roll resonance to be associated with a value of GM/B between 0.10 and 0.13, which, from the table above, suggests a value of $\delta I_\theta/\rho S_A B^2$ between 0.10 and 0.15. From a study of Vugts' experimental δI_θ values for lower h/B ratios, this range of δI_θ for the present h/B value appears to be a realistic estimate . Large roll motions of the body for the last two GM values are then expected responses.

6.3.4 Combined Heave and Roll

Here the combined heave and roll motions are simulated. The body is fixed in the sway mode.

Example : 1

The relevant parameters for this example are

$$
\begin{aligned}
h/B &: 0.5 \\
\lambda &: 6B \\
d/\lambda &: 0.5 \\
H/\lambda &: 0.05 \\
\omega\sqrt{B/2g} &: 0.723
\end{aligned}
\qquad .....(6.33)
$$

$$z_G(0)/B \ : \ -1/8$$

$$GM \ : \ B/24$$

$$I_\theta/\rho S_A B^2 \ : \ 0.10$$

Results for this case when the body was free to either heave or roll have already been presented. The excitation frequency here is very close to the heave natural frequency such that large heave motions can be anticipated. Results are shown in Figures 6.14 (a) - (d) for $L_1^* = 3.0\lambda, L_2^* = 2.0\lambda$. For comparison, results from the earlier run when the body was fixed in roll and sway mode but free to heave are also plotted. As can be observed, sway force and heave motion appear to be uninfluenced by roll motion. On the other hand, the roll moment histories show noticeable differences. The influence of heave on roll can be studied by comparing Figure 6.12 (c) with Figure 6.14 (d) (for these two results, all parameters are same except that for the result in Figure 6.12 (c), the body was allowed to roll only). Besides a qualitative change in the roll history, the amplitudes are considerably higher in the present simulation compared to when the body was constrained from heaving. These results suggest that heave motions are rather insensitive to roll motions while the reverse is not true.

Example : 2

This example has the following parameters:

$$h/B \ : \ 0.5$$

$$\lambda \ : \ 8B$$

$$d/\lambda \ : \ 0.5$$

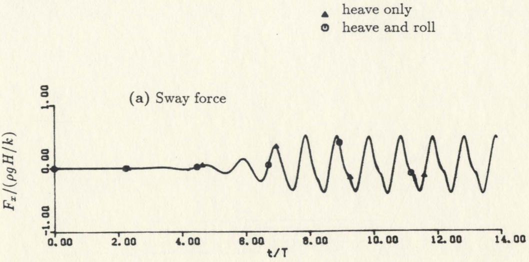

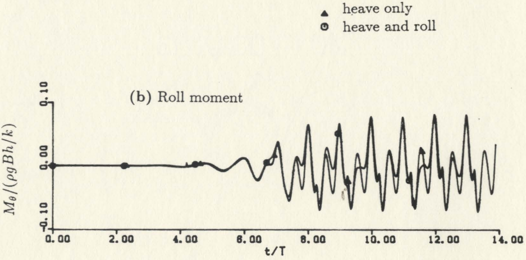

Figure 6.14 continued ⇓

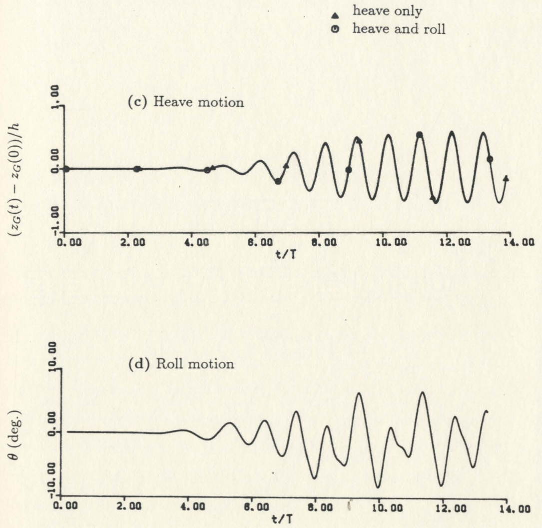

Figure 6.14 Force, moment and motions of a rectangular floating body of $h/B = 0.5$; the body is free to roll and heave; for the plots (a) - (c), results when the body is free to heave only (cf. Figure 6.8) are also plotted; $\lambda/B = 6$, $d/\lambda = 0.5$ and $H/\lambda = 0.05$; computational domain is, $L_1^* = 3\lambda$ and $L_2^* = 2.0\lambda$; $T_1 = 7\,T$, $T_2 = 13\,T$.

$$\begin{aligned} H/\lambda &: 0.04 \\ \omega\sqrt{B/2g} &: 0.627 \\ z_G(0)/B &: -1/8 \\ GM &: B/24 \\ I_\theta/\rho S_A B^2 &: 0.050 \end{aligned} \qquad .....(6.34)$$

A rough estimate of $\delta I_\theta/\rho S_A B^2 = 0.025$ from Vugts (1969) yields $\omega/\omega_n^r = 0.967$. Therefore, large roll motions can be anticipated.

Figures 6.15 (a) and (b) show the heave and roll displacements respectively for a domain of L_1 and $L_2 = 2.5\lambda$. These results are achieved by using $\Delta x/\lambda = 1/40$ and $\Delta t/T = 1/100$ (compared to $\Delta x/\lambda$ of 1/24 to 1/30 and $\Delta t/T$ of 1/48 to 1/60 used in all the preceding examples). The relatively finer discretization is found necessary for an adequate description of the body. In this regard, the requirement of keeping Δx comparable over all parts of the boundary, which follows from the necessity of keeping the adjacent segments at the intersections of the boundaries comparable in length (see §4.3.3) increases the computational burden considerably for smaller excitation frequencies (the operation count per time step roughly varies with $(\lambda/B)^3$).

Large roll amplitudes in the order of 50 deg. are evident in Figure 6.15 (b). It can be seen that the body tends to roll more towards the upstream side of the oncoming wave, similar to the roll results obtained earlier for larger GM values (cf. Figures 6.13 (e) and (f)). The body also undergoes considerable heave motion. The heave displacements are comparable to its resonant behaviour in that mode (cf. Figure 6.8 (c)), although in the present example, $\omega/\omega_n^h \approx 0.89$ (using $a_{22}/M_B = 1$ from Vugts 1969). Plots displaying the instantaneous position

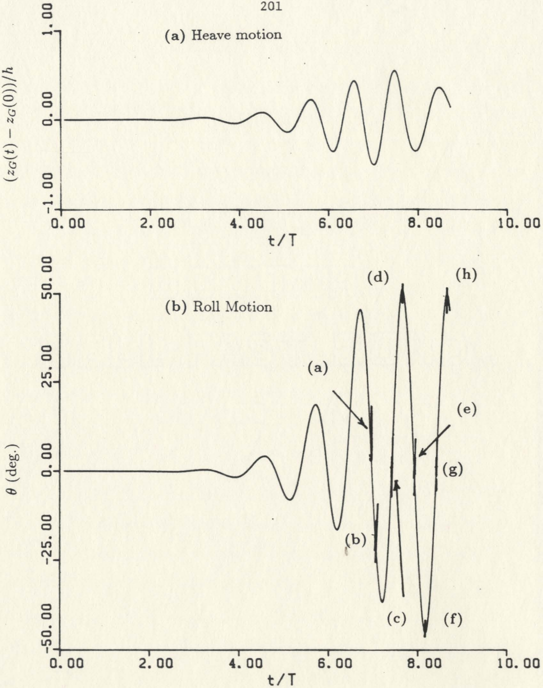

Figure 6.15 Heave and roll motions of a rectangular floating body of $h/B = 0.5$; the body is free to roll and heave; $\lambda/B = 8$, $d/\lambda = 0.5$ and $H/\lambda = 0.04$; $L_1 = 2.5\lambda$, $L_2 = 2.5\lambda$, $\Delta x_F/\lambda = 1/40$, $\Delta t/T = 1/100$; body is in (or very close to) roll resonance.

of the body with respect to the free surface for several time instants quarter of a period apart are shown in Figure 6.16. The capability of the method in simulating large motions is illustrated in Figure 6.17 where we show the evolution of the body and free surface motions over one cycle of roll oscillation at closely spaced time intervals. Although the free surface profiles in the vicinity of the body show some irregularities, inspection reveals that the body is rolling with the wave, which is typical rolling behaviours of vessels with relatively large roll stability in long waves (see e.g. Lewis 1977).

6.3.5 Motions of a Completely Unrestrained Body

Finally results are presented to demonstrate the capability of the method to simulate the motions of a completely unrestrained body.

Example : 1

In the first example, the parameters are same as in the example 1 of §6.3.1 (see (6.27) for the relevant values). This example is chosen since from earlier results we know that sway forces are expected to be large. Consequently, it is of some interest to study the resulting sway motions.

Figures 6.18 (a) - (c) show the evolution of the forces and moment in time while Figures 6.19 (a) - (c) show the time histories of the three modes of displacements. The time history of sway displacement clearly displays an oscillatory drifting pattern. Within the time of $6 \leq t/T \leq 10$, the body has drifted by a distance of over $0.25B$ ($\approx 0.06\lambda$). The heave and roll motions are very small which is to be expected considering that the excitation frequency is much higher

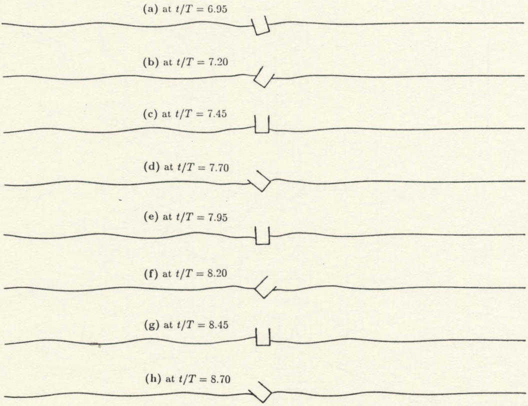

Figure 6.16 Plot of the instantaneous location of the body and free surface at several time instants at intervals of quarter of a period (the time instants correspond to the marks (a) - (h) in Figure 6.15 above)

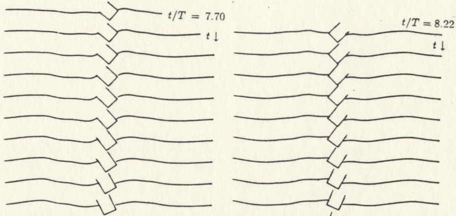

Figure 6.17 Plots displaying the instantaneous location of the body and a portion of the free surface over one complete period of oscillation at intervals of 2 time steps; the time interval corresponds to the period $7.70 \leq t/T \leq 8.70$ (i.e. (d) - (h) in Figure 6.15).

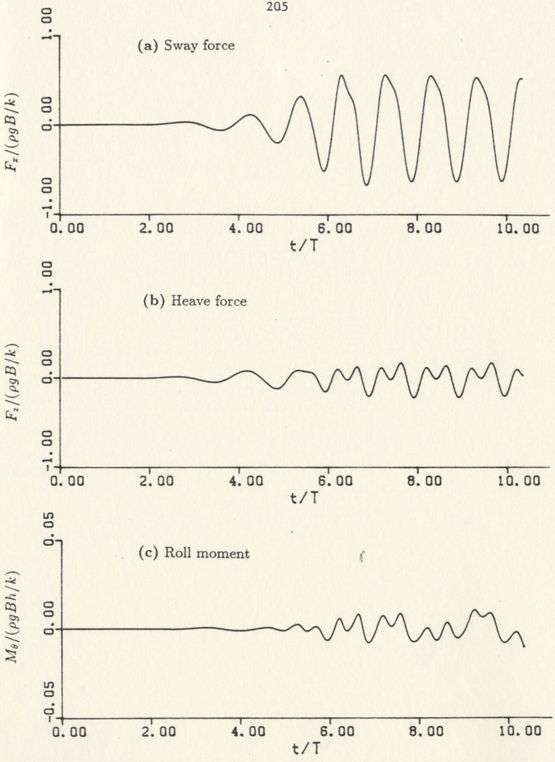

Figure 6.18 Forces and moment on a rectangular body of $h/B = 0.5$; the body is completely unrestrained; $\lambda/B = 2$, $d/\lambda = 0.5$ and $H/\lambda = 0.075$; $L_1^* = 2.5\lambda$, $L_2^* = 2.0\lambda$, $T_1 = 6\,T$ and $T_2 = 11\,T$.

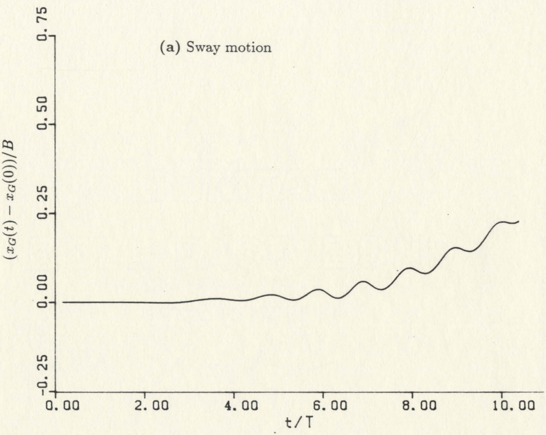

Figure 6.19 continued ⇓

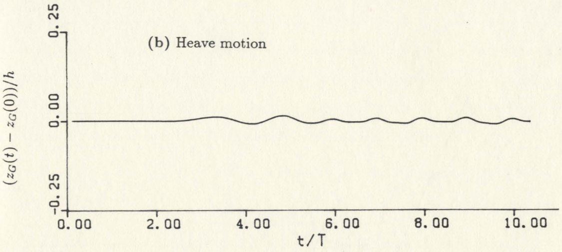

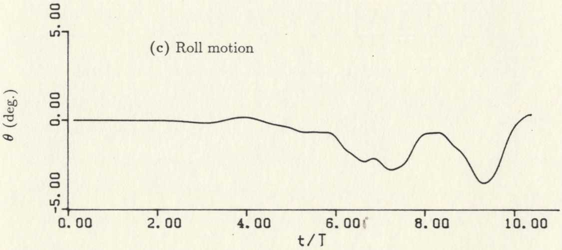

Figure 6.19 Motions of the body corresponding to Figure 6.18 above.

than the natural frequencies. Comparing the sway forces with those for the fixed body results (Figure 6.5 (b)), it is seen that although the magnitudes are almost same (the peak-to-peak values are within 5 %), the associated non-linear features displayed by the double peaks show a qualitative difference. Heave forces are found to be considerably reduced when the body is drifting.

Example : 2

This example corresponds to the example 1 of §6.3.4 where results have been presented for combined heave and roll motions of the body. The time histories for all three modes of displacements are plotted in Figures 6.20 (a) - (c). The drifting of the body is evident in Figure 6.20 (a). Between the time interval of $t/T = 6$ to 10, the body has drifted more than its width. Comparison with the earlier example reveals an increase of the average drift speed in longer waves. This feature is qualitatively similar to the experimental results of Harns (1987) on drift of two-dimensional ice-floe models. A comparison of Figure 6.20 (b) with Figure 6.14 (c) (which shows the corresponding heave displacements for the body when it is fixed in sway) reveals that the influence of sway on heave is negligible. On the other hand, considerable influence of sway on roll can be observed. The present results also show a delay in the initiation of the roll motion, which is believed to be due to drifting.

6.4 Summarizing Remarks

The results presented above demonstrate that it is possible to simulate large motions of floating bodies in steep waves by imposing an excitation potential

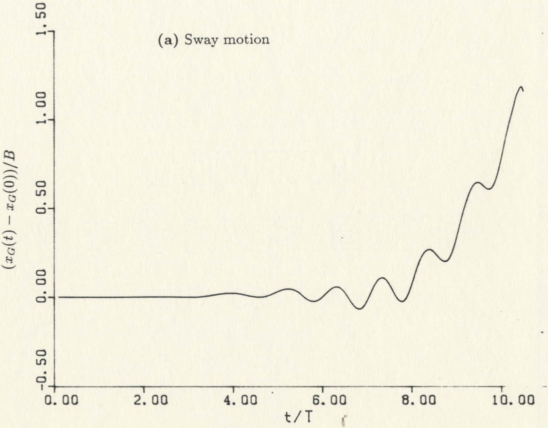

Figure 6.20 continued ⇓

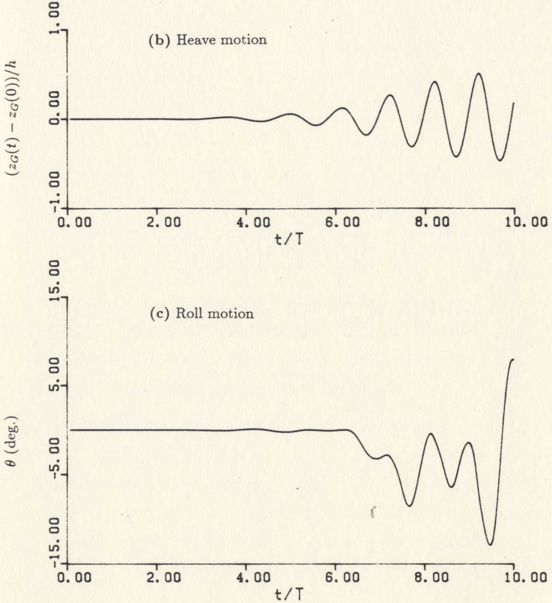

Figure 6.20 Motions of a completely unrestrained rectangular floating body of $h/B = 0.5$; $\lambda/B = 6$, $d/\lambda = 0.5$, $H/\lambda = 0.05$, $L_1^* = 2.5\lambda$, $L_2^* = 2.0\lambda$, $T_1 = 6\,T$ and $T_2 = 11\,T$.

and subsequently following the evolution of the body configuration. It has also been shown that a non-linear steady state solution can be approached in this manner. Results have been presented simulating large heave and roll motions. Also accomplished are sway motions featuring drifting of a body.

The insensitivity of the solution with regard to the size of the control (computational) domain has been demonstrated. Depending on the length of the interior domain, realistic simulations for relatively long time, typically a steady state behaviour of the solution over several periods, can be accomplished.

Several complications that arise from the coupled nature of the problem have been elucidated and appropriate techniques have been developed for their treatment. The method can be explored for other applications such as forced oscillations and free motions without anticipating difficulties. Applications to this latter problem will appear in a later section (§8.3.2).

The major problem presently associated with the method lies in the treatment of the body and free surface intersection points. Although no problems were encountered in the earlier application of wave interactions with vertical walls (§5), some problems are encountered when the body undergoes large roll motions. Further remarks on this will be made in the concluding section (§9.3).

7 The Experimental Program

7.1 General

7.1.1 Introductory Notes

Although the results of the preceding section (§6) have shown that it is possible to simulate large motions of two-dimensional floating bodies and to approach a fully non-linear steady state solution, the validity of the method remains subject to question. This section describes an experimental program which was undertaken to validate the presented numerical model. This was considered necessary due to inadequacy of published analytical, numerical or experimental results on analogous two-dimensional problems of motions of floating bodies in non-linear waves. As revealed in §1, the study considered is still unfolding in literature and consequently experimental results with which the present numerical simulation results can be compared are relatively scarce.

One of the earliest experimental studies on two-dimensional bodies was the small amplitude forced oscillation tests carried out by Vugts (1969) which provided important data on hydrodynamic coefficients for several cross-sectional geometries. Among the more recent experimental studies on similar problems, mention may be made of the following. Experiments on large amplitude forced heave oscillations of two-dimensional section shapes were conducted by Yamashita (1977) and Tasai and Koterayama (1976). In the experiment of Adachi and Ohmatsu (1980), the body was subjected to a transient wave excitation and the subsequent decaying motion was recorded. These authors have also conducted some small amplitude forced heave and sway experiments. The

'Salter's duck' experiment by Greenhow et al. (1982) focussed on capsizing of the body due to the passage of a single steep wave. Here the body was restricted from sway and heave and the objective was to essentially compare the still photograhic images of the experiment with that of the numerical simulation model. Comparisons have also been made for horizontal and vertical forces and the agreement obtained was considered to be quite good by the authors. Notwithstanding the highly transient and non-linear nature of the experiment, an idea of the good quality of agreement between the experimental and computed data, according to the authors, can be formed by examining Figure 7.1 where the authors' results are reproduced. A more recent contribution based on an analogous experimental study was reported in Miyata et al. (1986). Here the forces on submerged objects due to passage of steep breaking waves were determined. The agreement between experiment and numerical solution obtained by means of a finite-difference formulation was not very satisfactory (according to the authors), specially in horizontal forces.

Although experiments on large amplitude forced oscillations (i.e. the radiation problem) and wave forces on fixed bodies (i.e. the diffraction problem) provide important data for comparative purposes, to the author's knowledge, no systematic two-dimensional experimental data are readily available in open literature in which a floating body is subjected to an incident wave train such that the motions and waves contain significant 'non-linear' characteristics. The only exception appears to be the experiment by Kyozuka (1982), who conducted a similar experiment by subjecting a Lewis-form body to oncoming waves, and presented his results in the frequency domain. While experiments to determine motions of three-dimensional bodies in regular waves are routinely performed by

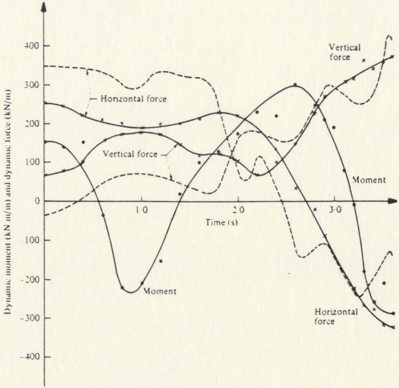

Figure 7.1 Computational and experimental forces and moment on 'Salter's Duck', as obtained by Greenhow et al. (1982); full line = computations, broken line = experiment (reproduced with permission).

various hydrodynamic laboratories, the two-dimensional counterparts of similar experiments are relatively rare due to their limited scope for direct application to the industrial sector. Such two-dimensional experiments are generally most suited for the purpose of comparison with analytical or numerical prediction models. Therefore it was felt that an appropriate two-dimensional experiment would not only produce valuable data for comparison with the present numerical model, but also serve as a reference for future works on similar numerical or analytical studies.

7.1.2 Objective

As indicated earlier, the objective of the experimental program is to asses the validity of the numerical method developed. Concern here is on accurate measurement of the responses of the body, both motions and forces, by subjecting it to an oncoming regular wave train of known characteristics. Considering the three permissible degrees of freedom, experimental investigations are possible, at least in principle, for a number of combinations of the forces and motions. A partial list of the possible combinations are shown in Table 7.1. Amongst these, the situation where the body is completely free to float was considered not to be favourable for experimental purposes, since it was felt that it would be difficult to prevent the body from undergoing some motions in the transverse plane (yaw and pitch). Additionally, a dynamometer was available which permitted measurement of forces in longitudinal direction while allowing the body to heave and roll. This lead to the choice of experiments in which the body is restricted from swaying. In addition, by appropriate modification of the mounting arrangement, it was possible to restrain the body from rolling. It was therefore decided to

Table 7.1 Some possible experimental arrangements; '$\times$' and '$\surd$' indicate respectively that the body is restrained from and free in particular modes of motions.

Serial No.	Degrees of Freedom			Measurements					
	Sway	Heave	Roll	Forces/Moment			Displacements		
				Sway	Heave	Roll	Sway	Heave	Roll
1	$\surd$	$\surd$	$\surd$				$\surd$	$\surd$	$\surd$
2	$\times$	$\surd$	$\surd$	$\surd$				$\surd$	$\surd$
3	$\times$	$\times$	$\surd$	$\surd$	$\surd$				$\surd$
4	$\times$	$\surd$	$\times$	$\surd$		$\surd$		$\surd$	
5	$\times$	$\times$	$\times$	$\surd$	$\surd$	$\surd$			

carry out the experiments for which heave only and heave and roll motions were permitted.

The conducted experiments conform to items 2 and 4 in Table 7.1 while items 1, 3 and 5 were omitted from further consideration due to difficulties in the measurements and/or the required modifications of the mounting arrangement (it is to be noted that the roll moment for item 4 could also not be measured due to lack of appropriate instrumentation). These two controlled test environments are believed to be adequate for the present purpose of comparison.

7.2 Design and Dimensions

The experiments were performed in the Memorial University wave tank. This tank has interior dimensions of 54.74 m. $\times$ 4.8 m. $\times$ 3.04 m. A piston type wave maker driven by an electro-mechanical servo mechanism generates waves at one end of the tank and a parabolic beach acts as an energy absorbing device (for more details on the tank, see Muggeridge and Murray 1981). The body chosen for testing is of rectangular cross section. The dimensions of the body were arrived at from the following considerations:

- The dynamometer poses an upper limit on the size of the body. Denoting B and L_B as the width and length of the body respectively, these dimensions must be such that the maximum anticipated force exerted on the body is within the capacity of the dynamometer.

- B should be preferably chosen such that the range of λ/B for which experiments can be performed is as wide as possible, preferably spanning from about 1 to 10 (corresponding to the non-dimensional frequency parameter

$B\omega\sqrt{B/2g}$ ranging from about 0.55 to 1.75). Since the wave maker has an upper limit of frequency (equivalently a lower limit of λ), this puts a constraint on the minimum possible value of B.

- To retain two-dimensionality of the phenomenon and to minimize possible end effects, L_B/B should be kept as large as possible.

- Larger models are expected to be proportionately less influenced by viscosity, consequently providing better data for comparison with the potential flow model. This suggests a larger model, i.e. a larger value of B.

From these considerations, the dimensions of the body were selected as 40 cm. $\times$ 40 cm. in cross section and 120. cm in length. To avoid sharp corners and to minimize resulting flow separations, a bilge radius of 2.5 cm. was provided. The body had a draft of 20 cm., which provided a relatively large freeboard of 20 cm. This was felt necessary to avoid flooding since from earlier computational experience, large run-ups on the lee side of the body were anticipated. The length chosen corresponded to $L_B/B = 3$ which was hoped to be adequate for simulating two-dimensional flow conditions. Indeed, no rigid rules are available in selecting this value of L_B/B and we have used guidance from previous analogous two-dimensional experiments where the following values were used:

		L_B/B
Adachi and Ohmatsu (1980)	:	6 to 8
Greenhow et al. (1982)	:	≈ 1.7
Kyozuka (1982)	:	1.4 to 3
Miyata et al. (1986)	:	1 to 1.5

The body was constructed from 1/4 inch aluminium plate with appropriate interior connections for mounting the dynamometer and to provide necessary ballast weights. The model was extremely rigid and no extra stiffening was required to retain its shape. Figure 7.2 provides an illustration of the body.

To achieve two-dimensionality of the flow, a channel within the wave tank was constructed by erecting vertical walls. The channel length was 6.1 m. (20 ft.). As with the L_B/B ratio, no rigid rules were available to establish the length (L_C) of the channel. It was felt that 6.1 m. was sufficient to generate a two-dimensional flow conditions near the test section. The present L_C/B value of 5.1 can however be compared with the corresponding value of approximately 4.5 in the experiment of Miyata et al. (1986) in which a similar channel was constructed.

The vertical walls were spaced such that the body occupied the entire width of the channel except for a small clearance in the order of few millimeters (typically 2 to 4 mm.). Each side of the channel consisted of two 8 ft. $\times$ 4 ft. plywood of 3/4 inch thickness with a central part made of a 4 ft. $\times$ 4 ft. $\times$ 1/2 inch plexiglass piece. This arrangement for the central part was introduced to maintain a smooth surface at the test section as well as to facilitate viewing from the sides. The walls were firmly attached to the bottom of the tank by means of bolts. Eight threaded rods connecting the side of the tank and the top of the walls provided additional supports. These threaded rods also allowed minor adjustments in the width of the channel such that a small gap between the body and the channel could be maintained. Figure 7.3 shows an illustration of the channel.

The dynamometer allows measurement of roll displacements upto a maximum of ± 30 deg. However, a direct connection of the dynamometer with the

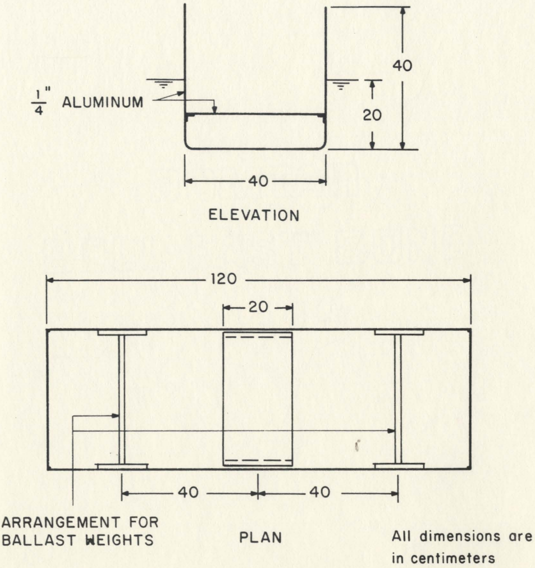

Figure 7.2 The model.

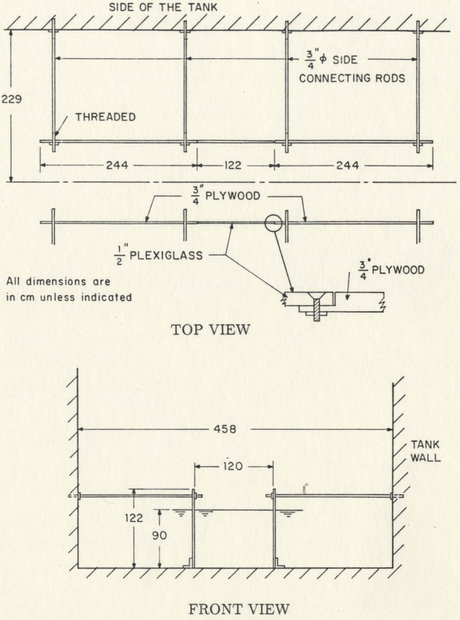

Figure 7.3 The channel.

body restricts the maximum roll displacement of the body to about ± 20 deg., due to the width of the heave-bar (the vertical movable part of the dynamometer, see Figure 7.4). In order that the body is free to roll upto ± 30 deg., an attachment rod was constructed to connect the body with the dynamometer. This arrangement was necessary also from a consideration of the main dimensions of the set-up (water depth and height of the carriage) which did not permit a direct attachment of the dynamometer with the body. The rod was constructed from a 2 inch $\times$ 2 inch steel beam of 1/4 inch wall thickness and was extremely rigid. The connections of this rod with the body and the dynamometer were also very firm. This attachment was made with the option that the body could be restrained from roll when desired by attaching it directly to the body without that part of the dynamometer which allows roll. Figure 7.4 illustrates details of the above arrangement.

7.3 Description

7.3.1 Model Characteristics

The desired weight of the model was achieved by adding appropriate ballast weights (lead), and was verified by weighing the model on a standard balance. To determine and adjust the location of the center of gravity (CG), an inclining test was performed in which heeling moments were applied by adding weights at marked locations and going through a standard sequence of operations (see Semyonov-Tyan-Shansky 1966). Inclinations were measured by a Sperry microlevel precision inclinometer (courtesy IMD, NRCC) with a resolution of 0.01 degrees. For the measured angles of the order of 4 deg., the error in KG (the

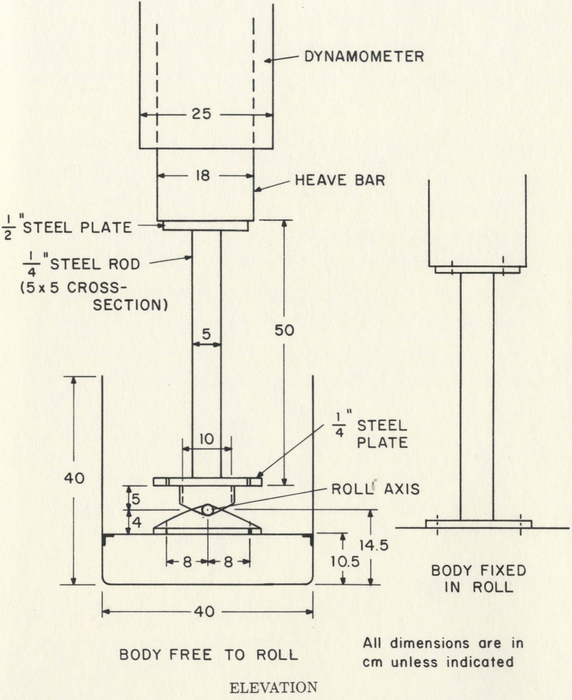

Figure 7.4 Dynamometer and body connections.

vertical distance of the CG measured from the keel) estimation translates to less than 0.5% . Indeed, successive inclining tests produced almost identical results, with KG values differing by less than 0.25%, and these values in turn agreed very well with the value calculated from independent measurement of the weights and locations of individual components.

The roll radii of gyration were calculated from weights and locations of individual components. In view of the agreement between measured and computed values of KG and weight, these computations are believed to be accurate within 1 to 2%, and experimental determination by means of the standard inclined table was not carried out. Experiments were performed for two different weight distributions which differed in radii of gyration of the model while KG remained unchanged. This was because the first arrangement when tested for natural roll period produced a value of 2.15 sec., which corresponded to a λ/B of about 18 to achieve roll resonance (λ here corresponds to the length of a deep water Airy wave of the same period). The second arrangement was to essentially reduce the roll natural period without changing any other parameter.

Table 7.2 summarizes the geometric characteristics of the body. Watertightness of the model was assured by leaving it afloat overnight.

7.3.2 Test Set-up, Instrumentation and Data Acquisition

The test section was located approximately 20 m. from the wave-board, which left a distance of about 30 m. from the beach. For the period for which test results were collected, these distances of the body from both ends of the tank were sufficient for reflected waves from either end not to interfere with the results.

Table 7.2 Geometric characteristics of the model

Geometry	:	rectangular (with rounded-off corners)
Length	:	120 cm.
Breadth	:	40 cm.
Depth	:	40 cm.
Draft	:	20 cm.
Bilge radius	:	2.5 cm.
Mass	:	96.3 kg.
GM (measured)	:	2.15 cm.
KG (from measurement)	:	14.5 cm.
...... (from calculation)	:	14.48 cm.
I_θ/L_B	:	167 kg. cm.^{2}/cm. (wt. dist. type I)
	:	107 kg. cm.^{2}/cm. (wt. dist. type II)
Natural period in heave	:	1.25 sec.
Natural period in roll	:	2.15 sec. (wt. dist. type I)
	:	1.82 sec. (wt. dist. type II)

Experiments were performed for a water depth of 0.9 m. (about 3 ft.), which provided a freeboard of about 0.3 m. ($\approx$ 1 ft.) on the vertical walls. For the range of wave heights for which experiments were conducted, this was sufficient to avoid spilling of water over the walls of the channel. The dynamometer was firmly mounted on the carriage (mass = 3.9 tons) and was attached to the body via the connecting rod.

The dynamometer used was a resistance type dynamometer, model R47 built by Kempf and Remmers, Hamburg. This instrument is originally intended for regular ship model towing tests, and is capable of measuring upto 200 KN of force in longitudinal direction. In addition, it allows vertical displacement (heave) of the model upto $\pm$20 cm. and angular displacement (roll or pitch) upto $\pm$30 deg. The body can be easily restricted from rolling by removing the part of the dynamometer which allows rotational modes of motion and attaching the connecting rod directly to the model, as illustrated in Figure 7.4. However, lack of appropriate instrumentation did not permit measurement of roll moment in this situation. A schematic view of the test arrangement is shown in Figure 7.5.

The wave field was monitored by means of standard resistor type twin wire wave probes. A total of 5 probes were used to measure wave heights. The collected data were therefore the wave heights, longitudinal force, roll and heave displacements. Data from all eight sources were collected in an eight channel HP 3968A instrumentation tape recorder capable of FM recording over a bandwidth of 0 to 5 Khz. and/or direct recording of signals upto 64 Khz. During testing, data were monitored by viewing the signals on a digital signal analyzer (model HP 5420). For final analysis, analog data from the FM recorder were digitized by means of a Keithley data acquisition instrument (system 570) at a sampling

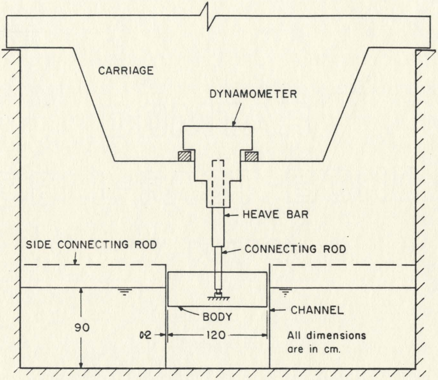

FRONT VIEW

Figure 7.5 A schematic view of the test arrangement.

rate of 40 hz. and transferred to the main frame VAX 8530/8800 computing systems for post processing. All subsequent processing and analyses were done on these systems.

Table 7.3 shows set-up voltages and the precision levels of the measuring units. The probes and the dynamometer were calibrated prior to, during, and at the end of the tests. For the range of values typical of the conducted tests, these precision levels result in less then 2% uncertainty in the measured quantities, e.g. typical values of sway force, heave and roll displacements of 10 kg., 10 cm. and 10 deg. result in uncertainties of 0.5%, 1% and 1% respectively.

Some views of the test arrangements and instrumentation are shown in Figures 7.6 - 7.8.

7.3.3 Test Sequences

Prior to the actual testing, a series of preliminary tests were performed in which waves over a range of frequencies and heights were generated and wave heights were measured at four locations along the centre line of the channel. The probe locations are shown in Figure 7.9. Probe no. 3 coincided with the location of the body. The purpose of these tests were to explore the range of frequency and heights for which acceptable quality of waves can be produced by the wavemaker. Additionally, these tests were intended to determine the effect of the channel on the generated waves and to serve as data when comparing with the numerical results. For each frequency, three wave heights were generated, ranging from very steep to modest steepnesses ($H/\lambda \approx 0.12$ to $H/\lambda \approx 0.03$). Indeed, these tests have shown that for higher frequencies and larger steepnesses, the

Table 7.3 Precision levels of the measuring devices

Dynamometer		
Measurement	Supply voltage	Precision level
Force	2.5 V	± 50 gm.
Heave	5 V	± 1 mm.
Roll	10 V	± 0.1 deg.
Wave probes	5 V	$\pm 2 \sim 3$ mm.

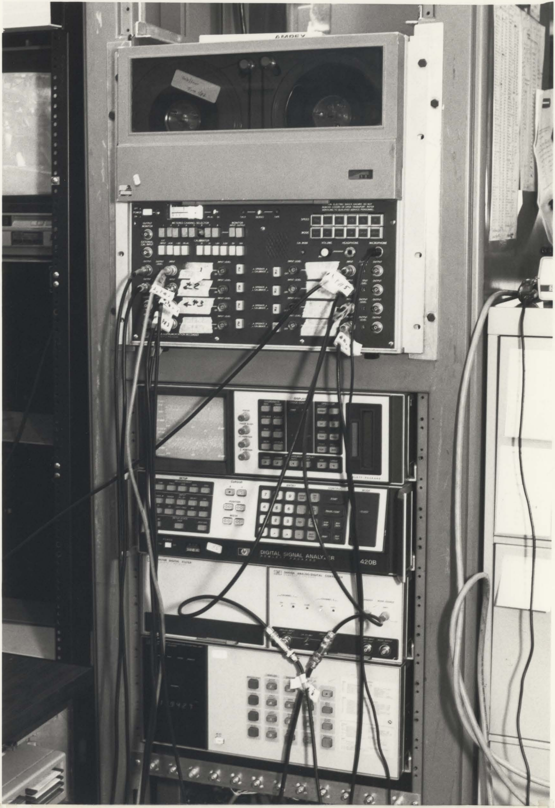

Figure 7.2 A view of the data acquisition

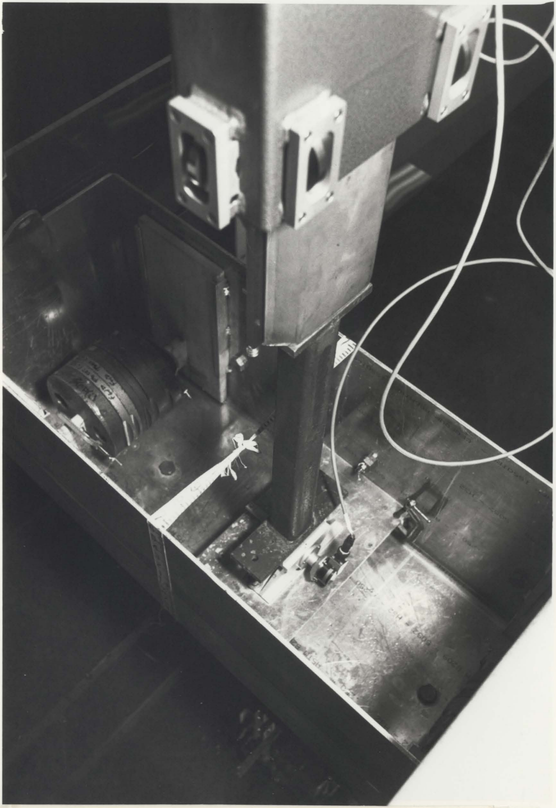

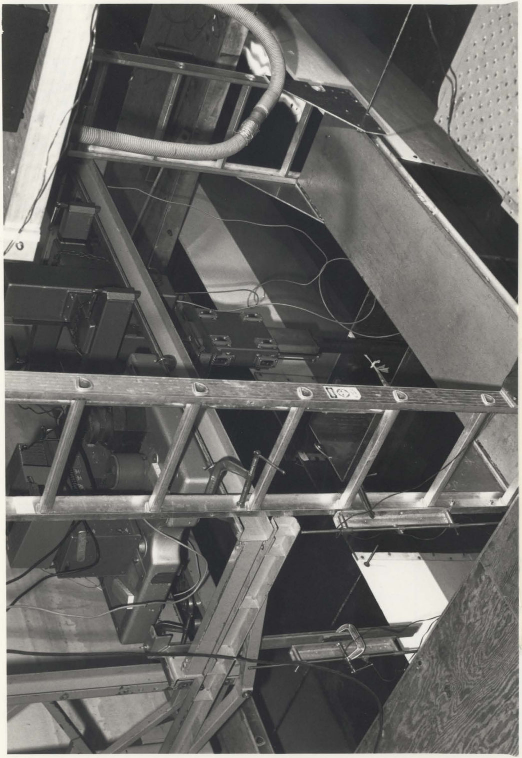

Figure 7.8 A view of the test set-up.

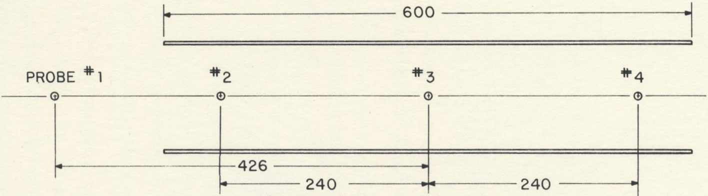

Figure 7.9 Wave probe locations for test series A.

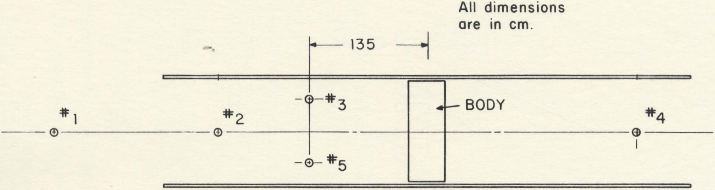

Figure 7.10 Wave probe locations for test series B, C and D.

waves produced were not capable of retaining their forms. Also, the combinations producing cross flows inside the channel and the tank were identified and omitted from subsequent tests. For convenience, these tests are termed as test series A.

The main tests consisted of a series of three tests, designated B, C and D respectively (see Table 7.4). The probe and body locations are shown in Figure 7.10 for these tests. Probe nos. 1, 2 and 4 were unaltered in location, while two probes (nos. 3 and 5) were placed abreast within the channel and close to the body, separated by a distance of about $0.6L_B$ (80 cm.). These two probes were intended to provide an indication of the quality of two-dimensionality of the near-field flow.

For test series B and C, the model was free to both roll and heave, while for test series D the model was free to heave but restrained from rolling. As mentioned earlier, due to lack of appropriate instrumentation, the roll moments were not measured in these tests. The model had a larger radius of gyration in B test series than the remaining series of tests (see Table 7.4). In most cases, the steepest wave generated in test series A could not be applied in the main series of the tests due to occurrence of flooding. Indeed, the run-ups were very high, and even for moderate steepnesses ($H/\lambda \approx 0.05$), waves close to the body displayed large steepnesses (in some situations close to breaking).

To complete the experiments, tests were also conducted with the model completely free to float (i.e. free in all modes of motion). For these tests no quantitative measurements were taken but the tests were video-taped for a qualitative analysis of the model behaviour. Also conducted were roll and heave transient

Table 7.4 Type of tests

Test series A	:	Measurement of wave heights without the presence of the body
Test series B	:	Experiment with the body, body free to roll and heave, weight distribution type I, $I_\theta/L_B = 167$ kg. cm.^{2}/cm.
Test series C	:	Experiment with the body, body free to roll and heave, weight distribution type II, $I_\theta/L_B = 107$ kg. cm.^{2}/cm.
Test series D	:	Experiment with the body, body free to heave only

tests, which were performed respectively by initially displacing the model in roll and heave and than releasing it.

In order to have some idea on the flow separation near the bilges, attempts were also made to visualize the flow field in the vicinity of these corners. This was done by introducing coloured dyes near the bilge for the test conditions for which the model displayed large motions. Unfortunately, due to difficulties in photographing, no conclusive data could be obtained from these tests.

Tables 7.5 (a) - (c) summarizes all tests conducted for which measurements were taken (excluding series A) together with comments as appropriate.

7.4 Experimental Results

For all tests, data were recorded for 32 secs. including the transient information. Additionally, with the exception of first few tests, all of the tests were video taped for future reference.

Except for the longitudinal force measurements, all other measurements (wave heights, heave and roll motions) were found to have insignificant amount of noise content, which was removed by a five point averaging technique. For the force measurement, however, the time record was found to contain a relatively large proportion of high frequency noises. This was probably caused by the absence of an analog filter while recording the data. These noises were subsequently removed by applying a digital filtering technique. The time record was first Fourier transformed to the frequency domain which was then digitally filtered by selecting a standardized window (signals of frequencies more than four times the excitation frequency were removed). Subsequently the smoothed

Table 7.5 (a) Series B experiments

No.	Frequency		H	λ	$\omega\sqrt{B/2g}$	H/λ	λ/B	Remarks†
	f	ω						
	(sec.$^{-1}$)	(rad./sec.)	(cm.)	(cm.)				
1	1.20	7.540	3.75	108	1.0771	0.0347	2.70	-
2	1.10	6.912	7.87	129	0.9874	0.0610	3.20	(a)
3	1.10	6.912	3.75	129	0.9874	0.0291	3.20	-
4	1.05	6.597	9.65	141	0.9425	0.0684	3.53	(b)
5	1.05	6.597	4.90	141	0.9425	0.0348	3.53	-
6	1.00	6.283	9.83	156	0.8976	0.0630	3.90	(a)
7	1.00	6.283	5.10	156	0.8976	0.0327	3.90	-
8	0.95	5.969	4.95	173	0.8527	0.0286	4.33	-
9	0.90	5.655	6.93	192	0.8078	0.0361	4.80	-
10	0.85	5.341	8.25	214	0.7630	0.0386	5.35	-

†<u>Remarks</u>

(a) : near-field waves close to breaking

(b) : near-field wave tips occasionally breaking; surf formation

Table 7.5 (b) Series C experiments

No.	Frequency f (sec.$^{-1}$)	Frequency ω (rad./sec.)	H (cm.)	λ (cm.)	$\omega\sqrt{B/2g}$	H/λ	λ/B	Remarks†
1	1.10	6.912	7.87	128	0.9874	0.0610	3.20	(a)
2	1.10	6.912	3.75	128	0.9874	0.0291	3.20	-
3	1.05	6.597	9.65	141	0.9425	0.0684	3.53	(a)
4	1.05	6.597	4.90	141	0.9425	0.0348	3.53	-
5	1.00	6.283	9.83	156	0.8976	0.0630	3.90	(a)
6	1.00	6.283	5.10	156	0.8976	0.0327	3.90	-
7	0.95	5.969	4.95	173	0.8527	0.0286	4.33	-
8	0.90	5.655	6.93	192	0.8078	0.0361	4.80	-
9	0.85	5.341	8.25	214	0.7630	0.0386	5.35	-
10	0.80	5.027	4.13	240	0.7181	0.0172	6.00	-
11	0.70	4.398	3.92	304	0.6283	0.0129	7.60	-
12	0.60	3.770	4.80	385	0.5386	0.0125	9.63	-
13	0.60	3.770	8.80	385	0.5386	0.0229	9.63	-
14	0.60	3.770	10.60	385	0.5386	0.0275	9.63	-

†Remarks

(a) : near-field waves close to breaking

Table 7.5 (c) Series D experiments

No.	Frequency f (sec.$^{-1}$)	Frequency ω (rad./sec.)	H (cm.)	λ (cm.)	$\omega\sqrt{B/2g}$	H/λ	λ/B	Remarks†
1	1.20	7.540	3.75	108	1.0771	0.0347	2.70	-
2	1.10	6.912	7.87	129	0.9874	0.0610	3.20	(b)
3	1.10	6.912	3.75	129	0.9874	0.0291	3.20	-
5	1.05	6.597	9.65	141	0.9425	0.0684	3.53	(b)
6	1.05	6.597	4.90	141	0.9425	0.0348	3.53	-
7	1.00	6.283	9.83	156	0.8976	0.0630	3.90	(a)
8	1.00	6.283	5.10	156	0.8976	0.0327	3.90	-
9	0.95	5.969	10.20	173	0.8527	0.0590	4.33	(a)
10	0.95	5.969	4.95	173	0.8527	0.0286	4.33	-
11	0.90	5.655	6.93	192	0.8078	0.0361	4.80	-
12	0.85	5.341	8.25	214	0.7630	0.0386	5.35	-
13	0.80	5.027	8.70	240	0.7181	0.0363	6.00	-
14	0.70	4.398	8.35	304	0.6283	0.0275	7.60	-
15	0.60	3.770	9.65	385	0.5386	0.0247	9.63	-

†Remarks

(a) : near-field waves close to breaking

(b) : near-field wave tips occasionally breaking; surf formation time records were retrieved by an inverse transform (this procedure did not alter the phase information of the signal).

To check the two-dimensionality of the flow, the records from the two probes placed abreast inside the channel (probe nos. 3 and 5, see Figure 7.10) can be compared. For most tests, the flow was found to possess an acceptable quality of two-dimensionality, particularly in the initial period of recording. For some tests, specially for the conditions of higher wave steepnesses, cross flows were found to develop inside the channel after some time. However, these did not affect the results, since such flows generally developed after the period upto which the data was collected for analysis. Typical sample records from these two probes are shown in Figure 7.11 (a) - (c) as an indication of two-dimensionality of the flow during the test period.

For lower values of λ/B (i.e. at higher frequencies), the model displayed negligible motions and acted very much like a floating breakwater (the lowest λ/B that could be achieved was about 2.7; the wave maker was not capable of producing waves of acceptable quality below this wave length). The waves transmitted to the other side of the body were negligible. As the frequencies approached heave natural period, the model began to display large heave motions. However, except close to the roll natural period, the model did not practically roll at any other frequencies (roll amplitudes were typically within 2 to 4 deg.).

A majority of the tests was conducted twice to verify repeatability of the tests. The results showed very good quality of repeatability. Most of the experimental results in conjunction with the corresponding results from the numerical model are presented in the following section. Here some sample results are in-

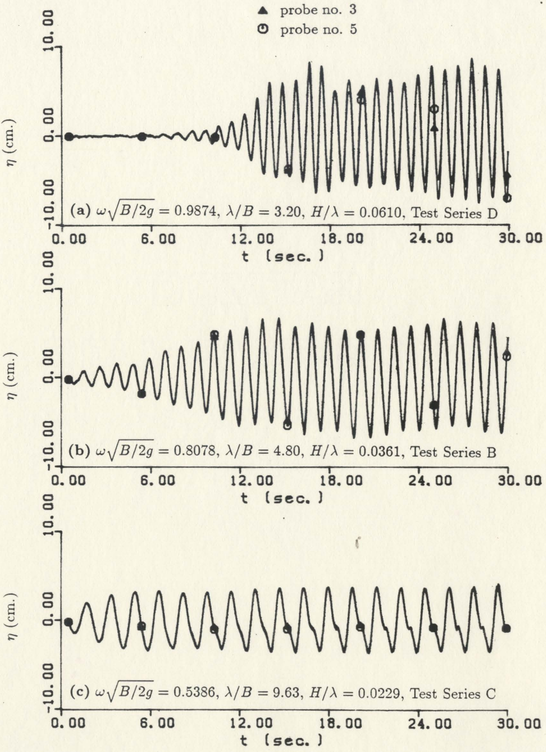

Figure 7.11 Time records for free surface elevations measured by probe no. 3 and probe no. 5 from the tests with the presence of the body.

cluded. Figures 7.12 (a) and (b) show sample results from test series A as a demonstration of the quality of the generated waves inside the channel, while Figures 7.13 (a) - (c) show sample results for the main series of tests demonstrating the quality of repeatability (note that the presented samples cover the range of tested frequencies).

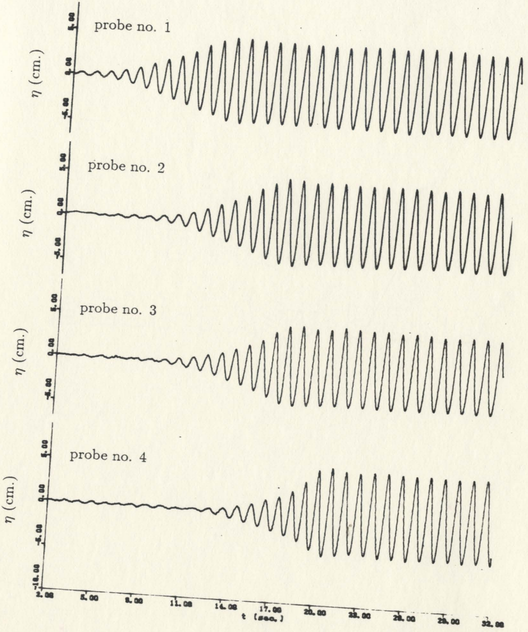

(a) $\omega\sqrt{B/2g} = 0.9425$, $\lambda/B = 3.53$, $H/\lambda = 0.0684$

Figure 7.12 continued ⇓

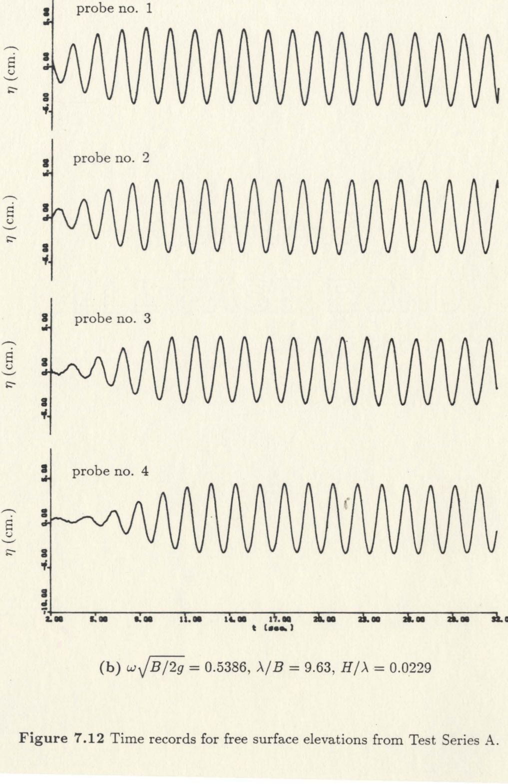

(b) $\omega\sqrt{B/2g} = 0.5386$, $\lambda/B = 9.63$, $H/\lambda = 0.0229$

Figure 7.12 Time records for free surface elevations from Test Series A.

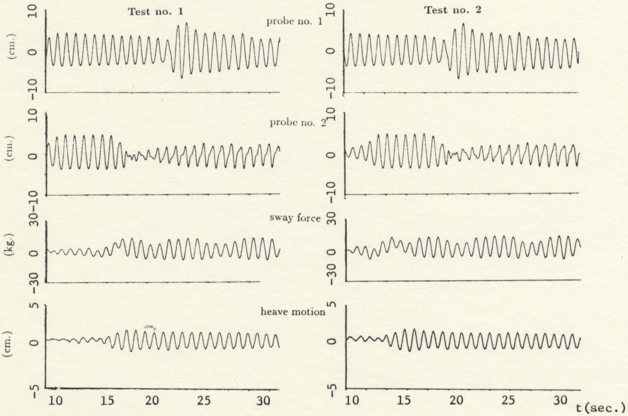

(a) $\omega\sqrt{B/2g} = 0.9874$, $\lambda/B = 3.20$, $H/\lambda = 0.0610$, Test Series D

Figure 7.13 continued ⇓

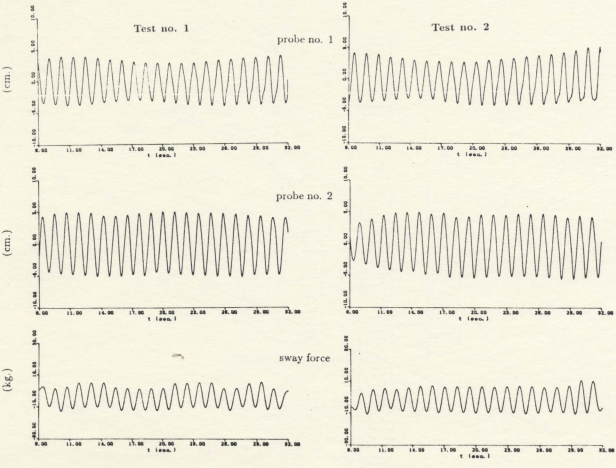

Figure 7.13 (b) continued ↓

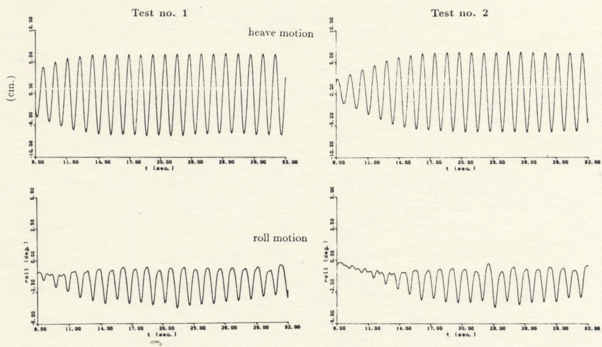

(b) $\omega\sqrt{B/2g} = 0.7630$, $\lambda/B = 5.35$, $H/\lambda = 0.0386$, Test Series B

Figure 7.13 continued ⇓

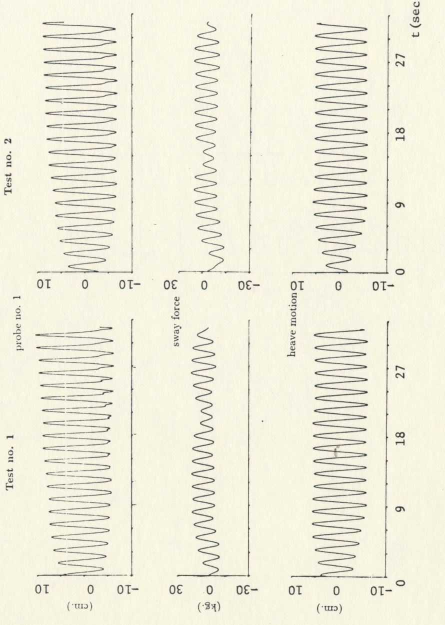

Figure 7.13 (c) continued ↓

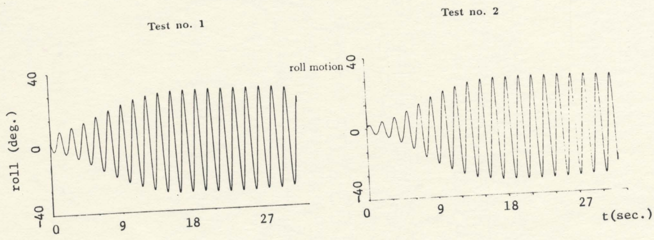

(c) $\omega\sqrt{B/2g} = 0.5386$, $\lambda/B = 9.63$, $H/\lambda = 0.0275$, Test Series C

Figure 7.13 Sample experimental records

8 Comparison of Experimental and Numerical Results

8.1 Introduction

The objective of this section is to provide a comparison between experimental and numerical results. For a proper comparison it is necessary that the experimental conditions are replicated in the numerical model. As described in the previous section, the experiments were conducted by permitting the body to respond in selected modes of motions. In this regard, the numerical model can be relatively easily tuned to imitate the experimental conditions. Computational results illustrating responses of a floating body constrained in particular modes of motion have already appeared in §6. For a valid comparison, another matter of equal importance is the correspondence of the input conditions. Although the numerical model closely resembles its physical experimental counterpart in that both represents initial value processes with waves being generated at one end of the tank (equivalently the control domain), it is not possible to directly replicate the experimental set up in the present simulation model for the following reasons:

1. The method of wave generation in the numerical model and the physical test system is not the same. Even if it was possible to numerically simulate a physically moving impermeable wave board generating waves at one end of a finite control domain, the difficulties in replication of the physical test system would still remain. This is because, considering the distance of the body from the wave board, which is about 20 m. (in order of 10 to 20 wave lengths for the range of frequencies tested), the computational

domain required would have been prohibitively large.

2. In the numerical model, a direct control of the height of the generated waves in the interior of the control domain is not possible; control can only be exercised on the imposed excitation potential.

3. Transient development of wave fields are expected to be different due to differences in the wave generation mechanism.

A direct one-to-one mode of comparison between the experimental and numerical results is therefore not available in general. Hence it is necessary that, prior to carrying out any comparisons, a reasonably acceptable basis of comparison be established.

8.2 Basis of Comparison

The primary input variables for the comparison are taken to be the fundamental wave period and wave height. Previous computational results (cf. §4) have shown that the height of the generated waves inside the control domain is closely comparable to the height (H) of the Airy wave corresponding to the excitation potential. Also, the fundamental period of the generated wave was shown to be very close to the excitation period. Ideally, the excitation potential should be selected such that the conditions of the generated waves at the location of the body's CG agrees with the test wave conditions, but this would have lead to a trial-and-error search for the correct excitation potential. Considering the simulation time and the amount of experimental conditions that were to be simulated, this process would have required prohibitively expensive and time consuming computational efforts. Instead, selection of an Airy excitation potential with H and ω taken from the test conditions were found to be close enough approximations for replicating the experimental waves. This will be apparent from the results presented below.

All of the numerical results, unless specifically mentioned, have been computed for a standardized control domain extending over $L = 4.0\lambda$. The CG of the undisturbed body is located at $L_1 = 2.5\lambda$ and $L_2 = 1.5\lambda$ from the boundaries ∂D_{C1} and ∂D_{C2} respectively (cf. Figure 6.4). The two periods T_1 and T_2 described earlier (see §6.3) provide a guidance for the time span within which comparisons are meaningful. For the size of the domain chosen, about 3 to 5 wave periods of results can be obtained within the interval between T_1 to T_2 for most of the tests. Considering the wide range of λ/B values for which numerical results are to be generated, the grid sizes were not standardized. The relative value of Δx (i.e. $\Delta x/\lambda$) for which the computed results are considered sufficiently reliable for the lower range of wavelength results in poor resolution of the body surface for large values of λ. This follows from the requirement of keeping Δx approximately uniform all over ∂D (see e.g. §4.3.3, where it is shown that the adjacent segments must be comparable in lengths for the numerical solution to be well behaved). On the other hand, retention of the relative $\Delta x/\lambda$ value chosen for the larger values of λ over the entire range of wavelengths leads to a very fine resolution of the free surface for low λ values at the expense of considerable additional computer time, without essentially improving accuracy of the solution (as we have seen in §4). The spatial grid sizes are therefore chosen such that a reasonably good description of the entire boundary can be obtained. Guidance from previous computations helps to choose appropriate values. Δt

for all computations are chosen so that the Courant-Friedrichs-Lewy condition given by eqn. (3.17) is satisfied. These discretization parameters for each computations are listed in Table 8.1. The other relevant parameters are: $\sigma/T = 1$ and $n = 4$ for all computations (this corresponds to a matching length between 0.1λ to 0.13λ). It need also be mentioned that the geometry of the body in the numerical model is rectangular, since the algorithm is not capable of modelling curvilinear geometry (recall that the body contour is approximated by straight line segments). This approximation is not likely to cause any significant errors, since the radii of curvature are very small.

For the chosen size of the control domain, T_2 for most runs is in order of 8 to 12 times the excitation period, depending on c_g values (see eqn. (5.7) and note that d/λ ranges from over 0.5 to about 0.25), or about 9 to 16 secs. in real time. From the experimental results, an appropriate window extending over this time interval was considered for the presentation of time histories for comparison. In most cases, the windows were selected by a visual inspection of the full time record and are such that the data contain a part of the transient information, i.e. the starting point of the window is a few periods ahead of reaching the steady state. Figure 8.1 illustrates such a typical window.

The comparison between the numerical and experimental time records are presented in the following manner.

Input conditions

The numerical wave is measured at a station inside the control domain located at a distance of 0.5λ from the excitation boundary. This distance is chosen

Table 8.1 Discretization parameters

f (sec.$^{-1}$)	$\omega\sqrt{B/2g}$	λ (cm.)	$\Delta x/\lambda$	$\Delta t/T$
1.15	1.0771	117.9	1/30	1/60
1.10	0.9874	128.9	1/30	1/60
1.05	0.9425	141.4	1/30	1/60
1.00	0.8976	155.8	1/30	1/60
0.95	0.8527	191.8	1/40	1/80
0.90	0.8078	191.8	1/40	1/80
0.85	0.7630	213.9	1/40	1/80
0.80	0.7181	239.8	1/40	1/80
0.70	0.6283	304.1	1/40	1/100
0.60	0.5386	385.0	1/40	1/100

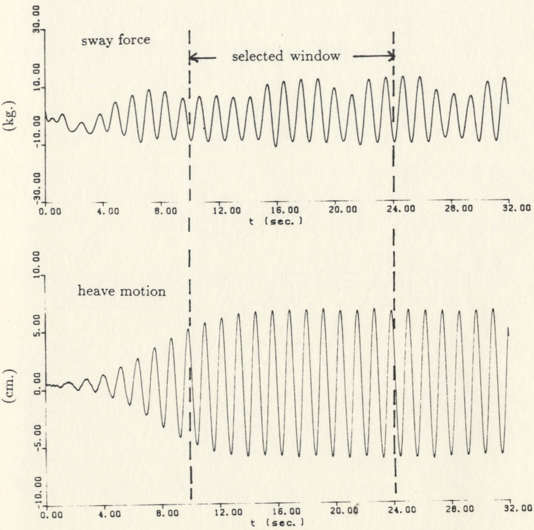

Figure 8.1 Illustration of a typical window chosen for the purpose of comparison and presentation of results; this record is from Test Series C; $\omega\sqrt{B/2g} = 0.7630$, $\lambda/B = 5.35$, $H/\lambda = 0.0386$; record from this window can be seen in Figures 8.7 (c) and (d) below.

such that the station is relatively close to ∂D_{C1} and about 0.4λ outside of the matching region on an average. Therefore the time history for the free surface elevation remains uninfluenced by any reflection from the body for a relatively long time. This elevation can then be taken as a measure of the oncoming wave. For the experimental input conditions, the wave elevation records from test series A (without the presence of the body) are considered. Comparison of these two records therefore provide the comparisons of oncoming wave conditions. For presentation, these two records are synchronized. The synchronization here is standardized by matching the peak of the numerical wave in the time interval $3 \leq t/T \leq 4$ with the peak of the experimental wave record.

Outputs

The primary outputs of the models are the two displacements (heave and roll) and the sway force. These results are plotted by synchronizing the records with respect to the undisturbed wave at the horizontal location of the body's CG. The synchronization is accomplished in the following manner.

Referring to Figures 8.2 (a) - (f), the phase difference between the wave at location of probe no. 2 and probe no. 3, henceforth referred to as P2 and P3 respectively, for the tests without the body (i.e. for test series A, see Figure 7.9) can be determined by measuring $\delta\tau_{2,3}$ (Figure 8.2 (a)). Similarly, from the tests with the body (i.e. test series B, C or D), the phase difference between P2 and the responses (for clarity, the responses are shown as a single curve and denoted as R(exp) in Figure 8.2 (b)) can be determined by measuring $\delta\tau_{2,R}$. Taking P2 to be a reference, the phase difference between the undisturbed wave

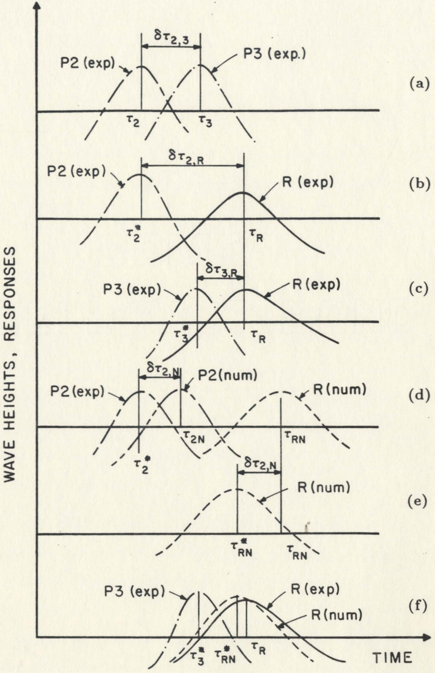

Figure 8.2 Synchronization of the results.

at the body's CG location (P3 in Figure 8.2 (a)) and the responses (R(exp)) are determinable by calculating $\delta\tau_{3,R}$:

$$\delta\tau_{3,R} = \delta\tau_{2,R} - \delta\tau_{2,3} \qquad ......(8.1)$$

Therefore the experimental time records are established with reference to the undisturbed wave at the body's CG location, as illustrated in Figure 8.2 (c).

To synchronize the numerical results with the experimental ones, time history for the free surface elevation at P2, which has been generated in the numerical model, is utilized. By measuring the time difference $\delta\tau_{2,N}$ between the experimental and numerical records for free surface elevations at this location (Figure 8.2 (d)), the entire time histories for all the responses in the numerical model (R(num)) are shifted by this amount to achieve the desired synchronization (see Figure 8.2 (e)). Referring to Figures 8.2 (c) and 8.2 (e), the synchronized records referenced with respect to the extrapolated undisturbed wave record at the body's CG location are established, as illustrated in Figure 8.2 (f) (in the Figure, a slight phase gap between the responses has been retained for clarity).

It is to be observed that synchronization of the results could have been achieved through a somewhat less lengthy procedure, by taking P2 as an absolute reference and measuring all other records with respect to it. However, here the procedure described above is adopted, since this is believed to follow standard practice of data presentation in the frequency domain where the phases are usually referenced relative to the incident wave crest at the body's CG location.

For extracting the phase information, times indicated as $\tau_2, \tau_3, \tau_2^*, \tau_R, \tau_{2N}$ and τ_{RN} shown in Figures 8.2 (a) - (f) need to be determined. These are calculated by an averaging process.

Consider a time record extending for a length of N_τ periods (Figure 8.3), and denote the time of occurrence of the peaks as $\tau_i, i = 1, ..., N_\tau$ (it is also possible to work with any other reference such as the troughs or zero-crossings). By measuring τ_i, the averaged value of τ_1 (i.e. τ at $i = 1$) is determined from

$$\tau_1 = \frac{1}{N_\tau}[\sum_{i=1}^{N} \tau_i - \sum_{i=1}^{N}(i-1)T] \qquad .....(8.2)$$

where T denotes the fundamental period of the signal.

The above procedure can be subdivided into the following steps.

(i) Determine τ_2 and τ_3 from the records of test series A (Figure 8.2 (a)) by selecting an appropriate window by a visual inspection of the full record. Find $\delta\tau_{2,3}$.

(ii) Select window from the test records of series B or C or D (as the case may be) and find τ_2^* and τ_R, and hence determine $\delta\tau_{2,R}$ (Figure 8.2 (b)). In most situations, the selected window coincides with the time span selected in (i) above.

(iii) Calculate $\delta\tau_{3,R}$ from eqn. (8.1) and establish the experimental record for the responses in relation to P3 of test series A (Figure 8.2 (c)):

$$\tau_3^* = \tau_R - \delta\tau_{3,R} \qquad .....(8.3)$$

(iv) Determine $\tau_{2,N}$ from the numerical results. The window selected for this is: $[1 + (2.5\lambda - L_{2,3})/c_g] \le t \le [1 + (2.5\lambda + L_{2,3})/c_g]$ which follows from consideration of linear group speed. Here $L_{2,3}$ is the distance between $P2$ and $P3$ (refer to Figure 7.9 or 7.10). Hence determine $\delta\tau_{2,N}$ (Figure 8.2 (d)).

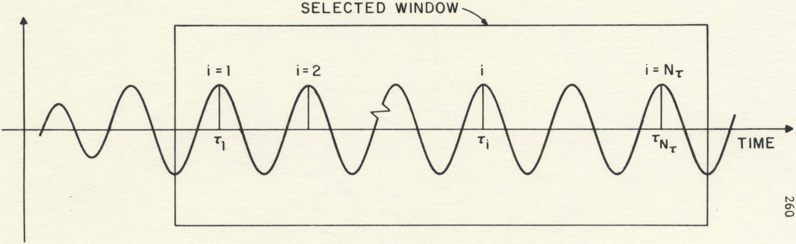

Figure 8.3 A typical time record.

(v) Shift the entire numerical record including wave information at P2 (Figure 8.2 (e)):

$$\tau^*_{RN} = \tau_{RN} - \delta\tau_{2,N} \qquad .....(8.4)$$

(vi) Compile and plot the records: the wave record at P3 from test series A, and the responses from the experimental and numerical results (Figure 8.2 (f)).

An interactive software is developed to process the data in the manner described above. The approximations implicit in this processing must now be stated:

(i) The tests have been assumed repeatable. This assumption is implicit by utilizing results of test series A for synchronization with other test results. This means, it is assumed that for an identical signal to the wave-maker, the generated waves are identical. Results illustrating the quality of repeatability presented earlier (Figure 7.13) justify this assumption.

(ii) The records are assumed to be periodic with the fundamental period of T, which is the period of the excitation signal (i.e. the wave-maker). This assumption is implicit in using eqn. (8.2).

Notwithstanding these assumptions which may lead to some inaccuracies in the synchronization procedure, it should be pointed out that the relative phases between the three responses for each set of records (experimental and numerical) are kept unaltered by the above processing.

8.3 Results

8.3.1 Sway Forces and Heave Motions

The comparisons between the time histories of the experimental and computed results are presented in Figures 8.4 - 8.7. The first plots in these ((a) in the Figures) compare the free surface elevations of the experimental and numerical waves. The sway force and heave motion histories ((c) and (d) in the Figures) are plotted in referenced to the undisturbed wave elevation at the location of the body's CG (which is shown as (b) in these Figures), obtained in the manner described above. For brevity, in this section only a limited number of time series plots are presented, covering the experimental range of frequencies and steepnesses. For $\omega\sqrt{B/2g} = 0.7630$, computational results were also been obtained for an extended control domain with $L_1 = 3.25\lambda$ as a further verification of the numerical model. Figure 8.8 shows this comparison. Note that the plotted sway force and heave motions are respectively the total force recorded by the dynamometer, $\hat{F}_x = F_x L_B$, and the vertical displacement of the body's CG, $\hat{z}_G = z_G(t) - z_G(0)$. Also, the quoted values of T_1 and T_2 are rounded-off to the nearest 0.5 sec. and adjusted by adding appropriate values such that they directly correspond to the time-axis of the plots.

Results in terms of the peak-to-peak values and phase relations were compiled and summarized in Tables 8.2 (a) - (c). The numerical wave height quoted here was computed from the corresponding time history by averaging wave heights. For this, the record in the time interval $4 \leq t/T \leq 7$ which lies well within T_1^* to T_2^* was considered. Here T_1^* and T_2^* indicate respectively the times at which the wave at the station (i.e. at the location of 0.5λ from ∂D_{C1} at which

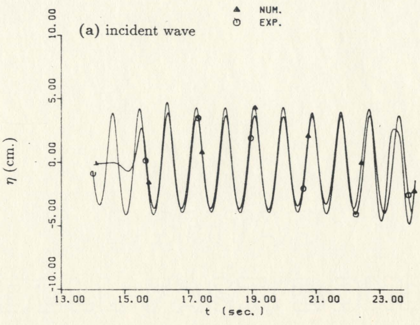

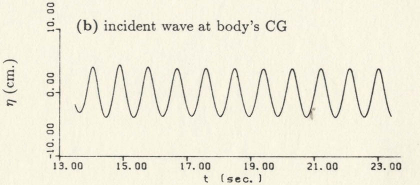

Figure 8.4 continued ⇓

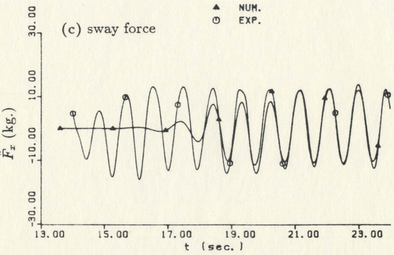

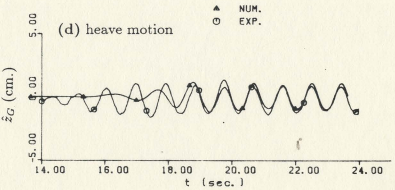

Figure 8.4 Comparison of experiment and theory
$\omega\sqrt{B/2g} = 0.9874$, $\lambda/B = 3.20$, $H/\lambda = 0.0610$, Test Series D
$T_1 \approx 19$ sec., $T_2 \approx 24$ sec.

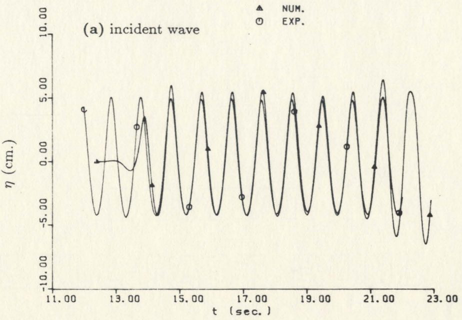

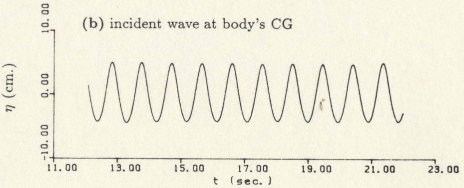

Figure 8.5 continued ⇓

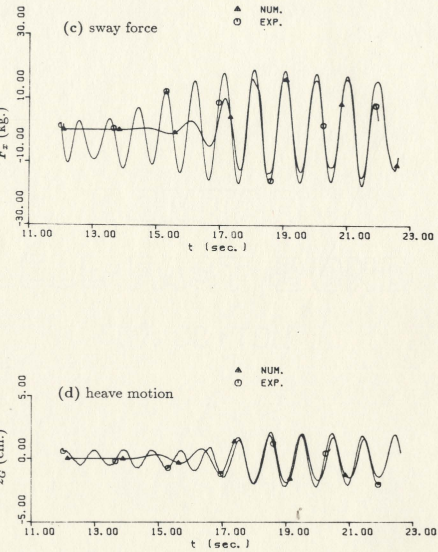

Figure 8.5 Comparison of experiment and theory
$\omega\sqrt{B/2g} = 0.9425$, $\lambda/B = 3.53$, $H/\lambda = 0.0684$, Test Series C
$T_1 \approx 17.0$ sec., $T_2 \approx$ 22.0 sec.

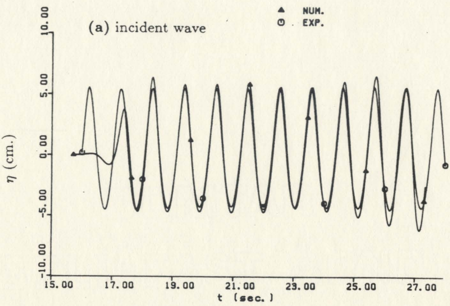

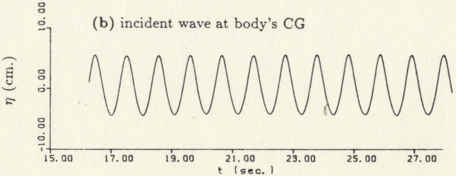

Figure 8.6 continued ⇓

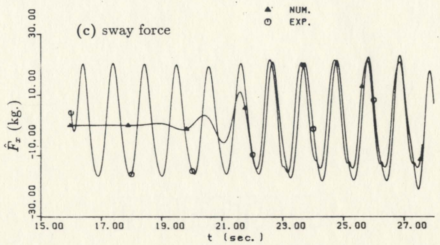

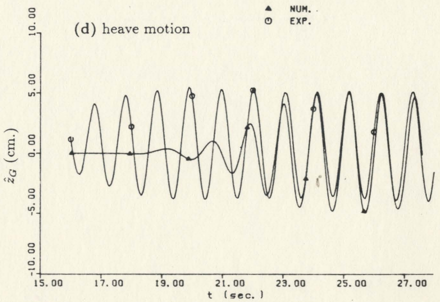

Figure 8.6 Comparison of experiment and theory
$\omega\sqrt{B/2g} = 0.8527$, $\lambda/B = 4.33$, $H/\lambda = 0.0590$, Test Series D
$T_1 \approx 22$ sec., $T_2 \approx 27.5$ sec.

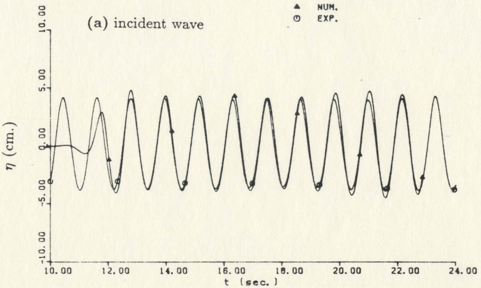

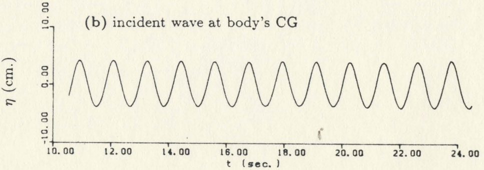

Figure 8.7 continued ⇓

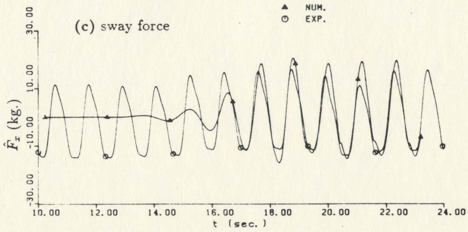

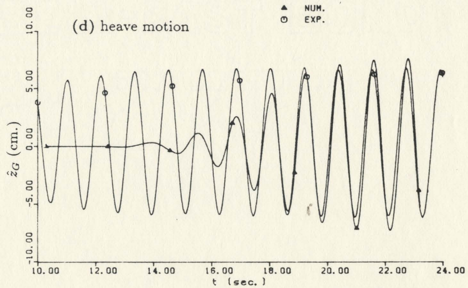

Figure 8.7 Comparison of experiment and theory
$\omega\sqrt{B/2g} = 0.7630$, $\lambda/B = 5.35$, $H/\lambda = 0.0386$, Test Series C
$T_1 \approx 17$ sec., $T_2 \approx 22.5$ sec.

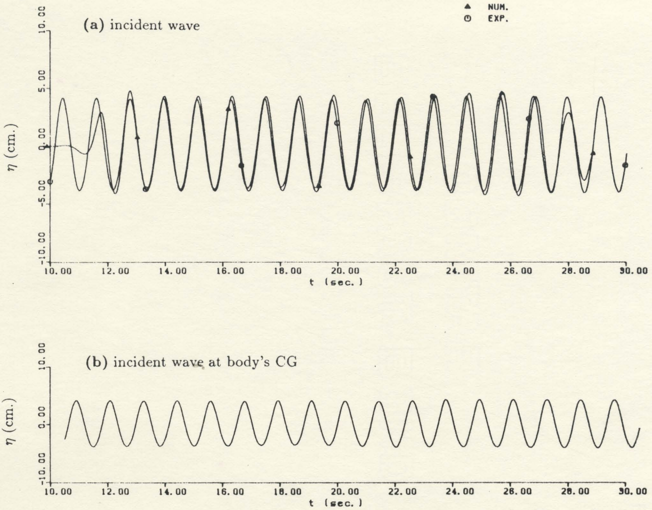

Figure 8.8 continued ⇓

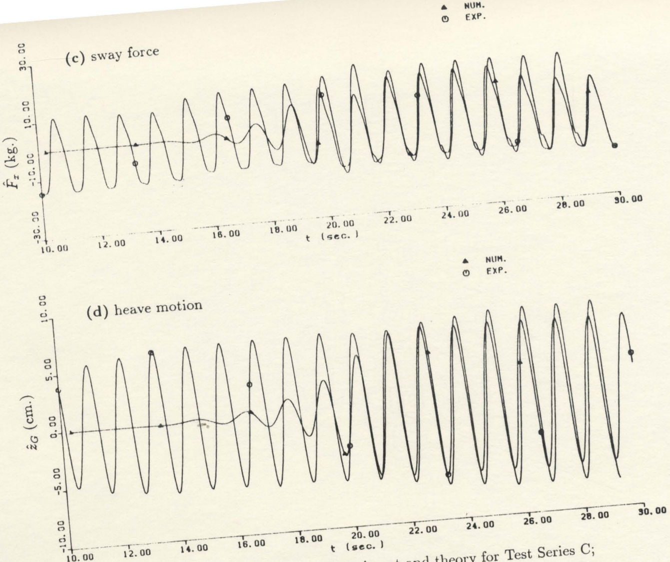

Figure 8.8 Comparison of experiment and theory for Test Series C; $\omega\sqrt{B/2g} = 0.7630$, $\lambda/B = 5.35$ and $H/\lambda = 0.0386$; this computation is performed for an extended control domain of $L_1 = 3.25\lambda$; $T_1 \approx$ 19.0sec., $T_2 \approx$ 26.5sec.

Table 8.2 (a) Comparisons for sway force and heave motion, test series B

$\frac{H_{\text{exp}}}{H_{\text{num}}}$	$\omega\sqrt{B/2g}$	λ/B	H/λ	Sway Force				Heave Motion			
				$\lvert\bar{F}_x\rvert$	$\lvert\bar{F}_x\rvert$	ΔF_x	$\Delta\beta_F$	$\lvert\bar{z}_G\rvert$	$\lvert\bar{z}_G\rvert$	Δz_G	$\Delta\beta_z$
				(exp.)	(num.)	(%)	(deg.)	(exp.)	(num.)	(%)	(deg.)
0.987	1.0771	2.70	0.0347	0.053	0.059	9.8	30	0.0375	0.0385	1.3	0
0.996	0.9874	3.20	0.0610	0.135	0.120	-11.0	0	0.0985	0.099	0.10	15
0.986	0.9874	3.20	0.0290	0.066	0.061	-7.7	30	0.064	0.0645	-0.60	0
0.985	0.9425	3.53	0.0684	0.154	0.159	3.4	-30	0.177	0.178	-1.0	-15
0.996	0.9425	3.53	0.0348	0.086	0.078	-9.7	-15	0.098	0.099	0.10	-15
0.998	0.8976	3.90	0.0630	0.146	0.161	8.3	-45	0.273	0.275	0.7	-15
0.996	0.8976	3.90	0.0327	0.086	0.089	2.6	-30	0.125	0.128	2.0	-15
0.971	0.8527	4.33	0.0286	0.096	0.098	-0.8	-15	0.207	0.217	1.8	-15
0.976	0.8078	4.80	0.0361	0.152	0.156	1.5	30	0.380	0.454	16.5	30
0.976	0.7630	5.35	0.0386	0.158	0.165	3.7	15	0.660	0.700	3.6	15

Table 8.2 (b) Comparisons for sway force and heave motion, test series C

$\frac{H_{\mathrm{exp}}}{H_{\mathrm{num}}}$	$\omega\sqrt{B/2g}$	λ/B	H/λ	Sway Force				Heave Motion			
				$\lvert\bar{F}_x\rvert$ (exp.)	$\lvert\bar{F}_x\rvert$ (num.)	ΔF_x (%)	$\Delta\beta_F$ (deg.)	$\lvert\bar{z}_G\rvert$ (exp.)	$\lvert\bar{z}_G\rvert$ (num.)	Δz_G (%)	$\Delta\beta_z$ (deg.)
0.962	0.9874	3.20	0.0610	0.144	0.123	-17.6	-15	0.099	0.099	-4.3	0
0.986	0.9874	3.20	0.0291	0.068	0.062	-8.8	-30	0.059	0.059	-2.2	-15
0.985	0.9425	3.53	0.0684	0.176	0.156	-12.9	0	0.197	0.190	-5.0	15
0.994	0.9425	3.53	0.0348	0.083	0.078	-6.8	0	0.098	0.098	-0.60	15
0.998	0.8976	3.90	0.0630	0.151	0.164	8.4	15	0.273	0.275	0.7	-15
1.0	0.8976	3.90	0.0327	0.088	0.089	1.2	-30	0.130	0.128	-1.9	-15
0.971	0.8527	4.33	0.0286	0.099	0.097	-4.5	-30	0.210	0.218	0.5	-30
0.976	0.8078	4.80	0.0361	0.156	0.154	-4.0	-15	0.390	0.455	13.8	0
0.976	0.7630	5.35	0.0386	0.148	0.162	6.5	15	0.670	0.700	2.0	15
0.993	0.7181	6.00	0.0172	0.091	0.090	-1.7	-30	0.390	0.401	1.9	15
0.992	0.6283	7.60	0.0129	0.0911	0.085	-7.5	0	0.295	0.304	2.1	0

Table 8.2 (c) Comparisons for sway force and heave motion , test series D

				Sway Force				Heave Motion			
$\frac{H_{exp}}{H_{num}}$	$\omega\sqrt{B/2g}$	λ/B	H/λ	$\lvert\bar{F}_x\rvert$	$\lvert\bar{F}_x\rvert$	ΔF_x	$\Delta\beta_F$	$\lvert\bar{z}_G\rvert$	$\lvert\bar{z}_G\rvert$	Δz_G	$\Delta\beta_z$
				(exp.)	(num.)	(%)	(deg.)	(exp.)	(num.)	(%)	(deg.)
0.987	1.0771	2.70	0.0347	0.053	0.059	9.8	0	0.0375	0.04	5.26	0
0.962	0.9874	3.20	0.0610	0.126	0.123	-6.2	0	0.10	0.099	-3.9	0
0.986	0.9874	3.20	0.0291	0.065	0.062	-6.9	-15	0.055	0.058	3.1	0
0.985	0.9425	3.53	0.0684	0.151	0.154	6.2	-30	0.190	0.195	1.1	-15
0.994	0.9425	3.53	0.0348	0.086	0.080	-7.2	-30	0.097	0.098	0.40	-15
0.997	0.8976	3.90	0.0630	0.151	0.164	8.3	-90	0.274	0.295	7.2	-90
1.0	0.8976	3.90	0.0327	0.083	0.088	5.0	-45	0.130	0.130	0.0	-30
0.971	0.8527	4.33	0.0590	0.185	0.172	-9.8	-30	0.455	0.474	1.4	-15
0.980	0.8527	4.33	0.0286	0.102	0.096	-6.9	-30	0.218	0.220	-0.8	-15
0.976	0.8078	4.80	0.0361	0.148	0.151	0.7	15	0.401	0.468	13.9	15
0.976	0.7630	5.35	0.0386	0.148	0.162	6.5	15	0.660	0.690	2.1	15
0.837	0.7181	6.00	0.0363	0.194	0.226	-2.6	-15	0.750	1.025	14.3	15
0.977	0.6283	7.60	0.0275	0.152	0.162	4.0	30	0.580	0.638	7.2	15
0.990	0.5386	9.63	0.0247	0.160	0.150	-7.8	15	0.448	0.488	8.8	15

the numerical wave height is monitored) is likely to be fully developed and free from the influence of reflection . From considerations of linear group speed and chosen computational parameters, $T_1^*/T = 1+0.5K$ and $T_2^* = 1+(4.5-B/\lambda)K$ where $K = c/c_g$. The other parameters shown have the following meanings:

$$
\begin{aligned}
|\bar{F_x}| &= \frac{|F_x|}{\rho g B^2} \\
|\bar{z_G}| &= \frac{|z_G|}{h} = \frac{|z_G|}{(B/2)} \\
\Delta F_x &= [\frac{(|F_x|/H)\mathrm{num} - (|F_x|/H)\mathrm{exp}}{(|F_x|/H)\mathrm{exp}} - 1] \times 100 \\
\Delta z_G &= [\frac{(|z_G|/H)\mathrm{num} - (|z_G|/H)\mathrm{exp}}{(|z_G|/H)\mathrm{exp}} - 1] \times 100
\end{aligned}
\qquad .....(8.5)
$$

$\Delta\beta_F$, $\Delta\beta_z$ = phase differences between measured and computed time histories for sway force and heave motions respectively, (positive indicates numerical record is leading)

where $|F_x|$ and $|z_G|$ were defined earlier (see §6.3). The values shown for the numerical results are computed by averaging the peak-to-peak values for the central two periods in the interval T_1 to T_2. For the experimental results, however, the entire time record (excluding the transient part of the record) was considered in determining the quoted values (not just the time record chosen to present the time history comparisons in Figures 8.4 - 8.8).

A measure of the discrepancies between experimental and computed results are therefore provided by ΔF_x and Δz_G values. Note that in defining these parameters, a normalization with respect to H was carried out such that any discrepancies arising from differences in H_{exp} and H_{num} are absorbed in them (much in the style of usual transfer functions). For the sampling rate of 40 hz. at which data was processed, and taking into account the data averaging procedure (a digital filtering technique for the force record and five point averaging formula for the rest of the records, see §7.4), the approximate level of accuracies for the phase values are estimated to be varying in the range of 10 to 20 deg., depending on the frequencies. The values quoted have been rounded-off to 15 deg., since this value is considered to be indicative of estimated average level of accuracies over the full data range.

The discrepancies between the measured and computed peak-to-peak values (i.e. ΔF_x and Δz_G) are grouped in the range of 5% and are shown in Figures 8.9 (a) - (f). A discussion of these results is provided latter (see §8.4 below). Note that in Tables 8.2 (a) and (b), roll results were not included since for those ranges of frequencies roll motions were very small (see §8.3.3 below).

8.3.2 Free Heave Tests

With some modifications, the numerical model can be used to simulate free motions of floating bodies. A variety of initial conditions can be examined by combining initial displacements and velocities. To achieve these simulations, the imposed excitation on ∂D_{C1} needs to be removed. The numerical model can be set up by either imposing condition (4.13) on ∂D_{C1} and ∂D_{C2} with c determined as the celerity of an Airy wave of period corresponding to the natural period of oscillation, or by placing these boundaries sufficiently far and imposing either $\phi = 0$ or $\partial \phi / \partial n = 0$ on them. The former method is expected to permit long time simulations with a relatively small computational domain, while in the latter method results are expected to be contaminated when the disturbances created by the body reach the outer boundaries. Nevertheless, depending on the

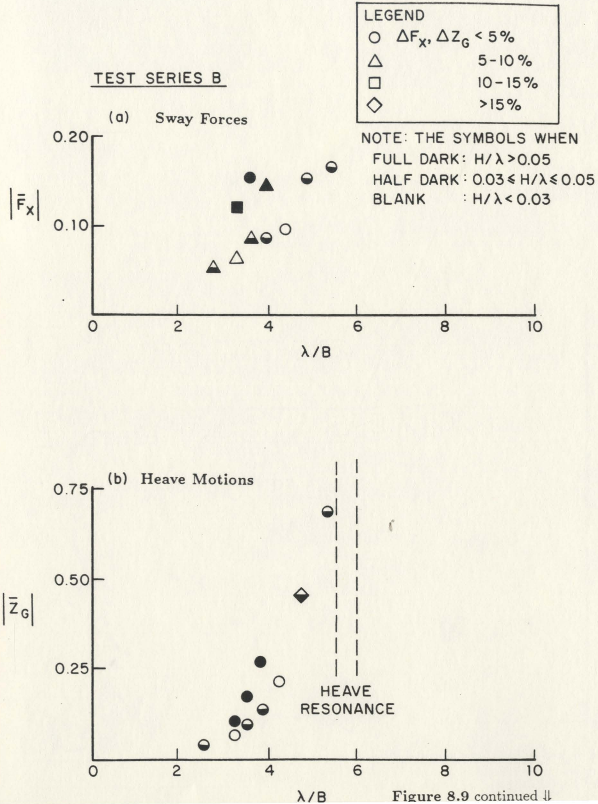

Figure 8.9 continued ⇓

TEST SERIES C

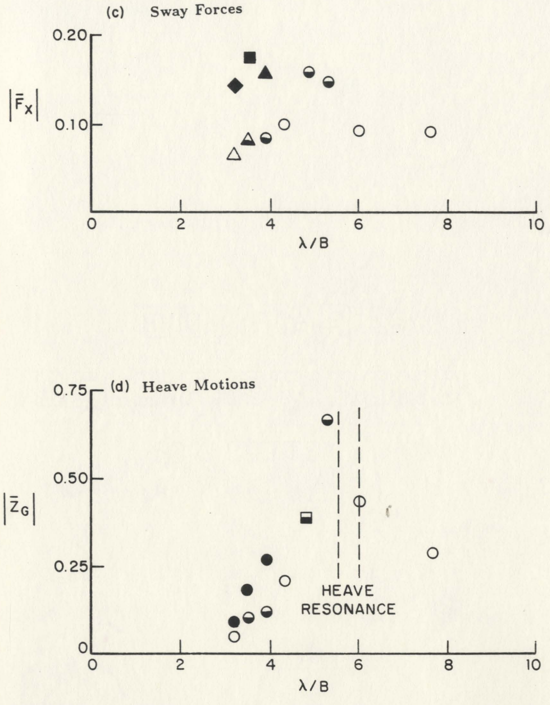

Figure 8.9 continued ⇓

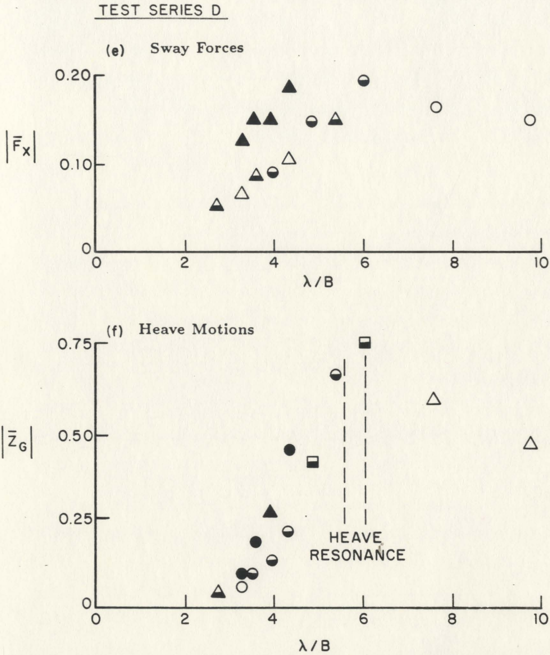

Figure 8.9 Comparison of peak-to-peak sway force and heave motion between experiment and theory.

length of the domain, uncontaminated results for a few periods of oscillations can be obtained at the expense of additional computer time. Considering ease of implementation in that additional algorithms need not be written for time integration of (4.13) on ∂D_{C1}, the latter method is adopted here for comparison with experimental results.

Prior to showing the comparisons, in Figure 8.10 the numerical results are shown, which are computed for different lengths of the domain, grid sizes and imposed conditions on the outer boundaries. The discretization parameters shown are normalized with respect to $T \equiv T^h$ and λ = length of an Airy wave of period T^h in water depth d. Here, T^h is the natural period of oscillation in heave. These plots show that results upto $t \leq 2.5T^h$ differ negligibly, except for the smallest control domain of $0.5L = 6B$. This case corresponds to a distance of only 1λ between the body and the outer boundaries. For $0.5L \geq 12B$, results upto $2.5T^h$ can therefore be considered reliable, regardless of the conditions imposed on the exterior boundaries.

The comparison between experiment and theory is presented in Figure 8.11 in which a plot for only one of the numerical results is shown for clarity. For the experimental results, the first half cycle of oscillation is omitted due to uncertain initial conditions (the experiments were performed by pushing the body down and releasing it; the force required for this was considerable, and consequently possibilities exist for non-zero initial velocities). The agreement between theory and experiment is in general quite good. The numerical result shows a slight over-prediction in the natural period, indicating some over-estimation in the heave added mass (cf. eqn. (6.29)). The experimental results for the two tests show some discrepancies. Considering that the restoring forces are linear,

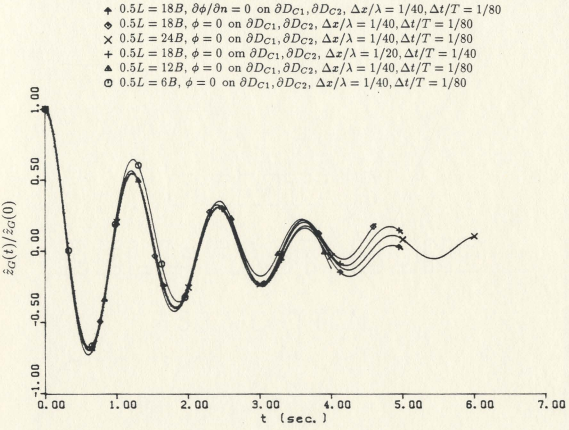

Figure 8.10 Numerical simulation for free heave motions of the body for different sizes of the control domain, different imposed conditions on the exterior boundaries and for different grid sizes; for all runs, $\hat{z}_G(0)/h = 0.5$.

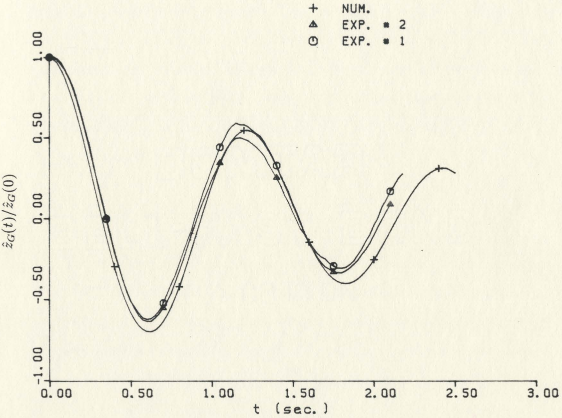

Figure 8.11 Comparison of experiment and theory for free heave motions of the body; the numerical result shown is for $0.5L = 18B$ with the condition $\phi = 0$ on the exterior boundaries, and $\Delta x \;/\lambda = 1/40$ and $\Delta t/T = 1/80$

the discrepancies are perhaps attributable to experimental inaccuracies rather than differences in initial conditions. The contribution of fluid viscosity in the damping of heave motion appears to be not very significant, although closer scrutiny reveals a marginal damping effect (see the lower part of the plots). These findings are consistent with results obtained by earlier investigators (see e.g. Adachi and Ohmatsu 1980). Since the variations in the two experimental records are almost as large as the difference between experiment and theory, further analysis of the comparison is not carried out.

8.3.3 Roll Motions

With the exception of the lowest experimental frequency in the vicinity of the roll natural frequency, the body displayed very small roll displacements at all other test frequencies. The roll amplitudes were mostly less than 4 deg. The numerical method predicts a similar behaviour as can be seen from results shown for several frequencies (Figures 8.12 (a) - (c)). This also provides a supporting evidence for the roll behaviour obtained earlier for a similar geometry at frequencies far from the natural frequency, see e.g. Figure 6.11 (c) in §6.

Large roll amplitudes were obtained experimentally for the frequency $\omega\sqrt{B/2g}$ $= 0.5386$ in test series C. At this frequency, experimental data was gathered for three different wave steepnesses, the largest being $H/\lambda = 0.0275$. Larger steepness could not be achieved due to the limitation of the dynamometer (maximum allowable roll of ± 30 deg.) as well as due to water spilling inside the body. Time histories showing the comparisons for incident wave, sway force, heave and roll motions for all the three wave steepnesses are presented in Figures 8.13 - 8.15.

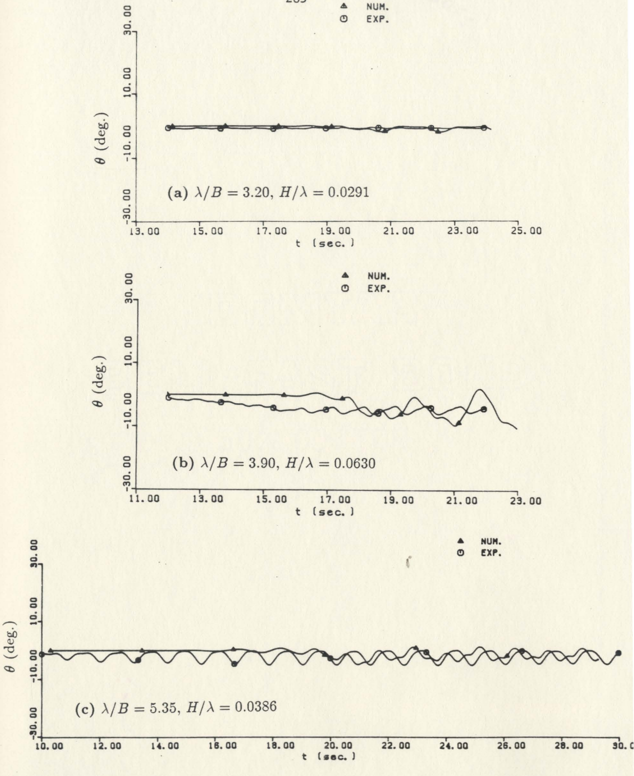

Figure 8.12 Roll motions : comparison of experiment and theory; all shown experimental results are from Test Series C; plot (c) shows the numerical result for the extended domain of $L_1 = 3.25\lambda$.

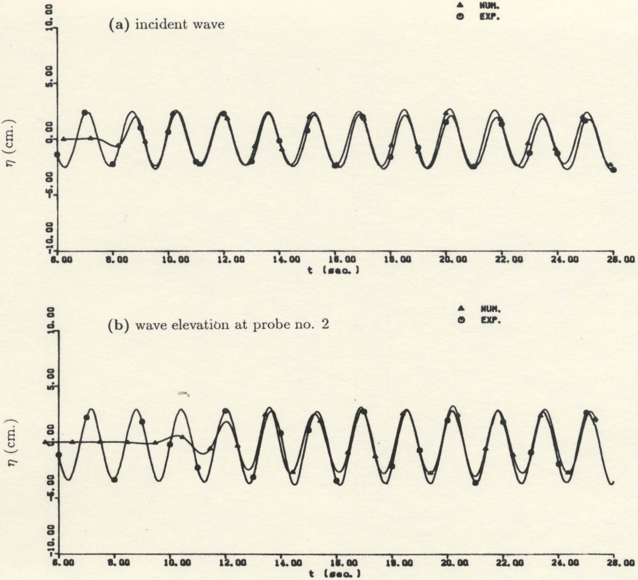

Figure 8.13 continued ⇓

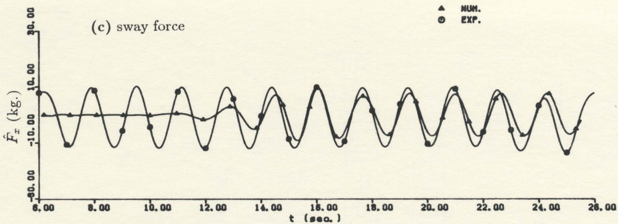

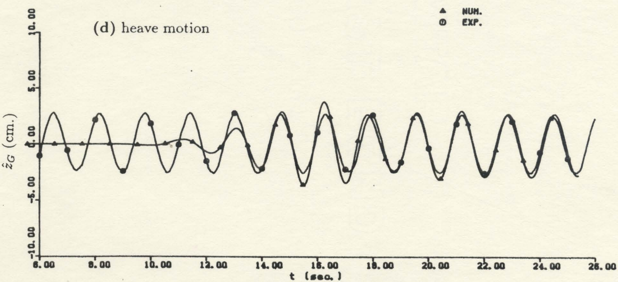

Figure 8.13 continued ⇓

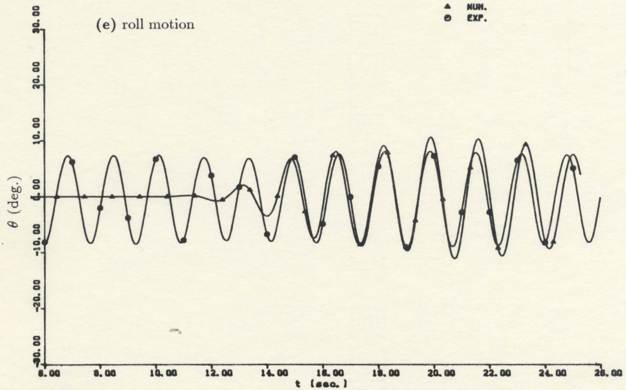

Figure 8.13 Comparison of experiment and theory for
$\omega\sqrt{B/2g} = 0.5386$ and $H/\lambda = 0.0125$
($T_1 \approx 14.5$ sec., $T_2 \approx 21.0$ sec.)

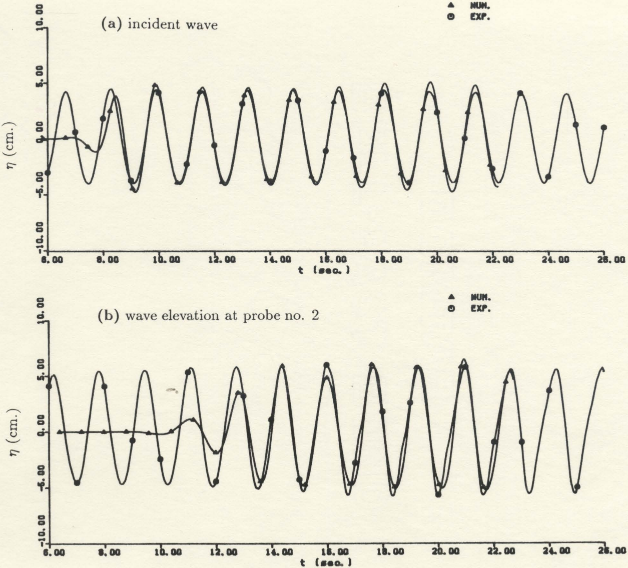

Figure 8.14 continued ⇓

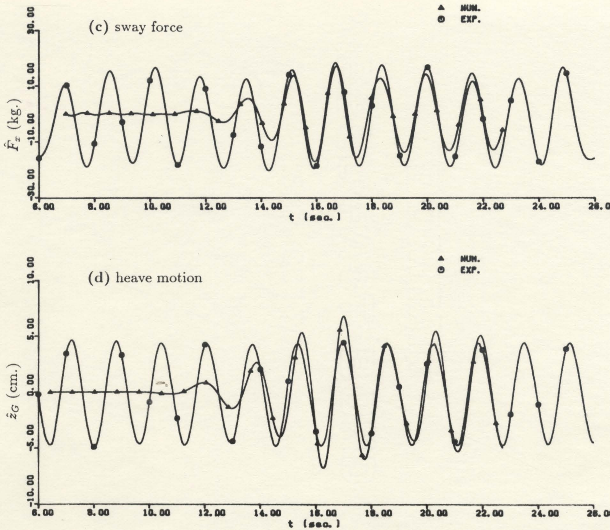

Figure 8.14 continued ⇓

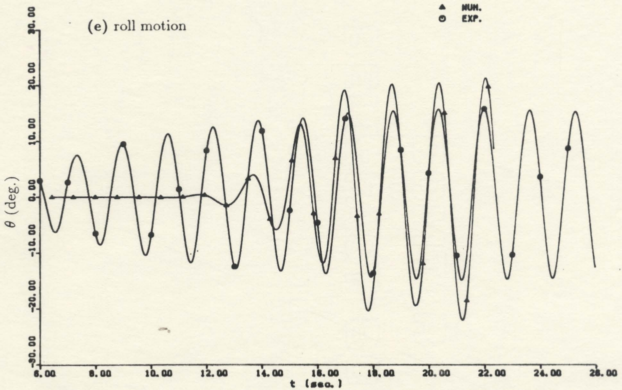

Figure 8.14 Comparison of experiment and theory for
$\omega\sqrt{B/2g} = 0.5386$ and $H/\lambda = 0.0229$
($T_1 \approx 14.5$ sec., $T_2 \approx 21.0$ sec.)

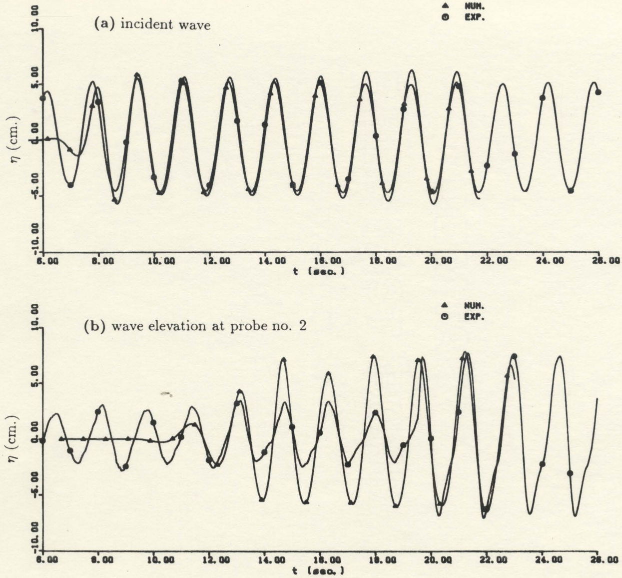

Figure 8.15 continued ⇓

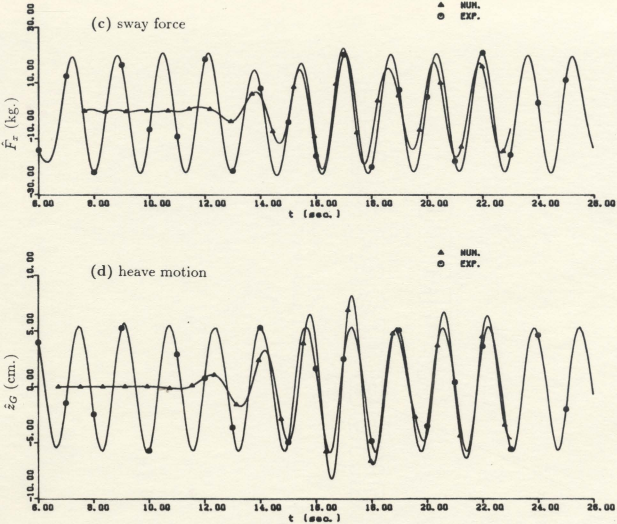

Figure 8.15 continued ⇓

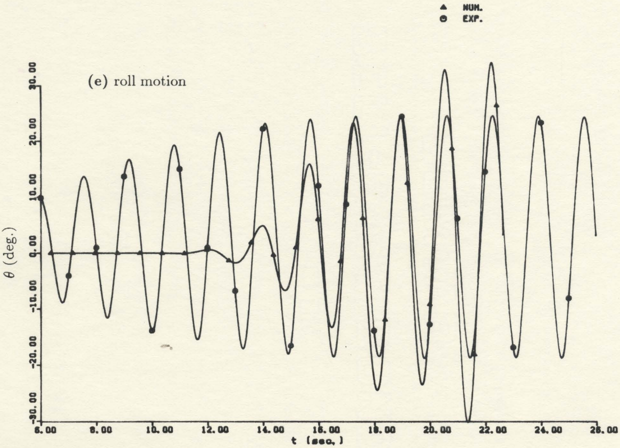

Figure 8.15 Comparison of experiment and theory for
$\omega\sqrt{B/2g} = 0.5386$ and $H/\lambda = 0.0275$
($T_1 \approx 14.5$ sec., $T_2 \approx 21.0$ sec.)

Also included are the comparisons of wave elevations at the location of probe no. 2 ((b) in these Figures). The peak-to-peak values and phase informations are compiled in Table 8.3, where

$$\Delta\theta = [\frac{(|\theta|/H)\text{num} - (|\theta|/H)\text{exp}}{(|\theta|/H)\text{exp}} - 1] \times 100 \qquad .....(8.6)$$

and $\Delta\beta_\theta$, which indicates the phase difference between the measured and computed roll time histories, are obtained in the same manner as for the other two records. Although the agreement of phases is very good, the roll motions are considerably over-predicted, $|\theta|$ values differing by about 17 % to 32 %. On the other hand, the sway forces are under-predicted while the heave motions have correlated reasonably well. It is worth mentioning that the agreement of free surface elevations at the location of probe no. 2 is also quite good.

The over-predictions of roll amplitudes are believed to be the effects of fluid viscosity which is not accounted for in the potential flow numerical model. The significant role played by fluid viscosity in the form of a damping mechanism for large roll motions is well documented in literature (see e.g. Himeno 1981). Incorporation of viscous effects is therefore expected to improve the predictions. In the following, an attempt has been made to incorporate these effects by including viscous damping terms in the roll equation of motion.

8.3.3.1 Inclusion of Viscous Damping

The single degree of freedom, uncoupled, roll equation of motion can be written as:

$$(I_\theta + \delta I_\theta)\ddot{\theta} + b_\theta(\dot{\theta}) + C_\theta(\theta) = \tilde{M}_\theta \qquad .....(8.7)$$

Table 8.3 Comparisons for sway force, heave and roll motions, test series C

$\frac{H_{\mathrm{exp}}}{H_{\mathrm{num}}}$	$\omega\sqrt{B/2g}$	λ/B	H/λ	Sway Force				Heave Motion				Roll Motion			
				$\lvert\bar{F}_x\rvert$	$\lvert\bar{F}_x\rvert$	ΔF_x	$\Delta\beta_F$	$\lvert\bar{z}_G\rvert$	$\lvert\bar{z}_G\rvert$	Δz_G	$\Delta\beta_z$	$\lvert\theta\rvert$	$\lvert\theta\rvert$	$\Delta\theta$	$\Delta\beta_\theta$
				(exp.)	(num.)	(%)	(deg.)	(exp.)	(num.)	(%)	(deg.)	(exp.)	(num.)	(%)	(deg.)
0.990	0.5386	9.63	0.0125	0.104	0.079	-24.0	15	0.28	0.29	2.5	0	18.0	21.3	17.3	15
0.989	0.5386	9.63	0.0229	0.172	0.151	-15.0	15	0.50	0.54	6.8	0	33.0	44.0	31.8	0
0.964	0.5386	9.63	0.0275	0.202	0.172	-17.0	15	0.565	0.625	6.6	0	43.9	59.5	30.6	15

where $b_\theta(\dot{\theta})$, $C_\theta(\theta)$ and $\tilde{M}_\theta$ represent damping, restoring and excitation moments respectively, single and double dots signify single and double differentiations with respect to time, and the other symbols are as defined earlier. The effects of fluid viscosity are contained in the b_θ term (the damping moment) above. The aim is to incorporate this effect in the numerical model.

In general, the damping moment results due to two effects: hydrodynamic or radiation damping and viscous damping. If radiation damping moment is assumed to be linear in $\dot{\theta}$ (justification of this assumption is provided latter, in Appendix B), we can write:

$$\begin{aligned} b_\theta &= b_\theta^H + b_\theta^V \\ &= B_\theta^H \dot{\theta} + b_\theta^V \end{aligned} \qquad .....(8.8)$$

where b_θ^H and b_θ^V are contributions of radiation and viscous damping moments respectively, and B_θ^H is the associated radiation damping coefficient. The radiation damping moment results from the dissipation of energy through the creation of radiated waves by the motion of the body. This is a part of the potential flow phenomenon and is therefore implicitly accounted for in the numerical model. The remaining part is then the contribution of the b_θ^V term.

This term was estimated by utilizing the results of the free roll experiments (the roll decay tests) as explained in Appendix B. The Newton's equation of motion for roll (eqn. 6.4 (c)), which is used in the numerical model, takes the following modified form:

$$I_\theta \ddot{\theta} = M_\theta - b_\theta^V(\dot{\theta}) \qquad .....(8.9)$$

Comparing eqn. (8.7) with eqn. (8.9), it may be noted that both forms are essentially identical, since M_θ in eqn. (8.9) is determined by taking into account the combined contributions of δI_θ, b_θ^H, C_θ and $\tilde{M}_\theta$ terms. In addition to these, form (8.9) also implicitly includes terms arising from hydrodynamic coupling between the motions. Integration of eqn. (8.9) in the numerical model is trivial since the required additional informations ($\dot{\theta}$ values at several past steps, see eqn. (B.6)) for the time stepping procedure are being determined as the solution is advancing in time.

Results obtained by means of the above procedure are shown in Figure 8.16 - 8.18 in form of time histories of the responses for all the three wave steepnesses. The phase information and peak-to-peak values are summarized in Table 8.4. Comparing these results with the results without the inclusion of viscous effects (Figures 8.13 - 8.15 and Table 8.3), it is observed that the roll predictions have significantly improved, the differences in $\Delta\theta$ values are now around only 5%. The sway force and heave motion histories have remained practically unaltered (these are not graphically distinguishable except for a slight improvement in sway forces and a marginal improvement in heave motions for the largest steepness of $H/\lambda = 0.0275$). Also of interest is the observation that the wave profile at the location of probe no. 2 (which is at a distance of 0.6λ ahead of the body's CG) has remained uninfluenced by the decrease of roll motions.

For convenience of comparison, the roll values obtained with and without the inclusion of viscous damping are summarized in Table 8.5 which illustrates more clearly the improvements in roll predictions.

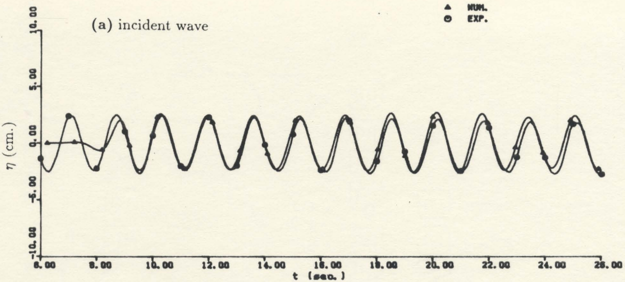

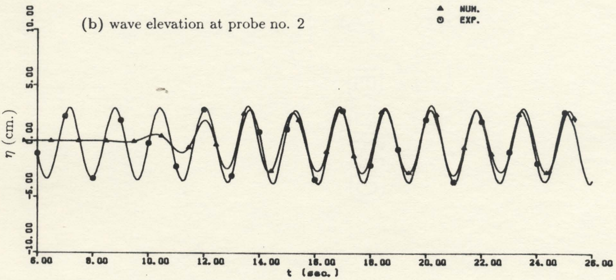

Figure 8.16 continued ⇓

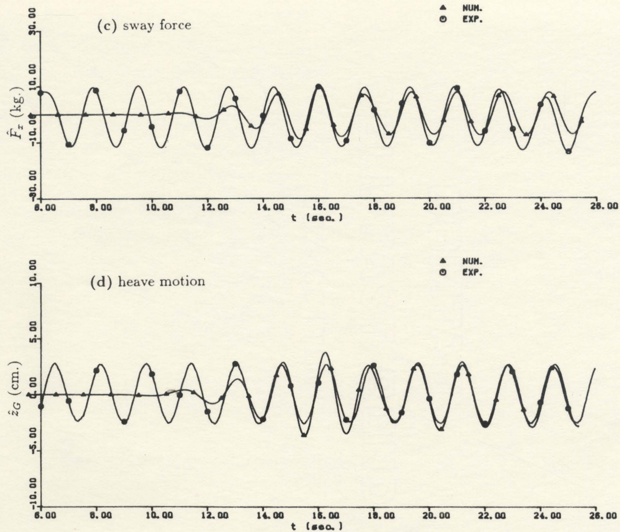

Figure 8.16 continued ⇓

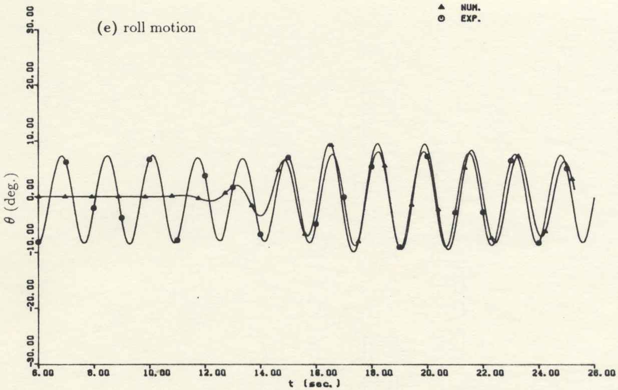

Figure 8.16 Comparison of experiment and theory for $\omega\sqrt{B/2g} = 0.5386$ and $H/\lambda = 0.0125$ when roll viscous damping is included in the numerical model ($T_1 \approx 14.5$ sec., $T_2 \approx 21.0$ sec.)

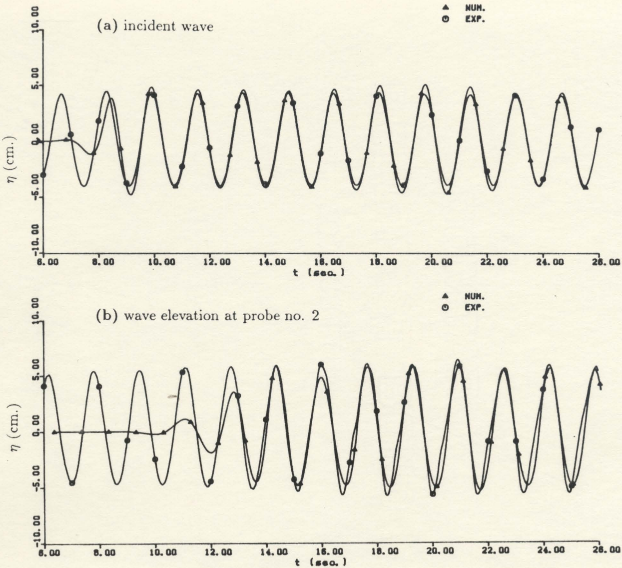

Figure 8.17 continued ⇓

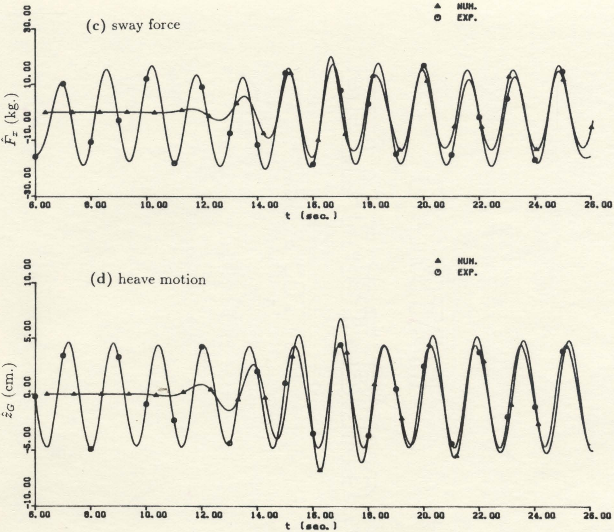

Figure 8.17 continued ⇓

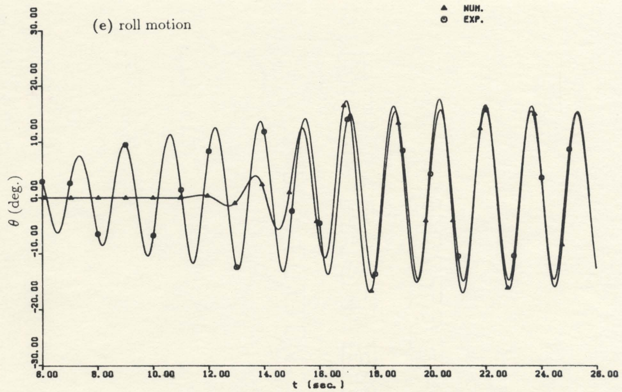

Figure 8.17 Comparison of experiment and theory for $\omega\sqrt{B/2g} = 0.5386$ and $H/\lambda = 0.0229$ when roll viscous damping is included in the numerical model ($T_1 \approx 14.5$ sec., $T_2 \approx 21.0$ sec.)

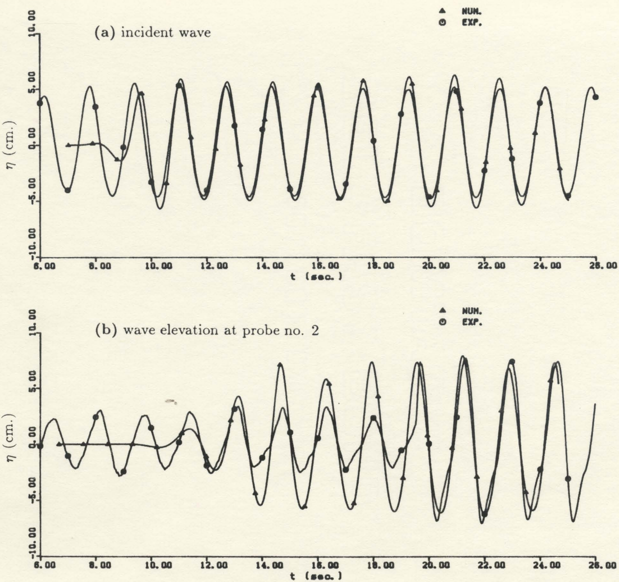

Figure 8.18 continued ⇓

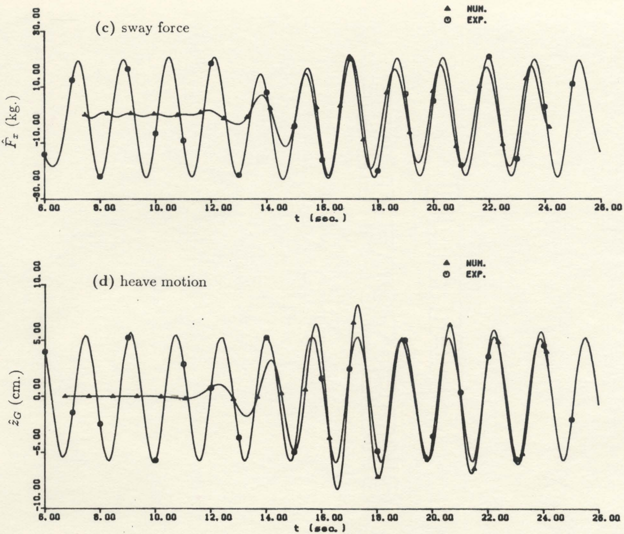

Figure 8.18 continued ⇓

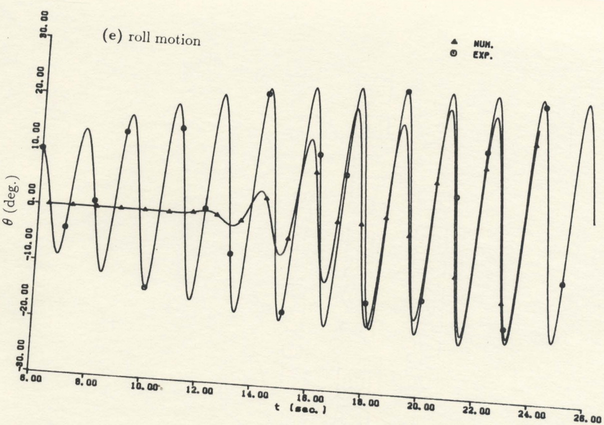

Figure 8.18 Comparison of theory and experiment for $\omega\sqrt{B/2g} = 0.5386$ and $H/\lambda = 0.0275$ when roll viscous damping is included in the numerical model ($T_1 \approx 14.5$ sec., $T_2 \approx 21.0$ sec.)

Table 8.4 Comparisons for sway force, heave and roll motions for test series C
(numerical model includes viscous roll damping)

$\frac{H_{num}}{H_{exp}}$	$\omega\sqrt{B/2g}$	λ/B	H/λ	Sway Force				Heave Motion				Roll Motion			
				$\lvert\bar{F}_x\rvert$	$\lvert\bar{F}_x\rvert$	ΔF_x	$\Delta\beta_F$	$\lvert\bar{z}_G\rvert$	$\lvert\bar{z}_G\rvert$	Δz_G	$\Delta\beta_z$	$\lvert\theta\rvert$	$\lvert\theta\rvert$	$\Delta\theta$	$\Delta\beta_\theta$
				(exp.)	(num.)	(%)	(deg.)	(exp.)	(num.)	(%)	(deg.)	(exp.)	(num.)	(%)	(deg.)
0.990	0.5386	9.63	0.0125	0.104	0.079	-24.0	15	0.28	0.29	2.5	0	18.0	19.0	4.5	15
0.989	0.5386	9.63	0.0229	0.172	0.151	-15.0	15	0.50	0.54	6.8	0	33.0	34.8	4.3	0
0.964	0.5386	9.63	0.0275	0.202	0.172	-17.0	15	0.565	0.625	6.6	0	43.9	42.8	-6.0	15

Table 8.5 Comparison of the roll results with and without inclusion of viscous roll damping in the numerical model

$\omega\sqrt{B/2g}$	H/λ	Exp.	Computed Results			
			without vis. damp.		with vis. damp.	
		$\|\theta\|$	$\|\theta\|$	$\Delta\theta(\%)$	$\|\theta\|$	$\Delta\theta(\%)$
0.5386	0.0125	18.0	21.3	17.3	19 .0	4.5
0.5386	0.0229	33.0	44	31.8	34.8	4.3
0.5386	0.0275	43.9	59.5	30.6	42.8	-6.0

8.3.4 Free Surface Elevations

Although measurements of free surface elevations were taken at several locations, comparison for the near-field flow (i.e. elevations at locations of probe nos. 3 and 5, cf. Figure 7.10) could not be carried out extensively due to difficulties in matching the time records. The wave elevations at this location show the influence of wave reflection from the body within a very short interval of time after the oncoming wave reaches this location (typically within 2 to 4 secs.). In some tests, specially for higher frequencies and steepnesses, the records contain reflection effects before the transient associated with the oncoming wave disappears (see e.g. Figure 7.11 (a)). This causes difficulties in matching the numerical and experimental results. The initial conditions are clearly not equivalent and consequently a direct comparison of this transient record is not available. A comparison of qualitative nature is however possible. Figures 8.19 (a) - (c) show the results from experiment and theory without synchronizing the records. The qualitative agreement is clearly noticeable.

Similar remarks apply to the flow on the other side of the body (at the location of probe no. 4, cf. Figure 7.9 or 7.10). This station is outside the computational domain for $\omega\sqrt{B/2g} > 0.89$ and therefore comparisons are not available. At this higher end of frequencies, virtually no energy was transmitted to the other side of the body. This feature is consistent in the numerical records, as can be seen from Figures 8.20 (a) - (c) where the free surface elevations from experiment and theory for several frequencies are shown (the numerical wave elevations are measured at a distance of λ downstream of the body's CG location).

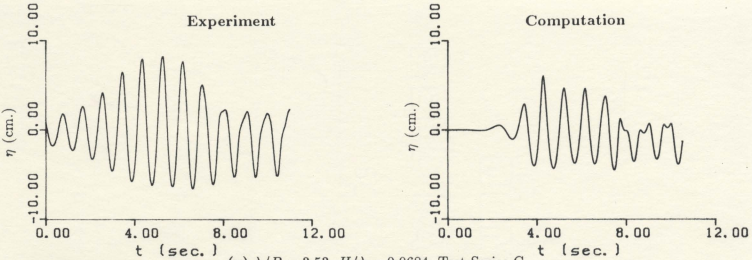

(a) $\lambda/B = 3.53$, $H/\lambda = 0.0684$, Test Series C

Figure 8.19 continued ⇓

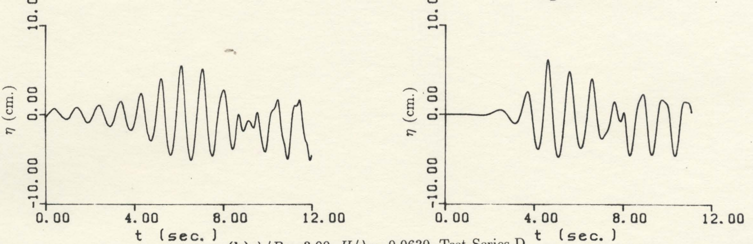

(b) $\lambda/B = 3.90$, $H/\lambda = 0.0630$, Test Series D

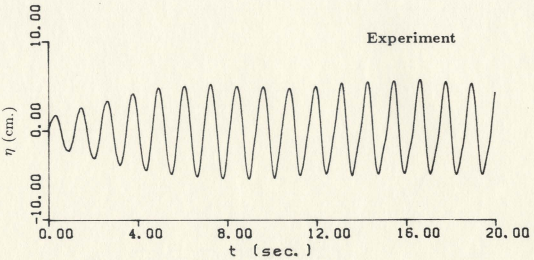

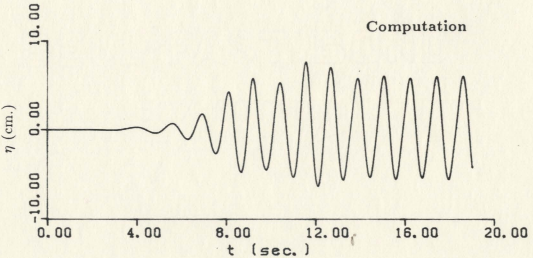

(c) $\lambda/B = 5.35$, $H/\lambda = 0.0386$, Test Series C

Figure 8.19 Wave elevations at the location of probe no. 3 (about 3.4 B ahead of the body); the experimental window is selected from a visual inspection of the record such that at the starting time the wave is still at a transient state and without the influence of reflection from the body; the experimental record is horizontally shifted for convenience of comparison.

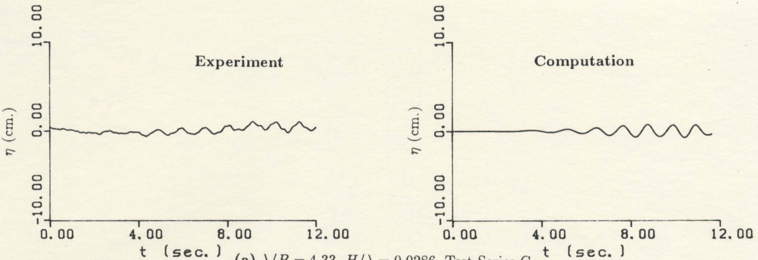

(a) $\lambda/B = 4.33$, $H/\lambda = 0.0286$, Test Series C

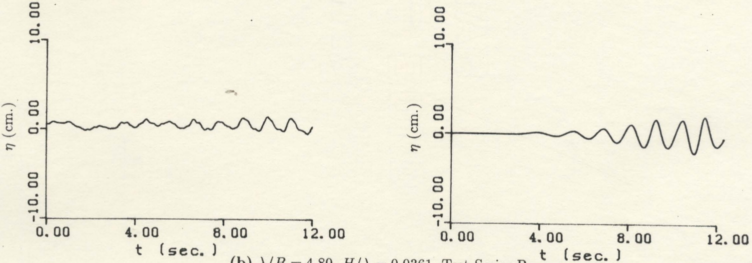

(b) $\lambda/B = 4.80$, $H/\lambda = 0.0361$, Test Series B

Figure 8.20 continued ⇓

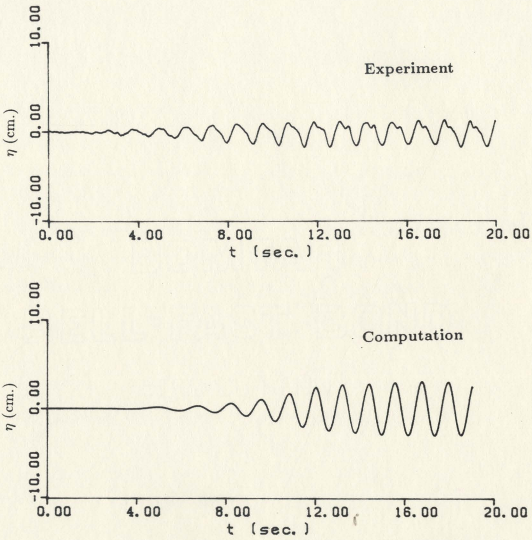

(c) $\lambda/B = 5.35$, $H/\lambda = 0.0386$, Test Series C

Figure 8.20 Wave elevations downstream of the body; the experimental record is for probe no. 4 while the numerical results are taken at a station located at λ downstream of the body; the window chosen for the experiment is such that it contains part of the transient information; this record is horizontally shifted for convenience of comparison.

In Figure 8.21 (a) - (e), we show the comparisons at the location of probe no. 2 (see Figure 7.9 or 7.10) for several frequencies. Although with regard to initial conditions, remarks made earlier apply, the plotted results are synchronized (since these records were used as a reference in synchronizing other records, see §8.2 above). Once more, most of the results are in good qualitative agreement. See for example, Figures 8.21 (a) - (d), where the amplifications and reductions in the elevations are similar between experiment and theory. At the lower end of the frequencies when the body begins to undergo relatively larger motions, the influence of reflection is smaller both in theory and experiment, as evidenced from Figure 8.21 (e) (see also (b) in Figures 8.13 - 8.18 presented earlier).

8.4 Discussion of the Results

The sway force results show discrepancies between 0 to 10% over most of the results. Although some of the results at higher frequencies show relatively larger discrepancies, no general trend indicating dependence of these differences on wave frequency or steepness could be observed. These few increased differences are believed to have resulted from experimental inaccuracies rather than errors in the numerical model. This is supported by the fact that the numerical results for the three test series at higher range of frequencies remained fairly consistent in force values, while the experimental force values lacked in consistency. Given that the body has displayed very small motions at these frequencies, the force amplitudes are expected to be fairly consistent in magnitudes. Indeed, the major source of experimental inaccuracies in the test data is perhaps in the force measurements, which is evidenced from examination of the measured force records. These records show some fluctuations for some of the tests, specially

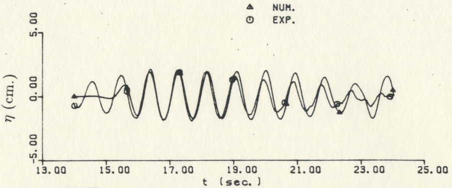

(a) $\omega\sqrt{B/2g} = 0.9874$, $\lambda/B = 3.20$, $H/\lambda = 0.0291$, Test Series C

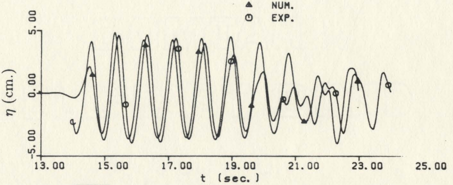

(b) $\omega\sqrt{B/2g} = 0.9874$, $\lambda/B = 3.20$, $H/\lambda = 0.0610$, Test Series C

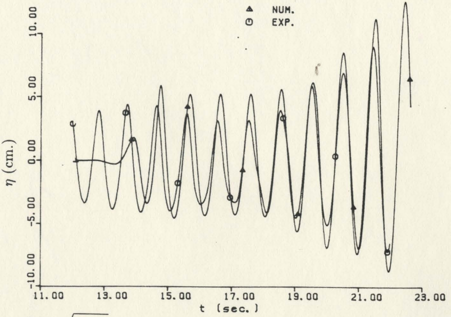

(c) $\omega\sqrt{B/2g} = 0.9425$, $\lambda/B = 3.53$, $H/\lambda = 0.0684$, Test Series C

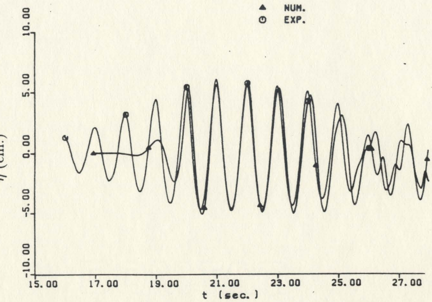

(d) $\omega\sqrt{B/2g} = 0.8527$, $\lambda/B = 4.33$, $H/\lambda = 0.0590$, Test Series D

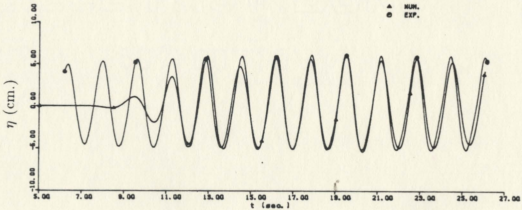

(e) $\omega\sqrt{B/2g} = 0.5386$, $\lambda/B = 9.63$, $H/\lambda = 0.0247$, Test Series D

Figure 8.21 Free surface elevations at the location of probe no. 2 : comparison between theory and experiment; the plots are synchronized and the window coincides with the selected window in presenting the force and motion results.

at higher frequencies (see e.g. the force histories shown in Figures 7.13 (a) - (c)). The problem is associated with the dynamometer which has a slight slack between its movable parts (the part that allows heaving). It should be pointed out that this instrument was originally designed for regular ship model towing tests in which the imposed forces are in one direction only while in the present experiment the forces are of oscillatory nature. Consequently some inaccuracies are unavoidable. With regard to force comparisons, another observation of interest is that the numerical model in general under-estimates the measured values (see Tables 8.2 (a) - (c)).

Considering the precision level of the dynamometer (see Table 7.3), the inaccuracies in the force histories do not appear to have resulted from the force tranducer itself. In order to assess the errors in the quoted peak-to-peak force values, comparisons have been made between the $|F_x|_{\text{exp}}$ values determined from the two repeated tests and also from the same record by choosing different window sizes, for a few randomly selected test cases. The values thus obtained scattered in the range of $\pm 4 - 10\%$, that is, the experimental results themselves fluctuate $\pm 4 - 10\%$ as a consequence of random factors inherent in the physical tests. This is felt to be the predominant source of error in the experimental results rather than the force tranducer. An average value of $\pm 7 - 8\%$ can be taken as a rough estimate of the errors in the quoted $|F_x|_{\text{exp}}$ values. This analysis indicates that the differences between the measured and computed peak-to-peak force values are mostly within experimental uncertainty (see Tables 8.2 (a) - (c)).

The agreement of heave results is very good. The discrepancies here are mostly less than 5% and increases slightly as the resonant frequency is approached. These increases in differences are perhaps attributable to viscous effects. Note that the numerical values over this frequency range consistently over-estimate the experimental values. The relatively large differences at a single frequency of $\omega\sqrt{B/2g} = 0.8078$ consistently in all the three tests have occurred due to an inaccuracy in the wave record from test series A at this frequency (the wave elevation records for the two repeated tests at this frequency showed a considerably larger difference than similar repeated tests at all other frequencies). An error estimate similar to the sway force results has not been carried out here, since the experimental time traces show practically no fluctuations. Here the uncertainty involved is primarily governed by the precision level of the measuring device (cf. Table 7.3). Considering the range of measured values, this uncertainty is estimated (conservatively) to be $\pm 2\%$. Similar remark applies for the roll measurements, and once more a conservative estimate of the uncertainty in the measured roll can be taken as $\pm 2\%$.

Comparison of the free heave results also shows good agreement between experiment and theory. Inspection of the results suggests that radiation damping predominates in heave motion. Considering the variation between the experimental results and the relative insignificance of viscous effects, no attempts were made to estimate and incorporate viscous damping in the numerical model, as was done for roll results. Note however that, albeit marginally, such a procedure would have improved the already good correlation of the heave results.

Except for the sway forces, the agreements for the heave and roll motions at $\omega\sqrt{B/2g} = 0.5386$ are very good when viscous effects are taken into account. Exclusion of viscous damping results in the expected over-predictions of roll motions. The slight over-predictions at the two lower steepnesses and a slight under-estimation for the steepest wave (see Table 8.4) may be attributed to the estimated viscous damping coefficients (which may introduce a small error, since these coefficients were considered independent of roll amplitudes). Nevertheless, the agreements are considered very good. With regard to sway forces, it is not clear whether the under-estimations resulted from a coupling between roll motion and sway forces in the numerical model. Careful observation however does not suggest so. See, for example, the force value at this frequency for test series D where the body has no roll motion. Although to a lesser extent, the numerical scheme nevertheless under-estimates the experiment. Also, the force values with and without inclusion of viscous damping have remained practically unaltered, suggesting that variations in roll amplitudes are inconsequential to the force history. As mentioned, experimental inaccuracies most certainly contribute to these differences. Another possible cause could be due to flow separation. At this value of $\lambda/B = 9.63$, an additional component of force (drag force) arising from flow separation is quite likely. Yet another possibility lies with the discretization of the boundary. To examine this, attempts were made to run the program with finer resolutions of the body contour. Unfortunately, for resolutions finer than that already used in the computations, the solution breaks down due to difficulties in locating the free surface and body intersection points. The numerical scheme does not appear to be able to handle large roll motions when collocation points are very close to the intersection point. This is most certainly related to a comparatively stronger singularity associated with large horizontal velocity components at these contact points.

The correlation of the phase information over the entire range of data is very satisfactory. Consideration of possible inaccuracies in compilation of the phase data (typically $\pm 10 - 20$ deg.) does not invalidate this general remark. Note that the relative phase differences between the three responses (F_x, z_G and θ) in experiment and theory are unaltered. Therefore, consistency in the differences between experiment and theory (i.e. comparable values of $\Delta\beta_F, \Delta\beta_z$ and $\Delta\beta_\theta$) confirms the quality of agreement, due to the coupled nature of the problem. As can be seen from Tables 8.2 (a) - (c), these values are fairly consistent over the entire set of data.

Considering the free surface elevations, the numerical model is found to reproduce flow evolutions in fairly good qualitative agreement with experiment. As noted earlier, differences in initial conditions did not permit a more thorough comparative study. The correlations between the input wave conditions are also very good. The relatively large difference at $\omega\sqrt{B/2g} = 0.7181$ in test series D occurred due to an erroneous choice of the H_{num} value.

Although much of the above discussion is focussed on the peak-to-peak values, considering that both the numerical and experimental systems are primarily of unsteady nature, correlation between the results is better judged by examining the comparative time records. To this end, relevant time histories showing the comparisons for rest of the data not included in this section are provided in appendix C.

8.5 Summarizing Remarks

In summary, taking into account possible experimental inaccuracies for unsteady tests of this nature, it would be fair to say that the agreement between the numerical model and experiment is between good and very good. It is worth noting that the experiments covered the following three ranges in which non-linearities in the system are not negligible:

(a) At higher frequencies and higher steepnesses, the near-field flow contains significant non-linearities. The free surface elevations in some conditions were found to be approaching the breaking limit. Indeed, in few of the tests, slight foam formation was observed (see Tables 7.5 (a) - (c)).

(b) Large heave motions of peak-to-peak displacements exceeding half of the body's draught were obtained. Analysis of the video-tape for these tests showed remarkable similarity of the run-up profiles with earlier computed results for an identical geometry in heave resonance (cf. Figure 6.10).

(c) Moderately large roll motions (ranging from 10 to 20 deg.) were obtained.

The results presented confirm the validity of the numerical method over the above ranges, in addition to the usual linear regime. It was also demonstrated that estimates of realistic values of roll can be obtained by such studies, provided viscous effects are duly accounted for.

9 Summary and Conclusions

9.1 Summary

A numerical algorithm has been presented for solution of a class of potential flow problems that contain a free surface. The method is based on an integral equation formulation in which the utilized integral relation is derived from Green's second identity. Despite the fact that the problems considered in this work is limited to two-dimensional flow phenomena, the formulation adopted is favoured over the strictly two-dimensional formulations based on Cauchy's integral theorem, in that possible future extensions in three dimensions can be envisioned. The procedure followed to discretize the boundary is in its simplest form in which the segments are straight lines and the collocation points are centrally placed. Some generality is maintained in the scheme detailed in §2 such that a variety of problems can be explored by prescribing appropriate initial conditions and boundary data. A suitable time-stepping algorithm for the treatment of the evolution equations for the boundary contour and data as appropriate, in conjunction with the solution of the integral relation in a discretized form, permits the solution to advance in time and follow the resulting fluid flow.

The solution algorithm is examined by applying it to three problems involving propagation of small amplitude surface waves for which linearized free surface conditions are applicable. The scheme is found to be sensitive on the imposed initial boundary data, which must be compatible to avoid adverse numerical effects. Results obtained in comparison with analytical solutions have shown that fluid motions of unsteady nature can be simulated over a considerable length of time with acceptable degree of precision.

Solutions for non-linear free surface motions are accomplished by taking into account the full non-linear free surface conditions. The procedure adopted for following the free surface motions allows only vertical displacements of the collocation points without translation, which differs from Lagrangian formulations where marked fluid particles are traced. The present formulation avoids the possibilities of particle clustering, which is believed to be intricately associated with the numerical stability characteristics of the solution, at the expense of the restriction to single-valuedness of the free surface contour.

Propagating unsteady steep waves are simulated by imposing a time-dependent velocity potential at one of the control boundaries encompassing a rectangular finite fluid region. This potential acts as a source of excitation to initiate motions in an initially unperturbed fluid, similar to a wave-maker. Prescription of an Airy wave potential as the excitation suffices this purpose. In order to preserve numerical stability, it is found necessary to apply a 'matching' technique, which is essentially a quadratic smoothing scheme in space. Application of this technique suppresses the instability which otherwise initiates at the intersection of the free surface and the boundary on which the excitation is applied. The root mechanism responsible for this instability is believed to be linked with the incompatibility of the free surface boundary conditions over the free surface at the intersection (hence the name 'matching' procedure). Additionally, the free surface contour and potential need to be smoothed. Numerical stability considerations are found to be crucial for the success of the algorithm, since initiation of instability at any instant results in rapid failure of the method.

Incorporation of a variant of Orlanski's radiation condition, which assumes the velocity potential at the downstream boundary to be travelling with the same celerity as on the upstream boundary, is found to make the downstream boundary sufficiently transmissive to the interior disturbances. A number of results are presented examining the efficacy of various numerical subcomponents embodied in the algorithm. Very steep non-breaking propagating waves are generated and subsequently followed over a considerable length of time, for example, over 20 wave periods. Results presented show that the solution remains well behaved over the entire simulation period and thereby demonstrate the robustness of the method.

Solutions for interactions of a steep propagating wave with a surface-piercing fixed rigid object is attained by introducing a vertical wall in the fluid region. Results presented in terms of the pressures, forces and run-up on the wall demonstrate that convergence to a steady state of the solution extending over several wave periods can be achieved. Comparison with perturbation solutions and available experimental data indicate that the algorithm is capable of producing results of excellent quality. The numerical solution is closely correlated with the experimental results, including the replication of certain non-linear features associated with the pressure histories not always obtainable by means of analytical solutions, such as double peaks in the pressure histories.

The solution algorithm is extended to simulate motions of a freely floating body subjected to the action of steep propagating waves by taking into account the equations of body motion and appropriate conditions on the body boundary. The problem is fully non-linear in that no approximations with regard to the motions of the body are necessary. Techniques are developed to overcome several numerical complications that arise in this problem. In particular, sensitivity of the algorithm to the discretization of the boundary leads to the necessity to regrid the body and free surface contours at every time step such that uniformity in the spatial grid sizes over the entire boundary can be retained. Another problem is associated with the evaluation of the dynamic component of the fluid pressure exerted on the body. This arises from the intricately coupled force-motion mechanism of the system, which in turn makes the algorithm very sensitive and numerically more demanding with respect to the evaluation of forces and motions. The problem is rectified by adopting a central difference rule for calculation of the dynamic pressure component at the predictor levels of the adopted Adams-Bashforth-Moulton rules, and following explicit rules for the integration of the equations of motion. Additionally, smoothing of the force histories is required.

A number of computed results are presented for ascertaining the effectiveness of the algorithm in simulating large-amplitude motions in steep waves. For most of the results shown, typically the oncoming wave has a steepness of $H/\lambda = 0.05$, since waves of larger steepnesses are found to cause excessive run-up and consequently result in a breakdown of the solution due to the occurrence of flooding. This is believed to be associated with two-dimensionality of the problem under consideration for which large run-ups are expected. Solutions exhibiting large heave and roll motions are achieved. Also simulated is oscillatory sway behaviour of completely unrestrained bodies.

In order that the simulated results can be relied upon, an experimental program was undertaken. The two-dimensionality of the flow was accomplished by constructing a channel inside the main wave tank. The body considered was of rectangular cross-section with rounded-off corners. The body displacements were restricted to heave and roll modes by means of an appropriate mounting device. The recorded measurements included heave and roll displacements, and sway force. In addition, free surface elevations were measured at several locations, with and without the presence of the body.

In comparing the results, possible differences in the initial conditions do not permit a thorough examination of the transient part of the results. Comparisons presented therefore primarily focus on the steady state behaviour of the forces and motions. The comparative time histories shown are synchronized by referencing the relevant records with respect to extrapolated undisturbed wave elevations at the body's centre of gravity, by means of which information on amplitudes and phases becomes available.

The agreement between the results is in general very satisfactory. The numerical model predicted the peak-to-peak values for the sway forces within 10% of the corresponding experimental values over most of the data range, many of which are within the estimated uncertainties of $\pm 7 - 8\%$ in the measured values. Similar values for heave displacements are even better. The differences here are mostly less than 5%, and once again close to the experimental uncertainties of $\pm 2\%$. The numerical values show a slight over-prediction in heave displacements at and in the vicinity of heave natural frequency, which may be due to additional damping effects arising from fluid viscosity which was not taken into account in the numerical model. Comparisons are also presented for free heave motions as well as for the evolution of free surface elevations at several locations. The qualitative and where possible quantitative agreements are found satisfactory.

Large roll motions were experimentally obtained for only one frequency in the vicinity of the roll natural frequency. The algorithm was found to yield comparatively larger roll displacements. This was evidently the influence of fluid viscosity not modelled in the potential flow solution algorithm. Subsequently, inclusion of viscous effects was found to improve the predictions considerably. The viscous damping moments were estimated from the roll decay test results and the simulation was carried out by incorporating these moments in the equation of roll motion. The predicted roll displacements, in terms of peak-to-peak values, were then found to be differing from the corresponding experimental values by only about 5%. Considering the estimated uncertainties of $\pm 2\%$ in the measured roll values, the comparisons are believed to be very good.

Taking into account possible experimental inaccuracies, the overall comparisons shown demonstrate that the algorithm is capable of producing reliable predictions over the full range of data tested, including large heave and moderately large roll displacements. The efficacy of the algorithm in simulating potential flow phenomena is demonstrated by these results. In addition, the results also demonstrate that a steady state behaviour for the motions can be accomplished.

All computations were performed in systems VAX 8500 and VAX 8800 of MUN. Typical CPU time for a total of 100 segments is about 15 sec. per time level in the latter system in single-precision arithmetic. Limited runs with double-precision arithmetic produced almost identical results.

9.2 Conclusions

Several concluding remarks related to the details of the algorithm have already been noted at the end of individual sections. Here the major conclusions that can be drawn from the work when considered as a whole are presented.

(i) Unsteady non-breaking steep waves progressing within a finite fluid region can be effectively modelled by imposing an Airy wave potential as a source of wave generation mechanism on a hypothetical vertical boundary. Application of a simplified condition, deduced from Orlanski's radiation condition, succeeds in transmitting the interior disturbances without apparent adverse effects to the interior solution and hence removes restrictions that otherwise are attached to this problem.

(ii) It is feasible to subject a surface-piercing object to a propagating wave and study the resulting responses and the flow evolution. The solution is fully non-linear. No approximations with respect to the steepness of the wave and body motions are made. The scope of applicability is however restricted to single-valued free surface elevations. Although the algorithm has not been applied to examine the responses of submerged bodies subjected to wave excitations, no major difficulties are anticipated for such applications; in principle the algorithm remains valid.

(iii) The solution can be advanced for sufficient length of time such that after the initial transients disappear, a steady state solution evolves extending over several wave periods. The length of the simulation time for which realistic predictions are available can be extended by enlarging the fluid domain, at the expense of additional computational efforts. In this respect, the upperbound on the simulation time is primarily dictated by limitations of available computing devices.

(iv) Confirmation of the computed results is exemplified by the comparative results presented at several levels. These include comparisons with linear and non-linear analytical solutions and available experimental results. Additionally, the algorithm is used to replicate a series of tests conducted by subjecting a partially restricted rectangular surface-piercing body to wave excitations. Good correlation observed between the results attests to the validity and reliability of the algorithm. The regime of comparison includes moderately large roll motions for which inclusion of viscous damping through a semi-empirical formulation proves necessary. This demonstrates how the algorithm based on potential flow assumptions can be effectively utilized to derive realistic estimates for modes of motions for which viscous effects are important.

(v) Numerical stability considerations are proved crucial for the success of the algorithm. Problems attached to this issue have occurred in several circumstances. Developed rectifying techniques include a matching procedure, avoidance of application of impulsive pressure and intermittent smoothing of the free surface. Further problems of similar nature arise from the coupling between forces and motions implicit in the simulation of partially or fully unrestrained bodies. Regridding at every time step, together with special considerations in evaluating forces and motions, provides an effective solution to these. Present computational experience leads to the conclusion that considerable emphasis must be placed on the issue of numerical stability. A previously reported stipulation suggesting that fulfilment of local Courant condition removes instabilities on the free surface (Dommermuth and Yue 1987) is found to be inadequate.

9.3 Further Developments

Despite considerable scope of applicability, developmental work of this nature is hardly terminal. The eventual goal is to be able to numerically simulate the behaviour of ships and offshore structures in realistic three-dimensional irregular stormy wave conditions. Although the work presented makes a modest contribution in that direction, it is still a prelude to such long term ambitious undertakings. Consequently, considerable scope for further developmental work exists. At the present time, the following works can be envisaged.

(i) The finite-difference and integration rules employed at a variety of levels in the algorithm can be systematically upgraded. A plethora of such rules exist (see Hilderbrand 1972). Incorporation of these is expected to improve the overall accuracy. More importantly, further relaxation of the grid sizes leading to reductions in computer time can be achieved.

(ii) The utilized boundary element formulation can be upgraded by adopting a higher order b.e.m. Further savings in computational efforts as well as possible improvements of accuracy are expected consequences.

(iii) The algorithm presently requires solution of the system of linear equations (2.10) at every time step. A possible means of affecting a reduction in computations is to investigate whether updating of the movable part of the boundary contour (∂D_F and ∂D_B) at every intermediate step can be avoided without reducing the overall accuracy beyond an acceptable level. Also, possibilities of utilizing iterative techniques for solution of the system of equations can be explored.

(iv) Some difficulties have been encountered in the treatment of the body-free surface intersection points while simulating large roll motions. This is believed to be due to the strength of the singularity at this point. It appears that the algorithm in its present form is not very suitable to accomodate a stronger singularity associated with large horizontal motion of the point, although not much difficulties are faced when the singularity is relatively weak. Improvements can be sought by incorporating the recently reported technique of treatment of this point (see §1.2.2.2 (b)). This issue is intimately related to (ii) above, since the discretization scheme in its present form is not directly amenable to such improvements[4].

(v) In contrast to all of the above modifications, work can be directed towards extensions to three-dimensional applications. This is believed to be more challenging. The method of generating a propagating steep wave will require re-examination since it is not yet known whether the procedure adopted here will necessarily hold good in three dimensions. Several parts of the methodology, however, are expected not to pose fundamental difficulties.

It may be noted that (i)-(iv) above relates to the efficiency of the algorithm. Notwithstanding these possible improvements, it is believed that the major contribution of this work has been to demonstrate that, in principle, large motions of floating bodies in non-linear waves can be effectively and reliably modelled.

[4]In a recent workshop (April 1988), further studies regarding this point have been reported by Joo and Schultz (1988) and Cointe (1988). Among these, the former authors' explored the analytical behaviour of the solution, while the latter provided a numerical treatment of this point. Both studies, however, suggest that reasonable accurate results can be obtained without any special treatment of the point, i.e. by simply avoiding this point from considering it as a collocation point, as the present results also showed. To keep the solution from 'blowing up', the numerical treatment suggested by the latter author can perhaps be implemented.

To the author's knowledge, many of the presented results, in particular, simulation of motions of floating bodies in a numerical wave tank, have not yet appeared in literature.

REFERENCES

Adachi, H. and Ohmatsu, S. 1980. On the time dependent potential and its application to wave problems. *Proc. 13th ONR Symp. Naval Hydro.*, Tokyo, pp. 281-302.

Ahlberg, J., Nilson, E. and Walsh J. 1967. *The theory of splines and their applications.* Academic press, New York.

Angell, T.S., Hsiao, G.C. and Kleinman, R.E. 1986. An integral equation for the floating body problem. *J. Fluid Mech*, **166**, pp. 161-171.

Alleney, S. 1981. A numerical study of water waves in sloping beaches. *Appld. Math. Modelling*, **5**, pp. 321-328.

Aref, H. 1986. The numerical experiment in fluid mechanics. *J. Fluid Mech.*, **173**, pp. 15-41.

Baddour, R.E. and Pawlowski, J.S. 1985. Some aspects of the implementation of the boundary element method. *N.A.C.E. Can. Reg. Conf. Integrated Prog. Corrosion Control*, Montreal, pp. 1-19.

Bai, K.J. and Yeung, R.W. 1974. Numerical solution to free surface flow problems. *Proc. 10th ONR Symp. Naval Hydro.*, Cambridge, Mass., pp. 609-647.

Baker, J.R., Meiron, D.I. and Orszag, S.A. 1981. Applications of a generalized vortex method to nonlinear free-surface flows. *Proc. 3rd Int. Conf. Num. Ship Hydro.*, Paris, pp. 179-191.

Baker, J.R., Meiron, D.I. and Orszag, S.A. 1982. Generalized vortex methods for free-surface flow problems. *J. Fluid Mech.*, **123**, pp. 477-501.

Banerjee, P.K. and Butterfield, R. 1981. *Boundary element methods in engineering sciences.* McGraw Hill.

Bass, D.W and Haddara, M.R. 1988. Non-linear models of ship roll damping. *Int. Ship. Prog., in press.*

Batchelor, G.K. 1967. *An introduction to fluid dynamics.* Cambridge Univ. Press.

Beck, R.F and Liapis, S. 1987. Transient motions of floating bodies at zero forward speed. *J. Ship Res.*, **31**, 3, pp. 164-176.

Betts, P.C. and Assaat, M.I. 1981. Finite element computation of large amplitude water waves. *Proc. 2nd Int. Conf. Finite Elements in Fluids*, Alberta, Canada, **2**, pp. 24-32.

Biesel, F. 1951. Les Appareils Generateures de houle en Laboratoire. *La Houille Blanche*, **6**, pp. 147-165.

Bourianoff, G.I. 1981. Three-dimensional time-dependent nonlinear ship motion simulation using the inertial marker particle technique. *Proc. 3rd Int. Conf. Num. Ship Hydro.*, Paris, pp. 249-256.

Bourianoff, G.I. and Penumalli, B.R. 1977. Numerical simulation of ship motion by Eulerian hydrodynamic techniques. *Proc. 2nd Int. Conf. Num. Ship Hydro.*, Berkely, Calif., pp. 358-370.

Breit, S.R., Newman, J.N. and Sclavounos, P.D. 1985. A new generation of panel programs for radiation-diffraction problems. *Proc. 3rd Int. Conf. Beh. Off. Str. (BOSS)*, Elsevier Sc. Pub. B.V., pp. 531-544.

Brevig, P., Greenhow, M. and Vinje, T. 1982. Extreme wave forces on submerged energy devices. *Appld. Ocean Res.*, **4**, 4, pp. 219-225.

Burton, A.J. and Miller, G.F. 1971. The application of integral equation methods to the solution of some exterior boundary value problems. *Proc. Royal Soc. Lond.* **A. 323**, pp. 201-210.

Calisal, S.M. and Chan, J.L.K. 1987. Breaking wave simulation. *Proc. Second International Workshop on Water Waves and Floating Bodies*, Rep. No. AM-87-6, Univ. Bristol, pp. 9-12.

Chakrabarti, S.K. 1972. Nonlinear wave forces on a vertical cylinder. *J. Hydraulic Div.*, Proc. ASCE, HY11, **96**, pp. 1895-1909.

Chakrabarti, S.K. 1975. Second order wave forces on a large vertical cylinder. *J. Water. Harbor Coast. Eng. Div.*, Proc. ASCE, WW3, **101**, pp. 311-317.

Chakrabarti, S.K. 1987. *Hydrodynamics of offshore structures.* Computational Mechanics Publications.

Chamberlain, R.R. and Yen, S.M. 1985. Numerical solution of the nonlinear ship wave problem. *Proc. 4th Int. Conf. Num. Ship Hydro.*, National Academy of Sciences, Washington,D.C., pp. 246-258.

Chan, R.K-C. 1975. Two-dimensional time dependent calculation of large amplitude surface gravity waves due to a surface disturbance. *Proc. 1st Int. Conf. Num. Ship Hydro.*, Gaithersburg, Md., pp. 315-332.

Chan, R.K-C. 1977. Finite difference simulation of the planer motion of a ship. *Proc. 2nd Int. Conf. Num. Ship Hydro.*, Berkeley, Calif., pp. 39-52.

Chan, R.K-C. and Chan, F.W-K. 1980. Numerical solution of transient and steady free surface flows about a ship of generalized hull shape. *Proc. 13th ONR Symp. Naval Hydro.*, Tokyo, pp. 257-280.

Chan, R.K.C. and Hirt, C.W. 1974. Two-dimensional calculations of the motions of floating bodies. *Proc. 10th ONR Symp. Naval Hydro.*, Cambridge, Mass., pp. 667 -682.

Chan, R.K-C and Street, R.L. 1970. A computer study of finite amplitude water waves. *J. Comp. Phy.*, **6**, pp. 68-94.

Chapman, R.B. 1979. Large amplitude transient motions of two dimensional floating bodies. *J. Ship Res.*, **23**, 2, pp. 20-31.

Cointe, R. 1988. Remarks on the numerical treatment of the intersection point between a rigid body and a free surface. *Third International Workshop on Water Waves and Floating Bodies*, Woods Hole, Mass., April 10-13.

Cointe, R., Jami, A. and Molin, B. 1987. Nonlinear impulsive problems. *Proc. Second International Workshop on Water Waves and Floating Bodies*, Rep. No. AM-87-06, Univ. Bristol, pp. 13-16.

Cokelet, E.D. 1977. Steep gravity waves in water of arbitrary uniform depth. *Philosophical Transactions, Royal Soc. Lond.*, Séries A, **286**, pp. 183-230.

Debnath, L. and Rahman, M. 1981. A theory of nonlinear wave loading on offshore structures. *Int. J. Math. Sc.*, **4**, pp. 589-613.

Dean, R.G. 1965. Stream function representation of nonlinear ocean waves. *J. Geophysical Res.*, **70**, pp. 4561-4572.

Demirbilek, Z. and Gaston, J.D. 1985. Nonlinear wave loads on a vertical cylinder. *Ocean Engng.*, **12**, 5, pp. 375-385.

Dold, J.W. and Peregrine, D.H. 1986. An efficient boundary-integral method for steep unsteady water waves. in *Numerical Methods for Fluid Dynamics II.* Ed. K.W. Morton and M.J. Baines, Oxford Univ. Press., pp. 671-679.

Dommermuth, D.C. and Yue, D.K.P. 1986a. Numerical methods for nonlinear two-dimensional wave : regridding versus smoothing. *First International Workshop on Water Waves and Floating Bodies*, MIT, Cambridge, Mass.

Dommermuth, D.G. and Yue, D.K.P. 1986b. Study of nonlinear axisymmetric body-wave interactions. *Proc. 16th ONR Symp. Naval Hydro.*, National Academic Press, Washington,D.C., pp. 116-136.

Dommermuth, D.G. and Yue, D.K.P. 1987. Numerical simulations of nonlinear axisymmetric flows with a free surface. *J. Fluid Mech.*, **178**, pp. 195-219.

Eatock Taylor, R. and Jefferys, E.R. 1986. Variability of hydrodynamic load prediction for a tension leg platform. *Ocean Engng.*, **13**, pp. 449-490.

Endo, O.H. 1987. Shallow water effect on the solution of three dimensional bodies in waves. *J. Ship Res.*, **31**, 1, pp. 34-40.

Evans, D.V. and Newman, J.N. 1987. Report on the first international workshop on water waves and floating bodies. *J. Fluid Mech.*, **174**, pp. 521-528.

Faltinsen, O.M. 1977. Numerical solution of transient nonlinear free-surface motion outside or inside moving bodies. *Proc. 2nd Int. Conf. Num. Ship Hydro.*, Berkeley, Calif., pp. 347-357.

Faltinsen, O.M. 1978. A numerical nonlinear method of sloshing in tanks with two dimensional flow. *J. Ship Res.*, **22**, 3, pp. 193-202.

Faltinsen, O.M. 1985. Hydrodynamic loads on marine structures. *IUTAM Theoretical and Applied Mechanics*, Ed. F.I. Niordson and N. Olhoff, Elsevier Sc. Pub. B.V., pp. 117-133.

Faltinsen, O.M. and Michelsen, F.C. 1974. Motions of large structures at zero froude number. *Int. Symp. Dynamics Mar. Veh. Str. Waves*, pp. 91-106.

Fenton, J.D. 1972. A ninth-order solution for the solitary wave. *J. Fluid Mech.*, **53**, pp. 257-271.

Fenton, J.D. 1979. A high-order cnoidal wave theory. J. Fluid Mech., **94**, pp. 129-161.

Fenton, J.D. 1985. Wave force on vertical walls. *J. Water. Port Coast. Ocean Div.*, Proc. ASCE, **111**, pp. 693-718.

Fenton, J.D. and Rienecker, M.M. 1982. A Fourier method for solving nonlinear water wave problems : application to solitary wave interactions. *J. Fluid Mech.*, **118**, pp. 411-443.

Finkelstein, A.B. 1957. The initial value problem for transient water waves. *Comm. Pure Appld. Math.*, **10**, pp. 511-522.

Finnigan, T.D. and Yamamoto, T. 1979. Analysis of semi-submerged porous breakwaters. *Proc. Civil Eng. Oceans*, San Fransisco, Calif., pp. 380-397.

Forsythe, G. and Moler, C.B. 1967. *Computer solution of linear algebraic equations.* Chapter 9, Prentice-Hall, Inc., Englewood, Cliff., N.J.

Garrison, C.J. 1974. Hydrodynamics of large objects in the sea : part I. hydrodynamic analysis. *J. Hydronautics*, **8**, pp. 5-12.

Garrison, C.J. 1975. Hydrodynamics of large objects in the sea : part II. motions of free floating bodies. *J. Hydronautics*, **9**, pp.58-63.

Garrison, C.J. 1984a. Nonlinear wave loads on large structures. *Proc. 3rd Int. Conf. Off. Mech. Arc. Eng.*, New Orleans, Lousiana, pp. 128-135.

Garrison, C.J. 1984b. Wave-structure interaction. *Proc. Speciality Conf. Comp. Meth. Off. Eng.*, Halifax, pp. 1-72.

Garrison, C.J. and Berklite, R.B. 1972. Hydrodynamic loads induced by earthquakes. *Proc. 4th Off. Tech. Conf.*, paper no. 1554, Houston, pp. 429-442.

Garrison, C.J. and Seetharama Rao, V. 1971. Interaction of waves with submerged objects. *J. Water. Harbor Coast. Div.*, Proc. ASCE, **97**, pp. 257-277.

Geers, T.L. 1982. A boundary element method for slamming analysis. *J. Ship Res.*, **26**, 2, pp. 117-124.

Goda, Y. 1967. The fourth order approximation to the pressure of standing waves. *Coastal Engineering in Japan*, **10**, pp. 1-11.

Greenhow, M. 1987. Water entry an exit of a horizontal cylinder. *Proc. Second International Workshop on Water Waves and Floating Bodies*, Rep. No. AM-87-6, Univ. Bristol, pp. 25-28.

Greenhow, M. 1988. Wedge entry into initially calm water. *Appld. Ocean Res.*, *in press.*

Greenhow, M. and Lin, W.M. 1983. Nonlinear free surface effects : experiments and theory. *MIT Dept. of Ocean Eng. Rep. No. 83-19.*

Greenhow, M. and Lin, W.M. 1985. Numerical simulation of free surface flows generated by wedge-entry and wave-maker motions. *Proc. 4th Int. Conf. Num. Ship Hydro.*, National Academy of Sciences, Washington,D.C., pp. 94-106.

Greenhow, M., Vinje, T., Brevig, P. and Taylor, J. 1982. A theoretical and experimental study of the capsize of Salter's duck in extreme waves. *J. Fluid Mech.*, **118**, pp. 221-239.

Han, F.S. and Stansby, P.K. 1987. On the application of the boundary element method to two-dimensional free surface interactions with bodies. *Proc. Second International Workshop on Water Waves and Floating Bodies*, Report. No. AM-87-06, Univ. of Bristol, pp. 39-42.

Harns, V.W. 1987. Steady wave-drift of modeled ice floes. *J. Water. Port Coast. Ocean Eng.*, **113**, 6, pp. 602-622.

Haussling, H.J. and Coleman, R.M. 1977. Finite-difference computations using boundary fitted coordinates for free-surface potential flows generated by submerged bodies. *Proc. 2nd Int. Conf. Num. Ship Hydro.*, Berkeley, Calif., pp. 221-233.

Haussling, H.J. and Coleman, R.M. 1979. Nonlinear water wave generated by an accelerated circular cylinder. *J. Fluid Mech.*, **92**, pp. 767-781.

Hess, J.L. 1973. Higher order numerical solution of the integral equation for the two-dimensional Neumann problem. *J. Comp. Meth. Appld. Mech. Eng.*, **2**, pp. 1-15.

Hess, J.L. 1975. The use of higher order surface singularity distribution to obtain improved potential flow solutions for the two-dimensional lifting airfoils. *J. Comp. Meth. Appld. Mech. Eng.*, **5**, pp. 11-35.

Hess, J.L. and Smith, A.M.O. 1964. Calculation of non-lifting potential flow about arbitrary three dimensional bodies. *J. Ship Res.*, **8**, pp. 22-44.

Hess, J.L. and Smith, A.M.O. 1967. Calculation of potential flow about arbitrary bodies. *Progress in Aero. Sc.*, Ed. D. Kuchemann, Pargamon Press, **8**, pp. 1-138.

Hilderbrand, F.B. 1972. *Introduction to numerical analysis.* McGraw Hill, New York.

Himeno, Y. 1981. Prediction of ship roll damping - a state of the art. *University of Michigan Dept. of Naval Arch. Rep. No. 239*, 65 pp.

Hunt, J.N. and Baddour, R.E. 1981. The diffraction of nonlinear progressive waves by a vertical cylinder. *Qt. J. Mech. Appld. Math.*, **34**, pp. 69-87.

Ijima, T. and Yoshida, A. 1976. Method of analysis for two-dimensional water wave problems. *Proc. 15th Coast. Eng. Conf.*, Hawaii, pp. 2717-2736.

Isaacson, M. St. Q. 1977. Shallow water wave diffraction around large cylinders. *J. Water. Port Coast. Ocean Div.*, Proc. ASCE, WW1, **103**, pp. 69-82.

Isaacson, M. St. Q. 1982. Nonlinear wave-effects on fixed and floating bodies. *J. Fluid Mech.*, **120**, pp. 267-281, *also* Corrigendum, **133**, pp. 469.

Isaacson, M. St. Q. 1983a. Solitary wave diffraction around large cylinders. *J. Water. Port Coast. Ocean Div.*, Proc. ASCE, **109**, WW1, pp. 121-127.

Isaacson, M. St. Q. 1983b. Steep wave forces on large offshore structures. *Soc. Petro. Eng. J.*, **23**, 1, pp. 184-190.

Isaacson, M. St. Q. 1985. Recent advances in the computation of nonlinear wave effects on offshore structures. *Can. J. Civil Eng.*, **12**, 3, pp. 439-452.

Israeli, M. and Orszag, S.A. 1981. Approximation of radiation boundary conditions. *J. Comp. Physics*, **4**, pp. 115-135.

Jensen, R.S. 1987. On the numerical radiation condition in the steady state wave problems. *J. Ship Res.*, **31**, 1, pp. 14-22.

Joo, S.W. and Schultz, W.W. 1988. Evolution of nonlinear waves due to a moving wall. *Third International Workshop on Water Waves and Floating Bodies*, Woods Hole, Mass., April 10-13.

Katopodes, N.D. and Wu, C-T. 1987. Computation of finite-amplitude dispersive waves. *J. Water Port Coast. Ocean Eng.*, Proc. ASCE, **113**, 4, pp. 327-346.

Kellog, O.D. 1929. *Foundations of potential theory*. Berlin Springer.

Kim, M.H. 1987. Second order diffracted waves around an axisymmetric body. *Proc. Second International Workshop on Water Waves and Floating Bodies*, Rep. No. AM-87-06, Univ. Bristol, pp. 59-63.

Kim, Y.J. and Hwang, J.H. 1986. Two-dimensional transient motions with large amplitude by time-domain method. *Proc. 16th ONR Symp. Naval Hydro.*, National Academic Press, Washington,D.C., pp. 415-426.

Kleinman, R.E. 1982. On modified green functions in exterior problems for the Helmholtz equation. *Proc. Royal Soc. Lond.*, **A. 383**, pp. 313-333.

Kobayashi, N., Otta, A.K. and Roy, I. 1987. Wave reflection and run-up on rough slopes. *J. Water. Port Coast. Ocean Eng.*, Proc. ASCE, **113**, pp. 282-298.

Korsmeyer, F.T. 1987. On the first- and second-order time-domain radiation problems. *Proc. Second International Workshop on Water Waves and Floating Bodies*, Rep. No. AM-87-06, Univ. Bristol, pp. 69-72.

Kravtchenko, J. 1954. Remarques sur le Calcul des Amplitudes de la Houle Lineaire Engendree par un Batteur. *Proc. 5th Conf. Coastal Eng.*, Council on Wave Research, France, pp. 50-61.

Kyozuka, Y. 1982. Experimental study on second-order forces acting on cylindrical bodies in waves. *Proc. 14th Symp. Naval Hydro.*, Tokyo, pp. 319-382.

Lamb, Sir H. 1945. *Hydrodynamics*, 6th Printing, Dover Pub.

Lee, C.M. 1968. The second order theory of heaving cylinders in a free surface, *J. Ship Res.*, **11**, pp. 313-327.

Lee, M-Y. 1985. Unsteady fluid-structure interaction in water of finite depth. *Ph.D. Thesis*, University of Calif. Berkeley, 105 p.

Lewis, E.V. 1977. Motions of ships in waves. Sec. 9 in *Principles of Naval Architecture*, edited by J.P. Comstock, SNAME, New York, pp. 607-717.

Ligget, J.W. 1977 Location of free surface in porous media. *J. of Hydraulics Div.*, Proc. ASCE, **103**, pp. 353-365.

Lighthill, J. 1979. Waves and hydrodynamic loading. *Proc. 2nd Int. Conf. Beh. Off. Str. (BOSS)*, Elsevier Pub. B.V., pp. 1-40.

Lighthill, J. 1986. Fundamentals concerning wave loading on offshore structures. *J. Fluid Mech.*, **173**, pp. 667-681.

Lin, W.M. 1984. Nonlinear motion of the free surface near a moving body. *Ph.D. Thesis*, Dept. Ocean Eng., MIT, 127 p.

Lin, W.M., Newman, J.N. and Yue, D.K.P. 1984. Nonlinear forced motions of floating bodies. *Proc. 15th ONR Symp. Naval Hydro.*, National Academy Press, Washington,D.C., pp. 33-49.

Longuet-Higgins, M.S. and Cokelet, E.D. 1976. The deformation of steep surface waves on water : I. a numerical method of computation. *Proc. R. Soc. Lond.*, Series A, **350**, pp. 1-26.

Longuet-Higgins, M.S. 1986. Eulerian and Lagrangian aspects of surface waves. *J. Fluid Mech.*, **173**, pp. 683-707.

Liu, P.L-F. and Ligget, J.A. 1979. Boundary solutions to two problems in porous media. *J. Hydraulics Div.*, Proc. ASCE, HY3, pp. 171-183.

Lu, C.C., Wang, J.D. and Le Mehaute, B. 1987. Boundary integral equation method for limit surface gravity waves. *J. Water. Port Coast. Ocean Div.*, Proc. ASCE, **113**, 4, pp. 347-363.

MacCamy, R.C. and Fuchs, R.A. 1954. Wave forces on piles : a diffraction theory. *Tech. Memo No. 69, Beach Erosion Board*, U.S. Army Corps. Engineering.

Mei, C.C. 1978. Numerical methods in water-wave diffraction and radiation. *Ann. Rev. Fluid Mech.*, **10**, pp. 393-416.

Mei, C.C. 1983. *Applied dynamics of ocean surface waves.* John Wiley & Sons.

Miche, R. 1944. Mouvements ondulatoires de la mer en profondeur croissante ou decroissante. *Annales des Ponts et Chausses.*

Miles, J.W. 1980. Solitary waves. *Ann. Rev. Fluid Mech.*, **12**, pp. 11-43.

Miloh, T. 1980. Irregularities in the solution of the nonlinear wave diffraction problem by vertical cylinder. *J. Water. Port Coast. Ocean Eng. Div.*, Proc. ASCE, **106**, pp. 279-284.

Miyata, H., Kajitani, H. Zhu, M. and Kawano, T. 1986. Nonlinear forces caused by breaking waves. *Proc. 16th Symp. Naval Hydro.*, National Academic Press, Washington,D.C., pp. 514-536.

Miyata, H., Nishimura, S. and Kajitani, H. 1985. Finite-difference simulation of non-breaking 3-D bow waves and breaking 2-D bow waves. *Proc. 4th Int. Conf. Num. Ship Hydro.*, National Academy of Sciences, Washington,D.C., pp. 259-292.

Miyata, H., Nishimura, S. and Masuko, A. 1985. Finite-difference simulation of nonlinear waves generated by ships of arbitrary three-dimensional configuration. *J. Comp. Phy.*, **60**, 3, pp. 391-436.

Miyata, H. and Nishimura, S. 1985. Finite-difference simulation of nonlinear ship waves. *J. Fluid Mech.*, **157**, pp. 327-357.

Molin, B. 1979. Second order diffraction loads upon three dimensional bodies. *Appld. Ocean Res.*, **1**, pp. 197-202.

Morison, J.R., O'Brien, M.P., Johnson, J.W. and Scharf, S.A. 1950. The forces exerted by surface waves on piles. *Tech. Rep. No. 2846*, Trans. American Inst. Mining, Metal. and Pet. Eng., **189**, pp. 149-154.

Moore, D.W. 1981. On the point vortex method. *SIAM J. Sc. Stat. Comp.*, **2**, pp. 65-84.

Muggeridge, D.B. and Murray, J.J. 1981. Calibration of a 58 m. wave flume. *Can. J. Civil Eng.*, **8**, 4, pp. 449-455.

Nagai, S. 1969. Pressures of standing waves on vertical wall. *J. Water. Harbor Div.*, Proc. ASCE, WW1, **95**, pp. 53-76.

New, A.L., McIver, P. and Peregrine, D.H. 1985. Computation of overturning waves. *J. Fluid Mech.*, **150**, pp. 233-251.

Newman, J.N. 1980. *Marine Hydrodynamics.* 3rd printing, The MIT Press, Camb., Mass., ix + 402 p.

Newman, J.N. 1984. Double-precision evaluation of the oscillatory source potential. *J. Ship Res.*, **28**, pp. 151-154.

Newman, J.N. 1985a. Transient axisymmetric motion of a floating cylinder. *J. Fluid Mech.*, **157**, pp. 17-33.

Newman, J.N. 1985b. Algorithms for the free-surface Green function. *J. Eng. Math.*, **19**, pp. 57-67.

Newman, J.N. 1985c. Evaluation of free-surface Green's functions. *Proc. 4th Int. Conf. Num. Ship Hydro.*, National Academy of Sciences, Washington,D.C., pp. 4-23.

Nichols, B.D. and Hirt, C.W. 1973. Calculating three dimensional free surface flows in the vicinity of submerged and exposed structures. *J. Comp. Phy.*, **12**, pp. 234-246.

Nichols, B.D. and Hirt, C.W. 1975. Methods for calculating multi dimensional transient free surface flows. *Proc. 1st Int. Conf. Num. Ship Hydro.*, Gaithersburg, Md., pp. 253-277.

Nichols, B.D. and Hirt, C.W. 1977. Nonlinear hydrodynamic forces on floating bodies. *Proc. 2nd Int. Conf. Num. Ship Hydro.*, Berkeley, Calif., pp. 382-394.

Noblesse, F. 1982. The Green function in the theory of radiation and diffraction of regular water waves by a body. *J. Eng. Math.*, **16**, pp. 137-169.

Ogilvie, T.F. 1963. First and second order forces on cylinders submerged under a free surface. *J. Fluid Mech.*, **16**, pp. 451-472.

Ogilvie, T.F. 1983. Second order hydrodynamic effects on ocean platforms. *Proc. International Workshop on Ship and Platform Motions*, Berkeley, Calif., pp. 205-265.

Ohring, S. and Telste, J.C. 1977. Numerical solution of transient three-dimensional ship wave problems. *Proc. 2nd Int. Conf. Num. Ship Hydro.*, Berkeley, Calif., pp. 88-103.

Orlanski, J. 1976. A simple boundary condition for unbounded hyperbolic flows. *J. Comp. Phy.*, **21**, pp. 251-269.

Papanikolaou, A. and Nowacki, H. 1980. Second order theory of oscillating cylinders in a regular steep wave. *Proc. 13th ONR Symp. Naval Hydro.*, Tokyo, pp. 303-333.

Papanikolaou, A. and Zaraphonitis, G. 1987. On the second order steady motions of 3D bodies in waves. *Proc. Second International Workshop on Water Waves and Floating Bodies*, Rep. No. AM-87-06, Univ. Bristol, pp. 89-93.

Pawlowski, J.S. 1985. Elements of kinematics and dynamics of the rigid body in Cartesian tensor notation. *Technical Rep. No. MTB 160*, IMD, NRCC, St. John's.

Pawlowski, J.S. 1987. Hydrodynamic loads and responses of marine structures. *The Can. Eng. Centennial Convention*, Montreal, pp. 1-29.

Penney, W.G. and Price, A.T. 1952. Some gravity wave problems in the motion of perfect fluids. *Philosophical Transactions, Royal Soc. Lond.*, Series A, **244**, 882, pp. 154-184.

Pinkster, J.A. 1976. Low frequency second order wave exciting forces on floating structures. *Publ. No. 650*, NSMB, Wageningen, Netherlands, 204 p.

Pinkster, J.A. 1979. Mean and low frequency wave drifting forces on floating structures. *Ocean Engng.*, **6**, pp. 593-615.

Polozhiy, G.N. 1967. *Equations of mathematical physics.* Haden Book Com., Chap. 3, pp. 62-154.

Potash, R.L. 1971. Second order theory of oscillating cylinders. *J. Ship Res.*, **14**, pp. 295-324.

Rahman, M. 1984. Wave diffraction by large offshore structures : an exact second order theory. *Appld. Ocean Res.*, **6**, 2, pp. 90-100.

Rahman, M. and Chakravartty, C. 1981. Hydrodynamic loading calculation for offshore structures. *Appld. Math.*, **6**, pp. 593-615.

Raman, H. and Venkatanarasaiah, P. 1976. Forces due to nonlinear waves on vertical cylinders. *J. Water. Harbor Coast. Eng. Div.*, Proc. ASCE, WW3, **103**, pp.301-316.

Raman, H., Jothishankar, N. and Venkatanarasaiah, P. 1977. Nonlinear wave interaction with vertical cylinder of large diameter. *J. Ship Res.*, **21**, pp. 120-124.

Rawson, K.J. and Tupper, E.C. 1976. *Basic ship theory.* Vol. I, Longman, London.

Rienecker, M.M. and Fenton, J.D. 1981. A Fourier approximate method for steady water waves. *J. Fluid Mech.*, **104**, pp. 119-137.

Roache, P. 1972. *Computational Fluid Dynamics.* Hermosa Pub.

Roberts, A.J. 1983. A stable and accurate numerical method to calculate the motion of a sharp interface between fluids. *J. Appld. Math.*, **31**, pp. 13-35.

Roberts, A.J. 1987. Transient free surface flows generated by a moving vertical plate. *Qt. J. Mech. Appld. Math.*, **40**, Part 1, pp. 129-158.

Sabuncu, T. and Goren, O. 1985. Second order vertical and horizontal force on a vertical dock. *Ocean Engng.*, **12**, pp. 341-361.

Sahin, J. and Magnuson, A.H. 1984. A numerical method for the solution of a line source under a free surface. *Ocean Engng.*, **11**, 5, pp. 451-561.

Salvesen, N. and von Kerczek, C. 1976. Comparison of numerical and perturbation solutions of two dimensional nonlinear water wave problems. *J. Ship Res.*, **20**, 3, pp. 160-170.

Sarpkaya, T. and Isaacson, M. St. Q. 1979. *Mechanics of wave forces on offshore structure.* Van Nostrand Reinhold.

Schultz, W.W. 1987. A complex-valued integral method for free surfaces with intersecting bodies. *Proc. Second International Workshop on Water Waves and Floating Bodies*, Rep. No. AM-87-06, Univ. Bristol, pp. 101-103.

Schultz, W.W., Griffin, O.M. and Romberg, S.E. 1986. Steep and breaking deep water waves. *Proc. 16th ONR Symp. Naval Hydro.*, National Academic Press, pp. 106-115.

Schwartz, L.W. 1974. Computer extension and analytic continuation of Stoke's expansion for gravity waves. *J. Fluid Mech.*, **62**, pp. 553-578.

Schwartz, L.W. and Fenton, J.D. 1982. Strongly nonlinear waves. *Ann. Rev. Fluid Mech.*, **14**, pp. 39-60.

Semyonov-Tyan-Shansky, V. 1966. *Statics and Dynamics of the Ship.* English Translation by M. Konyaeva, Peace Pub., Moscow, Appendix VI, pp. 567 - 580.

Sommerfeld, A.J.W. 1949. *Vor lesungen uber theoretische Physik. II. Mechanik der deforsebaren Medien.* Leipzig, Akademie.

Standing, R.G. 1984. Wave loading on offshore structures. *Ocean Sc. Eng.*, **9**, 1, pp. 25-134.

Stansby, P.K. and Dixon, A.G. 1983. Simulation of flows around cylinders by a Lagrangian vortex method. *Appld. Ocean Res.*, **103**, 3, pp. 167-178.

Stoker, J.J. 1966. *Water waves.* 3rd printing, Interscience Pub. Inc.

Tadjbaksh, I. and Keller, J.B. 1960. Standing surface waves of finite amplitude. *J. Fluid Mech.*, **8**, pp. 442-451.

Takagi, M., Arai, S-I., Takezawa, S., Tanaka, K. and Takarada, N. 1985. A comparison of methods for calculating the motion of a semisubmersible. *Ocean Engng.*, **12**, pp. 45-97.

Takagi, M., Furukawa, H. and Takagi, K. 1983. On the precision of various hydrodynamic solutions of two-dimensional oscillating bodies. *Proc. International Workshop on Ship and Platform Motions*, Berkeley, Calif., pp. 450-466.

Tasai, F. and Koterayama, W. 1976. Nonlinear hydrodynamic forces acting on cylinders heaving on the surface of a fluid. *Rep. No. 77, Res. Inst. Appld. Mech.*, Kyushu Univ.

Telste, J.C. 1985. Calculation of fluid motion resulting from large amplitude forced heave motion of a two-dimensional cylinder on a free surface, *Proc. 4th Int. Conf. Num. Ship Hydro.*, National Academy of Sciences, pp. 81-93.

Telste, J.G. and Noblesse, F. 1986. Numerical evaluation of the Green function of water-wave radiation and diffraction. *J. Ship Res.*, **30**, pp. 69-84.

Toro, E.F. 1986. Mesh effects on the computation of nonlinear gravity waves of arbitrary discharge. *Int. J. Num. Meth. Fluids*, **6**, pp. 479-493.

Toro, E.F. and O'Carroll, M.J. 1984. A Kantorovich computational method for free surface gravity flows. *Int. J. Num. Meth. Fluids*, **4**, pp. 1137-1148.

Troesch, A.W. and Kang, C-G. 1986. Hydrodynamic loads on impacting bodies. *Proc. 16th ONR Symp. Naval Hydro.*, National Academic Press, Washington,D.C., pp. 537-558.

Ursell, F. 1964. The decay of the free motion of a floating body. *J. Fluid Mech.*, **19**, pp. 305-319.

van Dyke, M. 1964. *Perturbation methods in fluid mechanics.* Academic Press.

Vinje, T. and Brevig, P. 1981a. Numerical simulation of breaking waves. *Adv. Water Resources*, **4**, pp. 77-82.

Vinje, T. and Brevig, P. 1981b. Numerical calculation of forces from breaking waves. *Int. Sym Hydro. Ocean Eng.*, Norwegian Inst. Tech., Trondheim, pp. 547-565.

Vinje, T. and Brevig, P. 1981c. Nonlinear ship motions. *Proc. 3rd Int. Conf. Num. Ship Hydro.*, Paris, pp. 257-268.

Vinje, T., Maogang, X. and Brevig, P. 1982. A numerical approach to nonlinear ship motion. *Proc. 14th ONR Symp. Naval Hydro.*, National Academy Press, pp. 245-278.

von Kerzcek, C. and Salvesen, N. 1974. Numerical solution of two dimensional nonlinear wave problems. *Proc. 10th ONR Symp. Naval Hydro.*, Cambridge, Mass., pp. 649-663.

Vughts, J.H. 1969. The hydrodynamic coefficient for swaying, heaving and rolling cylinders in a free surface. *Int. Ship. Prog.*, **15**, pp. 251-276.

Wehausen, J.V. 1967. Initial-value problem for the motion in an undulating sea of a body with fixed equilibrium position. *J. Eng. Math.*, **1**, pp. 1-17.

Wehausen, J.V. 1971. The motion of floating bodies. *Ann. Rev. Fluid Mech.*, **2**, pp. 237-268.

Wehausen, J.V. and Laitone, E.V. 1960. *Surface Waves.* in Vol. 9, Handbuch der Physik, Springer-Verlag, pp. 446-778.

Welch, J.E., Harlow, F.H., Shannon, J.P. and Daly, B.J. 1966. The MAC method, a computing technique for solving viscous, incompressible, transient fluid flow problems involving free surfaces. *Los Alamos Scientific Lab. Rep. LA-3425.*

Wellford, L.C. Jr. and Ganaba, T. 1981. A finite element method with a hybrid Lagrange line for fluid mechanics problems involving large free surface motion. *Int. J. Num. Meth. Eng.*, **17**, pp. 1201-1231.

Wiegel, R.L. 1964. *Oceanographical engineering.* Chapter two, Prentice-Hall, Inc., Englewood Cliffs, N.J., pp 11-64.

Wu, C-F. and Yeung, R.W. 1987. Nonlinear wave-body motion in a closed domain. *Proc. Second International Workshop on Water Waves Floating Bodies*, Rep. No. AM-87-06, Univ. Bristol, pp. 133-135.

Wu, D-M. and Wu, T.Y. 1982. Three dimensional nonlinear long waves due to a moving surface pressure. *Proc. 14th ONR Symp. Naval Hydro.*, National Academy Press, pp. 103-125.

Yamashita, S. 1977. Calculations of the hydrodynamic forces acting upon thin cylinders oscillating vertically with large amplitudes. *J. Soc. Naval Arch. Japan*, **141**, pp. 67-76.

Yen, S.M., Lee, K.D. and Akai, T.J. 1977. Finite element and finite difference solutions of nonlinear free surface wave problems. *Proc. 2nd Int. Conf. Num. Ship Hydro.*, Berkeley, Calif., pp. 305-318.

Yeung, R.W. 1973. A singularity distribution method for free surface flow problems for an oscillating body. *College on Eng. Rep.*, Univ. of Calif., Berkeley, vi + 124 p.

Yeung, R.W. 1982. The transient heaving motion of floating cylinders. *J. Eng. Math.*, **16**, pp. 97-119.

Yeung, R.W. 1982. Numerical methods in free surface flows. *Ann. Rev. Fluid Mech.*, **14**, pp. 245-266.

Zienkiewicz, O.C. 1979 *The finite element method*, Tata Mcgraw Hill, New Delhi.

APPENDICES

Appendix A

Numerical Formulae

A.1 Time-integrators for the Free Surface Conditions

Consider the ordinary linear differential equation (eqn. (2.15)):

$$\frac{dy}{dt} = f(y,t) \qquad .....(A.1.1)$$

The Adams-Bashforth-Moulton (A-B-M) rules are given by:

1st Order

$$y_{k+1}^{(1)} = y_k + \Delta t f_k + O(\Delta t) \qquad .....(A.1.2(a))$$

$$y_{k+1}^{(m)} = y_k + \frac{\Delta t}{2}(f_{k+1}^{(m-1)} + f_k) + O(\Delta t^2) \qquad .....(A.1.2(b))$$

2nd order

$$y_{k+1}^{(1)} = y_k + \frac{\Delta t}{2}(3f_k - f_{k-1}) + O(\Delta t^2) \qquad .....(A.1.2(c))$$

$$y_{k+1}^{(m)} = y_k + \frac{\Delta t}{2}(f_{k+1}^{(m-1)} + f_k) + O(\Delta t^3) \qquad .....(A.1.2(d))$$

3rd order

$$y_{k+1}^{(1)} = y_k + \frac{\Delta t}{12}(23f_k - 6f_{k-1} + 5f_{k-2}) + O(\Delta t^3) \quad .....(A.1.2(e))$$

$$y_{k+1}^{(m)} = y_k + \frac{\Delta t}{12}(5f_{k+1}^{(m-1)} + 8f_k - f_{k-1}) + O(\Delta t^4) \quad .....(A.1.2(f))$$

4th order

$$y_{k+1}^{(1)} = y_k + \frac{\Delta t}{24}(55f_k - 59f_{k-1} + 37f_{k-2} - 9f_{k-3}) + O(\Delta t^4) \quad ..(A.1.2(g))$$

$$y_{k+1}^{(m)} = y_k + \frac{\Delta t}{24}(9f_{k+1}^{(m-1)} + 19f_k - 5f_{k-1} + f_{k-2}) + O(\Delta t^5) \quad ..(A.1.2(h))$$

where the superscripts in parenthesis denotes the level of iterations; $m = 1$ for the predictor step and $m \geq 1$ for corrector steps. $y_i \equiv y(i\Delta t)$, $f_i \equiv f(y_i, i\Delta t)$, $f_i^{(m)} \equiv f(y_i^{(m)}, i\Delta t)$; Δt represents the time step size and a $O(\ )$ indicates the local order of error.

To apply the above formulae to the free surface conditions, comparison of (A.1) with relevant evolution equations give:

$$y \equiv \eta \ ; \ f \equiv \frac{\partial \phi}{\partial z} \quad \text{for eqn. (3.1)} \qquad \text{.....(A.1.3(a))}$$

$$y \equiv \phi \ ; \ f \equiv -g\eta \quad \text{for eqn. (3.2)} \qquad \text{.....(A.1.3(b))}$$

$$y \equiv \eta \ ; \ f \equiv \frac{\partial \phi}{\partial z} - \frac{\partial \phi}{\partial x}\frac{\partial \eta}{\partial x} \quad \text{for eqn. (2.2)} \qquad \text{.....(A.1.3(c))}$$

$$y \equiv \phi \ ; \ f \equiv -g\eta - \frac{1}{2}[(\frac{\partial \phi}{\partial x})^2 - (\frac{\partial \phi}{\partial z})^2] - \frac{\partial \phi}{\partial x}\frac{\partial \phi}{\partial z}\frac{\partial \eta}{\partial x} \quad \text{for eqn. (4.3)} \qquad \text{.....(A.1.3(d))}$$

For starting the integrations, formulae (A.1.2(a), A.1.2(d)); (A.1.2(c), A.1.2(f)); (A.1.2(e), A.1.2(h)) and (A.1.2(g), A.1.2(h)) are applied sequentially for $N_T =$ 1, 2, 3 and ≥ 4 , where N_T denote the time step level: $t = N_T \Delta t$. Note that for $N_T = 1$, 2 and 3, the rules adopted for the corrector steps are an order higher than the corresponding predictor steps.

A.2 Coefficients a_1, a_2, a_3 in (4.10 (b))

From (4.10 (a)) and (4.10 (c)) we have,

$$g(x_1) = 1 \qquad .....(A.2.1(a))$$

$$g(x_2) = \frac{f_2(x_2)}{f_1(x_2)} \qquad .....(A.2.1(b))$$

$$g'(x_2) = \frac{f_1(x_2)f_2'(x_2) - f_2(x_2)f_1'(x_2)}{f_1^2(x_2)} \qquad .....(A.2.1(c))$$

where $x_2 = (x_1 + l)$ and a prime ($'$) denotes differentiation with respect to x. From (4.10b) we have,

$$g(x_1) = a_1x_1^2 + a_2x_1 + a_3 \qquad .....(A.2.2(a))$$

$$g(x_2) = a_1x_2^2 + a_2x_2 + a_3 \qquad .....(A.2.2(b))$$

$$g'(x_2) = 2a_1x_2 + a_2 \qquad .....(A.2.2(c))$$

From (A.2.1) and (A.2.2), the coefficients are derived as:

$$a_1 = \frac{f_1(x_2) - f_2(x_2)}{f_1(x_2)(x_1 - x_2)^2} - \frac{f_1(x_2)f_2'(x_2) - f_2(x_2)f_1'(x_2)}{f_1^2(x_2)(x_1 - x_2)} \qquad ..(A.2.3(a))$$

$$a_2 = \frac{f_1(x_2)f_2'(x_2) - f_2(x_2)f_1'(x_2)}{f_1^2(x_2)} - 2a_1x_1 \qquad .....(A.2.3(b))$$

$$a_3 = 1 - a_1x_1^2 - a_2x_1 \qquad .....(A.2.3(c))$$

For evaluation of $f_2'(x_2)$, formula (A.4.1) below is applied.

A.3 Smoothing Formulae

(i) Formula base on the scheme of Longuet-Higgins and Cokelet (1976)

In the smoothing scheme of Longuet-Higgins and Cokelet, a function $f(x)$ is defined at equally spaced points $x_j, j = 1, 2, 3, \cdots, N$ and it is assumed that the alternate points lie in a smooth curve. $f(x)$ can then be locally approximated by two polynomials:

$$h(x) = (a_0 + a_1 x + a_2 x^2 + \cdots + a_n x^n) + (-1)^j (b_0 + b_1 x + \cdots + b_{n-1} x^{n-1}) \qquad .....(A.3.1)$$

Here the first polynomial represents a smooth mean curve while the rest part represents a quantity which oscillates with period 2 in j. The smoothed curve can then be taken to be the first polynomial:

$$\bar{h}(x) = a_0 + a_1 x + a_2 x^2 + \cdots + a_n x^n \qquad .....(A.3.2)$$

The coefficients $a_0, a_1, a_2, \cdots, a_n$ and $b_0, b_1, \cdots, b_{n-1}$ can be derived uniquely from the conditions that $h(x_j) = f(x_j)$ at $(2n+1)$ consecutive points $(j-n)$ to $(j+n)$ inclusive. When $n = 2$, the five point formula for a central point becomes:

$$\bar{f}_j = \frac{1}{16}(-f_{j-2} + 4f_{j-1} + 10f_j + 4f_{j+1} - f_{j+2}) \qquad .....(A.3.3)$$

where $f_j \equiv f(x_j); \bar{f}_j \equiv \bar{f}(x_j)$. For j = 1, 2, $N-1$ and N, the $(2n+1)$ consecutive points at which $h(x_j) = f(x_j)$ are to be considered are for the intervals: (j) to $(j+2n)$, $(j-1)$ to $(j+2n-1)$, $(j-2n+1)$ to $(j+1)$ and $(j-2n)$ to (j) respectively. After necessary algebra, the formulae are:

$$\bar{f}_j = \frac{1}{16}(11f_j + 12f_{j+1} - 6f_{j+2} - 4f_{j+3} + 3f_{j+4}) \text{ for } j = 1$$

$$\begin{aligned}
\bar{f}_j &= \frac{1}{16}(3f_{j-1} + 8f_j + 6f_{j+1} - f_{j+3}) \text{ for } j = 2 \\
\bar{f}_j &= \frac{1}{16}(-f_{j-3} + 6f_{j-1} + 8f_j + 3f_{j+1}) \text{ for } j = N-1 \\
\bar{f}_j &= \frac{1}{16}(3f_{j-4} - 4f_{j-3} - 6f_{j-2} + 12f_{j-1} + 11f_j) \text{ for } j = N
\end{aligned} \qquad \text{.....(A.3.4)}$$

(ii) Least square smoothing formulae

The smoothing formulae corresponding to a third-degree least square approximation over five points are given by:

$$\begin{aligned}
\bar{f}_j &= \frac{1}{35}(-3f_{j-2} + 12f_{j-1} + 17f_j + 12f_{j+1} - 3f_{j+2}) \text{ for } 2 \le j \le N-1 \\
\bar{f}_j &= \frac{1}{70}(69f_j + 4f_{j+1} - 6f_{j+2} + 4f_{j+3} - f_{j+4}) \text{ for } j = 1 \\
\bar{f}_j &= \frac{1}{35}(2f_{j-1} + 27f_j + 12f_{j+1} - 8f_{j+2} + 2f_{j+3}) \text{ for } j = 2 \\
\bar{f}_j &= \frac{1}{35}(2f_{j-3} - 8f_{j-2} + 12f_{j-1} + 27f_j + 2f_{j+1}) \text{ for } j = N-1 \\
\bar{f}_j &= \frac{1}{70}(-f_{j-4} + 4f_{j-3} - 6f_{j-2} + 4f_{j-1} + 69f_j) \text{ for } j = N
\end{aligned} \qquad \text{.....(A.3.5)}$$

A.4 Numerical Difference Formulae

(i) Second-order difference rules

Consider a function $f(x)$ defined at equally spaced points $x_j = 1, 2, 3, \cdots, N$. The second order central difference formula for $f'(x)$ is given by:

$$f'(x_j) = \frac{1}{2\Delta h}[f(x_{j+1}) - f(x_{j-1})] \qquad .....(A.4.1)$$

where the prime denotes differentiation with respect to x and Δh denotes the spacing between the points, $\Delta h = x_{j+1} - x_j$. This rule is inapplicable for $j = 1$ and $j = N$, for which second order forward and backward rules respectively are applicable. These are:

$$\begin{aligned} f'(x_j) &= \frac{1}{2\Delta h}[-f(x_{j+2}) + 4f(x_{j+1}) - 3f(x_j)] \text{ for } j = 1 \quad ..(A.4.2) \\ f'(x_j) &= \frac{1}{2\Delta h}[3f(x_j) - 4f(x_{j-1}) + f(x_{j-2})] \text{ for } j = N \quad ..(A.4.3) \end{aligned}$$

(ii) Second order interpolation/extrapolation formula

The second order Lagrangian interpolation/extrapolation three-point formula which utilizes the points at three equispaced ordinates x_{j-1}, x_j and x_{j+1} is given by:

$$f(x_j + p\Delta h) = \frac{p(p-1)}{2} f(x_{j-1}) + (1 - p^2) f(x_j) + \frac{p(p+1)}{2} f(x_{j+1}) \qquad .....(A.4.4)$$

where $\Delta h = x_{j+1} - x_j = x_j - x_{j-1}$.

A.5 Time-integrators for the Equations of Motion

Consider the sway equations of motions, 6.22 (a) and (b):

$$\frac{\partial u_G}{\partial t} = \frac{F_x}{M_B} \qquad \text{.....(A.5.1(a))}$$

$$\frac{\partial x_G}{\partial t} = u_G \qquad \text{.....(A.5.1(b))}$$

In the adopted procedure, only the predictor rules (i.e. explicit rules) shown in (A.1) apply for the first equation. However for eqn. (A.5.1 (b)), the corrector rules are utilized since an estimate for the value of u_G at the advanced level is available. For $N_T \geq 4$, the formulae are:

$$\begin{aligned} u_G^{(m)}(t+\Delta t) = u_G(t) \; &+ \; \frac{\Delta t}{24M_B}[55F_x(t) - 59F_x(t-\Delta t) \\ &+37F_x(t-2\Delta t) - 9F_x(t-3\Delta t)] \quad \text{..(A.5.2(a))} \\ x_G^{(m)}(t+\Delta t) = x_G(t) \; &+ \; \frac{\Delta t}{24}[9u_G^{(m)}(t+\Delta t) + 19u_G(t) \\ &-5u_G(t-\Delta t) + u_G(t-2\Delta t)] \quad \text{..(A.5.2(b))} \end{aligned}$$

For the heave and roll equations of motions, same formulae apply.

Appendix B

Estimation of Roll Damping

General Considerations

The damping moment $b_\theta(\dot{\theta})$ in (8.7) can be expressed as a series expansion of $\dot{\theta}$ and $|\dot{\theta}|$ in the following form:

$$b_\theta(\dot{\theta}) = B_1\dot{\theta} + B_2\dot{\theta}|\dot{\theta}| + B_3\dot{\theta}^3 + \cdots \qquad .....(B.1)$$

Depending on the terms considered, a variety of models can be constructed from the above representation. Different models have in fact been proposed over the past years (see Himeno 1981 for a review), including recently suggested models that consider angle-dependent terms not shown in (B.1) (see e.g. Bass and Haddara 1988).

In order to adopt a model that will suite the present requirements, guidance may be sought from the state-of-the-art method for prediction of ship roll damping outlined in Himeno (1981). According to this method, the total roll damping coefficient can be estimated by summing several component damping coefficients, each of which arises from a specific flow phenomenon. Omitting terms not applicable for the present model, the following expression for the total equivalent linear damping coefficient (B_e) emerges:

$$B_e = B_R + B_F + B_E \qquad .....(B.2)$$

Here B_R represents the hydrodynamic or radiation damping coefficient associated with the energy expended in generating free surface waves. The damping moment due to this component is usually considered linear, which makes B_R equivalent to B_θ^H in (8.8) as well as justifies the form of (8.8). The remaining two terms B_F and B_E in (B.2), known as friction damping and eddy damping coefficients respectively, arise from viscous effects.

A study of the formulae for B_F proposed by various investigators indicates that frictional damping moment can be further decomposed into two components associated with laminar and turbulent flow conditions respectively (see Himeno 1981). The formula for the former of these is linear, which suggests that the damping moment caused by laminar flow around the hull is essentially linear in $\dot{\theta}$. Considering the size of the model and the smoothness of the surface and keeping in mind the absence of forward speed, the flow conditions in the experimental setting is expected to be laminar. It is then fair to assume that the damping moment arising from skin-friction tensor is linear in $\dot{\theta}$, which means B_F is a part of B_1 in (B.1).

The last term in (B.2), that is, the eddy damping moment, is caused by the flow separation near the bilges. This term is known to be non-linear and dependent on $\dot{\theta}|\dot{\theta}|$ (see Himeno 1981). Therefore the term associated with B_2 in (B.1) can be attributed to this effect.

From the above, it would appear that form (B.1) where the only non-zero terms present are B_1 and B_2 is an appropriate model for the required estimations. Although this turns out to be the classical quadratic form for roll damping known since the time of Sir William Froude, the discussion above provides a rationale for adopting this model. As a further examination, the three coefficients B_1, B_2, B_3 in (B.1) have been estimated from the experimentally obtained extinction curves. The procedure is detailed in Himeno (1981) and hence omitted here. The estimated value of B_3 is found to be consistently very small over the entire range of the data set. Typical non-dimensionalized values are : $\bar{B}_1 \approx 0.001, \bar{B}_2 \approx 0.020, \bar{B}_3 \leq 0.00005$ (for the non-dimensionalizing factors, see Table B.1). This provides additional evidence on appropriateness of adopting a quadratic model.

The uncoupled equation of motion for free roll is given by (8.7) with $\tilde{M}_\theta = 0$. This can now be written as

$$(I_\theta + \delta I_\theta)\ddot{\theta} + B^H_\theta \dot{\theta} + B^V_1 \dot{\theta} + B_2 \dot{\theta}|\dot{\theta}| + C_\theta(\theta) = 0 \qquad .....(B.3)$$

where B^V_1 denotes the viscous damping coefficient associated with the linear part of the corresponding damping moment. Neglecting the influence arising from coupling with heave, which is usually minimal and is a standard practice to ignore this effect, (B.3) can be taken to represent the motions in a roll decay experiment. The objective is to estimate the viscous terms B^V_1 and B_2 from the test results. To achieve this, the contribution of hydrodynamic damping implicit in the experimental records need to be isolated.

Estimation of the Hydrodynamic Damping Coefficient

As described in §8.3.2, the numerical method can be used to simulate free motions in any mode by prescribing suitable initial conditions. Numerical experiments have shown that motions in roll mode are less sensitive to the conditions imposed on the outer boundaries as compared to heave mode. Considering that the energy expended in generating free surface motions is considerably less in roll mode than in heave mode, this is to be expected. For the present purpose, the

Table B.1 Non-dimensionalizing factors for the damping coefficients

$$\bar{B}_1 = B_1\sqrt{B/2g}\;/\;(1/\rho S_A B)$$

$$\bar{B}_e = B_e\sqrt{B/2g}\;/\;(1/\rho S_A B)$$

$$\bar{B}_\theta^H = B_\theta^H\sqrt{B/2g}\;/\;(1/\rho S_A B)$$

$$\bar{B}_1^V = B_1^V\sqrt{B/2g}\;/\;(1/\rho S_A B)$$

$$\bar{B}_2 = B_2\,(1/\rho S_A B)$$

$$\bar{B}_3 = B_3\,(B/2g)\,(1/\rho S_A B)$$

numerical results used are generated in a control domain of length $0.5L = 40B$ with the conditions $\phi = 0$ prescribed on the outer boundaries. Results could be obtained for more than five cycles of oscillation without detectable influence of the conditions imposed on the exterior boundaries to the solution. This simulated roll motion can be considered equivalent to a record obtained from a roll decay test conducted in an inviscid fluid tank where the damping mechanism involved is contribution from hydrodynamic damping alone.

To determine the value of B_θ^H , (B.3) is numerically solved by employing a fifth order Runge-Kutta method. An IMSL routine is utilized for this purpose whose convergence and accuracy has been tested. The restoring moment $C_\theta(\theta)$ is generally non-linear, specially for large θ values, and is known for wall sided geometries (Rawson and Tupper 1976):

$$C_\theta(\theta) = gM_B[GM + 0.5BM\tan^2\theta]\sin\theta \qquad .....(B.4)$$

where BM denotes the vertical distance between the center of buoyancy and the metacenter for $\theta = 0$. Solution of (B.4) requires the value of δI_θ. An initial estimate of this is available from eqn. (6.31). Subsequently adjustments are made such that the period of oscillation obtained from (B.4) are in agreement with the numerical results. The value of δI_θ is found to be: $\delta I_\theta/\rho S_A B^2 = 0.045$ (S_A = wetted surface = Bh), which compares well with Vugts (1969) corresponding experimental values (Vugts' results are given for an axis whose origin is at the undisturbed water level; taking into account the necessary corrections, his value ranges approximately between 0.040 to 0.060, the lower value being for the experiment with roll amplitude of 0.2 rad. or 11.5 deg., which comes closest to the present computational value of $\theta_{\text{mean}} \approx 10$deg.).

The required estimate for B_θ^H is accomplished through an iterative search such that the numerically simulated results and the solution from (B.3) for the same initial conditions are in close agreement. This is a somewhat more elaborate procedure compared to methods where only the peak values in a decay record are used. However, apart from being less demanding on the length of the record required for a reliable estimate, this procedure is believed to be superior in precision in that data over the entire time span is utilized. Although it is possible to obtain a quantitative measure for the closeness of fit between the plots, presently the agreement between these is judged from a visual examination. The estimated value of the coefficient is found to be : $\bar{B}_\theta^H = 0.00125$, for which the plots are shown in Figure B.1. As a demonstration of the influence of non-linearities in the restoring moment to the solution, an additional result computed from (B.3) with linear restoring moment : $C_\theta(\theta) = gM_B GM\theta$ is also plotted.

To investigate the sensitivity of this coefficient on the solution, additional results for neighbouring B_θ^H values ($\sim \pm 10\%$) are shown in Figure B.2. Some latitude in the estimated value is clearly available.

Estimation of Viscous Damping Coefficients

The viscous damping coefficients B_1^V and B_2 are estimated from the experimental decay records. Results for the two tests performed are presented in Figures B.3 (a) and (b). Owing to uncertainties involved in the initial velocities, the records shown exclude the first cycle of oscillation. Excellent quality of repeatability is apparent from Figure B.4 where the results shown are for a range such that

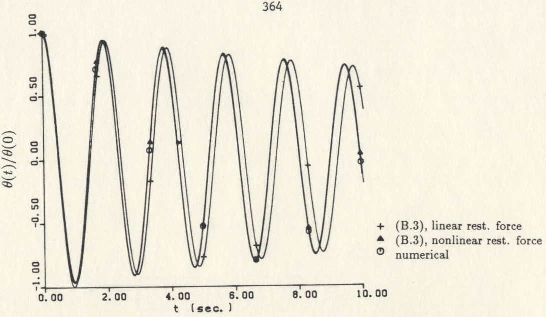

Figure B.1 Free roll motions of the body; for the numerical simulation, $0.5L = 40B$ and the imposed conditions on the exterior boundaries are: $\phi(t) = 0$; in solution of (B.3), $\bar{B}_\theta^H = 0.00125$; for all calculations, $\theta(0) = 15$ deg. and $\dot{\theta}(0) = 0$.

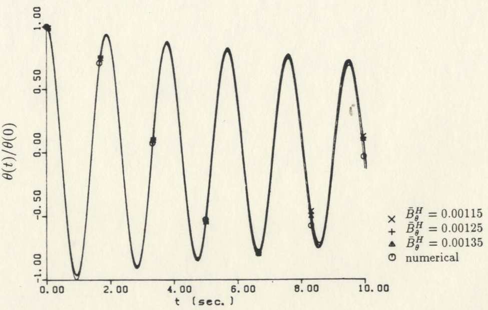

Figure B.2 Sensitivity of the hydrodynamic damping coefficient (B_θ^H) in solution of (B.3).

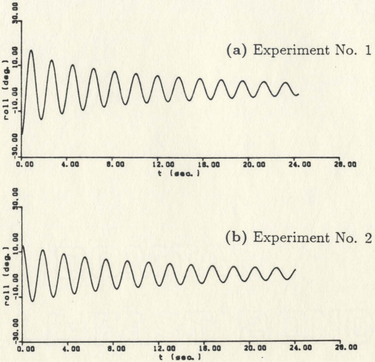

Figure B.3 Experimental roll decay records.

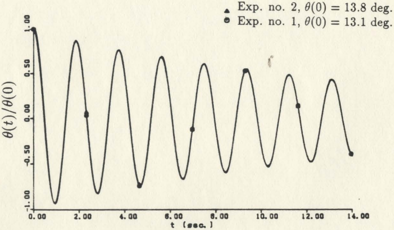

Figure B.4 Repeatability of the roll decay tests.

$\theta(t=0) \approx 15$ deg. (the exact values are quoted in the Figure).

The procedure followed in determining the coefficients are same as in obtaining B_θ^H above. However, presently there are two coefficients to be determined, and a number of combinations of B_1^V and B_2 values are likely to fit the test record with almost same degree of accuracy. In order to arrive at a reliable estimate, guidance is sought from available experimental results for different ship forms. A study of results shown in Himeno (1981) reveals dominance of the B_2 term over the linear term. Rough estimates of these values calculated from the extinction curve also suggest the same (typical values for the cubic damping model have already been indicated). The required estimates are therefore achieved by first tuning the B_2 term, and then making the final adjustments by means of the B_1^V term in (B.3). The results obtained in this manner are summarized in Table B.2 together with some experimental results from Himeno (1981). The corresponding plots are shown in Figure B.5. A sensitivity study have shown that these coefficients within about $\pm 10\%$ of the values quoted produce almost identical results. As seen from Table B.1, the trend in relative magnitudes between the two coefficients is similar. The reductions in magnitudes here as compared to the corresponding values for ship forms are to be expected because of absence of bilge keels as well as two-dimensionality of the model.

To improve confidence in the above estimated values, computations have also been performed by employing a linear model for the total damping moment, i.e. by taking $B_2 = 0$ in (B.1) and following the same procedure. Figure B.6 plots the results. In addition, the following relation can be used to determine an equivalent linear damping coefficient (B_e) for the quadratic model (Himeno

Table B.2 Damping coefficients for the quadratic model

Coeffi- -cients	Ship forms at 0 speed (from Himeno 1981)				Present Model
	Ore Carrier	Tanker	Container Ship	Cargo Ship	
$\bar{B}_1$	0.00193	0.00161	0.0006	0	0.0014†
$\bar{B}_2$	0.05667	0.05180	0.05563	0.0699	0.022

† $\bar{B}_1 = \bar{B}_\theta^H + \bar{B}_1^V$; $\bar{B}_\theta^H = 0.00125$; $\bar{B}_1^V = 0.00015$

Table B.3 Damping coefficients from linear and quadratic models

Coeffi- -cients	Linear model	Quadratic model
$\bar{B}_1$	0.0030	0.0014
$\bar{B}_2$	-	0.023
$\bar{B}_e$	0.0030	0.0030†

† in using eqn. (B.5), θ_A is taken as $\theta_{\text{mean}} = 10$ deg.

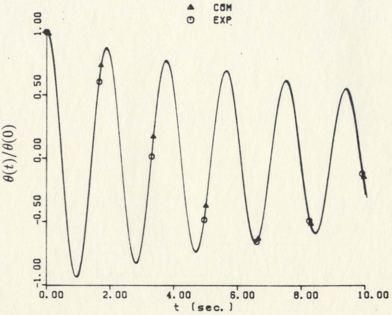

Figure B.5 Comparison of experimental roll decay record with the quadratic damping model; for the computed plot shown, (B.3) is solved with the coefficients : $\bar{B}_\theta^H = 0.00125$, $\bar{B}_1^V = 0.00015$ ($\bar{B}_1 = 0.0014$) and $\bar{B}_2 = 0.022$.

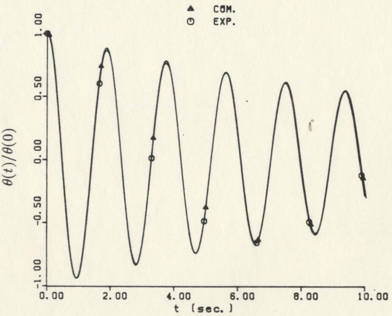

Figure B.6 Comparison of experimental roll decay record with the linear damping model; for the computed plot shown, (B.3) is solved with the coefficients : $\bar{B}_\theta^H = 0.00125$, $\bar{B}_1^V = 0.00175$ ($\bar{B}_1 = 0.0030$) and $\bar{B}_2 = 0$.

1981):

$$B_e = B_1 + \frac{8}{3\pi}\omega_n^r \theta_A B_2 \qquad \text{.....(B.5)}$$

where ω_n^r and θ_A denote the roll natural (radian) frequency and amplitude of oscillation. These results are compiled in Table B.3 and show that the models yield closely comparable B_e values (no difference in $\bar{B}_e$ values till the 4th decimal places). In view of the insensitivity of the coefficients to the solution and the results of Table B.3, we can be fairly confident about the above estimates. The values finally adopted are those from the quadratic model (Table B.2).

Comparing (B.3) with eqns. (8.7) and (8.8), the viscous damping moment b_θ^V in (8.9) is

$$b_\theta^V = B_1^V \dot{\theta} + B_2 \dot{\theta}|\dot{\theta}| \qquad \text{.....(B.6)}$$

Appendix C

Experimental and Numerical Time-histories

This appendix presents a number of plots showing the comparison of time-histories between experiment and theory.

Figures C.1 (a) - (j), C.2 (a) - (i) and C.3 (a) - (i) show the comparative time histories of the incident wave, sway force and heave motion for test series B, C and D respectively, and include results for all of the tests excluding those already presented in the main text. Figure C.4 shows the comparison of roll motion for a number of tests. The included plots are such that, between these and the results which already appeared earlier (Figure 8.12), there is at least one comparison for each of the tested frequency (the only exception being the highest frequency of $\omega\sqrt{B/2g} = 1.0771$). Figure C.5 presents the comparison for evolution of the free surface profile at the location of probe no. 2, and once more, in conjunction with the results already presented, provides at least one comparison for each of the tested frequency and wave steepness from a combination of the three test series. Figures C.6 and C.7 contain comparison of the near-field profile (at probe no. 3/5) and the profile downstream of the body respectively, covering the full range of test-frequencies.

All plots are arranged sequentially in a decreasing order of frequency (i.e. at an increasing order of λ/B).

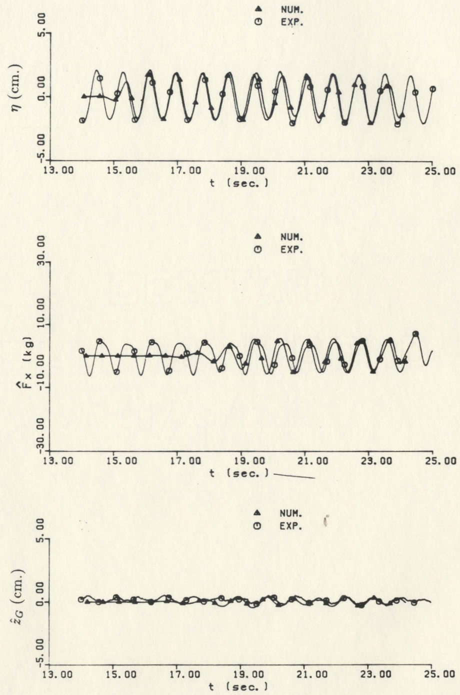

(a) $\omega\sqrt{B/2g} = 1.0771$, $\lambda/B = 2.70$, $H/\lambda = 0.0347$
($T_1 \approx 19.0$ sec., $T_2 \approx 23.0$ sec.)

Figure C.1 continued ⇓

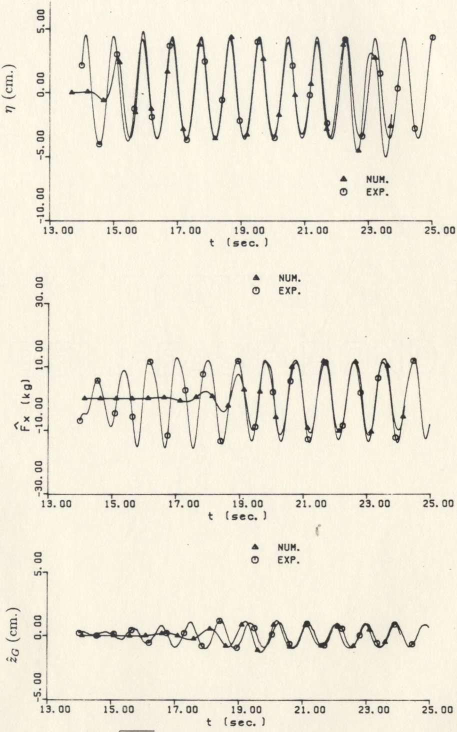

(b) $\omega\sqrt{B/2g} = 0.9874$, $\lambda/B = 3.20$, $H/\lambda = 0.0610$
($T_1 \approx 19.0$ sec., $T_2 \approx 24.0$ sec.)

Figure C.1 continued ⇓

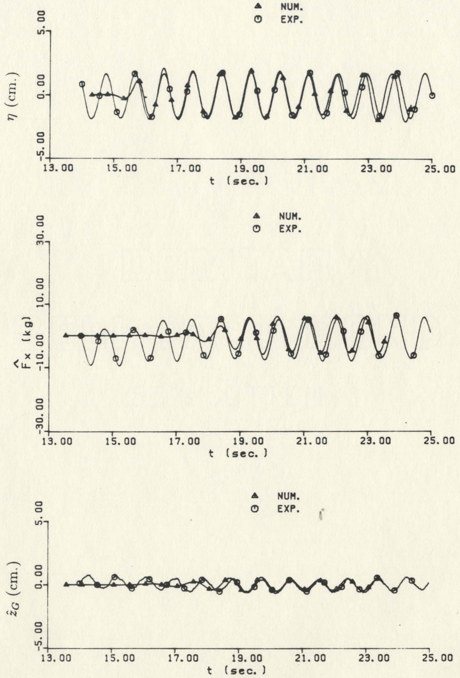

(c) $\omega\sqrt{B/2g} = 0.9874$, $\lambda/B = 3.20$, $H/\lambda = 0.0291$
($T_1 \approx 19.0$ sec., $T_2 \approx 24.0$ sec.)

Figure C.1 continued $\Downarrow$

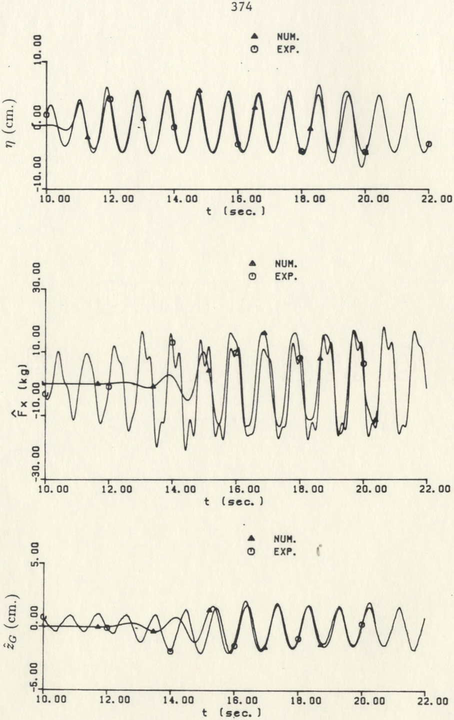

(d) $\omega\sqrt{B/2g} = 0.9425$, $\lambda/B = 3.53$, $H/\lambda = 0.0684$
($T_1 \approx 15.5$ sec., $T_2 \approx 20.5$ sec.)

Figure C.1 continued ⇓

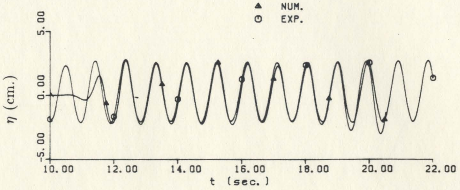

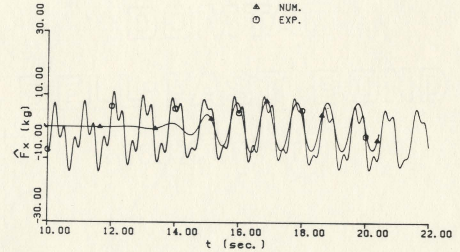

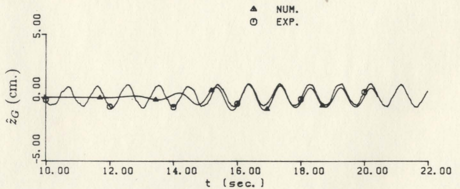

(e) $\omega\sqrt{B/2g} = 0.9425$, $\lambda/B = 3.53$, $H/\lambda = 0.0348$
($T_1 \approx 15.5$ sec., $T_2 \approx 20.5$ sec.)

Figure C.1 continued $\Downarrow$

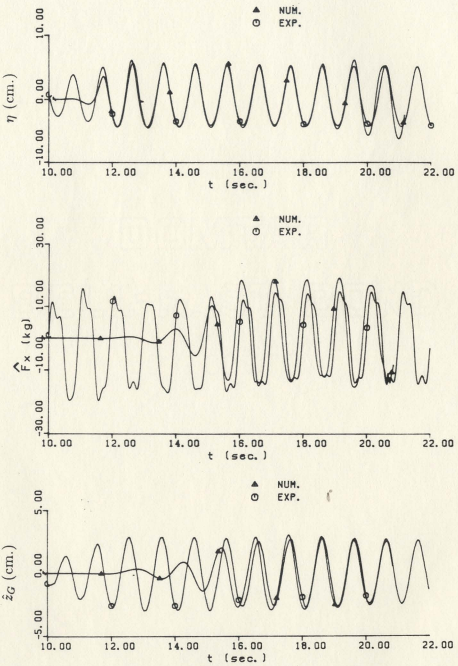

(f) $\omega\sqrt{B/2g} = 0.8976$, $\lambda/B = 3.90$, $H/\lambda = 0.0630$
($T_1 \approx 16.0$ sec., $T_2 \approx 21.0$ sec.)

Figure C.1 continued $\Downarrow$

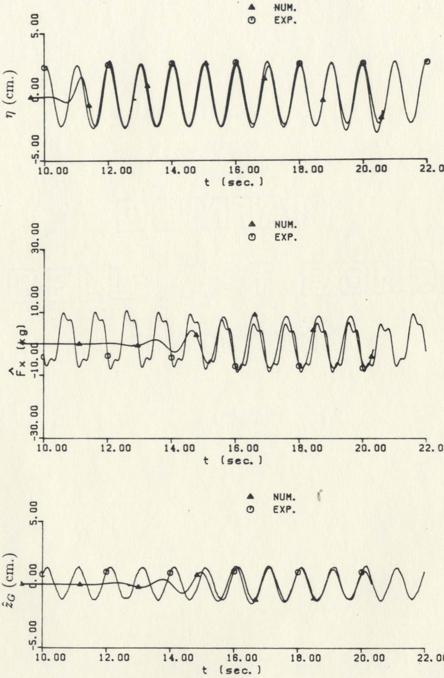

(g) $\omega\sqrt{B/2g} = 0.8976$, $\lambda/B = 3.90$, $H/\lambda = 0.0327$
($T_1 \approx 15.5$ sec., $T_2 \approx 20.5$ sec.)

Figure C.1 continued ⇓

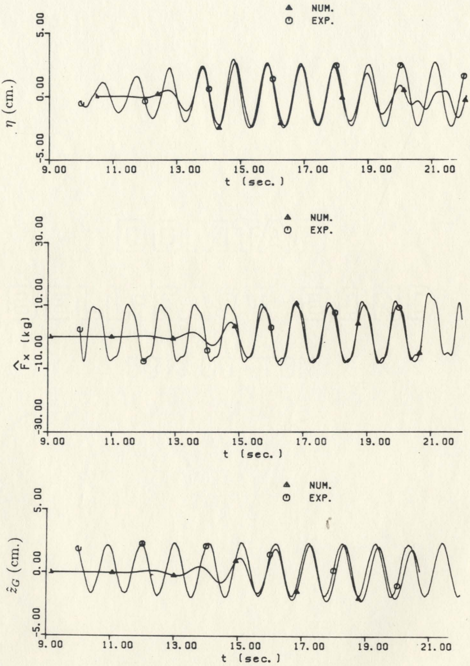

(h) $\omega\sqrt{B/2g} = 0.8527$, $\lambda/B = 4.33$, $H/\lambda = 0.0286$
($T_1 \approx 15.0$ sec., $T_2 \approx 20.5$ sec.)

Figure C.1 continued ⇓

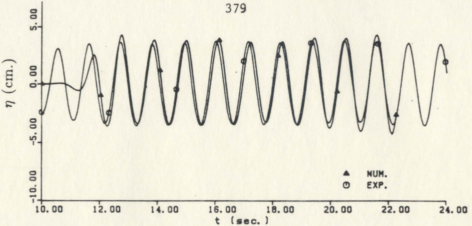

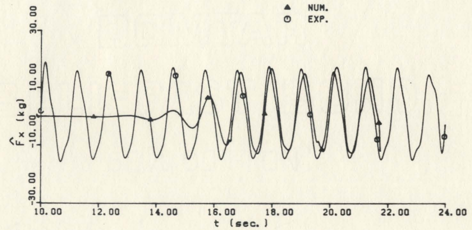

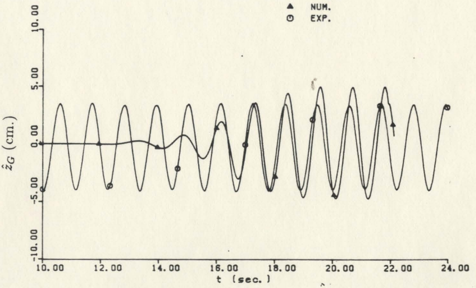

(i) $\omega\sqrt{B/2g} = 0.8078$, $\lambda/B = 4.80$, $H/\lambda = 0.0361$
($T_1 \approx 16.5$ sec., $T_2 \approx 22.0$ sec.)

Figure C.1 continued ⇓

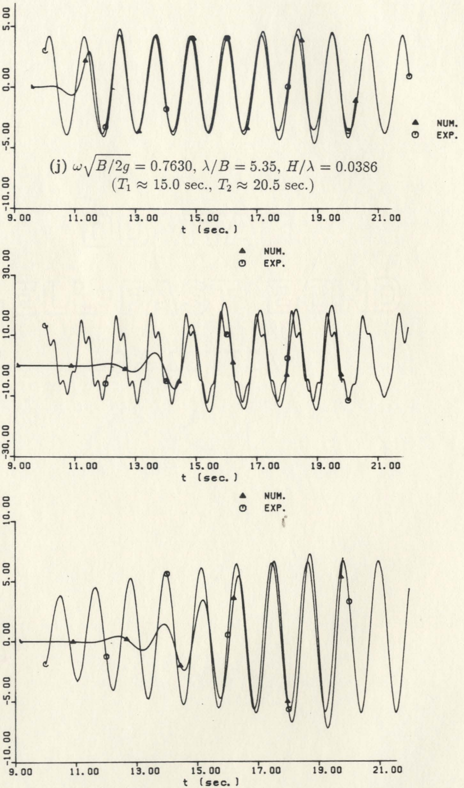

Figure C.1 Test Series B : comparison of experiment and theory

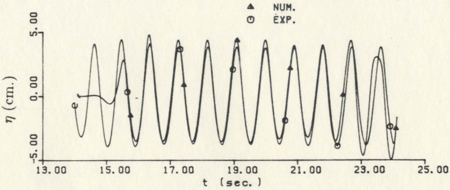

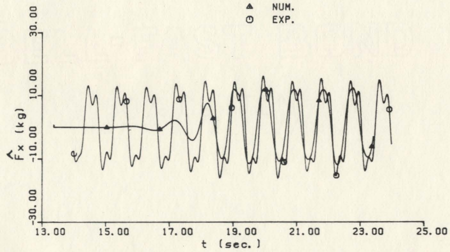

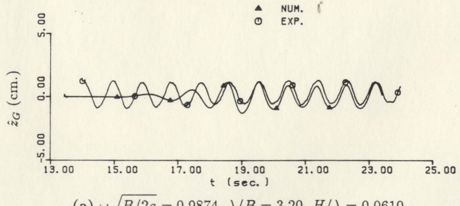

(a) $\omega\sqrt{B/2g} = 0.9874$, $\lambda/B = 3.20$, $H/\lambda = 0.0610$
($T_1 \approx 18.5$ sec., $T_2 \approx 23.5$ sec.)

Figure C.2 continued ⇓

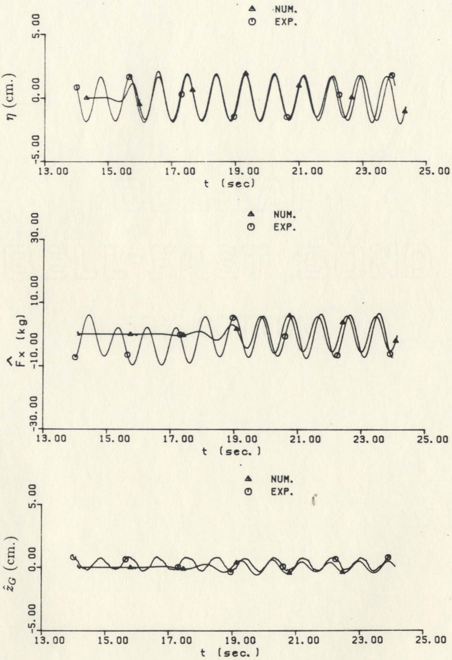

(b) $\omega\sqrt{B/2g} = 0.9874$, $\lambda/B = 3.20$, $H/\lambda = 0.0291$
($T_1 \approx 18.5$ sec., $T_2 \approx 23.5$ sec.)

Figure C.2 continued ⇓

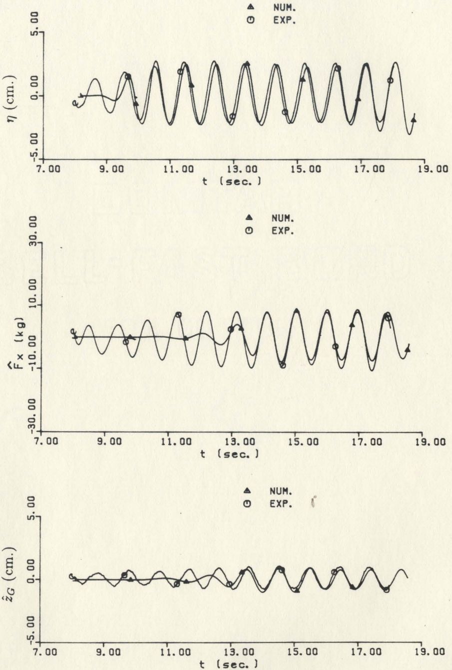

(c) $\omega\sqrt{B/2g} = 0.9425$, $\lambda/B = 3.53$, $H/\lambda = 0.0348$
($T_1 \approx 13.5$ sec., $T_2 \approx 18.5$ sec.)

Figure C.2 continued

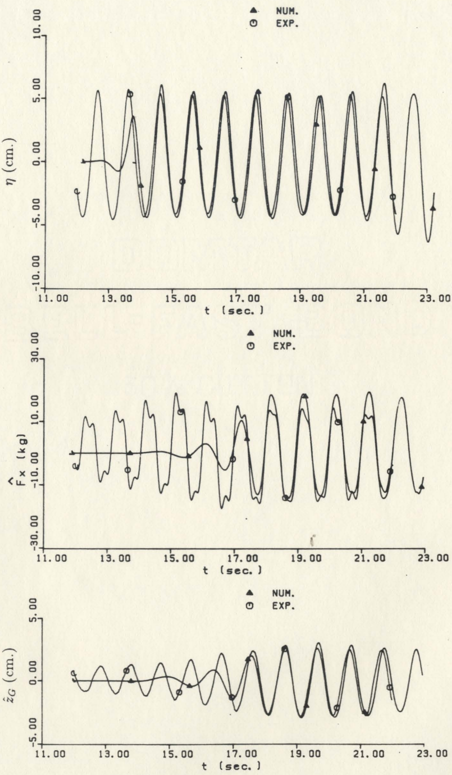

(d) $\omega\sqrt{B/2g} = 0.8976$, $\lambda/B = 3.90$, $H/\lambda = 0.0630$
($T_1 \approx 17.5$ sec., $T_2 \approx 22.5$ sec.)

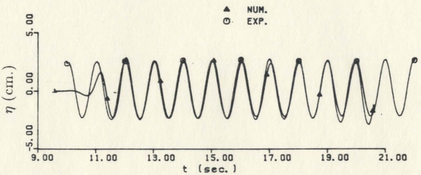

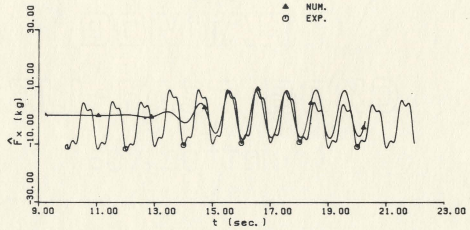

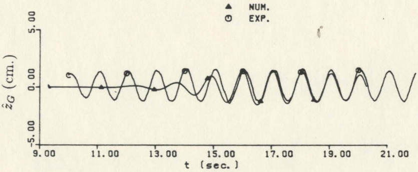

(e) $\omega\sqrt{B/2g} = 0.8976$, $\lambda/B = 3.90$, $H/\lambda = 0.0327$
($T_1 \approx 15.5$ sec., $T_2 \approx 20.5$ sec.)

Figure C.2 continued $\Downarrow$

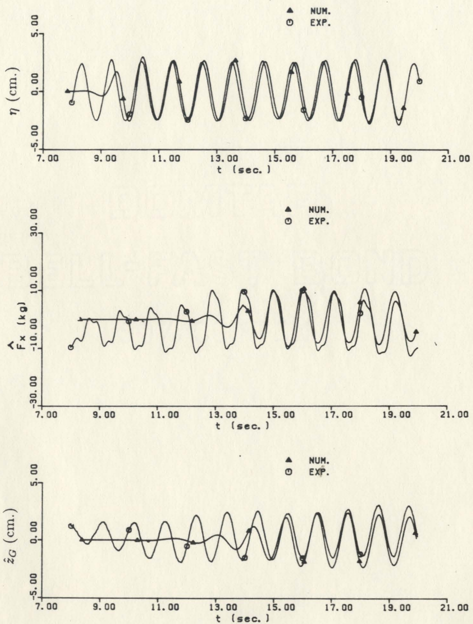

(f) $\omega\sqrt{B/2g} = 0.8527$, $\lambda/B = 4.33$, $H/\lambda = 0.0286$
($T_1 \approx 14.5$ sec., $T_2 \approx 20.0$ sec.)

Figure C.2 continued ⇓

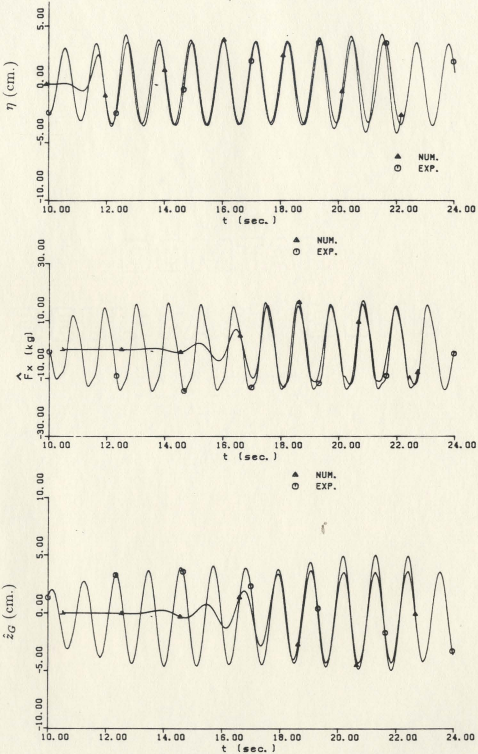

(g) $\omega\sqrt{B/2g} = 0.8078$, $\lambda/B = 4.80$, $H/\lambda = 0.0361$
($T_1 \approx 17.0$ sec., $T_1 \approx 22.5$ sec.)

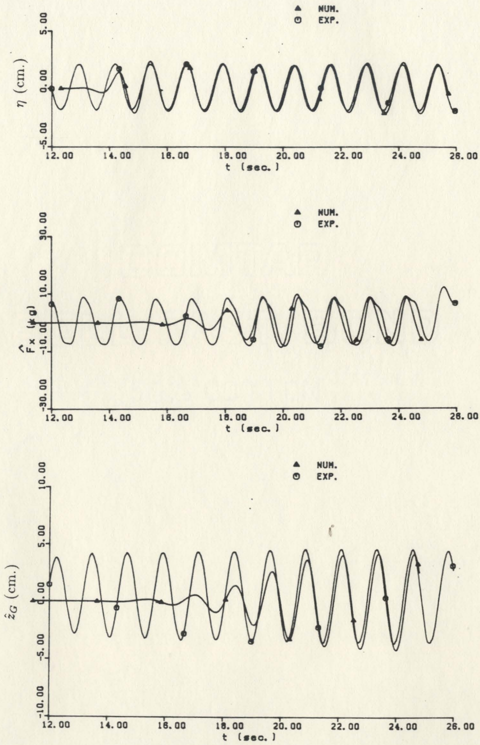

(h) $\omega\sqrt{B/2g} = 0.7181$, $\lambda/B = 6.00$, $H/\lambda = 0.0172$
($T_1 \approx 18.5$ sec., $T_2 \approx 24.5$ sec.)

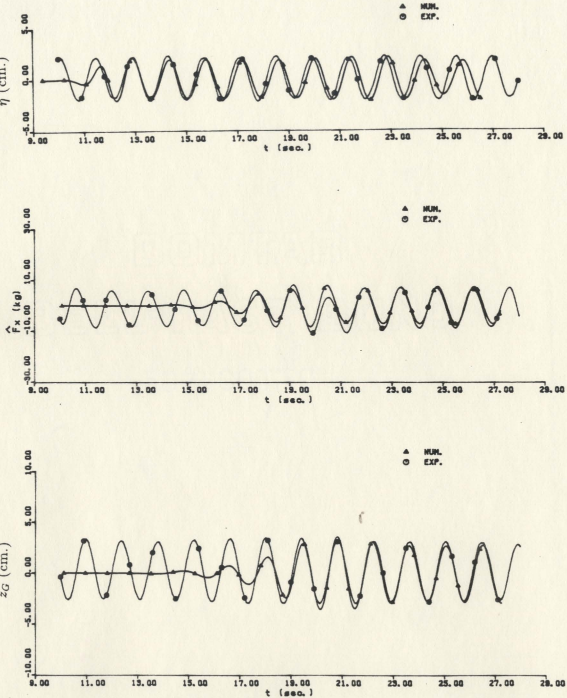

(i) $\omega\sqrt{B/2g} = 0.6283$, $\lambda/B = 7.60$, $H/\lambda = 0.0129$
($T_1 \approx 18.0$ sec., $T_2 \approx 24.5$ sec.)

Figure C.2 Test Series C : comparison of experiment and theory.

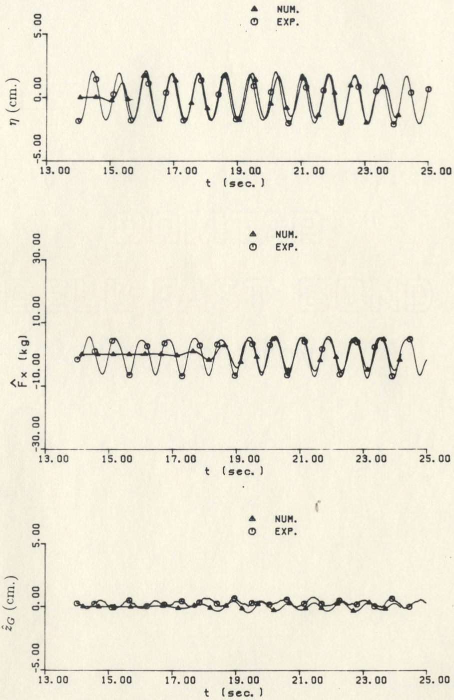

(a) $\omega\sqrt{B/2g} = 1.0771$, $\lambda/B = 2.70$, $H/\lambda = 0.0347$
($T_1 \approx 19.0$ sec., $T_2 \approx 23.0$ sec.)

Figure C.3 continued

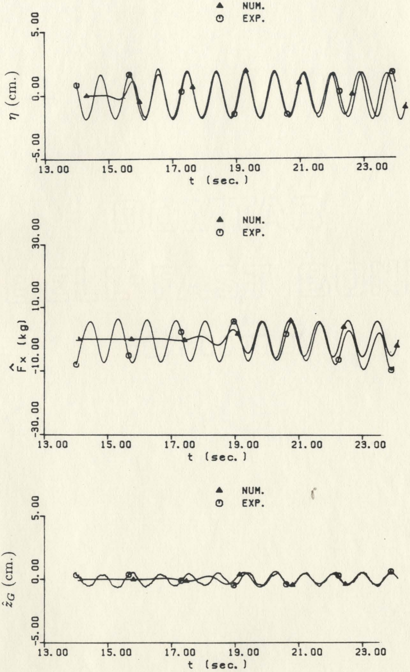

(b) $\omega\sqrt{B/2g} = 0.9874$, $\lambda/B = 3.20$, $H/\lambda = 0.0291$
($T_1 \approx 18.5$ sec., $T_2 \approx 23.5$ sec.)

Figure C.3 continued ||

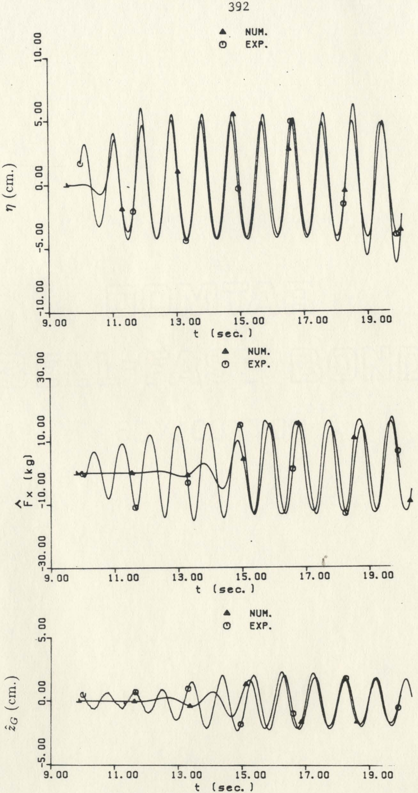

(c) $\omega\sqrt{B/2g} = 0.9425$, $\lambda/B = 3.53$, $H/\lambda = 0.0684$
($T_1 \approx 15.0$ sec., $T_2 \approx 20.0$ sec.)

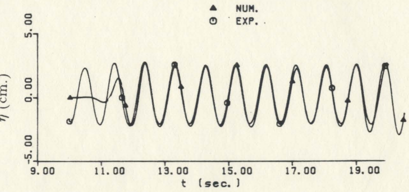

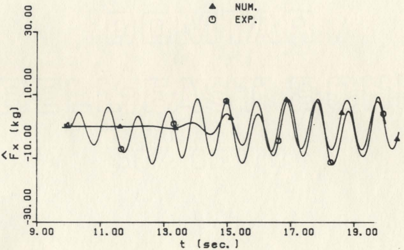

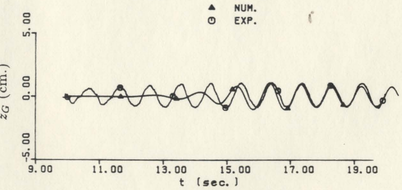

(d) $\omega\sqrt{B/2g} = 0.9425$, $\lambda/B = 3.53$, $H/\lambda = 0.0348$
($T_1 \approx 15.0$ sec., $T_2 \approx 20.0$ sec.)

Figure C.3 continued ⇓

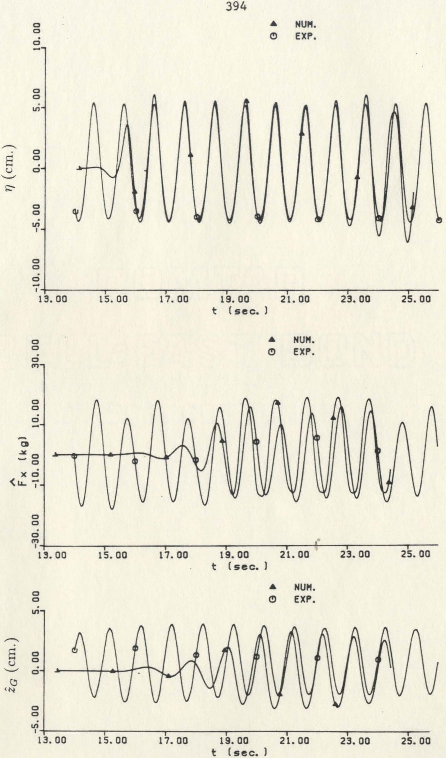

(e) $\omega\sqrt{B/2g} = 0.8976$, $\lambda/B = 3.90$, $H/\lambda = 0.0630$
($T_1 \approx 19.5$ sec., $T_2 \approx 24.5$ sec.)

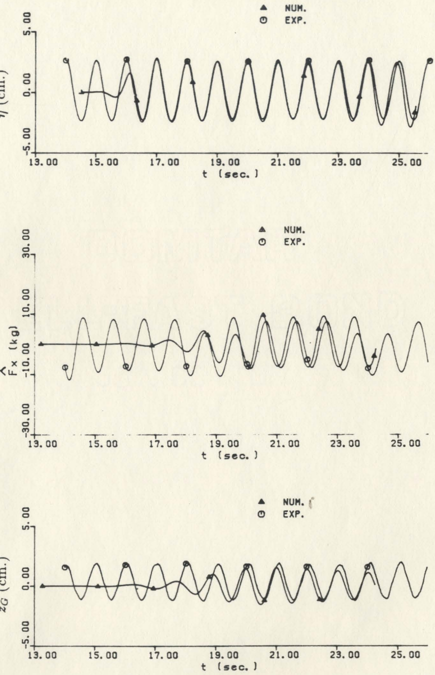

(f) $\omega\sqrt{B/2g} = 0.8976$, $\lambda/B = 3.90$, $H/\lambda = 0.0327$
($T_1 \approx 19.5$ sec., $T_2 \approx 24.5$ sec.)

Figure C.3 continued ⇓

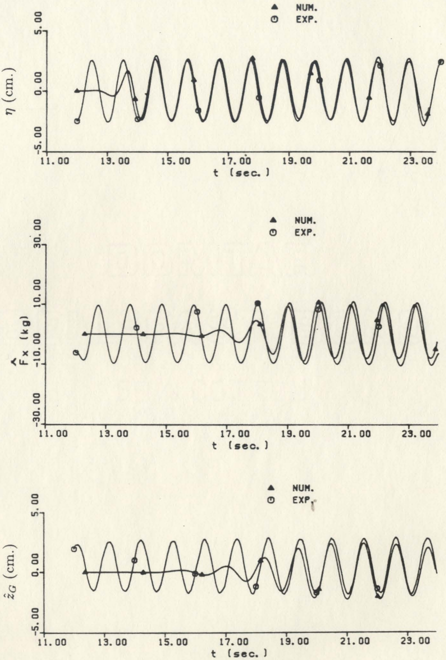

(g) $\omega\sqrt{B/2g} = 0.8527$, $\lambda/B = 4.33$, $H/\lambda = 0.0286$
($T_1 \approx 18.5$ sec., $T_2 \approx 24.0$ sec.)

Figure C.3 continued ⇓

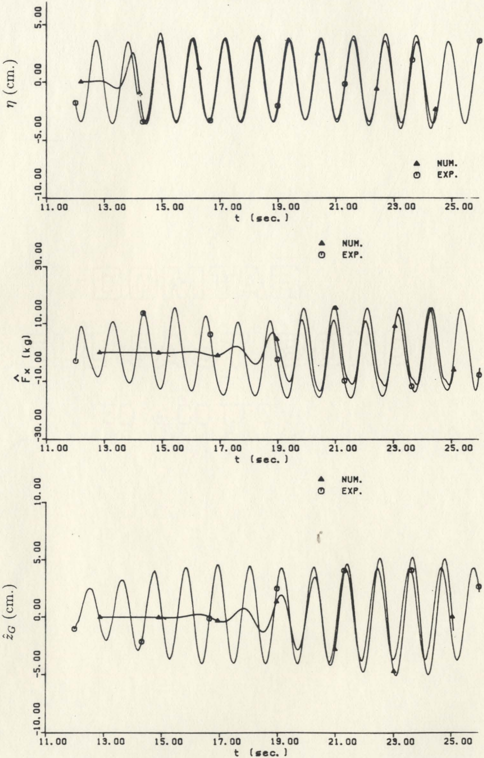

(h) $\omega\sqrt{B/2g} = 0.8078$, $\lambda/B = 4.80$, $H/\lambda = 0.0361$
($T_1 \approx 19.0$ sec., $T_2 \approx 24.5$ sec.)

Figure C.3 continued

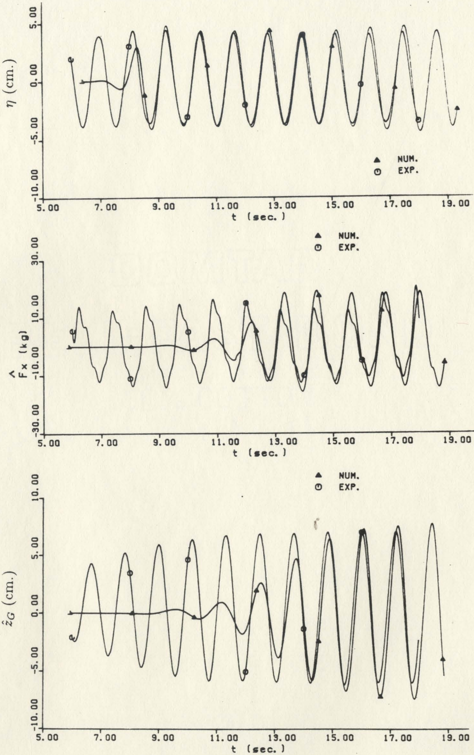

(i) $\omega\sqrt{B/2g} = 0.7630$, $\lambda/B = 5.35$, $H/\lambda = 0.0386$
($T_1 \approx 13.0$ sec., $T_2 \approx 18.5$ sec.)

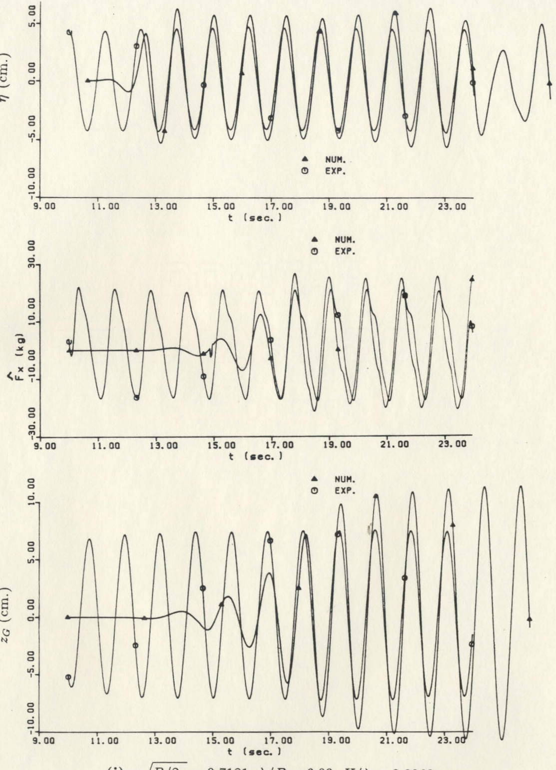

(j) $\omega\sqrt{B/2g} = 0.7181$, $\lambda/B = 6.00$, $H/\lambda = 0.0363$
($T_1 \approx 17.5$ sec., $T_2 \approx 23.5$ sec.)

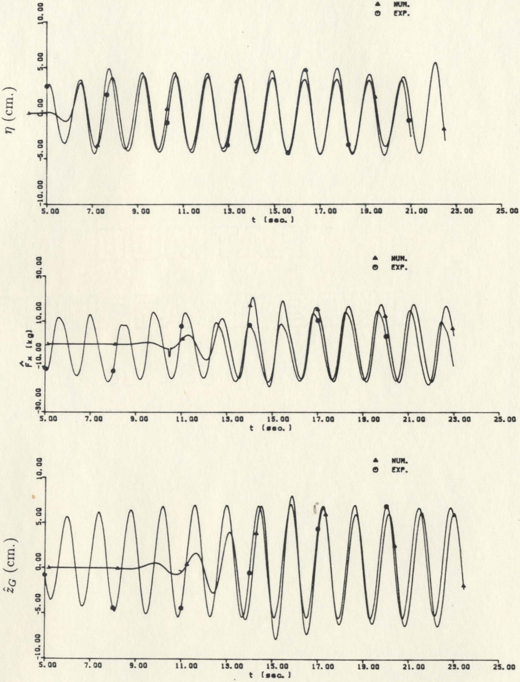

(k) $\omega\sqrt{B/2g} = 0.6283$, $\lambda/B = 7.60$, $H/\lambda = 0.0275$
($T_1 \approx 14.0$ sec., $T_2 \approx 20.5$ sec.)

Figure C.3 continued ⇓

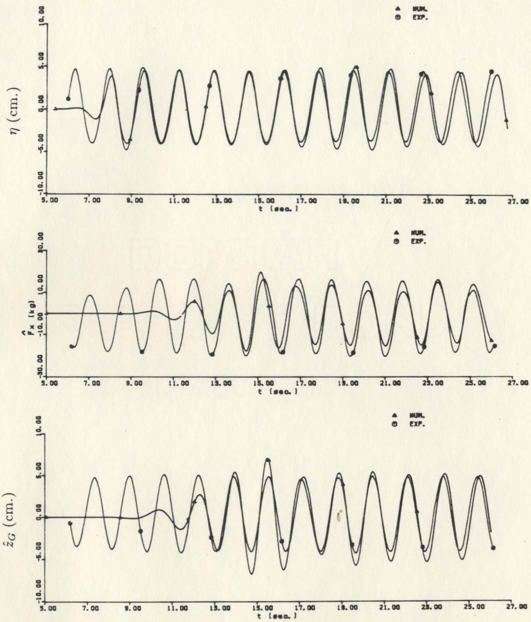

(l) $\omega\sqrt{B/2g} = 0.5386$, $\lambda/B = 9.63$, $H/\lambda = 0.0247$
($T_1 \approx 15.0$ sec., $T_2 \approx 21.5$ sec.)

Figure C.3 Test Series D : comparison of experiment and theory.

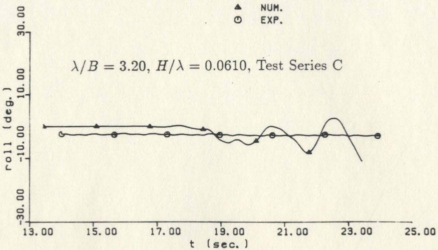

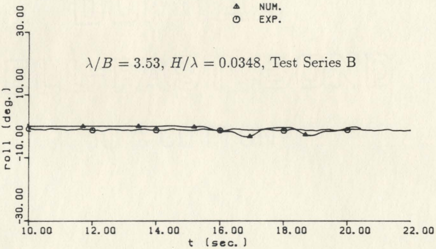

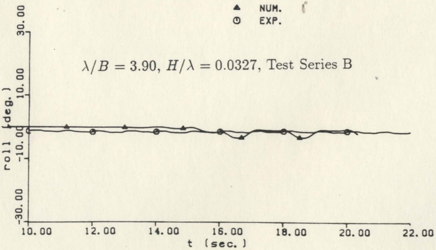

Figure C.4 continued II

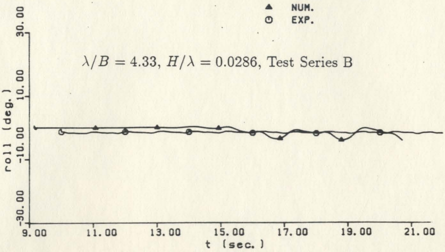

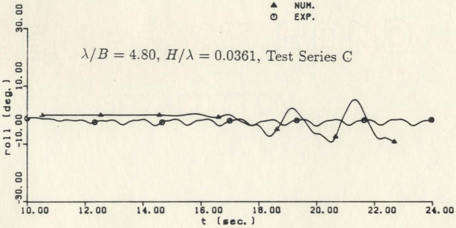

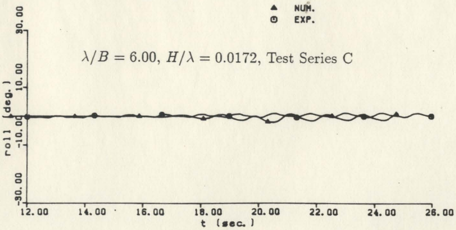

Figure C.4 Roll comparison of experiment and theory

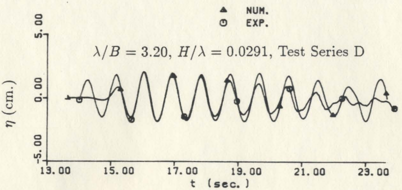

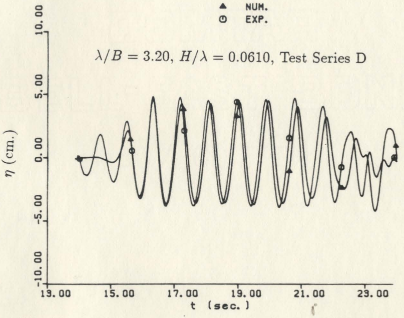

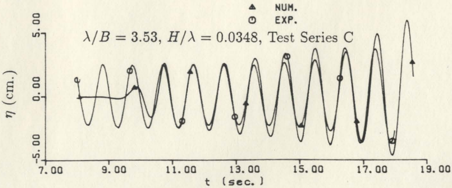

Figure C.5 continued ⇓

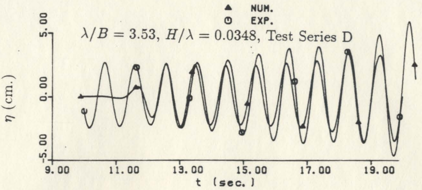

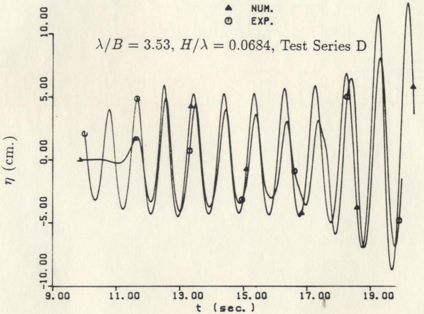

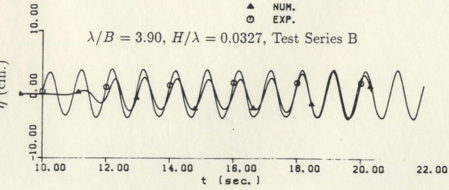

Figure C.5 continued ⇓

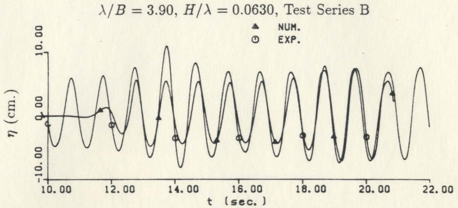

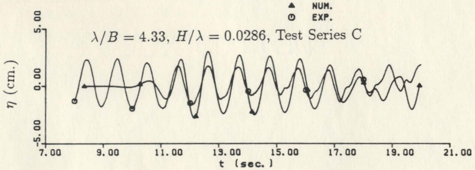

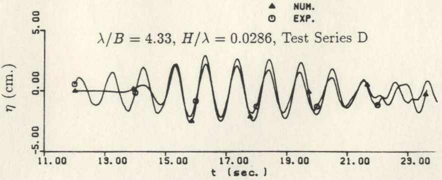

Figure C.5 continued ⇓

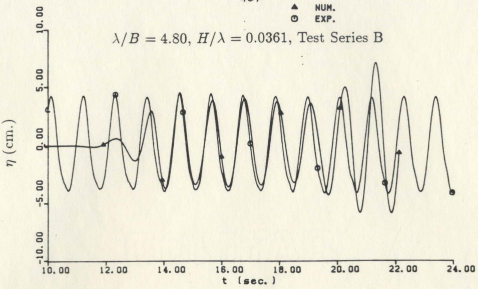

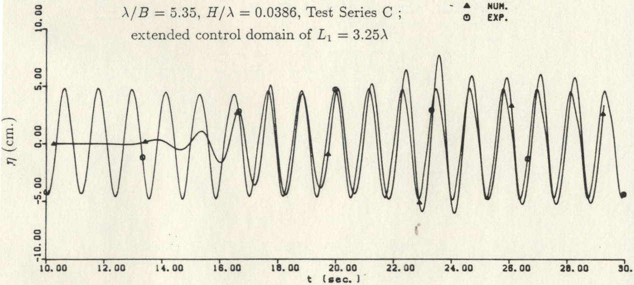

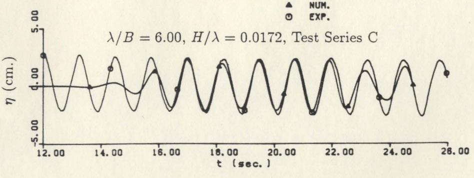

Figure C.5 continued ||

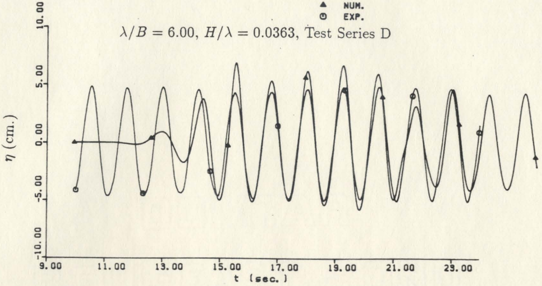

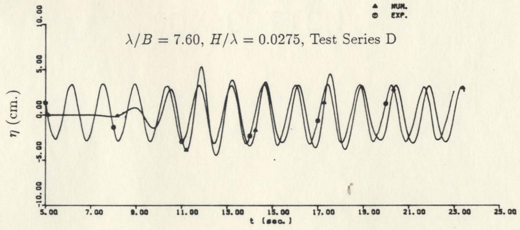

Figure C.5 Wave elevation at the location of probe no. 2 comparison of experiment and theory.

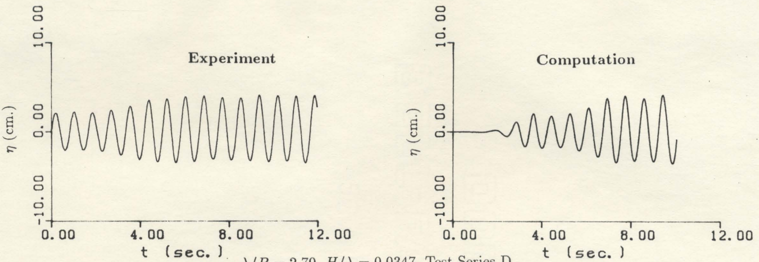

$\lambda/B = 2.70$, $H/\lambda = 0.0347$, Test Series D

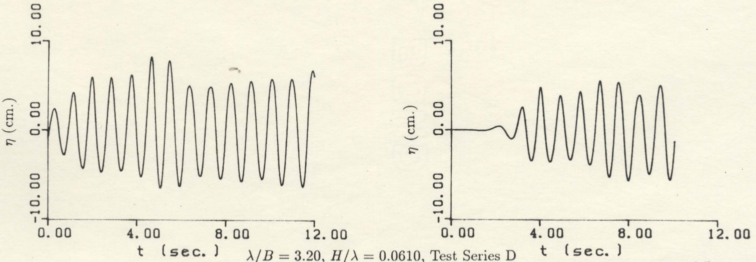

$\lambda/B = 3.20$, $H/\lambda = 0.0610$, Test Series D

Figure C.6 continued ⇓

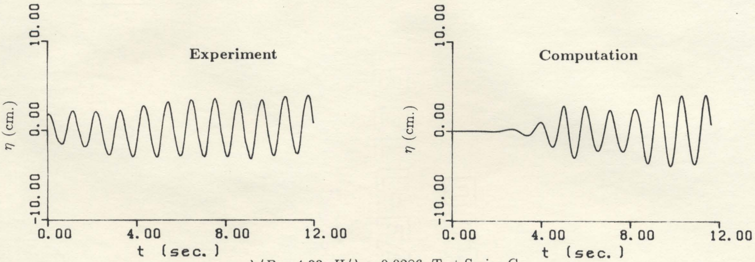

$\lambda/B = 4.33$, $H/\lambda = 0.0286$, Test Series C

Figure C.6 continued ⇓

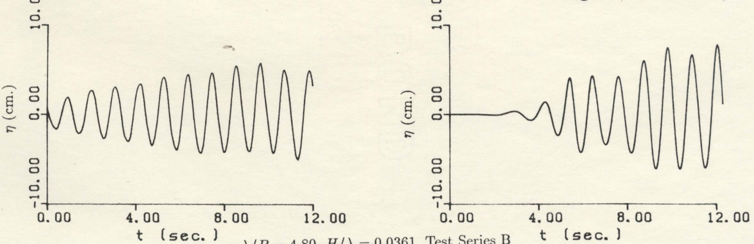

$\lambda/B = 4.80$, $H/\lambda = 0.0361$, Test Series B

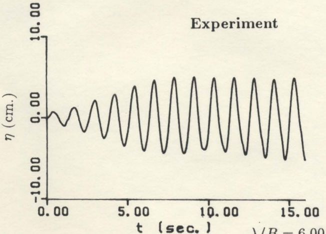

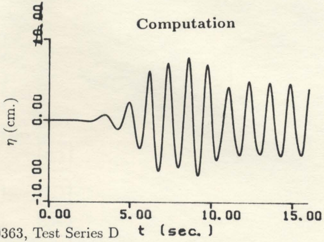

$\lambda/B = 6.00$, $H/\lambda = 0.0363$, Test Series D

Figure C.6 continued ⇓

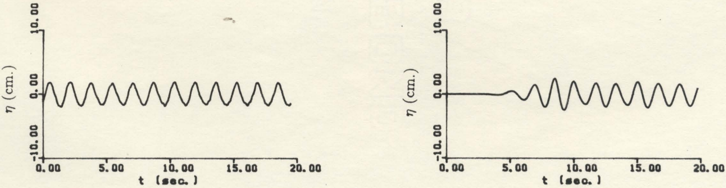

$\lambda/B = 9.63$, $H/\lambda = 0.0125$, Test Series C

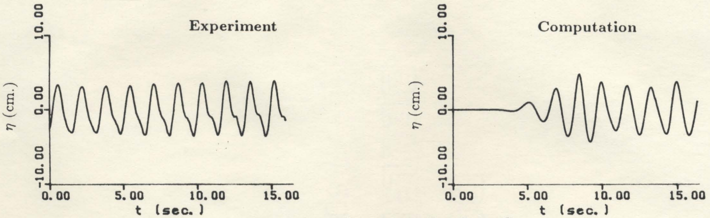

$\lambda/B = 9.63$, $H/\lambda = 0.0229$, Test Series C

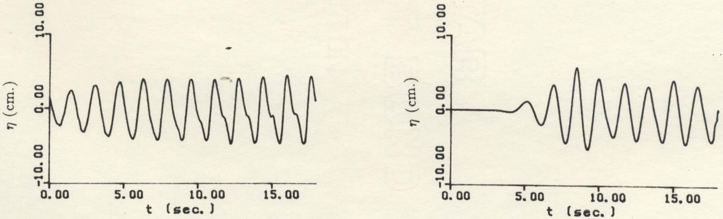

$\lambda/B = 9.63$, $H/\lambda = 0.0275$, Test Series C

Figure C.6 Wave elevation at the location of probe no. 3 (or 5) comparison of experiment and theory.

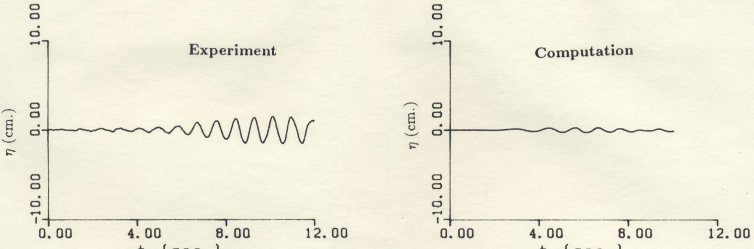

$\lambda/B = 3.20$, $H/\lambda = 0.0610$, Test Series D

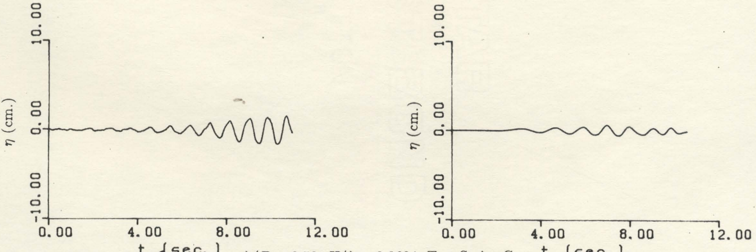

$\lambda/B = 3.53$, $H/\lambda = 0.0684$, Test Series C

Figure C.7 continued ⇓

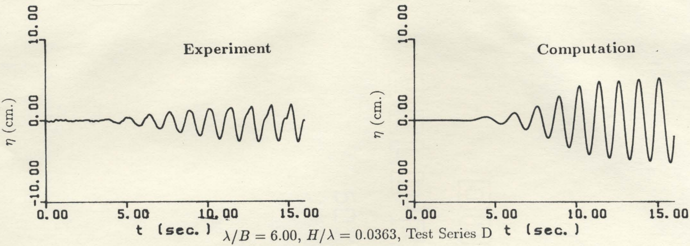

$\lambda/B = 6.00$, $H/\lambda = 0.0363$, Test Series D

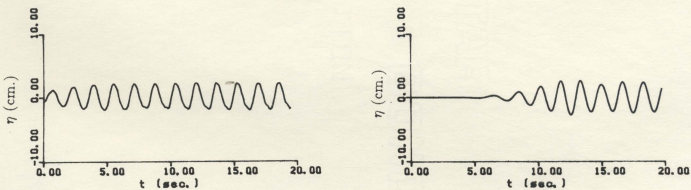

$\lambda/B = 9.63$, $H/\lambda = 0.0125$, Test Series C

Figure C.7 continued ⇓

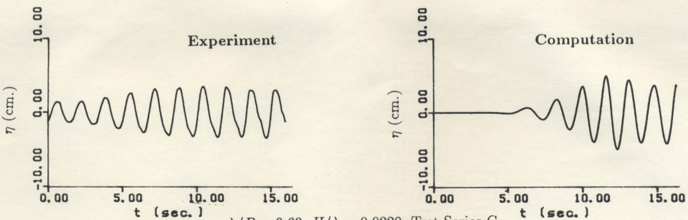

$\lambda/B = 9.63$, $H/\lambda = 0.0229$, Test Series C

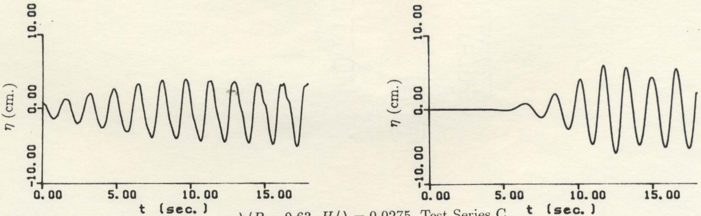

$\lambda/B = 9.63$, $H/\lambda = 0.0275$, Test Series C

Figure C.7 Wave elevations downstream of the body : comparison of experiment and theory; experimental plot is for probe no. 4 while the numerical results are taken at a station at a distance of λ downstream of the body, measured from body's CG location.